ADA045651

AFAL-TR-76-213

ADVANCED ARCHIVAL MEMORY

Corporate Research and Development
General Electric Company
Schenectady, New York 12345

July 1977

Quarterly Report No. 1   April 15, 1976 — July 15, 1976

DDC FILE COPY
AD No.

D D C
RECEIVED
OCT 27 1977
B

AIR FORCE AVIONICS LABORATORY
AIR FORCE WRIGHT AERONAUTICAL LABORATORIES
AIR FORCE SYSTEMS COMMAND
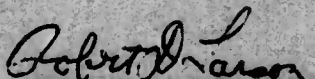WRIGHT-PATTERSON AIR FORCE BASE, OHIO 45433

NOTICE

When Government drawings, specifications, or other data
are used for any purpose other than in connection with a
definitely related Government procurement operation, the United
States Government thereby incurs no responsibility nor any
obligation whatsoever; and the fact that the government may have
formulated, furnished, or in any way supplied the said drawings,
specifications, or other data, is not to be regarded by impli-
cation or otherwise as in any manner licensing the holder or
any other person or corporation, or conveying any rights or
permission to manufacture, use, or sell any patented invention
that may in any way be related thereto.

This report has been reviewed by the Information Office (OI) and is
releasable to the National Technical Information Service (NTIS). At NTIS it
will be available to the general public, including foreign nations.

This technical report has been reviewed and is approved for publication.

JOHN M. BLASINGAME
Project Engineer

FOR THE COMMANDER

ROBERT D. LARSON, Chief
Electronic Research Branch
Air Force Avionics Laboratory

Copies of this report should not be returned unless return
is required by security considerations, contractual obligations,
or notice on a specific document.

REPORT DOCUMENTATION PAGE	READ INSTRUCTIONS BEFORE COMPLETING FORM

1. REPORT NUMBER	2. GOVT ACCESSION NO.	3. RECIPIENT'S CATALOG NUMBER
AFAL-TR-76-213		

4. TITLE (and Subtitle)	5. TYPE OF REPORT & PERIOD COVERED
Advanced Archival Memory.	Quarterly Report No. 1 April 15-July 15, 1976
	6. PERFORMING ORG. REPORT NUMBER SRD-77-058

7. AUTHOR(s)	8. CONTRACT OR GRANT NUMBER(s)
C. Q. Lemmond, G. E. Possin, C. G. Kirkpatrick, H. G. Parks, J. F. Norton	F33615-76-C-1322

9. PERFORMING ORGANIZATION NAME AND ADDRESS	10. PROGRAM ELEMENT, PROJECT, TASK AREA & WORK UNIT NUMBERS
Corporate Research and Development, General Electric Company Schenectady, New York 12301	ARPA Order 3194

11. CONTROLLING OFFICE NAME AND ADDRESS	12. REPORT DATE
Defense Advanced Research Project Agency 1400 Wilson Boulevard Arlington, Virginia 22209	Jul 77
	13. NUMBER OF PAGES 332

14. MONITORING AGENCY NAME & ADDRESS(if different from Controlling Office)	15. SECURITY CLASS. (of this report)
Department of the Air Force (AFAL/DHR) Air Force Avionics Laboratory (AFSC) Wright-Patterson Air Force Base, Ohio 45433	Unclassified
	15a. DECLASSIFICATION/DOWNGRADING SCHEDULE

16. DISTRIBUTION STATEMENT (of this Report)

Approved for public release; distribution unlimited.

Quarterly rept. no. 1, 15 Apr - 15 Jul 76,

17. DISTRIBUTION STATEMENT (of the abstract entered in Block 20, if different from Report)

D D C
RECEIVED
OCT 27 1977
B

18. SUPPLEMENTARY NOTES

19. KEY WORDS (Continue on reverse side if necessary and identify by block number)

Computer
Memory Systems
Electron Optics
Ion Optics
Ion Implantation
Alloy Junction

20. ABSTRACT (Continue on reverse side if necessary and identify by block number)

During this reporting period, effort in the archival memory program included experimental work and theoretical studies on a planar diode structure (memory target substrate), implantation of ions to write information on a planar diode structure, feasibility studies of the alloy junction method of writing, and the specification of a high performance electron beam write station for alloy junction writing. (continued on next page)

DD FORM 1473 EDITION OF 1 NOV 65 IS OBSOLETE
1 JAN 73

next page

406 617

20.

A detailed analytical modeling study was initiated in order to properly design the planar diode and to understand the results of experimental testing. The initial model design was used during the period to compare test results with theory and define new processing experiments.

An improved method of ion writing using inert ions to form damage sites was shown to be feasible. Preliminary results indicate a lower writing fluence will be required.

Alloy junction diodes were formed using a laser beam. Diodes as small as 5 microns were formed.

An electron optical system, consisting of a high performance field emission source and focusing optics, was specified and a purchase order was placed.

ACCESSION for

NTIS	White Section	☑
DDC	Buff Section	☐
UNANNOUNCED		☐
JUSTIFICATION		

BY
DISTRIBUTION/AVAILABILITY CODES

| Dist. | AVAIL and/or | SPECIAL |
| A | | |

The objective of this basic research program is to investigate the feasibility of new storage techniques for large archival memories using ion and electron beam with semiconductor targets. The goal is the development of an archival memory capable of storing 10^{14} to 10^{15} bits with rapid access to the stored information.

The currently funded effort (Phase I) deals with feasibility studies of key technical areas. The program covers experimental and analytical investigations: (1) to demonstrate the feasibility of ion implanted and alloy junction storage media, (2) to determine the feasibility of beam optics design required for writing/reading on the media, and (3) to select the better of the two storage methods and perform a preliminary paper design of the concept for further development.

During this reporting period, effort in the archival memory program included experimental work and theoretical studies on a planar diode structure (memory target substrate), implantation of ions to write information on a planar diode structure, feasibility studies of the alloy junction method of writing, and the specification of a high performance electron beam write station for alloy junction writing.

A detailed analytical modeling study was initiated in order to properly design the planar diode and to understand the results of experimental testing. The initial model design was used during the period to compare test results with theory and define new processing experiments.

An improved method of ion writing using inert ions to form damage sites was shown to be feasible. Preliminary results indicate a lower writing fluence will be required.

Alloy junction diodes were formed using a laser beam. Diodes as small as 5 microns were formed.

An electron optical system, consisting of a high performance field emission source and focusing optics, was specified and a purchase order was placed.

TABLE OF CONTENTS

TABLE OF CONTENTS
(continued)

Section I

SUMMARY

Program Objectives

The objective of this basic research program is to investigate the feasibility of new storage techniques for large archival memories using ion and electron beams with semiconductor targets. The goal is the development of an archival memory capable of storing 10^{14} to 10^{15} bits with rapid access to the stored infromation.

The currently funded effort (Phase I) deals with feasibility studies of key technical areas. The program covers experimental and analytical investigations: (1) to demonstrate the feasibility of ion implanted and alloy junction storage media, (2) to determine the feasibility of beam optics design required for writing/reading on the media, and (3) to select the better of the two storage methods and perform a preliminary paper design of the concept for further development.

Accomplishments

During this reporting period, effort in the archival memory program included experimental work and theoretical studies on a planar diode structure (memory target substrate), implantation of ions to write information on a planar diode structure, feasibility studies of the alloy junction method of writing, and the specification of a high performance electron

1

beam write station for alloy junction writing.

1. Planar Diode Studies

The target substrate on which data will be stored is a large area planar diode. The diode provides a mechanism for signal amplification within the target structure. The top layer of the diode is much thinner than more normal planar diodes and constitutes a departure in design. In order to resolve the 0.1 micron stored data bits, the junction must be within ~ 1000Å of the surface and the electron beam energy must be in the 2-3 keV range. This dictates a diode with little or no "dead" region near the surface and a junction depth ~ 1000Å. A "dead layer" is defined as the region in which carriers generated by the electron beam are not collected by the diode.

Various combinations of materials are possible. Both germanium and silicon with a wide variety of dopants are candidate diode structures. In order to properly design the diode and to understand the results of experimental testing, a detailed analytical modeling study was initiated. The model is designed to consider the probability of carrier capture at the planar junction, as affected by doping gradients and other parameters. The initial model design was used during the period to compare test results with theory and define new processing experiments.

2

2. Ion Writing Experiments

One of the two storage concepts under study is to write bits of information as small (0.1 micron diameter) surface diodes by ion implantation. During the period an interesting possibility for an improved writing mechanism was discovered. This new method involves the use of inert ions to form damage sites rather than doped sites. To test the concept, helium implants were made and showed excellent readout characteristics. More detailed work is planned for the next reporting period. However, preliminary results would indicate that a much lower fluence will be required for this form of writing.

3. Alloy Junction Writing Experiments

Alloyed junctions between a thin metal coating and the surface of a planar diode will be made with a high brightness, finely focused electron beam. Until an experimental electron beam test facility is established, experiments were conducted using a laser as the writing beam. Alloy junction diodes were formed at the surface of a planar diode and demonstrated basic feasibility for this type of archival memory storage. Diodes in size of 5-7 microns were formed (limited by the spot size of the focused laser beam). Additional experiments are anticipated. However, future efforts will be more concentrated on the thermal mechanisms at the metal-semiconductor interface and the selection of the most desirable systems.

3

4. Electron Beam Write Column

An electron optical system, consisting of a high performance field emission source and focusing optics, was specified and a purchase order was placed. Delivery is expected during the second quarter of the contract. This equipment will be used to conduct alloy junction writing experiments.

Plans for Next Quarter

The overall Program Schedule lists the major areas of development envisioned for the next period. The current investigation will continue with refinements to the analytical modeling studies. In addition, studies of both electron and ion optics will be initiated as beam performance parameters become known as a result of the theoretical and experimental work. The electron optical system for alloy junction writing is expected during the quarter.

Data Included in this Report

To provide a fuller understanding of the physics of these recording methods, a large body of substantiating information is included in this report. Specifically the two Appendices, "Ion Implantation" and "Electron Penetration into Solids" contain background information pertinent to the methods under study.

PROGRAM SCHEDULE

SYSTEM (Project) NUMBER: F33615-76-C-1322

SUBSYSTEM: General Electric Co.

TYPE OF SCHEDULE: Monthly Progress

AS OF DATE: July 15, 1976

L I N E	Task	COMPLETION DATES
1	Advanced Archival Memory	
2	Develop Planar Diode-Ion Implant	
3	Demonstrate Resolution Limits -	
4	Ion Implant	
5	Modeling Studies of Surface Diodes	
6	Ion and Alloy Junction	
7	Develop Planar Diode - Alloy Junc.	
8	Laser Fabricated Alloy Junction	
9	Surface Diodes	
10	Determine Surface Diode Character-	
11	istics - Ion & Alloy Junction	
12	Beam Optics Study	
13	Procure Electron Optics for Alloy	
14	Junction Diode Writing	
15	Determine Better of Two Storage	
16	Approaches	
17	Demonstrate Resolution Limits-	
18	Alloy Junction	
19		
20		
21		
22	Monthly Report	
23	Interim Report - Draft	
24	Interim Report - Final	
25	Final Report - Draft	
26	Final Report - Final	
27		

FY 1976 CY 1976 FY 19 77 CY 19 FY 19 19 19 19

Expenditure X $1,000

500
400
300
200
100
0

AUTHENTICATION $489,500

April 15, 1976 to July 15, 1977

Section II

MEMORY CONCEPT

The approach selected for the development of a large
advanced archival memory with rapid access employs beams for
the writing and reading processes. Finely focused beams can
permanently inscribe a material, producing a record of archival
character. Beams can also be used to read or sense the stored
information. Data can be written, read, and accessed rapidly,
because beams can be deflected at extremely high rates.
Finally, for a memory of 10^{14} - 10^{15} bits, the density of storage
is a critical parameter. Beams can be imaged to spot diameters
that are fractions of a micron in size.

This research effort is directed toward the writing of
data by the formation of small diodes at the surface of a semi-
conductor plane (silicon or germanium) by the action of a finely
focused beam (ion or electron). The presence or absence of
diodes represents stored zeros or ones.

For writing data, two methods for forming surface diodes
will be evaluated, and the more promising one will be selected
for further development. The two writing methods are:

- Ion Implanted Surface Diodes
- Alloy Junction Surface Diodes

Data Storage

Ion implantation of surface diodes is a candidate storage technique. A finely focused ion beam is scanned over a small area of a silicon wafer and modulated on-off to form by implantation small surface diodes. Once the field is written, the wafer is stepped to a new location for additional writing. This method is shown schematically in Figure 1.

It is the goal of this study to show that it is feasible to form 0.1 micron size diodes in the surface of a silicon wafer by use of a finely focused ion beam. It is believed that diodes of this size can be formed and that this high resolution can be preserved because the implanted ions will have very little lateral spread. Diodes as small as 0.5 microns have been formed by ion implantation through a mask.

Formation of surface diodes by the alloy junction method involves the use of an electron beam to alloy two materials. As example, a germanium target coated with a thin indium layer would be exposed to a finely focused electron beam. A thermal bias would maintain the target within a few degrees of the alloying temperature of 160°C. The electron beam would locally heat the surface to 160°C, causing the alloy to form where data are to be recorded. Figure 2 illustrates this method schematically. The finely focused electron beam would be electronically positioned to any location on the memory storage plane by use of a matrix

7

ION SOURCE

ELECTRON SOURCE

BEAM DEFLECTION

BEAM DEFLECTION

MATRIX LENS

X-Y TARGET MOTION

WRITE STATION
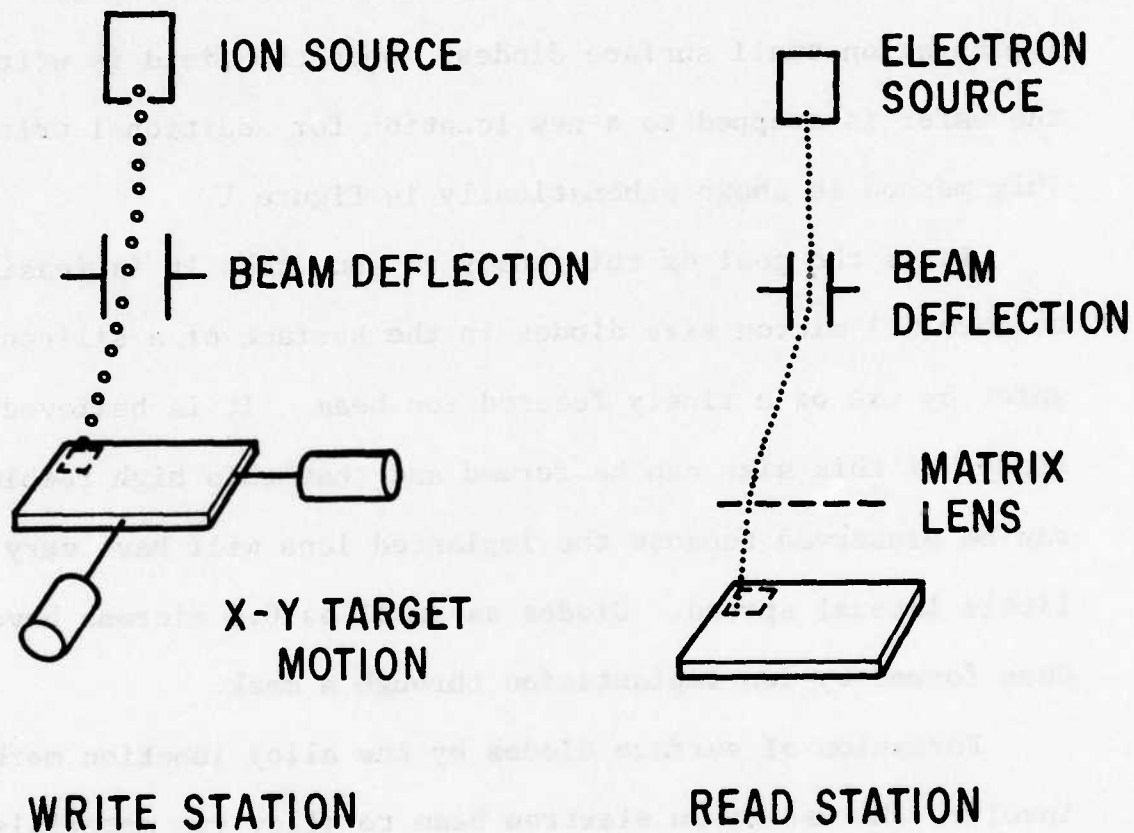
READ STATION

Figure 1.   Schematic Diagram - Ion Implanted Surface Diodes Write-Read
            Stations.

8

ELECTRON SOURCE

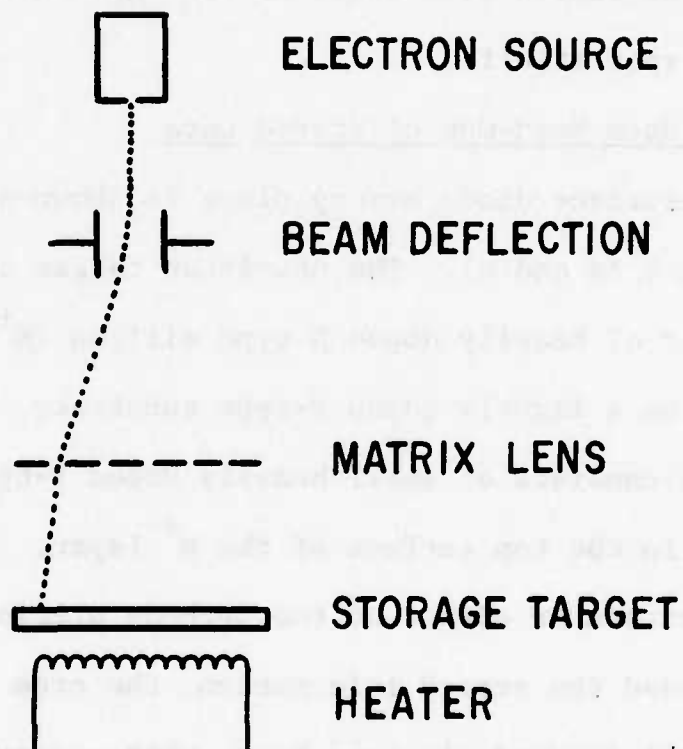BEAM DEFLECTION

MATRIX LENS

STORAGE TARGET

HEATER

Figure 2. Schematic Design - Alloy Junction Surface Diode
Write-Read Station.

9

lens. This lens, sometimes called a fly's eye lens, is an array of small electron lenses (lenselets), each with the capability of beam deflection. In this case the complete memory plane could be written without the need for mechanical motion.

This technique has very high resolution because the thermal diffusion of heat in a germanium substrate is very rapid. The heated area would be confined to the size of the electron spot itself.

Electron Beam Read-Out of Stored Data

The surface diode memory plane is shown schematically in Figure 3 (a and b). The unwritten target consists of a thin layer of heavily doped N-type silicon (N^+ layer), as example, on a lightly doped P-type substrate. Stored information consists of small heavily doped P-type regions (P^+ regions) in the top surface of the N^+ layer. These diodes can be written by either of the methods previously described.

To read the stored information, the area is scanned with a well focused electron beam, with energy ~2.5 keV. This produces one electron hole pair for every 3.6 eV of beam energy (~700 pairs for a 2.5 keV beam). When the electron beam impinges on an unrecorded area (one), the minority carriers (holes) diffuse to the N^+P diode depletion region and generate a signal current, I_s, in the external diode biasing circuit
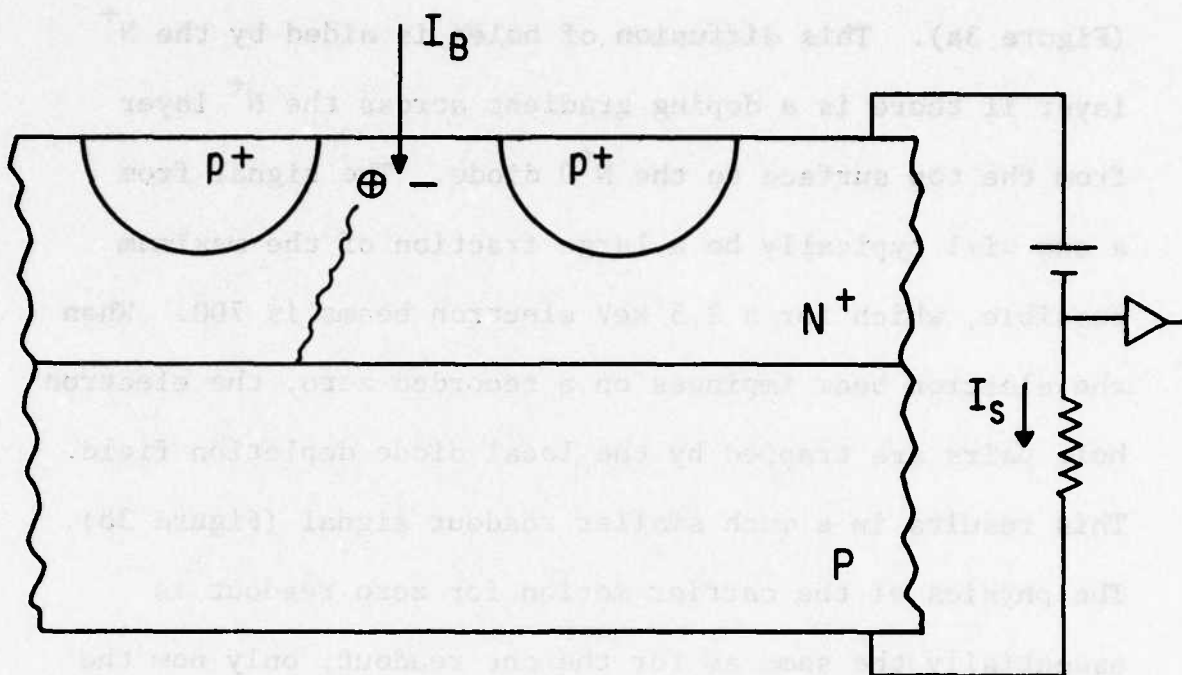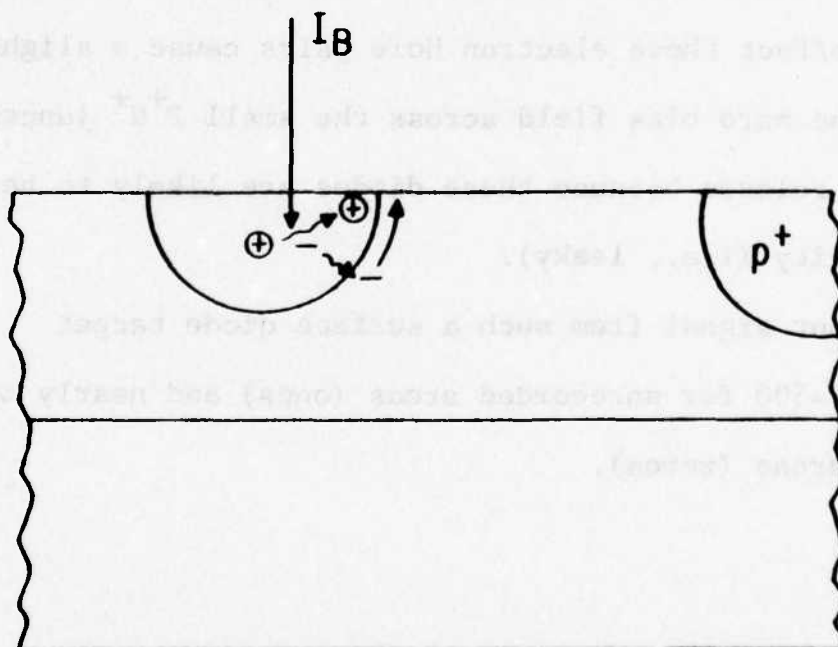
Figure 3-a. Readout of One

Figure 3-b. Readout of Zero

11

(Figure 3a). This diffusion of holes is aided by the N^+ layer if there is a doping gradient across the N^+ layer from the top surface to the N^+P diode. The signal from a one will typically be a large fraction of the maximum possible, which for a 2.5 keV electron beams is 700. When the electron beam impinges on a recorded zero, the electron hole pairs are trapped by the local diode depletion field. This results in a much smaller readout signal (Figure 3b). The physics of the carrier motion for zero readout is essentially the same as for the one readout, only now the collecting junction (P^+N^+ instead of N^+P) is not connected to the readout circuit and the generated carriers recombine locally. In effect these electron hole pairs cause a slight collapse of the zero bias field across the small P^+N^+ junction, which quickly relaxes because these diodes are likely to be of very poor quality (i.e., leaky).

The readout signal from such a surface diode target would then be ~500 for unrecorded areas (ones) and nearly zero for recorded areas (zeros).

12

Section III

PLANAR DIODE STUDIES

Introduction

During the first quarter of the Archival Memory Program much
of the experimental work has centered upon achieving the appropriate
planar diode substrate on which the information may be later written.
Both schemes of writing, the ion implantation and alloy junction
methods, require such a planar diode structure. Ion implantation
was employed for fabrication of these planar diodes because of the
uniformity and control that can be achieved by this method.

This section first summarizes the surface diode target concept
with emphasis on those aspects which relate to the requirements on
the planar diode structure. Then work during the first quarter
directed towards meeting these goals is discussed.

Target Concept

The target concept is shown schematically in Figure 4. The
unwritten target consists of a thin layer of heavily doped N-type
silicon (N^+ layer) on a lightly doped P-type substrate. Stored
information consists of small heavily doped P-type regions (P^+
regions) or damaged regions in the top surface of the N^+ layer.
The complementary structure with N^+ diodes in a P^+ surface on N is
also possible. For clarity, on the N^+ on P structure is discussed.
The small P^+ regions form small unbiased diodes with the N^+ layer.
These diodes can be written by several methods, such as focused
ion beams, alloy writing, or variations on electron beam lithography.
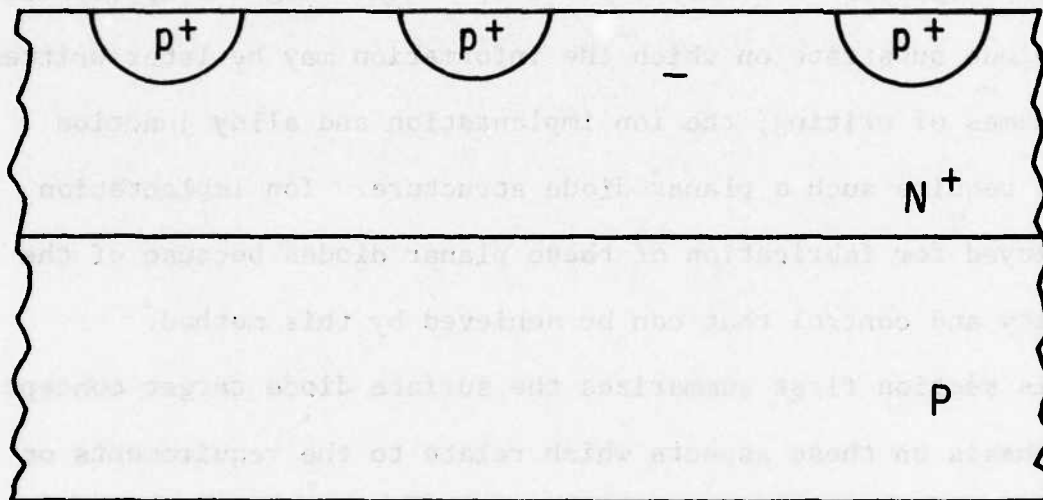
-13-

p+   p+   p+

−

N+

P

Figure 4. Surface Diode Target with Recorded Data.

To read the stored information, the area is scanned with a well focused electron beam, with energy $\sim$2.5 keV. This produces one electron hole pair for every 3.6 eV of beam energy ($\sim$700 pairs for a 2.5-keV beam). When the electron beam impinges on an unrecorded area (one), the minority carriers (holes) diffuse to the N^+P diode depletion region and generate a signal current, I_s, in the external diode biasing circuit (Figure 5). This diffusion of holes is aided by the N^+ layer if there is a doping gradient across the N^+ layer from the top surface to the N^+P diode. The signal from a one will typically be a large fraction of the maximum possible, which for 2.5-keV electron beams is 700. When the electron beam impinges on a recorded zero, the electron hole pairs are trapped by the local diode depletion field. This results in a much smaller readout signal (Figure 6). The physics of the carrier motion for zero readout is essentially the same as for the one readout, only now the collecting junction (P^+N^+ instead of N^+P) is not connected to the readout circuit and the generated carriers recombine locally. In effect these electron hole pairs cause a slight collapse of the zero bias field across the small P^+N^+ junction, which quickly relaxes because these diodes are likely to be of very poor quality (i.e., leaky). To further short the diodes and speed the relaxation, a thin metal top layer or very heavy N^+ surface doping can be used.
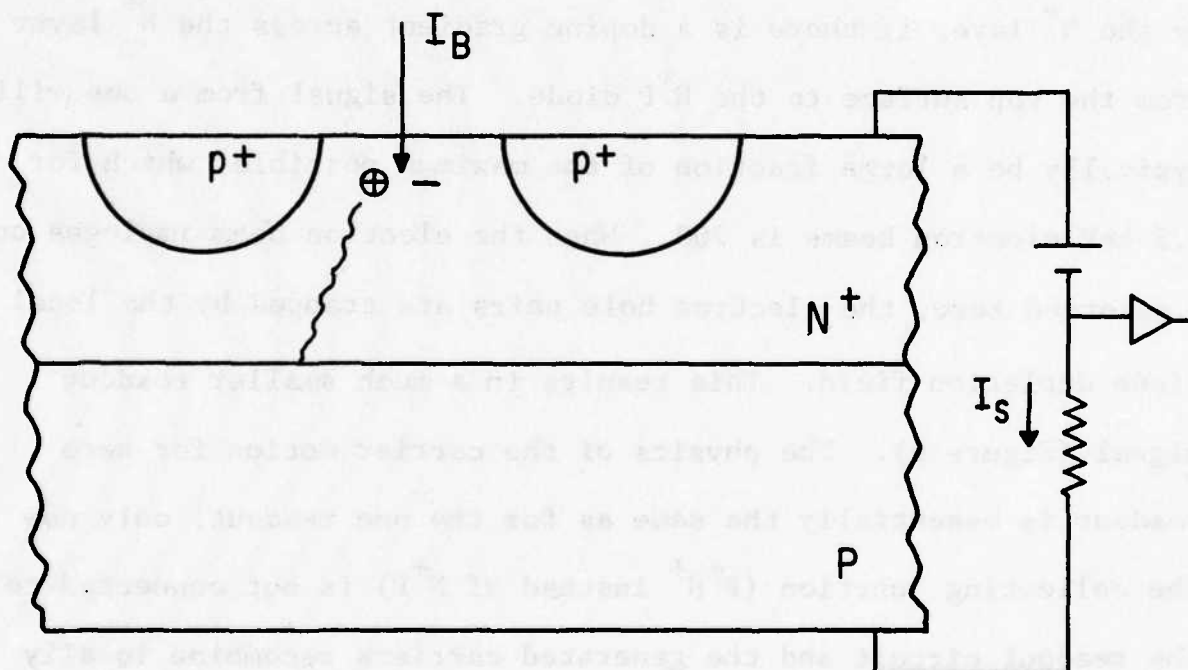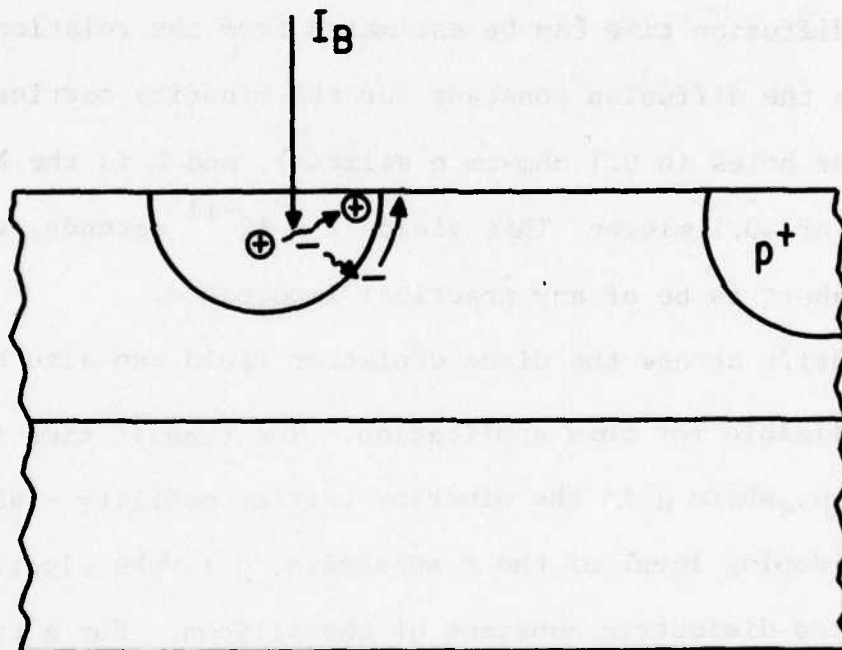
Figure 5   Readout of One

Figure 6   Readout of Zero

The readout signal from such a surface diode target would then be ~500 for unrecorded areas (ones) and nearly zero for recorded areas (zeros).

Frequency Response

The frequency response of the target can be extremely high. The intrinsic target limitations on frequency response are the diffusion or drift of carriers to and across the depletion layer of the N^+P junction and the RC response of the diode capacitance.

The diffusion time can be estimated from the relation $\tau_d = L^2/D$, where D is the diffusion constant for the minority carriers (D = 5 cm^2/sec for holes in 0.1 ohm-cm n silicon), and L is the N^+ layer thickness of ~0.1 micron. This yields 2×10^{-11} seconds, which is much too short to be of any practical importance.

The drift across the diode depletion field can also be shown to be negligible for this application. The transit time is $\tau_t = 2\epsilon/qN_A\mu$, where μ is the minority carrier mobility = 480 cm^2/V sec, N_A is the doping level of the P substrate, q is the electronic charge, and ϵ is the dielectric constant of the silicon. For a typical doping level of $10^{13}/cm^2$, this gives 2.7×10^{-9} seconds.

The dominant response limitation is therefore the RC time constant of the diode capacitance and the resistance of the N and P layers. The resistance of the P layer (back side of the target) can be made negligible by a heavily doped back surface and a back

metalization. These same methods can be applied with caution to the top surface, but they may interfere with the target operation and in particular introduce a dead layer. The resistance of the top target surface without a metal layer would be $(10^{16}/N_s)$ ohms/square where N_s is the surface doping in dopant atoms/cm^2. For the range contemplated for this device, N_s would be between 10^{12} and 10^{14}/cm^2. This gives a top surface layer resistance of between 10^4 and 10^2 ohms/square. The diode capacitance is limited ultimately by the avalanche breakdown of the diode and by the substrate doping. For 100 ohm-cm p substrates operated near avalanche, this minimum capacitance limit is 50 pF/cm^2. Diodes operating near this limit are now used in similiar devices such as particle detectors, electron beam bombarded microwave amplifiers and BEAMOS devices.

The target frequency response can be modeled as an RC transmission line where the resistance and capacitance are proportional to 1/R and R, respectively, where R is the distance from the target center (Figure 7). The target is assumed circular and the beam is assumed incident at the target center, for simplicity. The solution for the external target current $(i_o(t))$ for an impulse current input beam current pulse $(i_1(t) = \delta(t))$ is shown in Figure 8. a is the target radius, r is the resistance per square of the N$^+$-layer and c is the diode capacitance/cm^2. The response
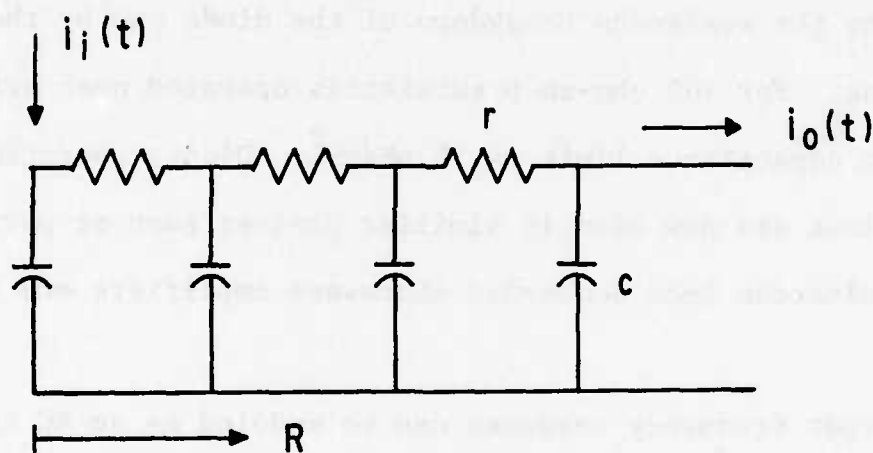
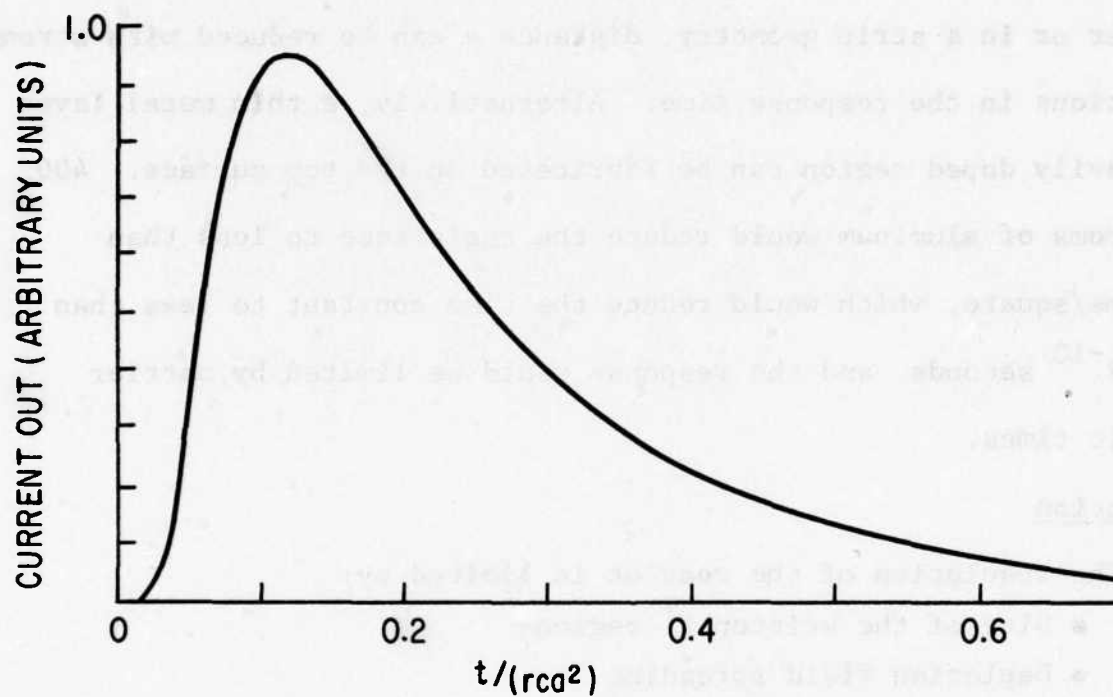Figure 7. Frequency Response Schematic Equivalent Circuit

Figure 8. Output Current for Impulse Current Input to Radial RC Transmission Line

time is approximately $0.3a^2 rc$ or the frequency response cutoff $f_c \sim 3/a^2 rc$. For a 2-cm-diameter target with 100-pF/cm^2 diode capacitance and 1000 ohms/square N$^+$ layer, this gives 33 MHz, which is acceptable. To reduce the response time still further, several approaches can be taken. By fabricating the target segments smaller or in a strip geometry, distance a can be reduced with strong reductions in the response time. Alternatively, a thin metal layer or heavily doped region can be fabricated on the top surface. 400 angstroms of aluminum would reduce the resistance to less than 10 ohms/square, which would reduce the time constant to less than 3×10^{-10} seconds, and the response would be limited by carrier transit times.

Resolution

The resolution of the readout is limited by:
- Size of the written P$^+$ regions
- Depletion field spreading
- Lateral diffusion of minority carriers in the N$^+$ layer
- Scattering of the reading electron beam
- Electron beam spot size

Size of Written P$^+$ (or N$^+$) Regions

This size will depend on the writing process used. It will be assumed in this section that doped regions of any size can be produced by the writing process.

Depletion Field Spreading

The built-in voltage of the P^+N^+ junction spreads in both directions from the metallurgical junction. The depleted region spreads until the number of ionized dopants in the depleted region balances the built-in voltage. The width of the depleted region in the abrupt junction approximation is given by

$$W = \sqrt{\frac{2\,\varepsilon_{si}}{q}\,\frac{N_A + N_D}{N_A N_D}\,\varphi_T} \qquad (1)$$

where ε_{si} is the dielectric constant of the semiconductor, q is the electronic charge, N_A and N_D are the doping levels of the acceptor and donors in the P^+ and N^+ sides of the junction, respectively, and φ_T is the built-in voltage of the junction. φ_T depends on doping levels, but for heavily doped junctions such as those considered here, $\varphi_T \cong 0.9$ volt. For a symmetric junction, $N_A = N_D$ and the electric field distribution is shown in Figure 9, where x is measured relative to the matallurgical junction; $\varepsilon_m = \varphi_{T/W}$ for a symmetric junction. The dependence of W on N_A for $N_A = N_D$ is shown in Figure 10. Hence the effective size of the P^+ doped region is D + W, where D is the diameter of the doped region. It should also be noted that the N^+ layer must be thick enough so that the depth of the doped P^+ region + W/2 does not exceed the N^+ region thickness, or the small P^+ diode would short to the P^+ substrate and give high (not low) readout gain, as desired.
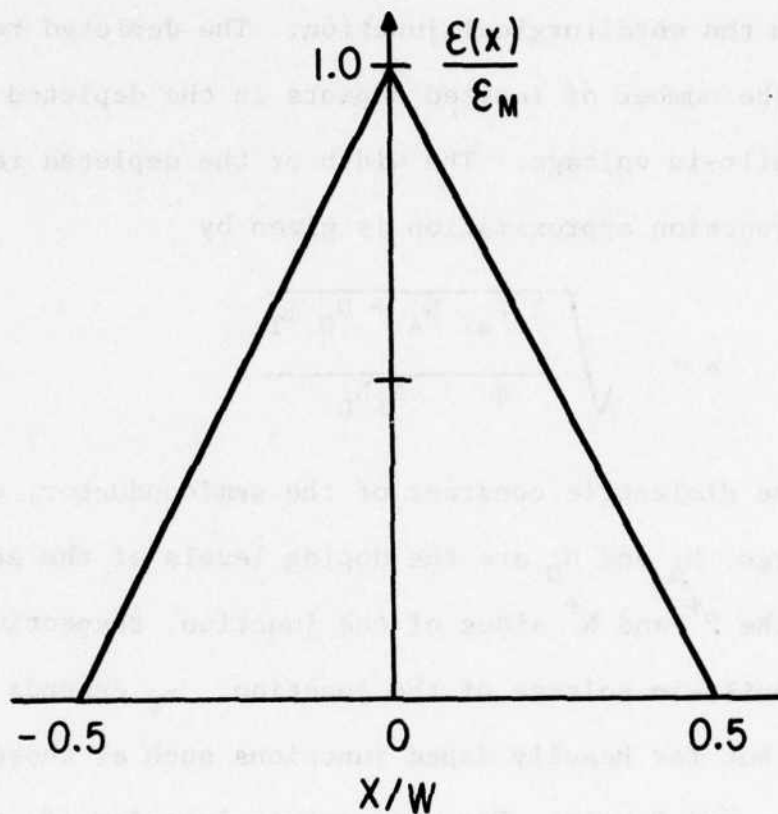
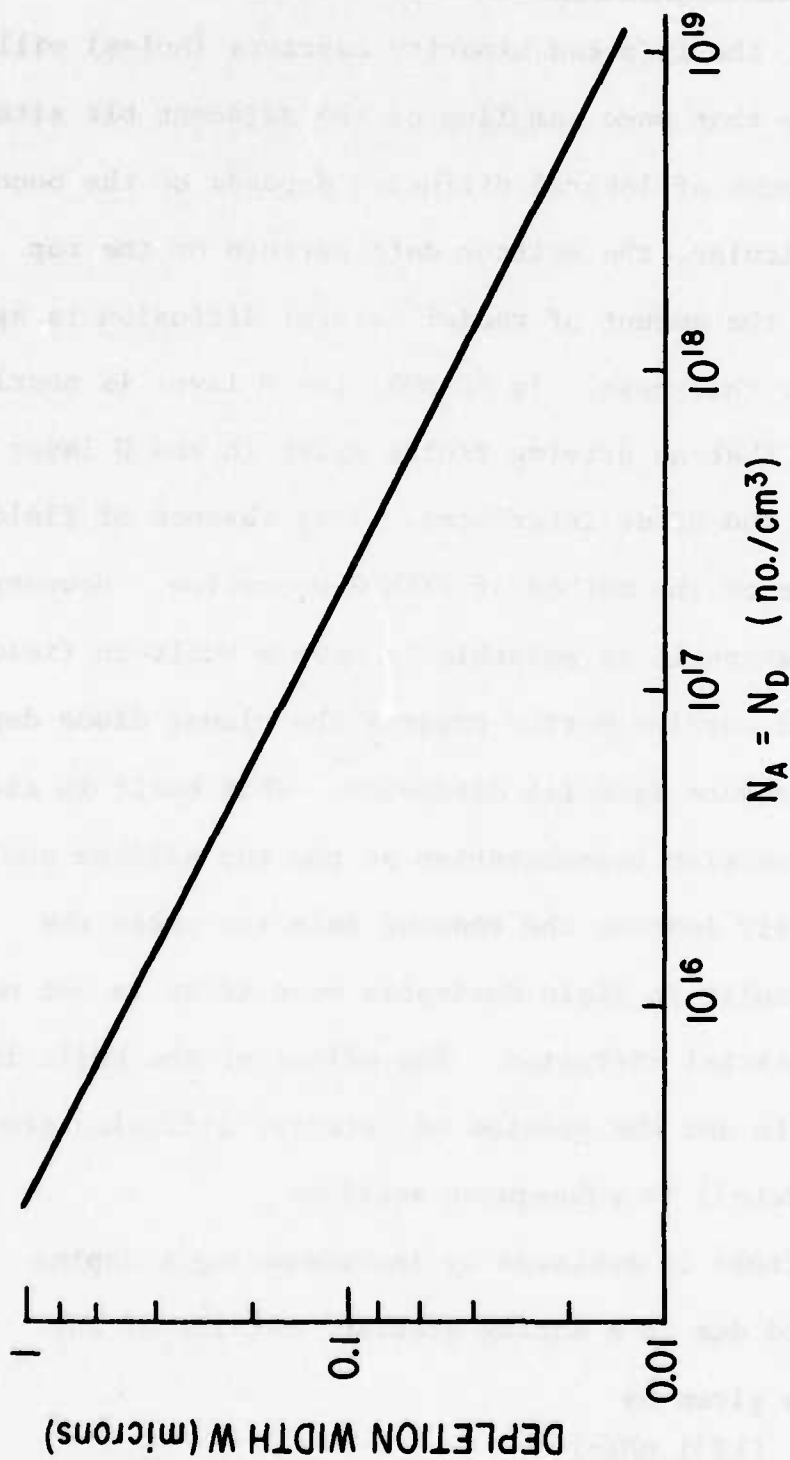Figure 9. Electric Field Distribution in Symmetric Junction

$N_A = N_D$ (no./cm^3)

DEPLETION WIDTH W (microns)

Figure 10. Diode Depletion Width W Versus Doping Level for Silicon Symmetric Junction

Lateral Diffusion of Minority Carriers in N^+ Layer

During reading, the injected minority carriers (holes) will diffuse laterally so that some sampling of the adjacent bit site will occur. The amount of lateral diffusion depends on the boundary conditions, in particular, the written data pattern on the top surface. Typically the amount of radial lateral diffusion is approximately the N^+ layer thickness. In. BEAMOS, the N layer is nearly uniformly doped, so that no driving fields exist in the N layer except near the top and diode interfaces. This absence of fields is necessary because of the method of BEAMOS operation. However in the Archival application it is possible to have a built-in field in the N^+ layer, to aid carrier motion towards the planar diode depletion region and thereby reduce lateral diffusion. This built in electric field also reduces carrier recombination at the top silicon surface. This will dramatically improve the readout gain and makes the doping gradient or built in field desirable even if it is not necessary to minimize lateral diffusion. The effect of the built in field on readout gain and the problem of lateral diffusion are discussed in more detail in subsequent sections.

The built in field is achieved by incorporating a doping gradient. The field due to a doping gradient outside of any depleted regions is given by

$$E = -\left(\frac{kT}{q}\right)\frac{1}{N} \frac{dN(x)}{dx} \tag{2}$$

where kT is the thermal energy and $N(x) = N_D(x) - N_A(x)$.

An idealized N^+ doping profile that could be well approximated by conventional processing techniques is shown in Figure 11. The electric field distribution, which is a constant 10^4V/cm, is shown in Figure 12.   Figure 13 shows an acceptor distribution N_A for a written zero that is taken as Gaussian. This distribution could be obtained by thermal diffusion or by ion implantation. In the case of ion implantation, this particular distribution would be obtained for $\wedge R_p$ = 0.025 micron and with a top metal layer, so that R_p falls at the top surface of the silicon. A possible choice in this case would be boron ions at 20 keV or gallium at 140 keV with a metal layer about 0.08 micron in each case. Figure 14 shows the net doping profile N_D - N_A obtained, and Figure 15 shows the approximate electric field distribution. The sharp negative electric field spike around 0.04 micron is due to the depletion field of the P^+N^+ diode. This can in principle be calculated exactly for nonuniform doping profiles; however, this is an estimate based on the abrupt junction approximation. Note that for z<0.04 micron, the field is negative, so that this region is a potential well for holes (minority carriers in the N^+ region). The effect of such built in fields on carrier motion is discussed in the dead layer modeling section.

Scattering of Reading Electron Beam

The distribution of the ionization due to a low-energy electron beam is shown in Figure 16. (Appendix II, "Electron Penetration in Solids," discusses this subject in detail.) Figure 16 is a normalized
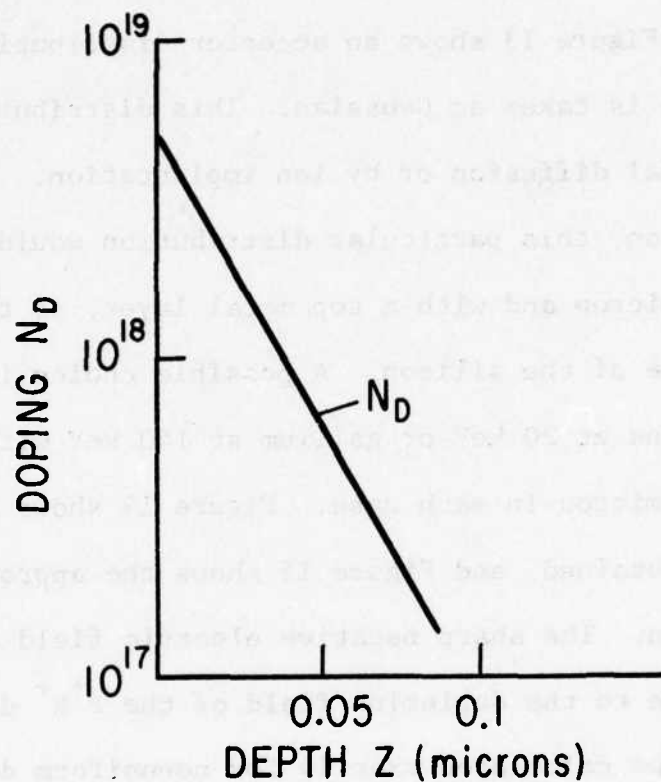
Figure 11. Idealized Doping Distribution for N$^+$ Layer of Archival Target.
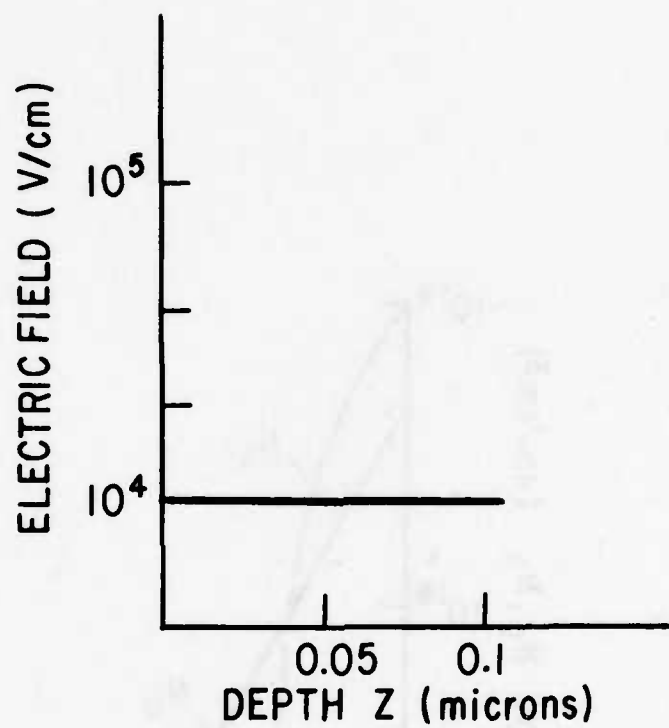
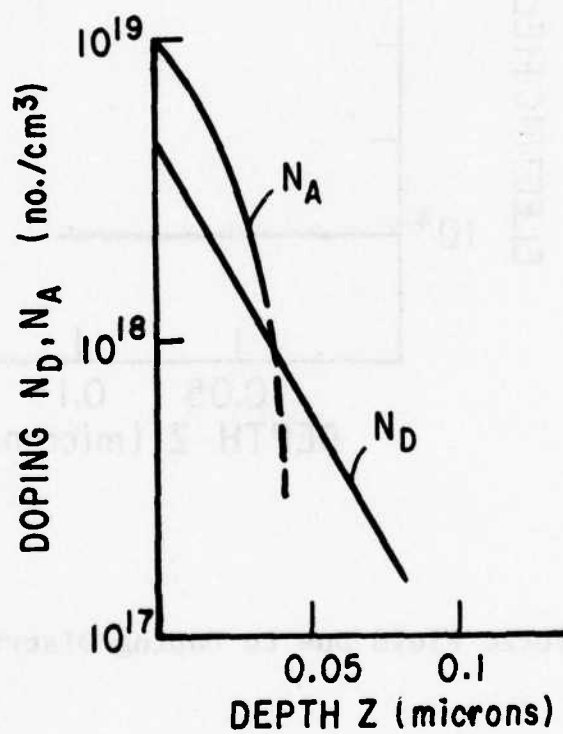Figure 12.   Electric Field Due to Doping Distribution of Figure 11.

Figure 13   Acceptor and Donor Doping
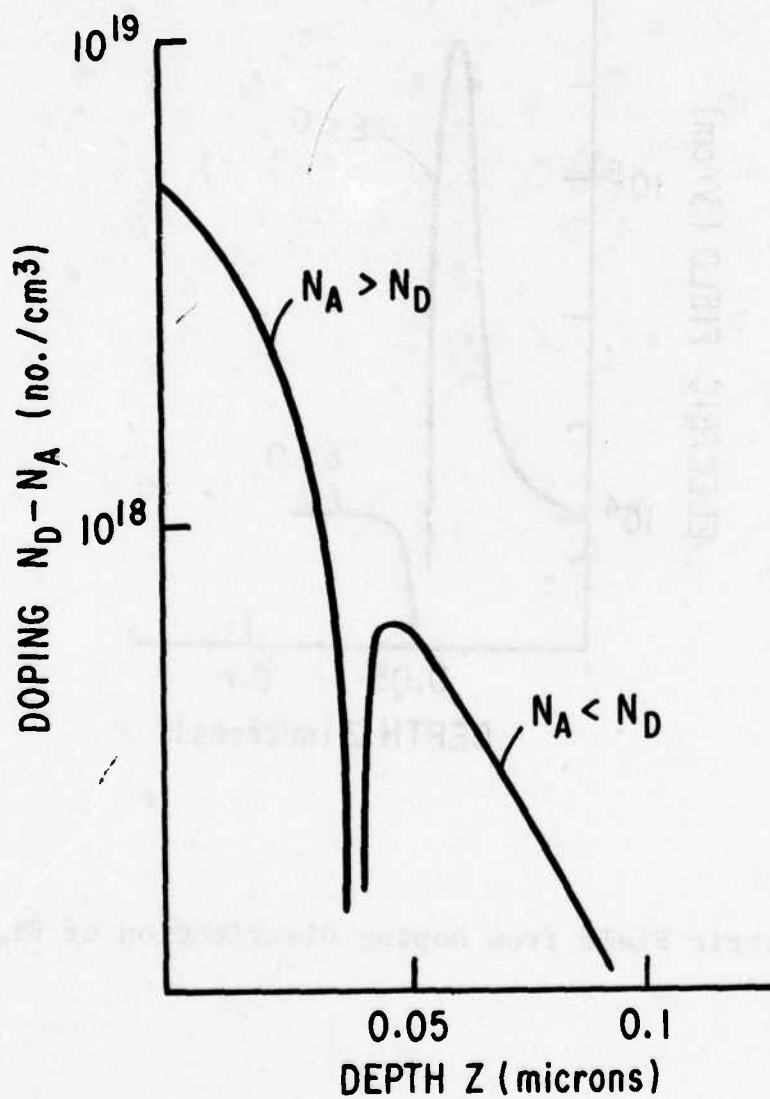Distribution for Written Zero

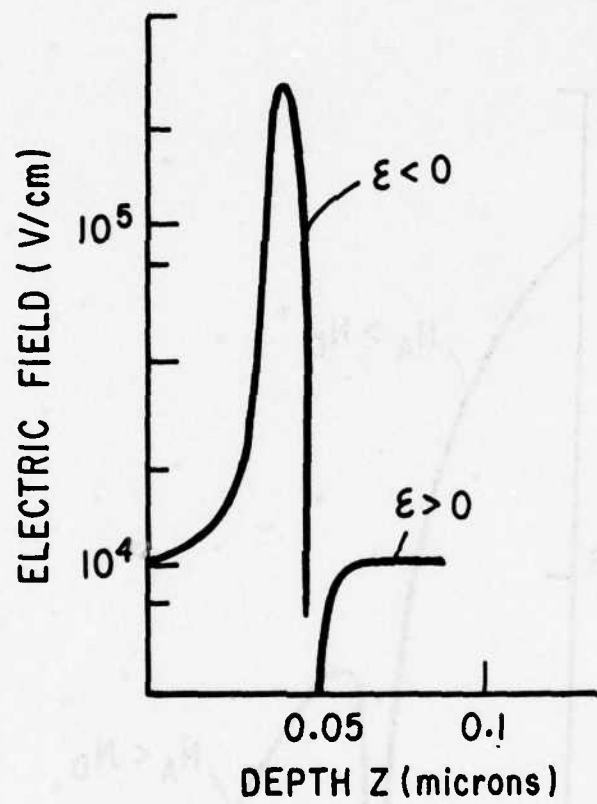Figure 14   Net Doping Level for Figure 13

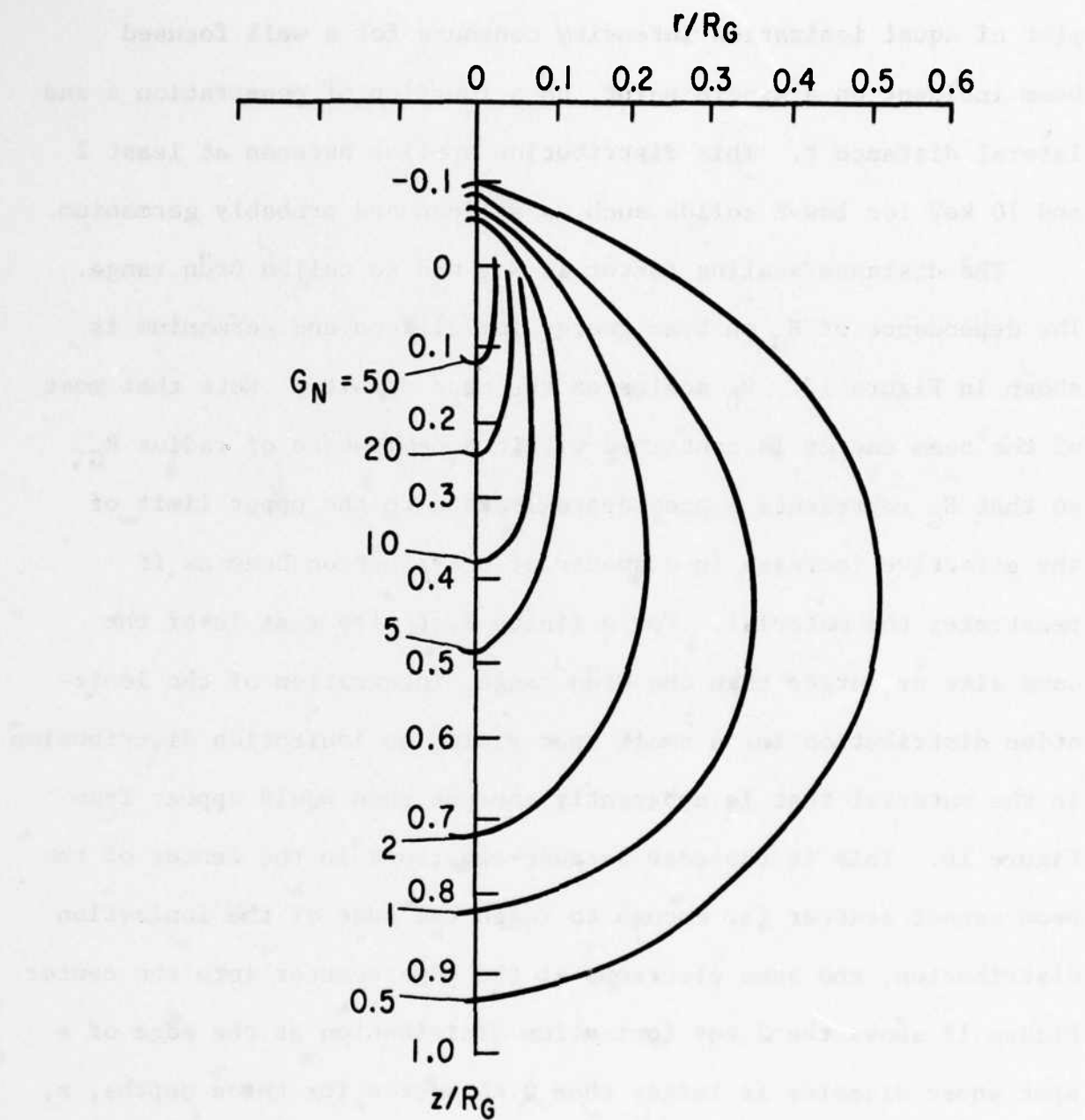Figure 15.   Electric Field from Doping Distribution of Figure 14.

Figure 16. Isointensity Plot of Ionization Generated by a Focused Electron Beam Incident at r = 0 and z = 0.

plot of equal ionization intensity contours for a well focused

beam incident on a single point, as a function of penetration z and

lateral distance r. This distribution applies between at least 2

and 10 keV for low-Z solids such as silicon and probably germanium.

The distance scaling factor is R_G, the so called Grün range.

The dependance of R_G on beam energy for silicon and germanium is

shown in Figure 17. R_G scales as the mass density. Note that most

of the beam energy is contained within a hemisphere of radius R_G,

so that R_G represents a good approximation to the upper limit of

the effective increase in diameter of the electron beam as it

penetrates the material. For a finite spot size that is of the

same size or larger than the Grün range, integration of the ioniz-

ation distribution for a small spot yields an ionization distribution

in the material that is apparently sharper than would appear from

Figure 16. This is the case because electrons in the center of the

beam cannot scatter far enough to reach the edge of the ionization

distribution, and some electrons at the edge scatter into the center.

Figure 18 shows the 2-keV ionization distribution at the edge of a

spot whose diameter is larger than 0.04 micron for three depths, z,

in silicon. This curve is for the case in which the beam scans in

a line rather than dwells on one spot and is based on the measure-

ments of Possin and Norton. Note that the broadening of the beam

is < 0.02 micron in radius. Hence for a 0.4-micron spot at 2 keV,

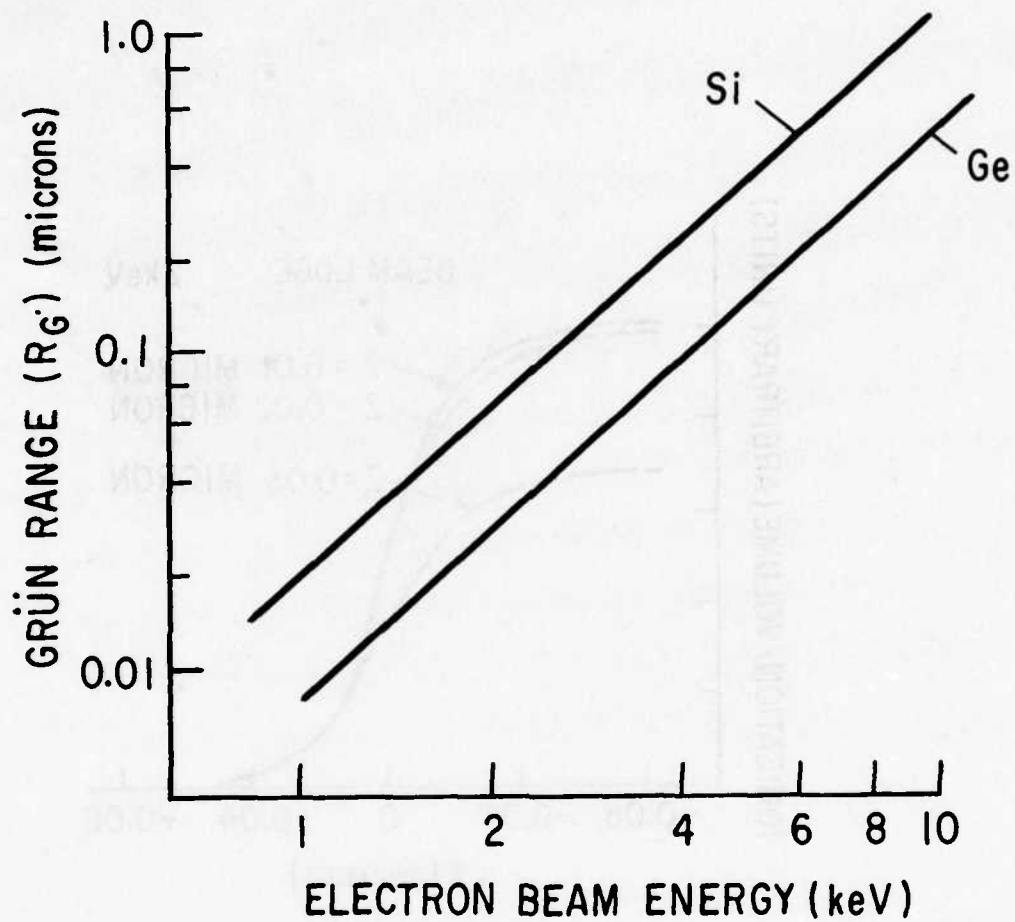a cylinder of ~0.08-micron diameter and a 0.06-micron depth should

-34-

Figure 17. Dependence of R_G on Beam Energy for Silicon and Germanium.
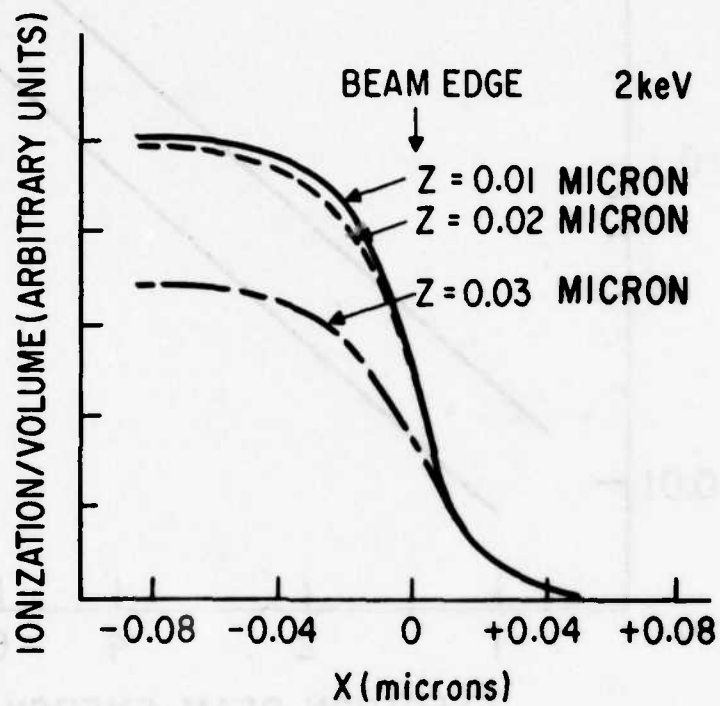
Figure 18. Ionization per Unit Volume in Arbitrary Units as a
Function of Lateral Distance x and Penetration z
for Sharp Edged Beam of Diameter Greater than 0.06
Micron. (Calculated from 5-kV Beam Penetration Data
in PMM; Scaled to 2-keV and Silicon Mass Density).

-36-

contain 80 percent of the beam energy for silicon. For other low-Z materials, both distances can be scaled inversely as the density.

For targets constructed of germanium, the situation is therefore even more favorable. The Grün range is smaller by a factor of two at the same voltage (because of the increased mass density), and the electron hole pair production rate is 30 percent larger (because of the small band gap). Hence higher energy reading beams can be used to give the same size ionization region, but with a target gain larger by a factor of two.

The above discussion has indicated the factors to be considered in fabricating surface diode targets. Figure 19 shows a possible target with a magnitude of all of these quantities indicated to scale for bits recorded on 0.1-micron centers. The two P^+ areas are on 0.2-micron centers, which correspond to a 010 pattern on 0.1-micron centers. Figure 19 shows a one surrounded by zeros, which is the most difficult pattern for this device to read. The x_n and x_p are the penetration of the diode depletion region into the N^+ and P layers, respectively. For this figure it is assumed that the P substrate is 400-ohm-cm material; the N^+ doping profile is shown in Figure 11. The main N^+P diode is shown back biased to 100 volts. As can be seen, nothing but lateral carrier diffusion prevents achieving 0.1-micron readout resolution. The P^+N^+ diode depletion field is based on the doping levels in Figure 14. The depletion width could be reduced even more by utilizing higher doping levels in the P^+ and N^+ regions.
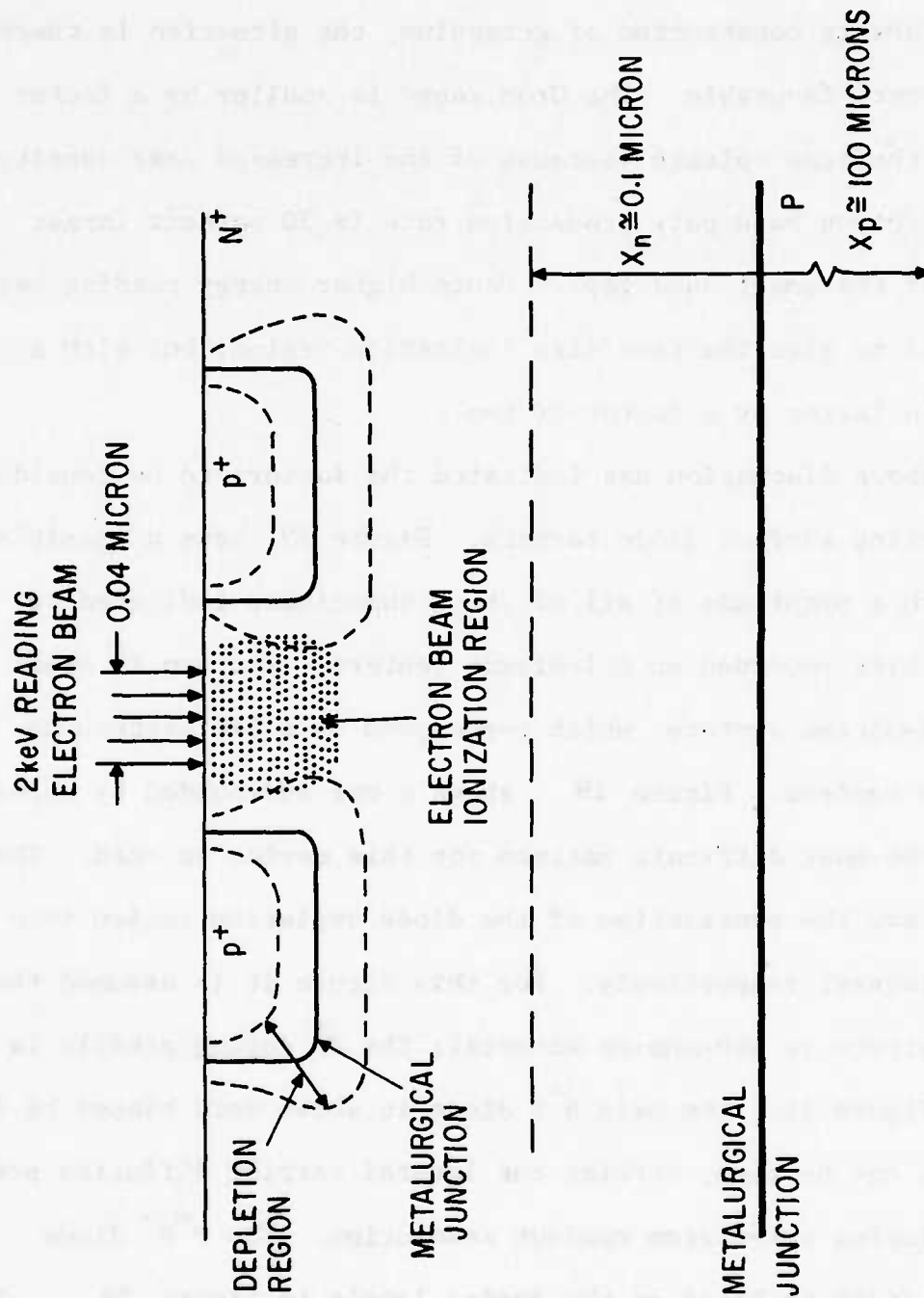
Figure 19. Cross Section of 101 Pattern Recorded on Surface Diode Target (All Dimensions Shown to Scale).

Based on these considerations it will be the goal of the fabrication effort to produce planar diodes with doping levels $\sim5 \times 10^{18}$ cm^{-3} near the surface and with doping profiles like figure 11. The primary reason for the strong doping gradients is to produce built in electric fields which will increase target readout gain by minimizing carrier recombination at the top surface. This is very important because the effect of writing on the planar diode is to increase carrier recombination in the top surface region. To maximize the readout modulation the unwritten target state must have minimum recombination in this top surface layer. High doping levels near the surface are also necessary to prevent depletion field spreading of the written diodes and loss of spatial resolution or bit packing density. In addition, heavily doped surface layers increase the electrical conductivity of the n^{+} layer and thereby increase the frequency response of the readout signal.

Fabrication of Planar Diodes

The planar diode studies consisted of a number of implantations with differing processing parameters. The diode structures were examined in an effort to determine the optimum conditions for producing the desired doping with a minimal dead layer region at the surface. The influence of ion species, fluence, and energy as well as substrate crystallographic orientation, surface oxide layers, and annealing temperature were investigated as a part of a continuing effort in this area.

-39-

The "dead" layer referred to is a short-lifetime region near the top surface of the target which appears dead to the reading electron beam. Carriers generated by the beam in this area recombine at the many nearby trapping sites, with little chance to diffuse down to the collecting junction of the planar diode. This results in low gain for the device at low beam voltage and impairs the device resolution. Therefore, it is desirable to make the dead layer as thin as possible.

The dead layer phenomena has been observed by other researchers working in the area of solar cells and nuclear particle detectors. Dead layers are quite prevalent for very heavy phosphorus diffusions. It has been speculated that the presence of large numbers of oversize atoms in the lattice can produce sufficient disorder to cause the region to appear dead. In the case of nuclear particle detectors, for example, extreme care is used in preparing the junctions. Implantations at very low energies, 5-10 kV, directly onto the crystallographic axis results in the ions being gently nudged into the crystal to produce as little damage as possible and to confine the damage to a thin surface region. (Ref. 1). Since the archival memory device requires relatively heavy dopant concentrations to a depth of $\sim 0.1 \mu$ this kind of approach is not a feasible solution for the planar diode substrate.

Solar cell researchers have had some success in producing

adequately thin dead layers for solar cell applications by careful

phosphorus diffusions and special surface preparations. However,

even with these procedures the dead layers are often unacceptable

for our application as the dead region is around 500 $\overset{\circ}{A}$. (Ref. 2).

The approach pursued in these studies instead, has been to

achieve the necessary doping levels and gradients through the use

of ion implantation, and by selecting the appropriate combination

of ion, energy, fluence, crystal orientation, surface preparation,

and annealing cycle, to restore a high quality crystalline structure

with a minimal dead layer at the top surface of the device.   The

influence of a number of these parameters has already been investig-

ated.   Some of these will be looked into further while work on

others not yet begun will start in the upcoming quarter.

For this initial work the most widely accepted implantation

dopants, phosphorus, arsenic, and boron, were used to form planar

diode structures under a number of implantation conditions in

~5-20 $_\Lambda$ -cm float zone silicon using the 400 KeV Extrion ion implan-

ter at the Center.   The popularity of these column III and IV

elements is due in large part to the known high degree of electrical

activity of these ions following implantation and annealing.   The

ready availability of these ions due to their ease of implantation

made them ideal first candidates.   It is foreseen that the suitabil-

ity of other less common ions will be evaluated in the future as well.

All of these ions were implanted at room temperature at a beam angle 7° from the crystallographic. It was felt that at present, variation of the implant temperature would not really be profitable. Hot implants, for example, would result in less damage immediately after implantation. However, higher temperatures, and thus spreading of the profile, would be needed to anneal out residual radiation damage. Cold implants, on the other hand, would result in a greater degree of channeling, which might be undesirable in view of the highly uniform, shallow junction being sought. For similar reasons no attempts at angular variation were attempted to utilize channeling to an advantage, since variation in profile and changes in surface conditions can result.

Energies of 30 kV and 100 kV were selected for the first studies to offer contrasting situations for investigation of dead layer formation. At 30 kV, as shown in Figure 20, the depth of ion penetration, and the resulting damage profile, is located much closer to the top surface of the device than at 100 kV. Although the lower energy implant would put the peak of the dopant distribution near the surface as desired, the higher energy implant could still be used to form the profile shown in Figure 11, by implanting through a layer of another material such as oxide or metal, or by layer removal at the surface down to the peak of the distribution. Either of these schemes would allow the production of a top highly doped region with a steep gradient through the upper n (or p) layer.
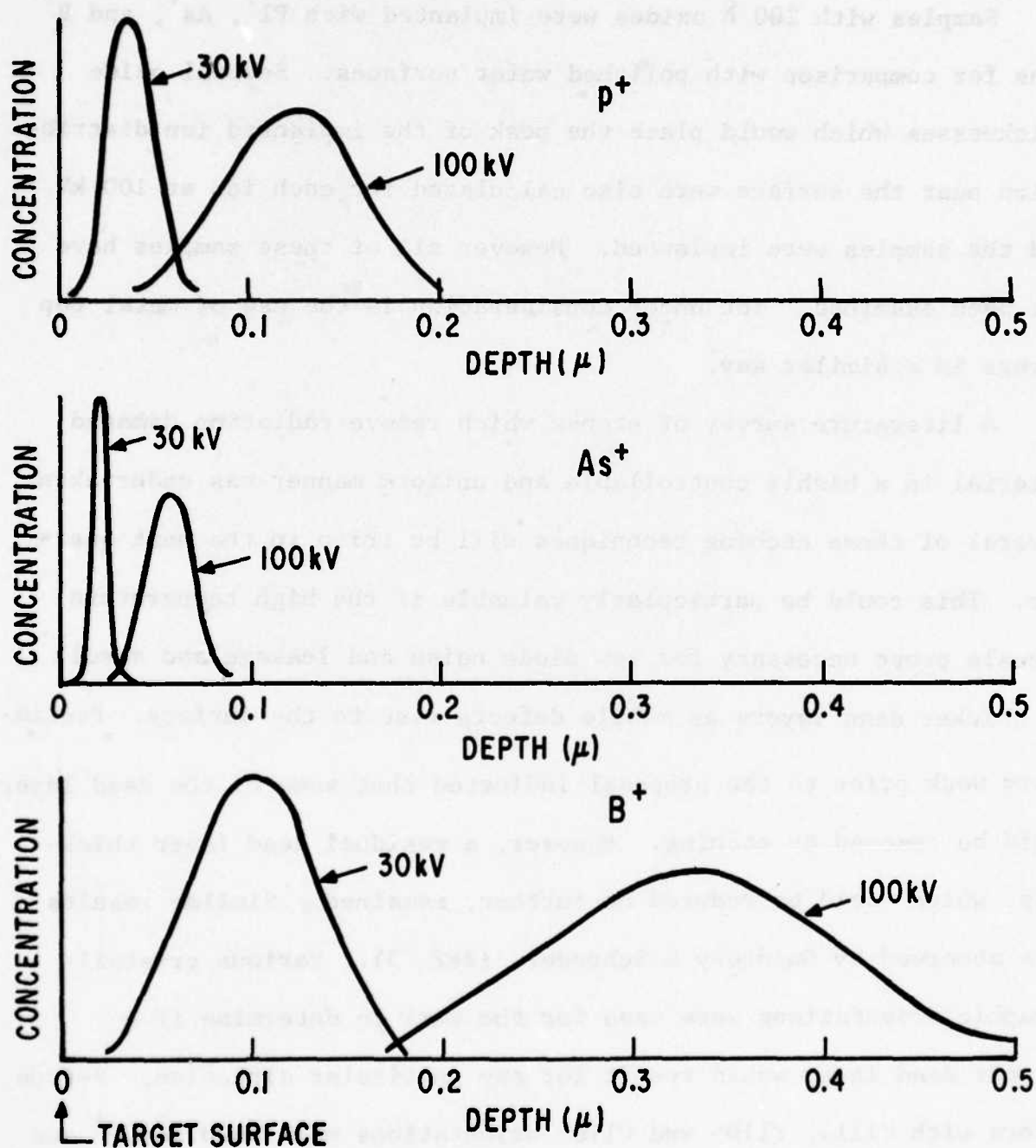
Figure 20.   Projected Ranges for P^+, As^+ and B^+ at 30 and 100 kV.

Samples with 200 $\overset{o}{A}$ oxides were implanted with $P1^+$, As^+, and B^+ ions for comparison with polished wafer surfaces. Several oxide thicknesses which would place the peak of the implanted ion distribution near the surface were also calculated for each ion at 100 kV and the samples were implanted. However all of these samples have not been examined. Yet under consideration is the use of metal top layers in a similar way.

A literature survey of etches which remove radiation damaged material in a highly controllable and uniform manner was undertaken. Several of these etching techniques will be tried in the next quarter. This could be particularly valuable if the high temperature anneals prove necessary for low diode noise and leakage and result in thicker dead layers as mobile defects rise to the surface. Preliminary work prior to the proposal indicated that some of the dead layer could be removed by etching. However, a residual dead layer thickness, which could be reduced no further, remained. Similar results were observed by Guldbery & Schroder. (Ref. 3). Various crystallographic orientations were used for the work to determine if a thinner dead layer would result for any particular direction. P-type wafers with $\langle 111 \rangle$, $\langle 110 \rangle$ and $\langle 110 \rangle$ orientations were used for P^+ and As^+ implants. $\langle 110 \rangle$ and $\langle 111 \rangle$ wafers received B^+ implants.

Other research has produced evidence that significant differences can occur in the regrowth of highly damaged regions during

-44-

anneal depending on the orientation selected. (Ref. 4) (Ref. 5).
In particular, they have observed more residual damage in $\langle 111 \rangle$ Si.
However, for lower doses $< 10^{14}$, little difference has been noticed
(Ref. 6) in the annealing of damaged regions. Figure 21 shows the
regrowth of heavily damaged Si. The $\langle 111 \rangle$ sample did not completely
anneal.

The sharpness of the profile can also be altered by the crystal
orientation. Supertailing, thought to occur as a result of anomalous
diffusion effects or scattering into channels, shows a marked varia-
tion with sample direction (Fig. 22). The effect here, makes $\langle 111$
Si take on a sharper dopant gradient.

Ion fluence is, of course, also known to have considerable
effect on the amount of damage a crystalline material such as
silicon. For the doping levels required for the planar diode
structure, fluences of 10^{13} or more likely 10^{14} are needed, and thus
both were studied. The device described in Section IV however,
may not require this high a doping level. These fluences are not
high enough, in general, to drive the crystal amorphous. Amor-
phousness, although indicative of very heavy lattice damage, allows
regrowth with high electrical activities at significantly lower
annealing temperatures. (Ref. 5). Pre-implants of heavy fluences
$(\sim 10^{15})$ of inert ions are planned to determine if this will produce
higher quality diodes for low temperature anneals. A preliminary
experiment using 10^{15} cm^{-2} of He$^+$ ions for post damage before anneal
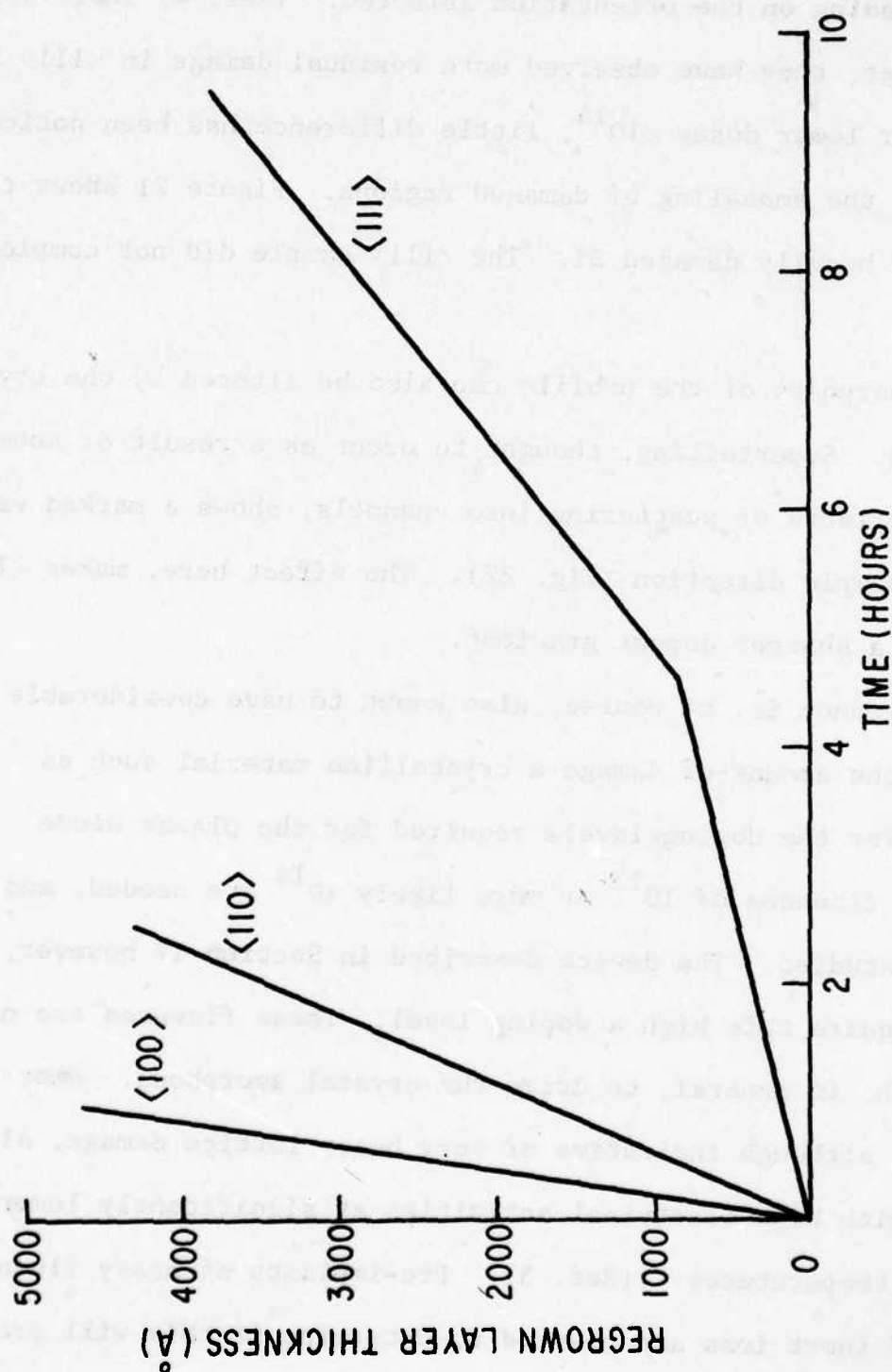was not successful in reducing the dead layer.

Figure 21. Regrowth layer thickness versus time for Si samples annealed at 550°C. These samples were implanted with a total dose of 8×10^{15} cm^{-2} Si$^+$ ions at multiple energies between 50 and 250 keV. (Ref. 5).
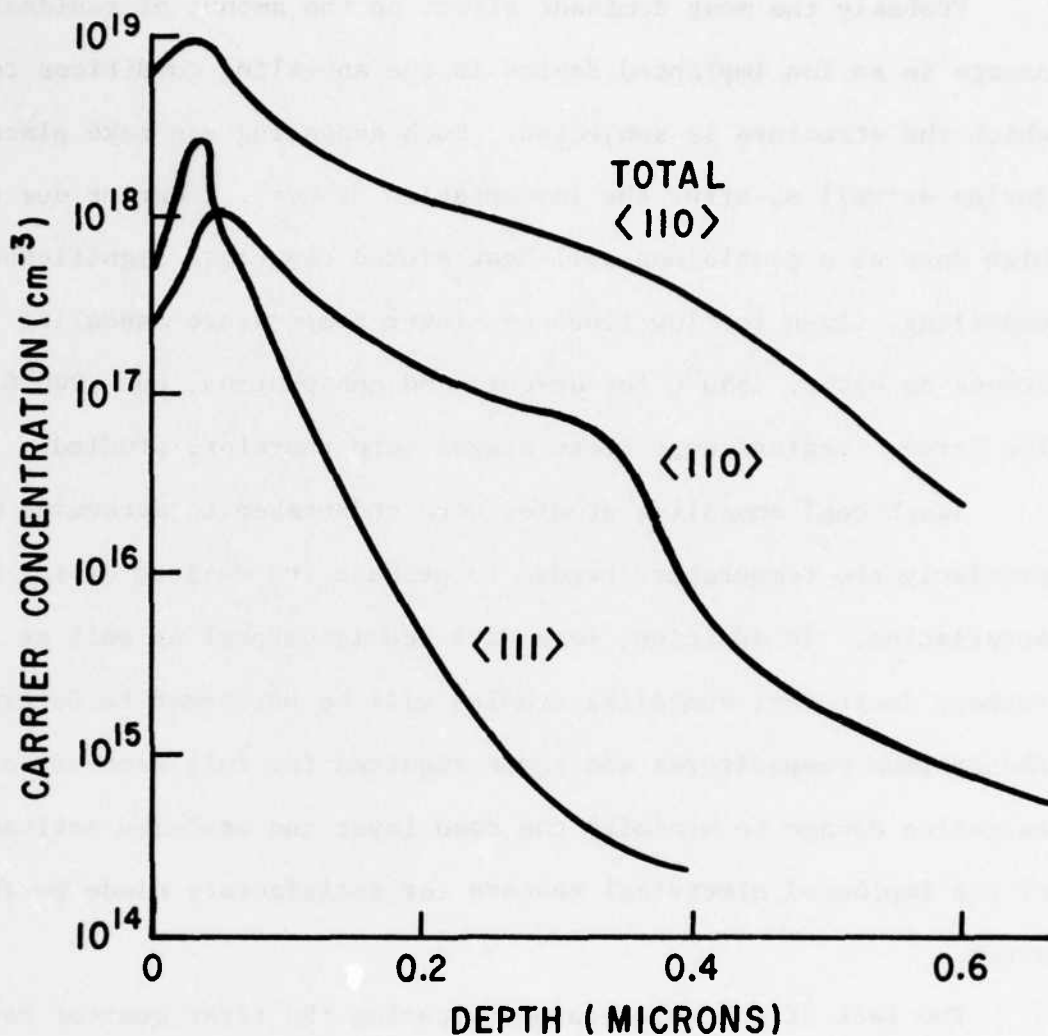
TIME (HOURS)

REGROWN LAYER THICKNESS (Å)

⟨111⟩

⟨110⟩

⟨100⟩

Figure 22. Comparison of depth profiles in <111> and <110> Silicon
for 20 keV P implants at 10^{14} cm^{-2}. Curve labeled total
is the total P concentration (electrically active plus
active) measured by the radioactive tracer method from
Ref. 7 for implantation on axis into <110> after anneal-
ing at 400°C. Other curves are the electrically active
P dopant measured by stripping and four point probe,
(Ref. 8), after annealing at 420°C. The <110> implant
was on axis and the <111> implants were on axis and 15°
off axis. Note that the profiles are the same for on and
off axis implants into <111>.

Probably the most dominant effect on the amount of residual damage in an ion implanted device is the annealing conditions to which the structure is subjected. Such annealing can take place during as well as after the implantation process. Heating due to high dose of a sample not well heat sinked can cause significant annealing. Even for low fluences, lower temperature annealing stages do exist, $\sim650^{\circ}$C for arsenic and phosphorous, and $\sim900^{\circ}$C for boron. Regions near these stages were therefore studied.

Isochronal annealing studies were undertaken to determine more precisely the temperature needed to produce the desired device characteristics. In addition, more detailed isochronal as well as perhaps isothermal annealing studies will be performed to determine the optimum temperatures and times required for full recovery of radiation damage to minimize the dead layer and maximize activation of the implanted electrical centers for satisfactory diode performance.

The lack of suitable equipment during the first quarter has precluded the investigation of the device potential of germanium. Particularly due to its possible application in the alloy junction device, this material requires additional study. Studies of a type similar to those aforementioned can be undertaken for this substrate material during the next quarter.

Evaluation of Planar Diodes

The planar diodes fabricated as described in the preceeding

pages of this section were evaluated in the Cambridge Mark II Scanning

Electron Microscope (SEM). For these measurements the instrument

is used in a diode current imaging mode as indicated in Figure 23.

The specimen current amplifier (SCA) of the SEM is used to amplify

the diode current signal which is then used to modulate the z-axis

of the SEM displays and is also displayed on monitor oscillscope.

The diode back bias (V diode) is normally 1.5 volts. The electron

beam induced gain of the target is defined as

$$\text{Gain} = G = I_s/I_B \tag{3}$$

where I_s is the increase in diode leakage with the beam on and I_B

is the beam current. All beam currents are measured using a

Faraday cup and the SCA operated in the electrometer mode. The

beam energy is measured using a calibrated electrostatic voltmeter

attached directly to the filament lead of the SEM.

The electron beam induced gain, G, is measured as a function of

beam energy. The complete set of gain measurements on all targets

studied so far is contained in Figures 24 through 59. All of the

gain data has been plotted against the first order dead layer model

to be described later in this section. As will be explained, there

is no reason to expect the experimental results to follow this simple

model. However it does help in visualizing the spatial dimensions

involved, and in providing a criteria for comparing targets. For

example, target sample P3A in Figure 25 can be said to behave at

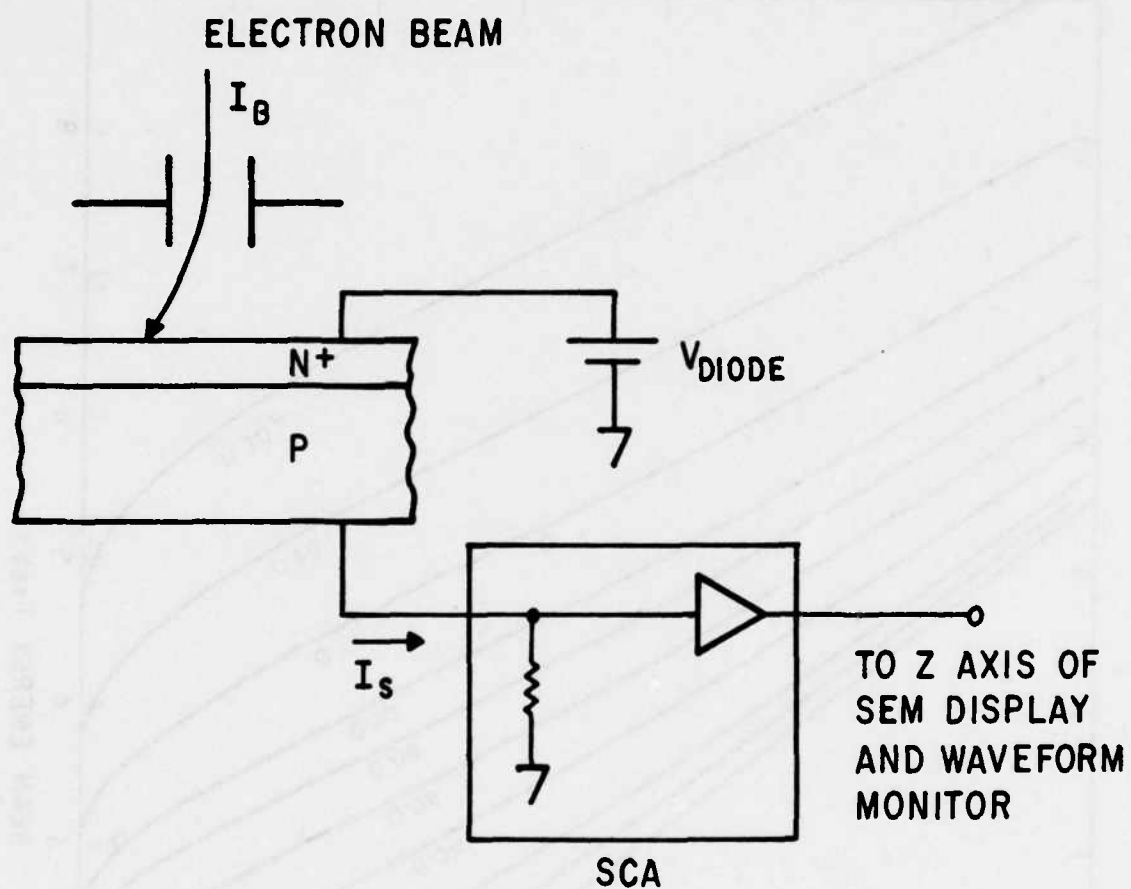2.5 keV as though it had a dead layer of thickness $T_D = 0.06$ microns

-49-

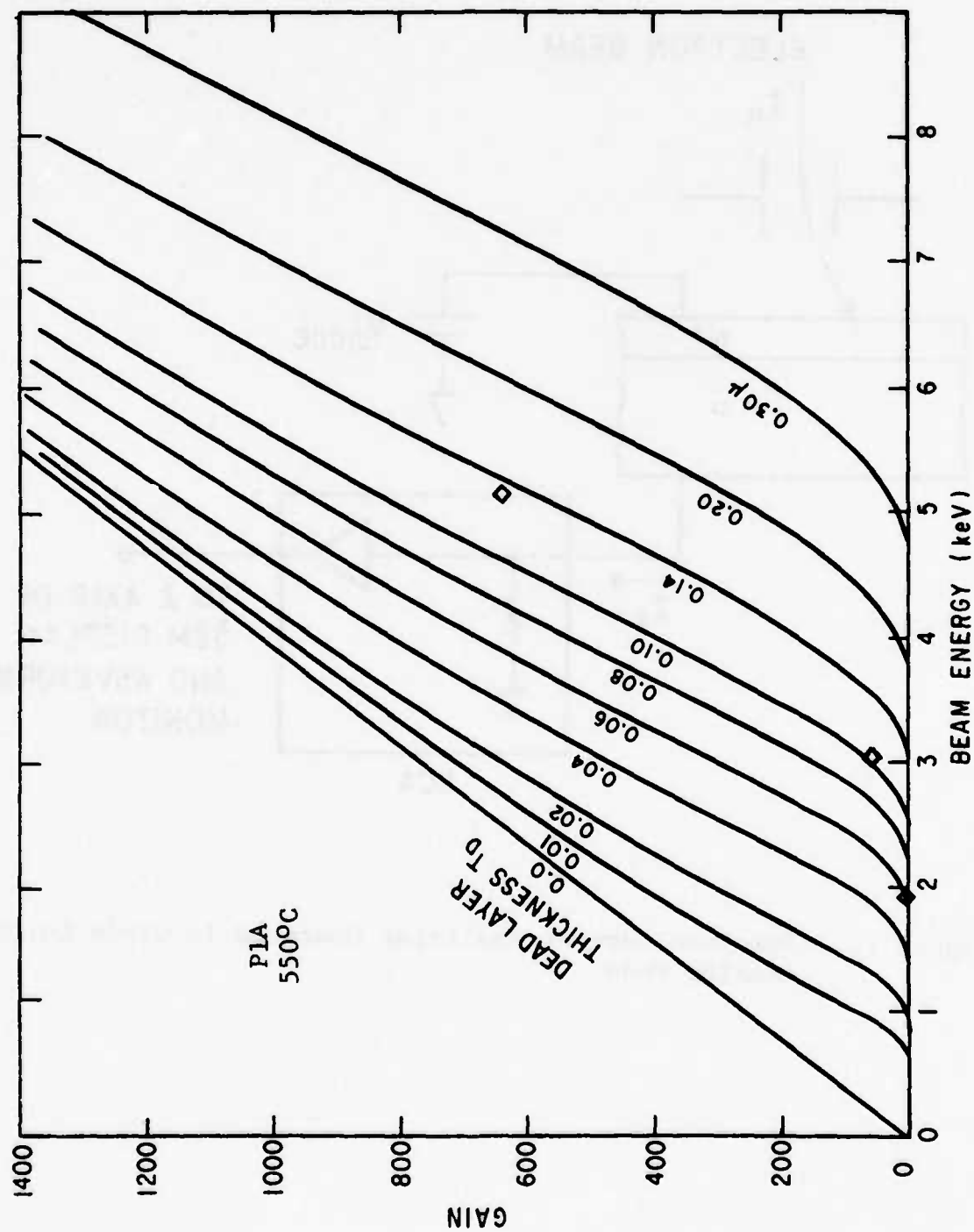Figure 23. Specimen Current Amplifier Operated in Diode Current Imaging Mode

Figure 24. Gain vs. voltage measurements for 12-18 ohm-cm, <111> p-Si, implanted at 100 kV to a fluence of 10¹³ ions/cm².

at room temperature 7° off axis

Figure 25. Gain vs. voltage measurements for 12-18 ohm-cm, <111> p-Si, implanted at 100 kV to a fluence of 10¹³ ions/cm². at room temperature 7° off axis
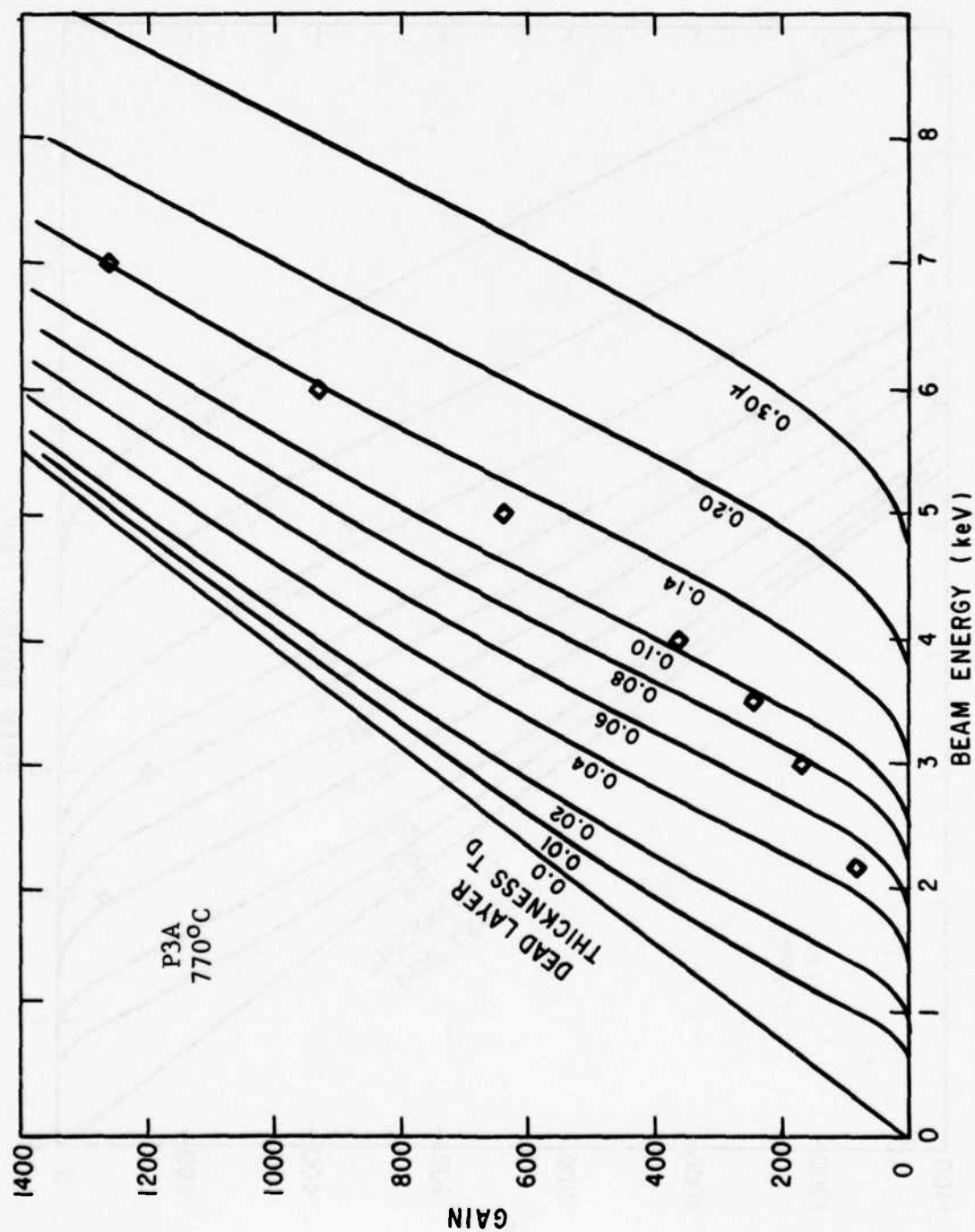
Figure 26. Gain vs. voltage measurements for 12-18 ohm-cm, <111> p-Si, implanted at room temperature 7° off axis at 100 kV to a fluence of 10^{14} ions/cm^2.

Figure 27. Gain vs. voltage measurements for 12-18 ohm-cm, <111> p-Si, implanted at room temperature 7° off axis at 100 kV to a fluence of 10^{14} ions/cm^2.

Figure 28a. Gain vs. voltage measurements for 12-18 ohm-cm, <111> p-Si, implanted 2 at room temperature 7° off axis at 100 kV to a fluence of 10^{14} ions/cm ^{2}.
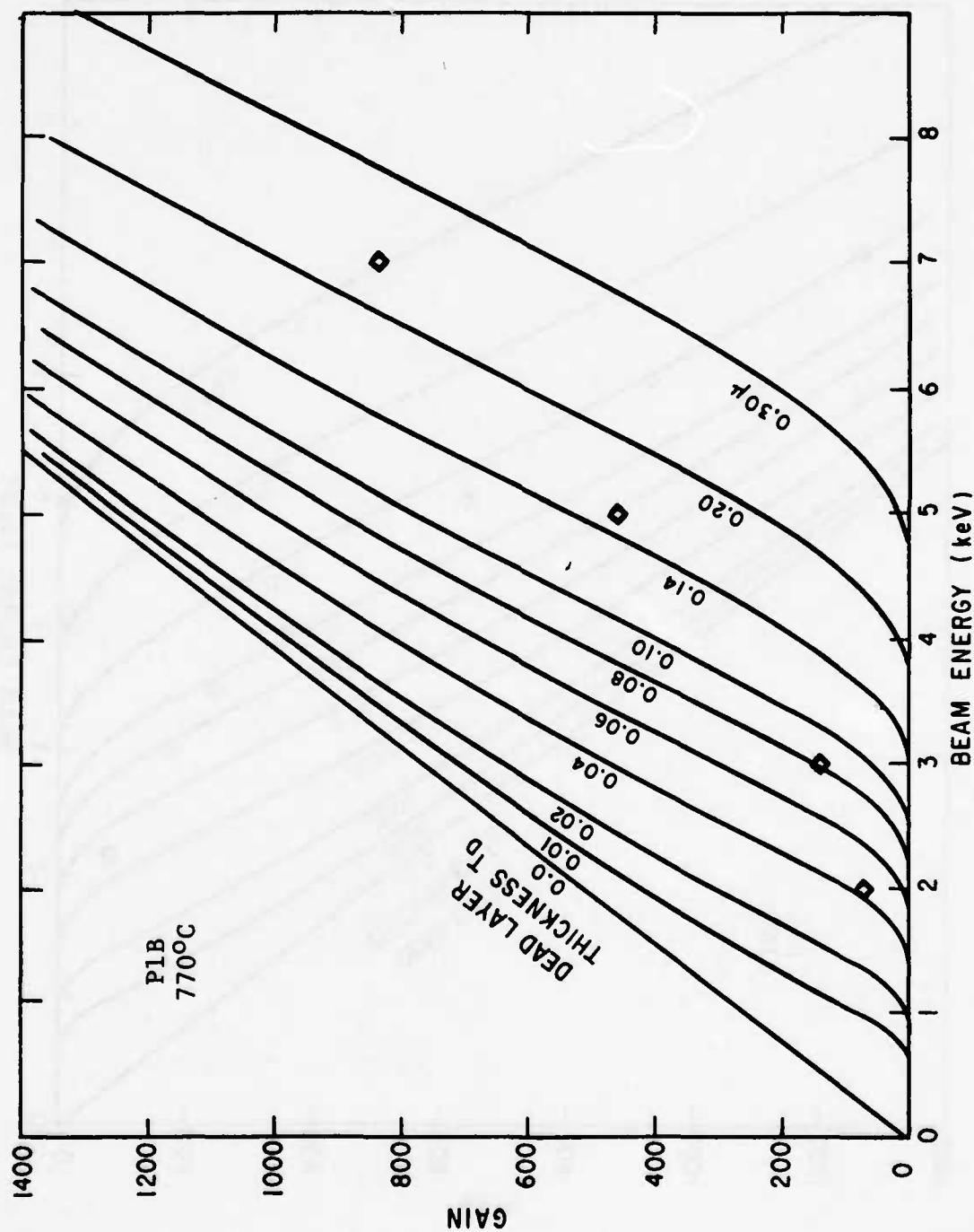
-54-

Figure 28b. Gain vs. voltage measurements for 12-18 ohm-cm, <111>, p-Si, implanted at room temperature 7° off axis at 100 kv to a fluence of 10^{14} ions/cm^2.

Figure 29.   Gain vs. voltage measurements for 12-18 ohm-cm, <111> p-Si, implanted at room temperature 7° off axis at 100 kV to a fluence of 10^{14} ions/cm^2.
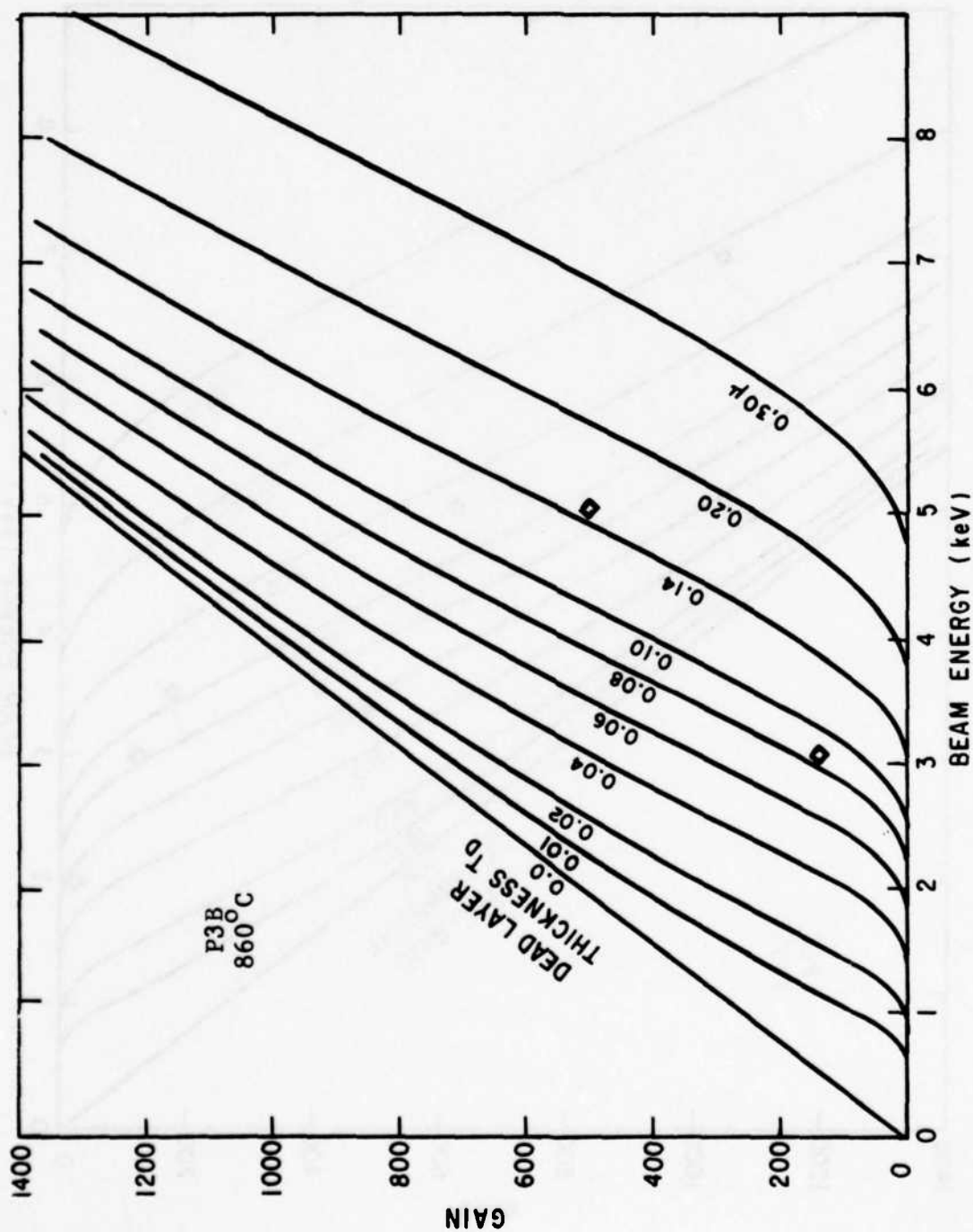
Figure 30. Gain vs. voltage measurements for 12-18 ohm-cm, <111> p-Si, implanted at room temperature 7° off axis at 100 kV to a fluence of 10^{14} ions/cm^2.
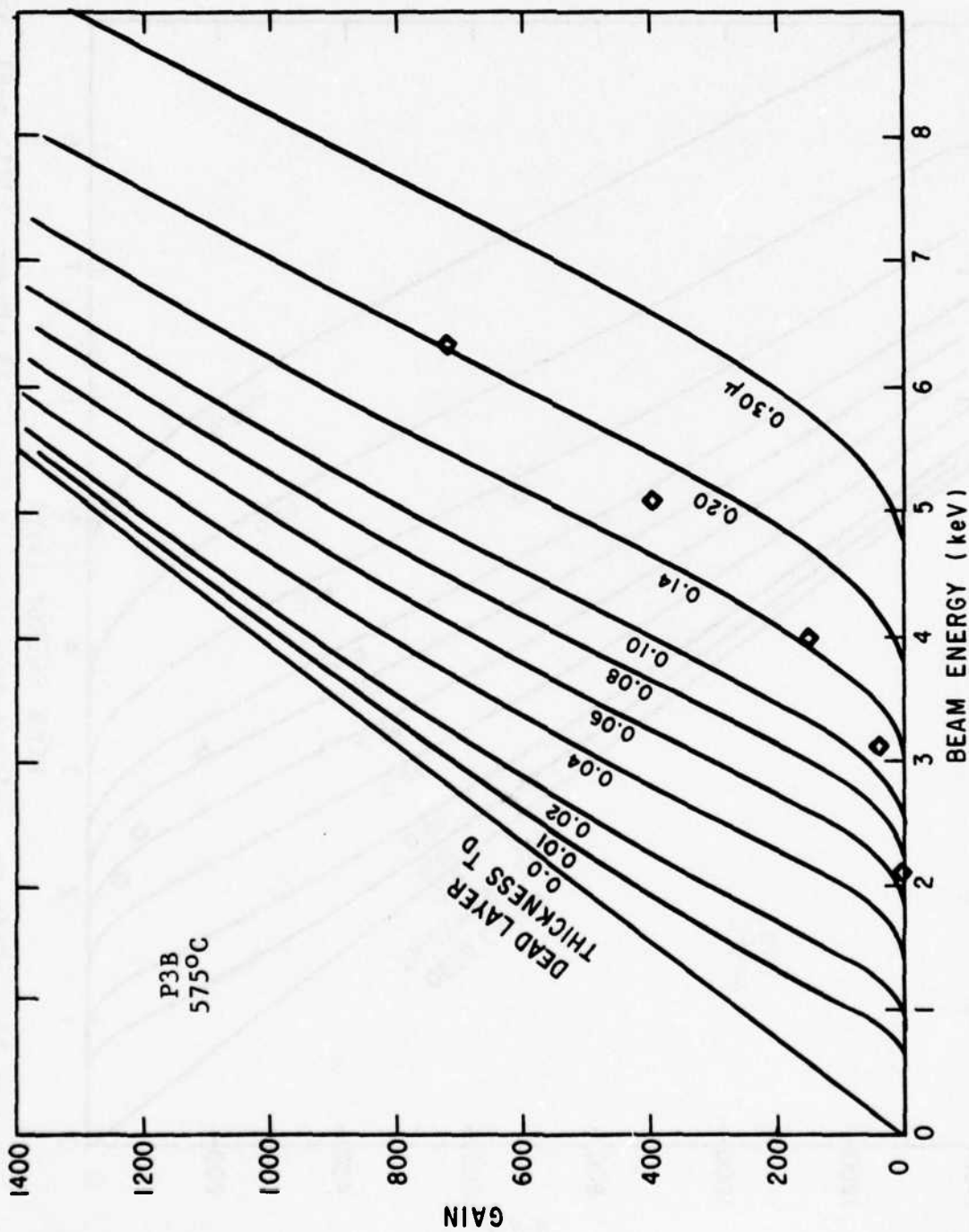
Figure 31. Gain vs. voltage measurements for 12-18 ohm-cm, <111> p-Si, implanted at room temperature 7° off axis at 100 kV to a fluence of 10^{14} ions/cm^2.

Figure 32a. Gain vs. voltage measurements for 12-18 ohm-cm, <111> p-Si, implanted at room temperature 7° off axis at 100 kV to a fluence of 10^14 ions/cm^2.

Figure 32b. Gain vs. voltage measurements for 12-18 ohm-cm, ⟨111⟩ p-Si, implanted at room temperature 7° off axis at 100 kV to a fluence of 10^{14} ions/cm^2.
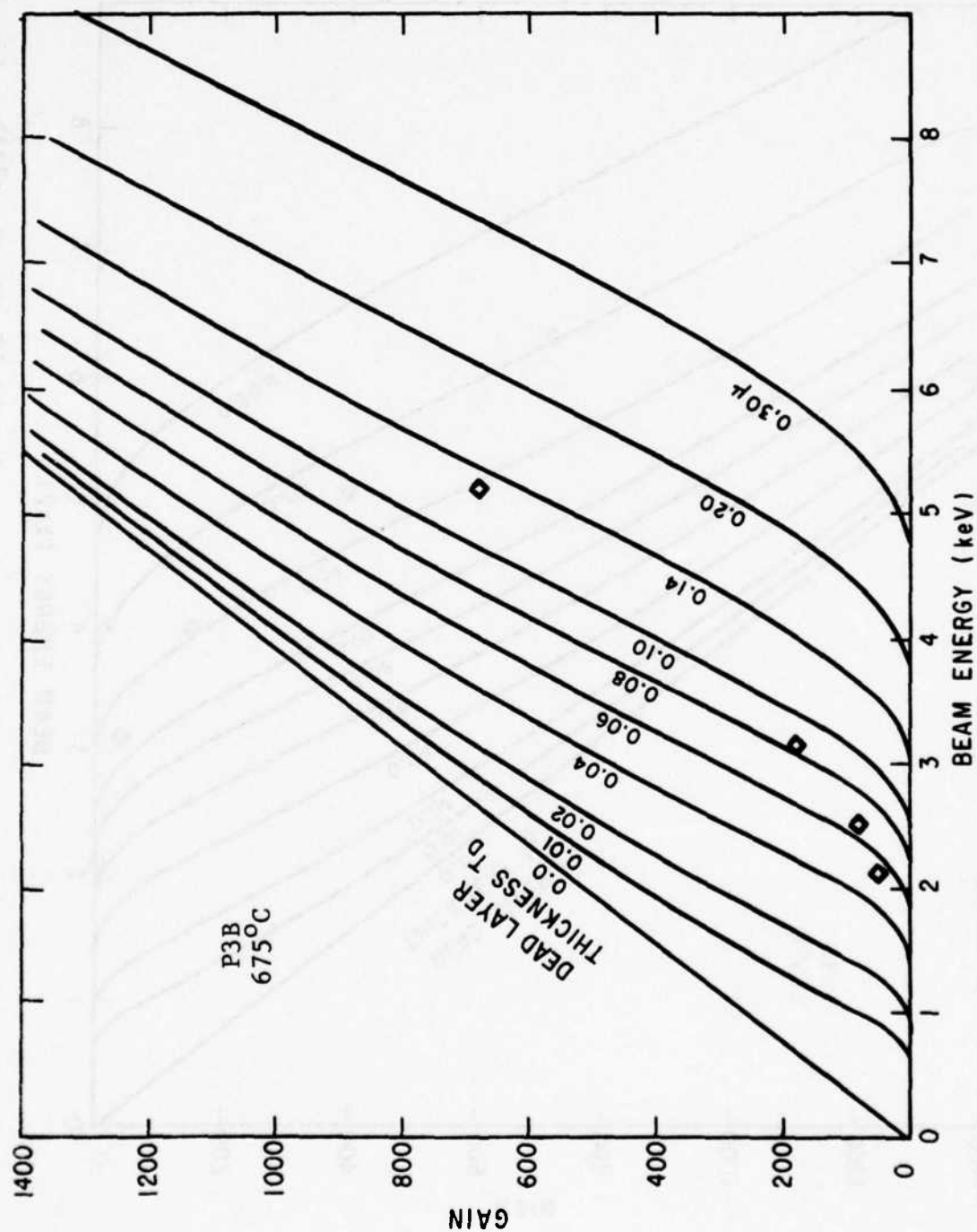
Figure 33. Gain vs. voltage measurements for 12-18 ohm-cm, <111> p-Si, implanted at room temperature 7º off axis at 100 kV to a fluence of 10^{14} ions/cm².
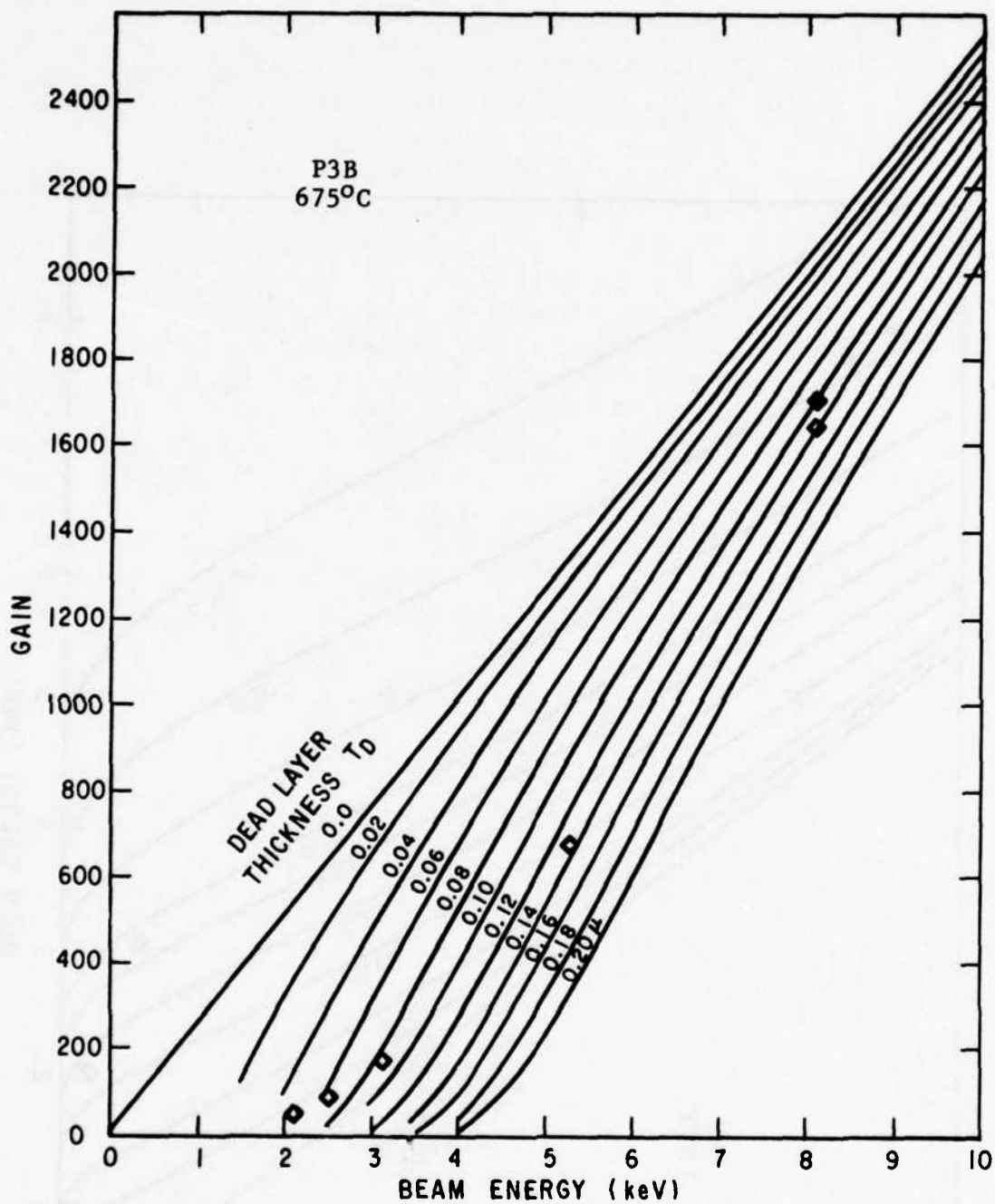
Figure 34. Gain vs. voltage measurements for 12-18 ohm-cm, <111> p-Si, implanted at room temperature 7° off axis at 100 kV to a fluence of 10^{14} ions/cm^2.
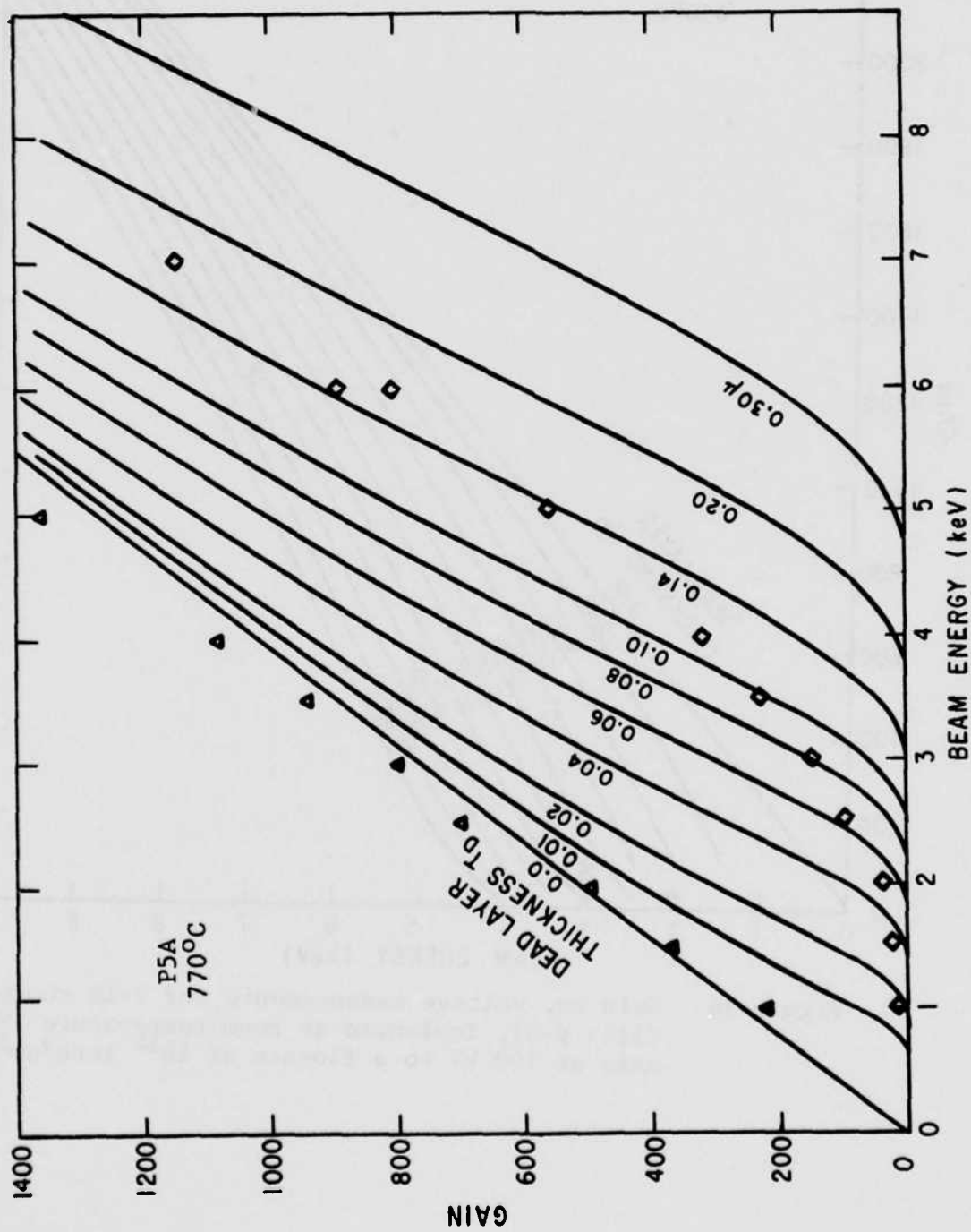
Figure 35. Gain vs. voltage measurements for 7-10 ohm-cm, <111> p-Si, implanted at room temperature 7° off axis at 100 kV to a fluence of 10¹⁴ ions/cm.²

Figure 36. Gain vs. voltage measurements for 7-10 ohm-cm, <111> p-Si, implanted at room temperature 7° off axis at 100 kV to a fluence of 10^{14} ions/cm^2.

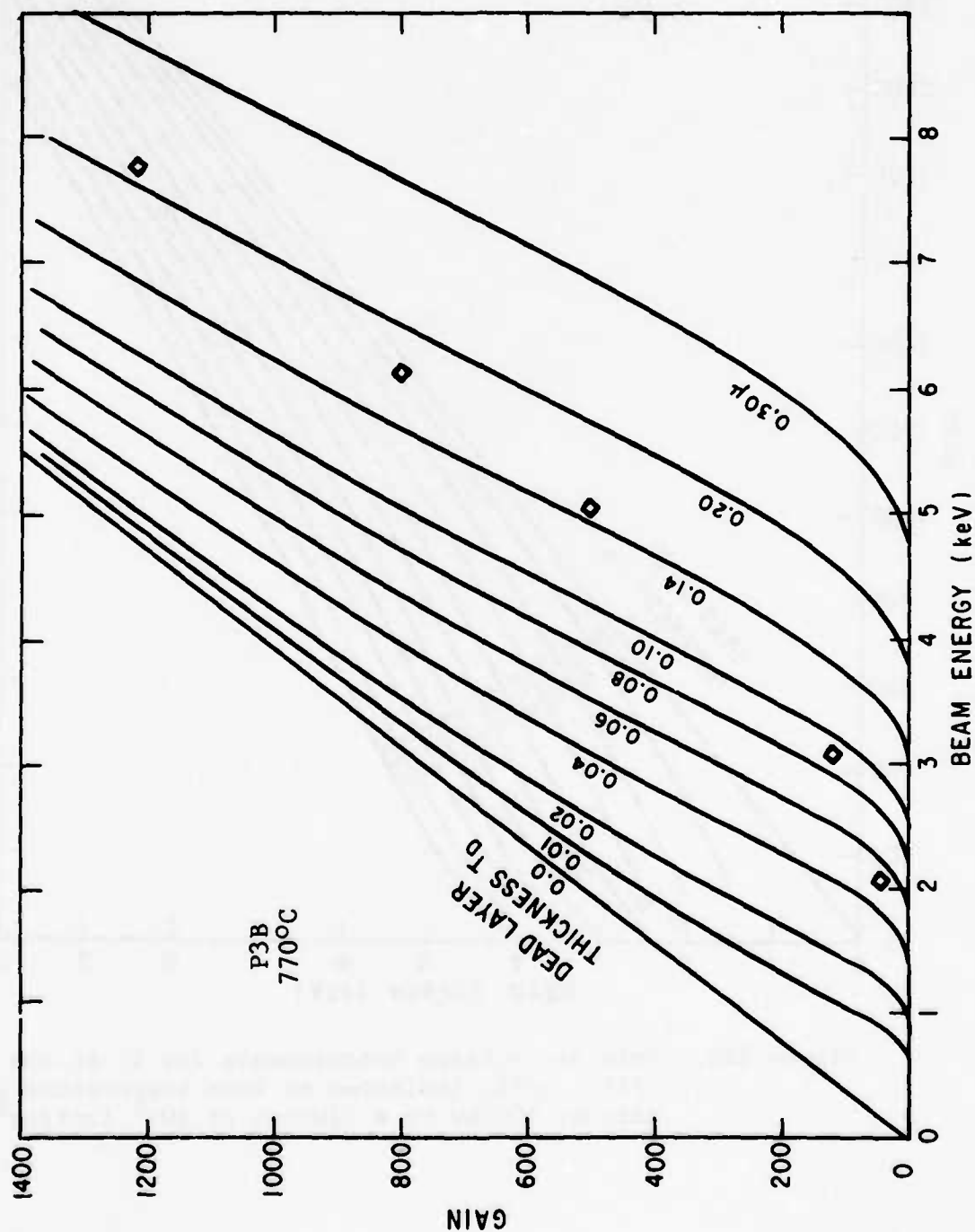Figure 37. Gain vs. voltage measurements for 4.8-7.2 ohm-cm, <100> p-Si, implanted at room temperature 7° off axis at 100 kV to a fluence of 10^{14} ions/cm^2.

Figure 38. Gain vs. voltage measurements for 4.8-7.2 ohm-cm, <100> p-Si, implanted at room temperature 7° off axis at 100 kV to a fluence of 10^{14} ions/cm².

Figure 39. Gain vs. voltage measurements for 12-18 ohm-cm, <111> p-Si, implanted at room temperature 7° off axis at 30 kV to a fluence of 10^{14} ions/cm^2.
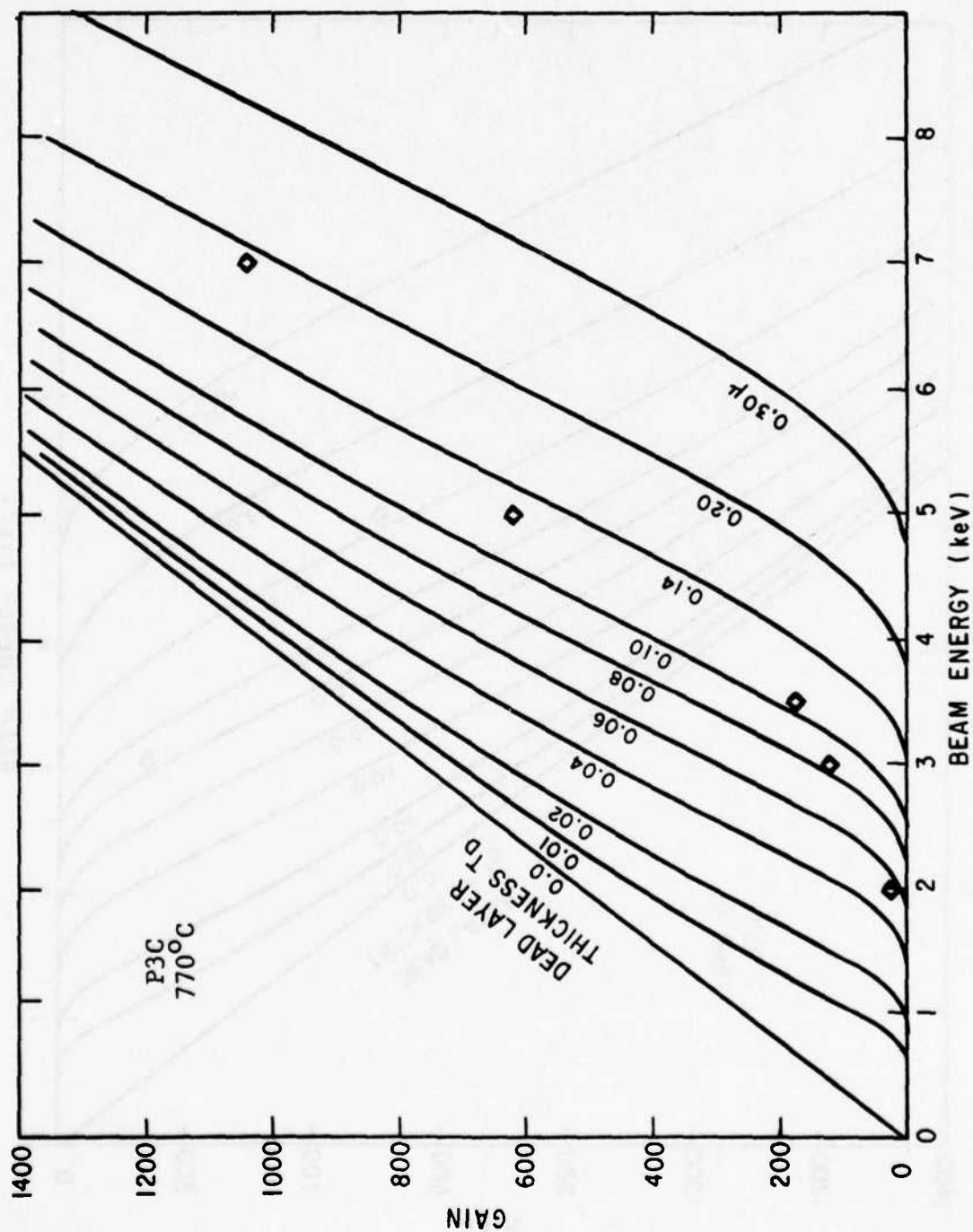
Figure 40. Gain vs. voltage measurements for 12-18 ohm-cm, <111> p-Si, implanted at room temperature 7° off axis at 100 kV to a fluence of 10^14 ions/cm^2.

Figure 41. Gain vs. voltage measurements for 12-18 ohm-cm, <111> p-Si, implanted at room temperature 7° off axis at 100 kV to a fluence of 10^{14} ions/cm^2, through 1000 Å oxide.

Figure 42. Gain vs. voltage measurements for 12-18 ohm-cm, <111> p-Si, implanted at room temperature 7° off axis at 100 kV to a fluence of 10^{14} ions/cm^2, through 1200 Å oxide.

Figure 43. Gain vs. voltage measurements for 12-18 ohm-cm, $\langle 111 \rangle$ p-Si, implanted at room temperature 7° off axis at 100 kV to a fluence of 10^{14} ions/cm^2, through 1400 Å oxide.
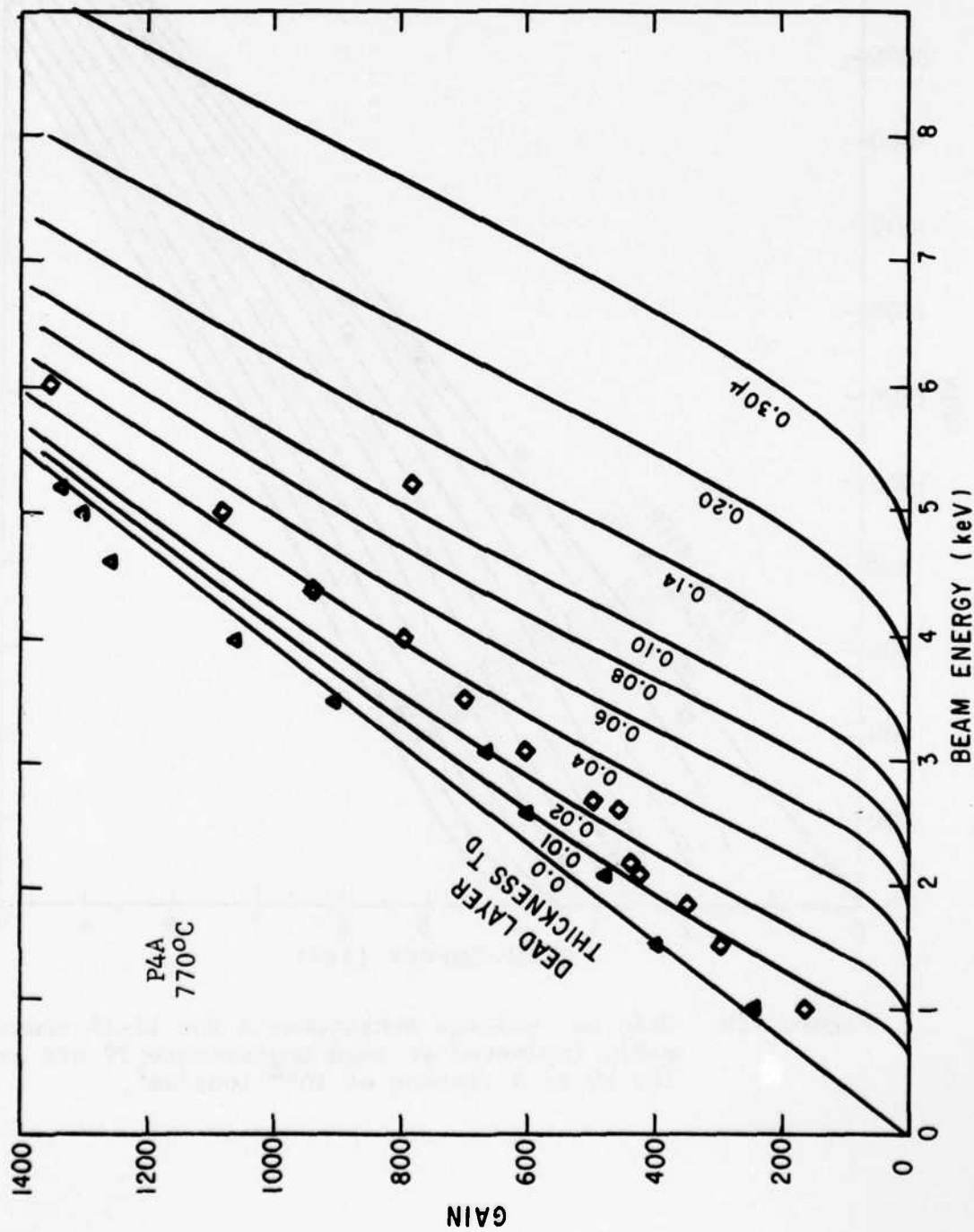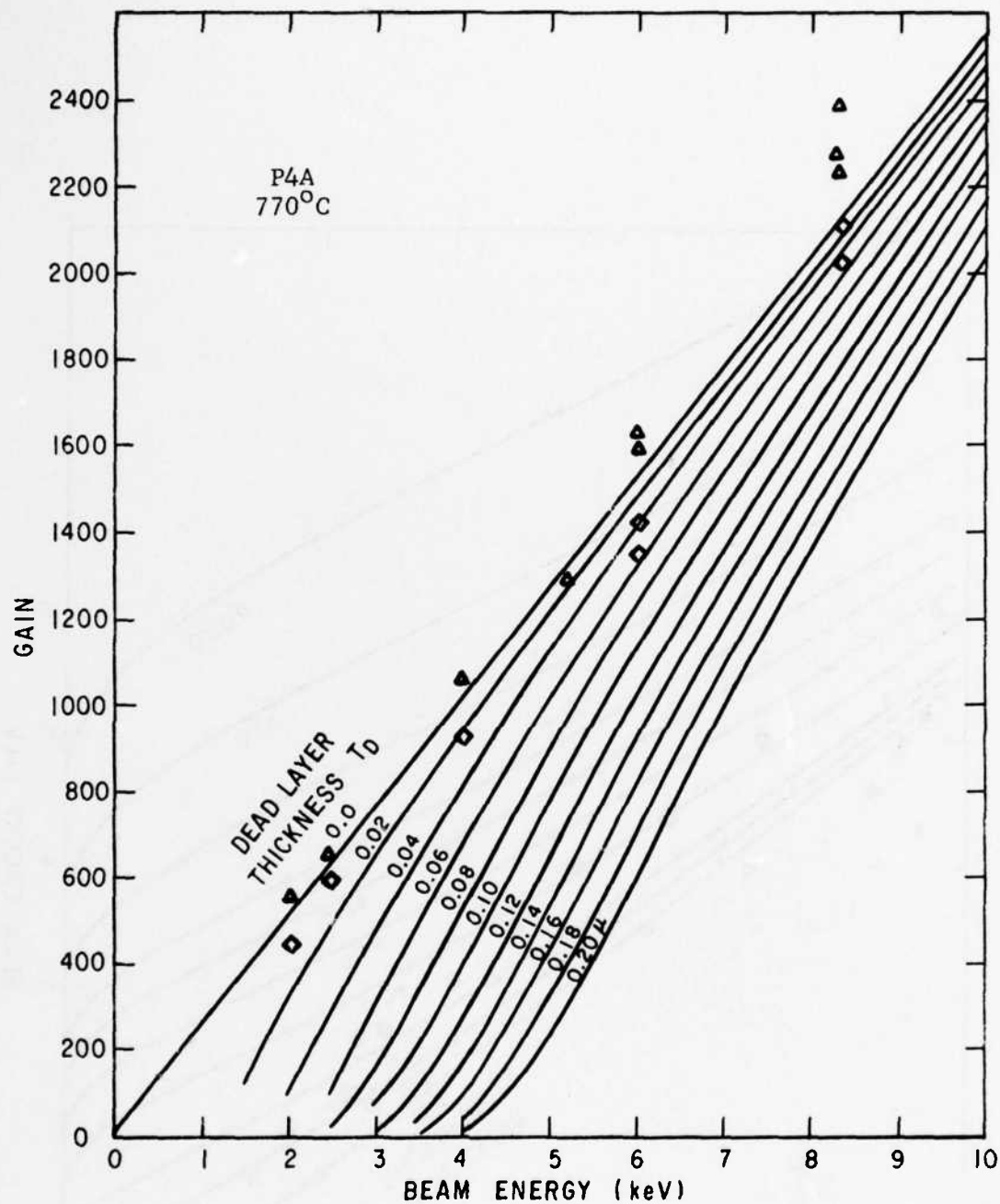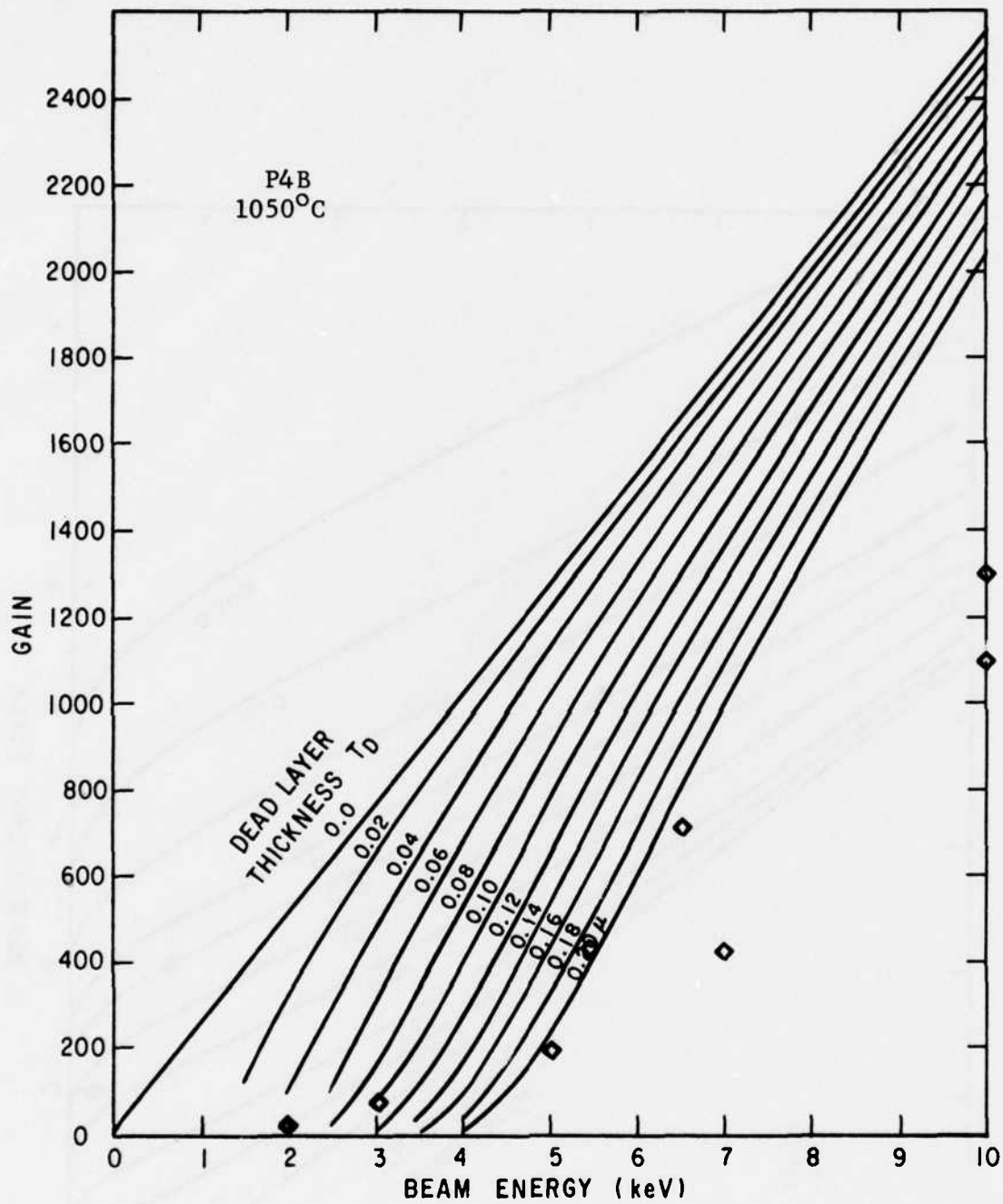
Figure 44. Gain vs. voltage measurements for 12-18 ohm-cm, $\langle 111 \rangle$ p-Si, implanted at room temperature 7° off axis at 100 kV to a fluence of 10^{14} ions/cm², through 1400 ! oxide.
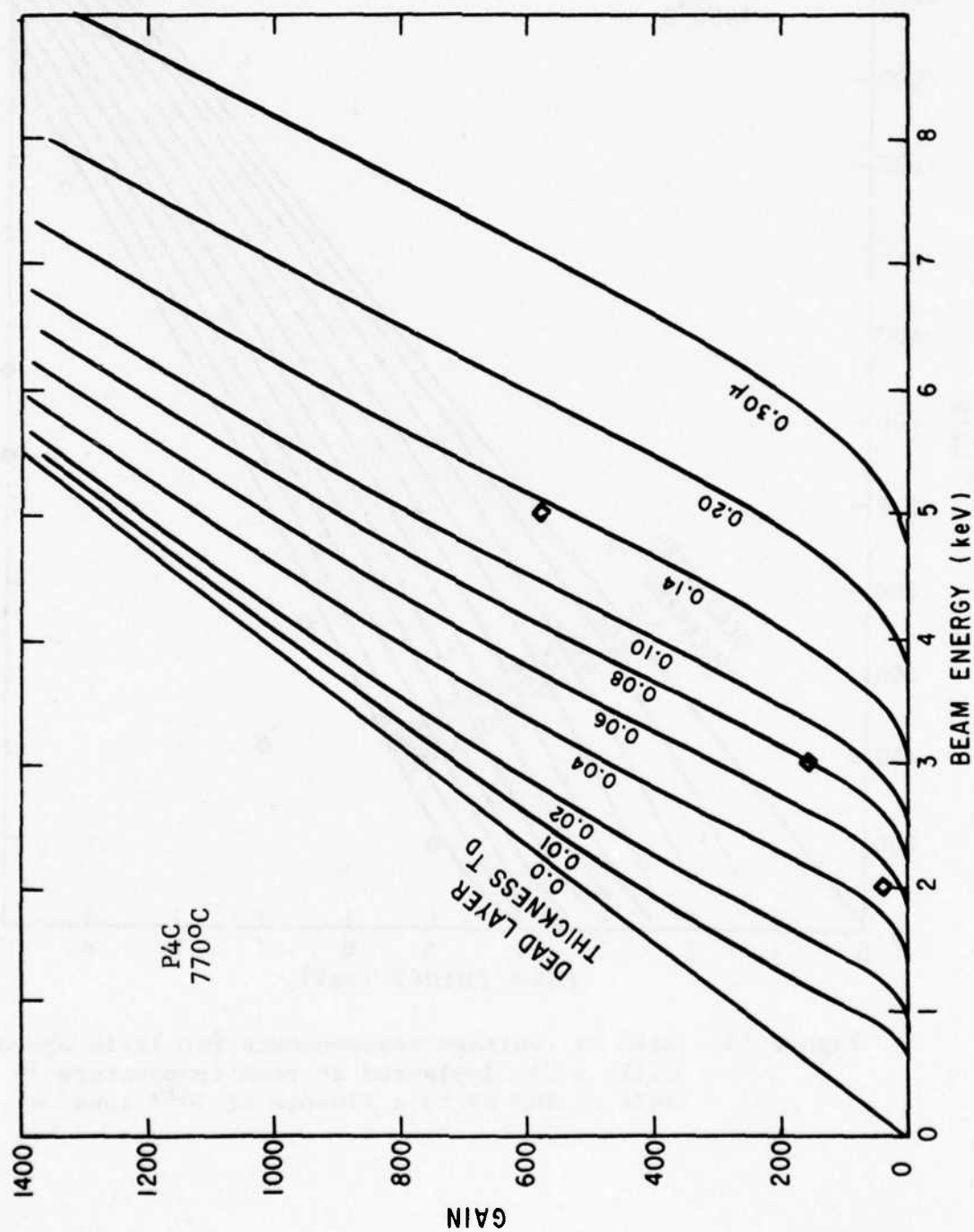
Figure 45. Gain vs. voltage measurements for 12-18 ohm-cm, <111> p-Si, implanted at room temperature 7° off axis at 100 kV to a fluence of 10¹⁴ ions/cm², through 1400 Å oxide.

Figure 46. Gain vs. voltage measurements for 12-18 ohm-cm, <111> p-Si, implanted at room temperature 7° off axis at 100 kV to a fluence of 10^{14} ions/cm^2.
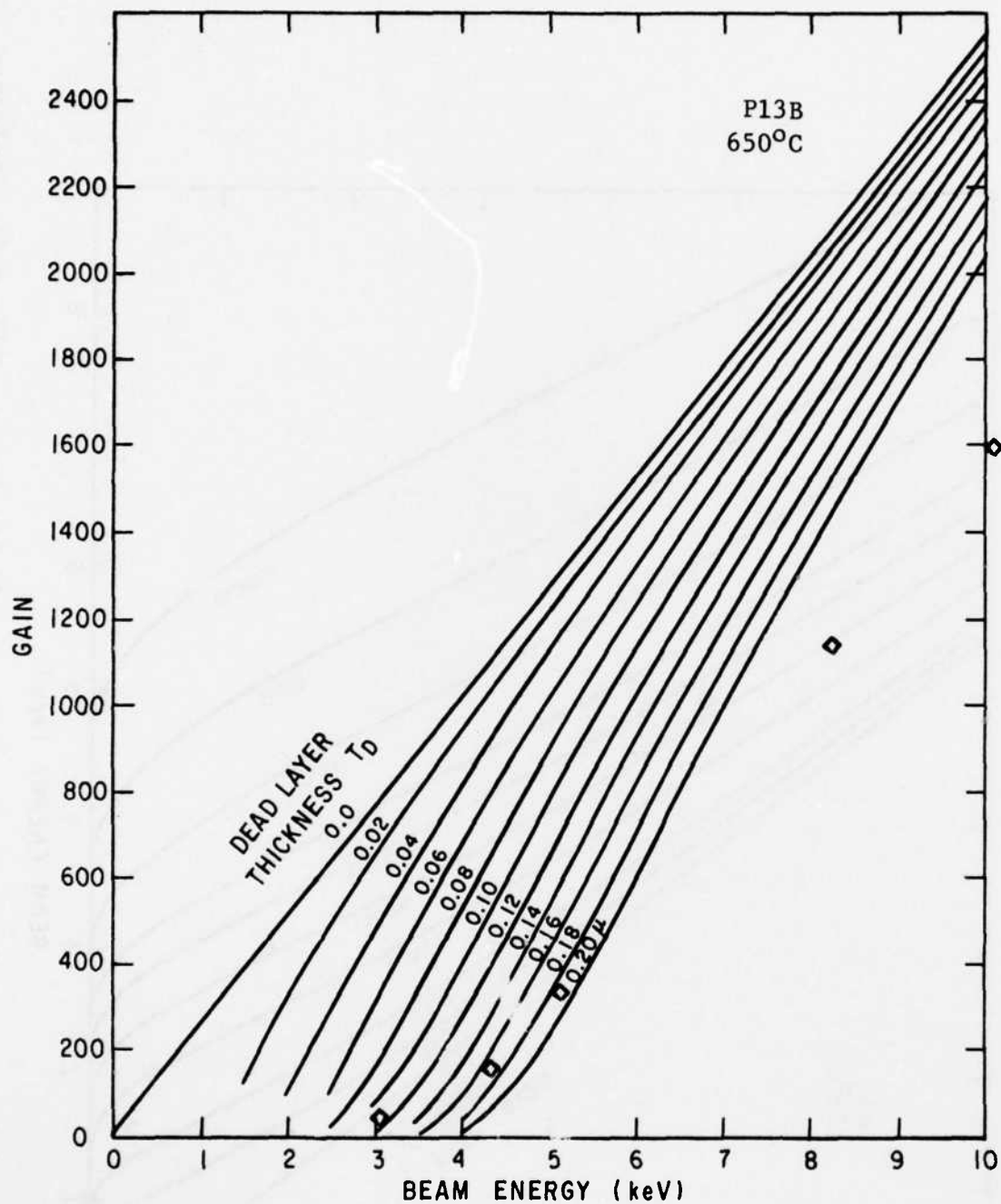
Figure 47. Gain vs. voltage measurements for 12-18 ohm-cm, <111> p-Si, implanted at room temperature 7° off axis at 100 kV to a fluence of 10^{14} ions/cm^2.
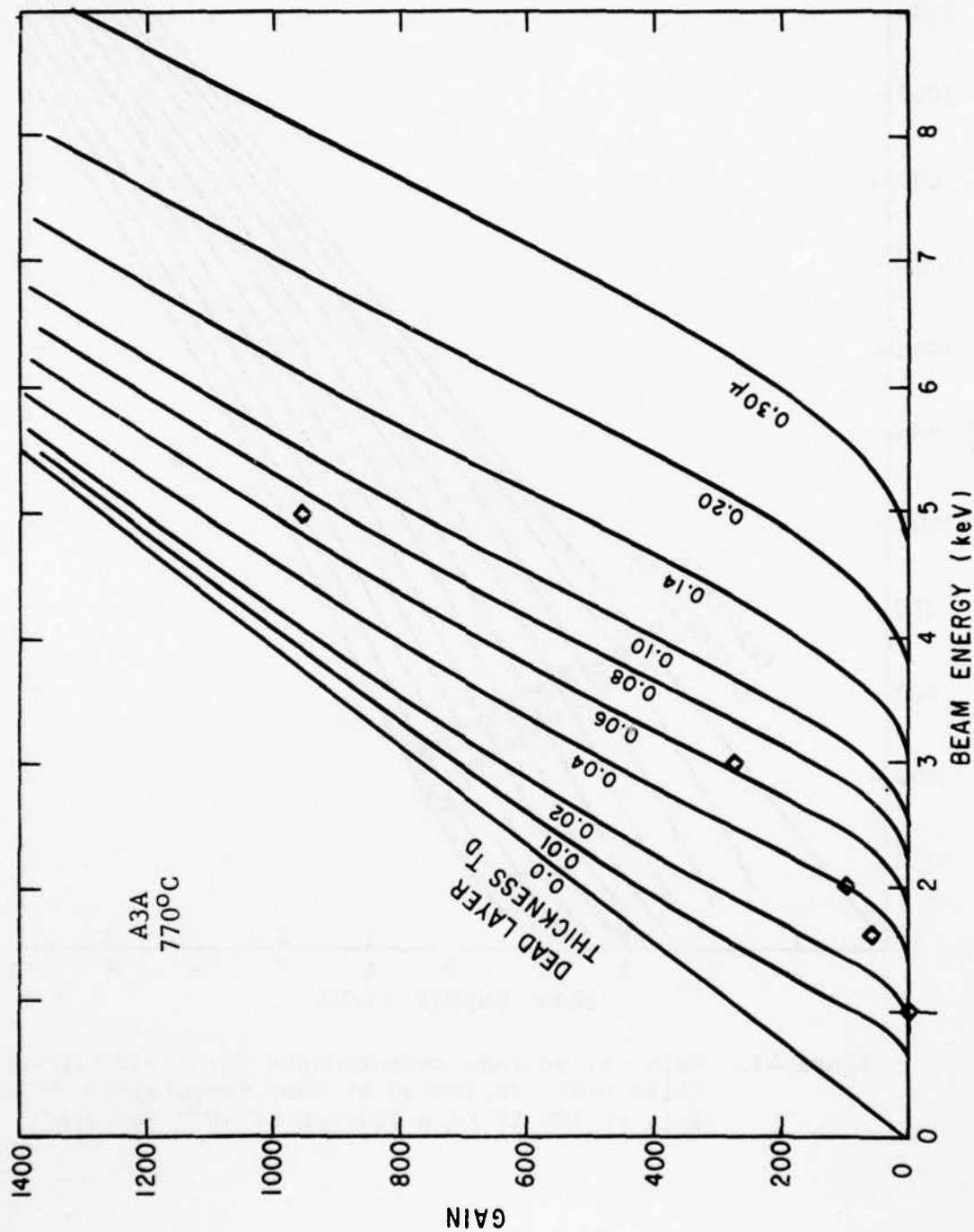
Figure 48. Gain vs. voltage measurements for 12-18 ohm-cm, <111> p-Si, implanted at room temperature 7° off axis at 100 kV to a fluence of 10^{14} ions/cm².
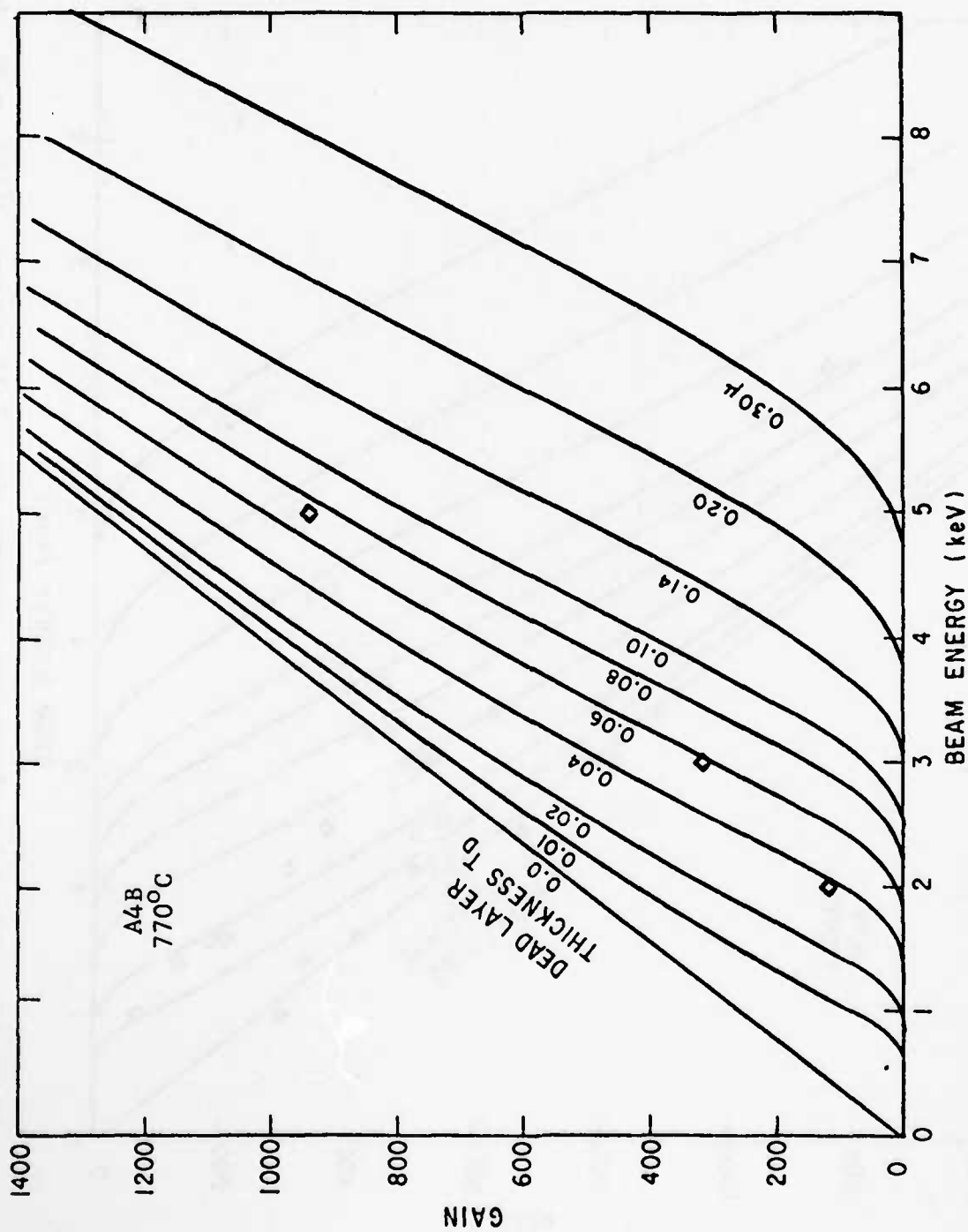
Figure 49. Gain vs. voltage measurements for 12-18 ohm-cm, <111> p-Si, implanted at room temperature 7° off axis at 100 kV to a fluence of 10^{14} ions/cm^2.
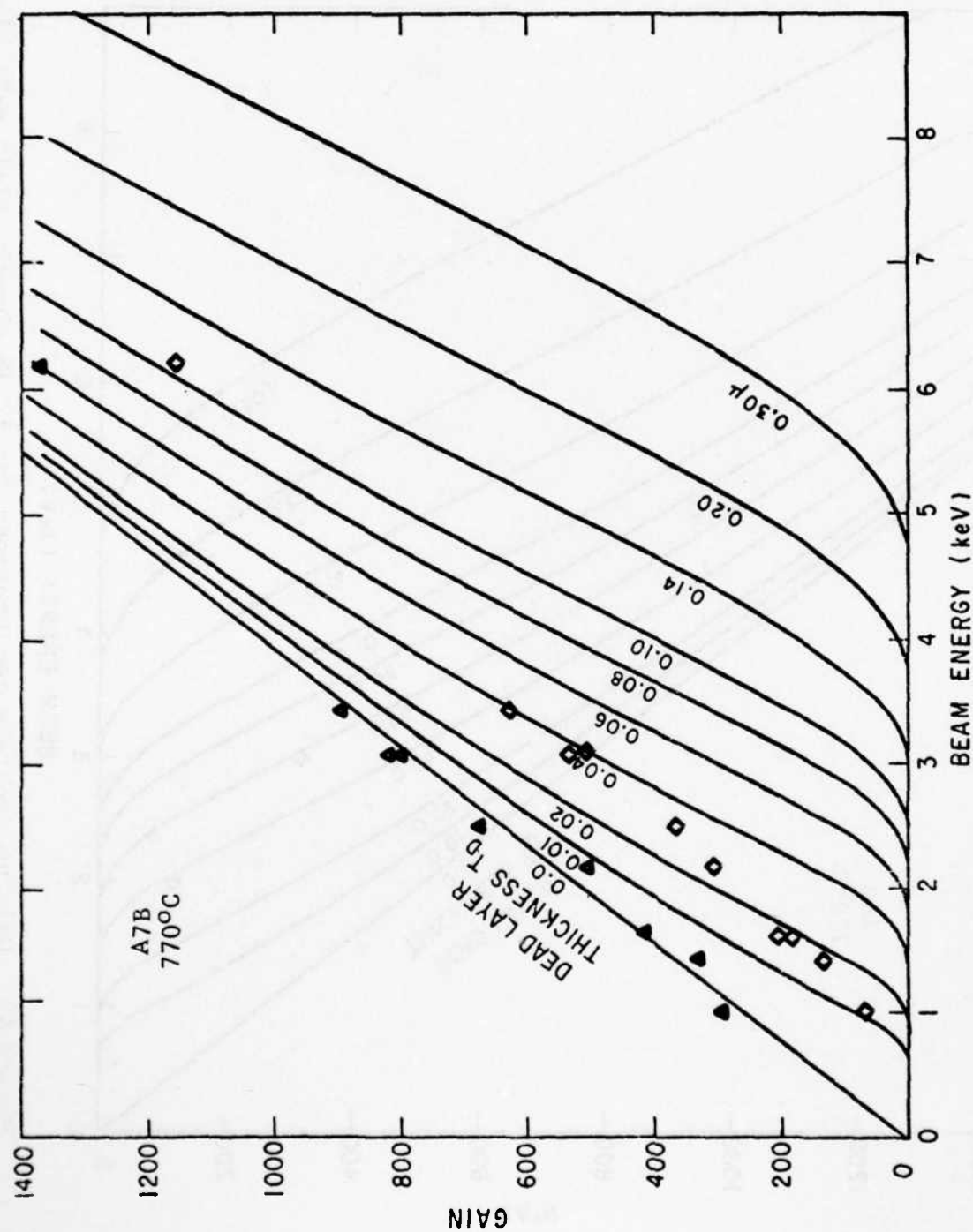
Figure 50. Gain vs. voltage measurements for 12-18 ohm-cm, <111>, p-Si implanted at room temperature 7° off axis at 30 kV to a fluence of 10^{14} ions/cm^2.
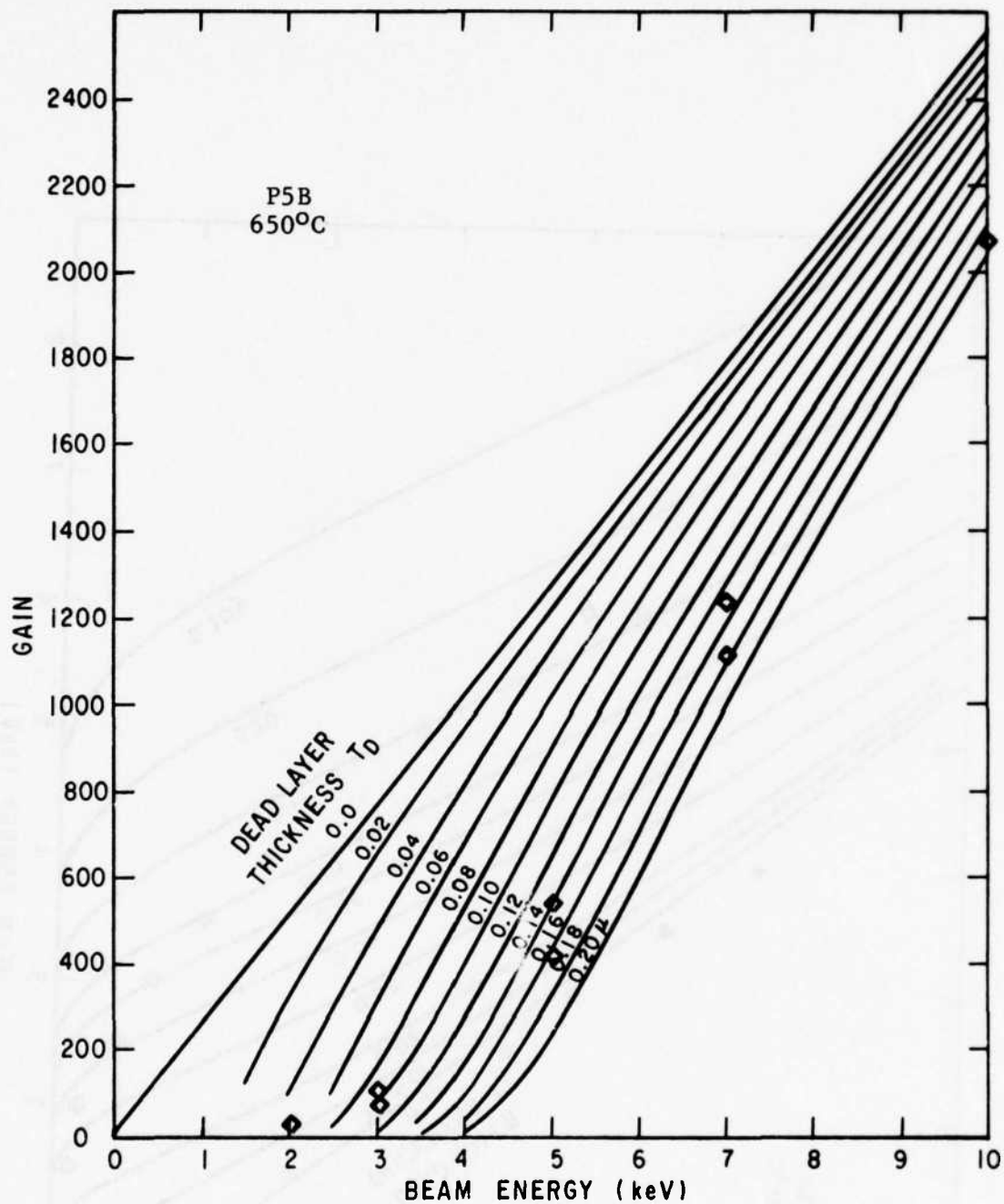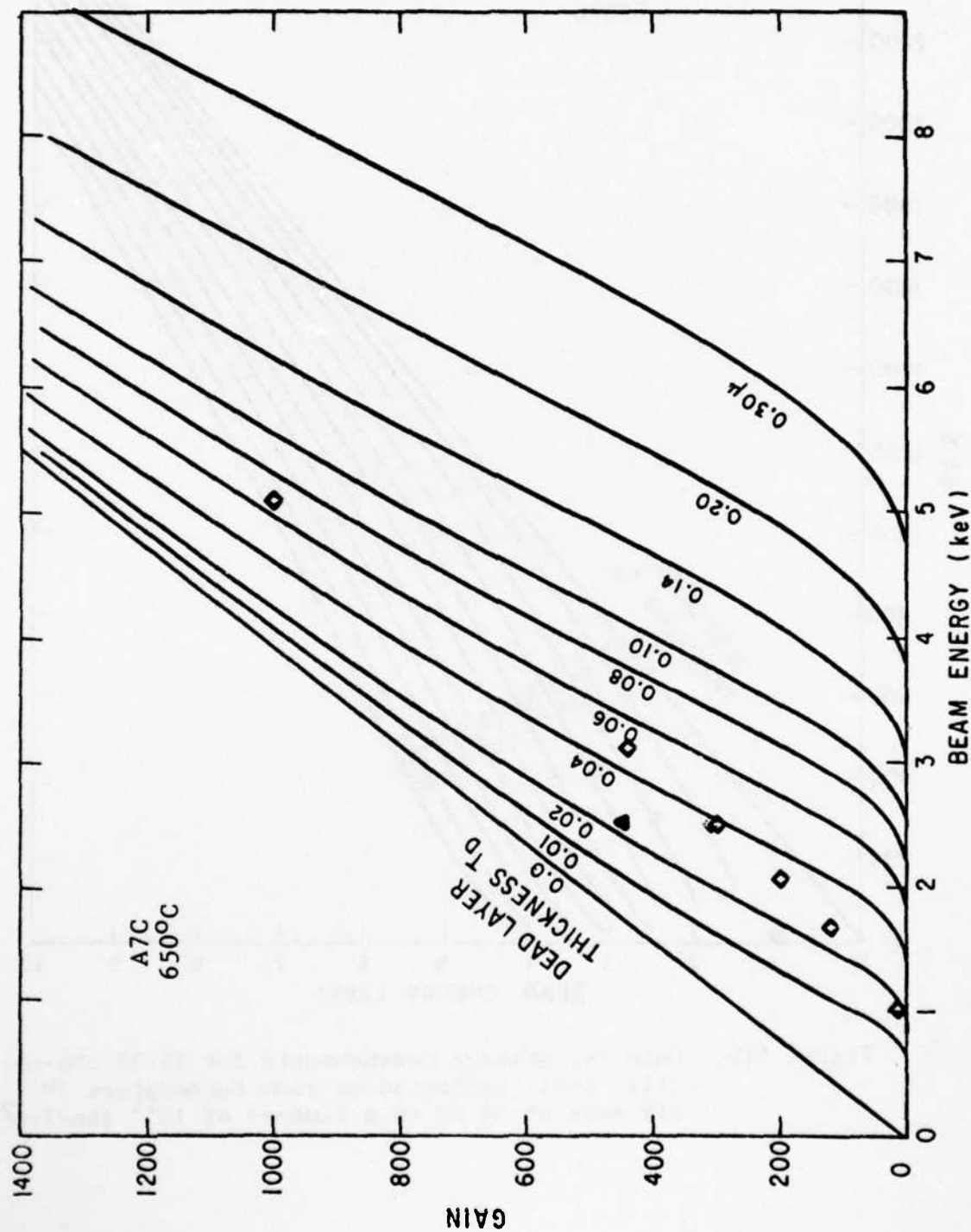
Figure 51a. Gain vs. voltage measurements for 12-18 ohm-cm, <111> p-Si, implanted at room temperature 7° off axis at 30 kV to a fluence of 10^{14} ions/cm^2.
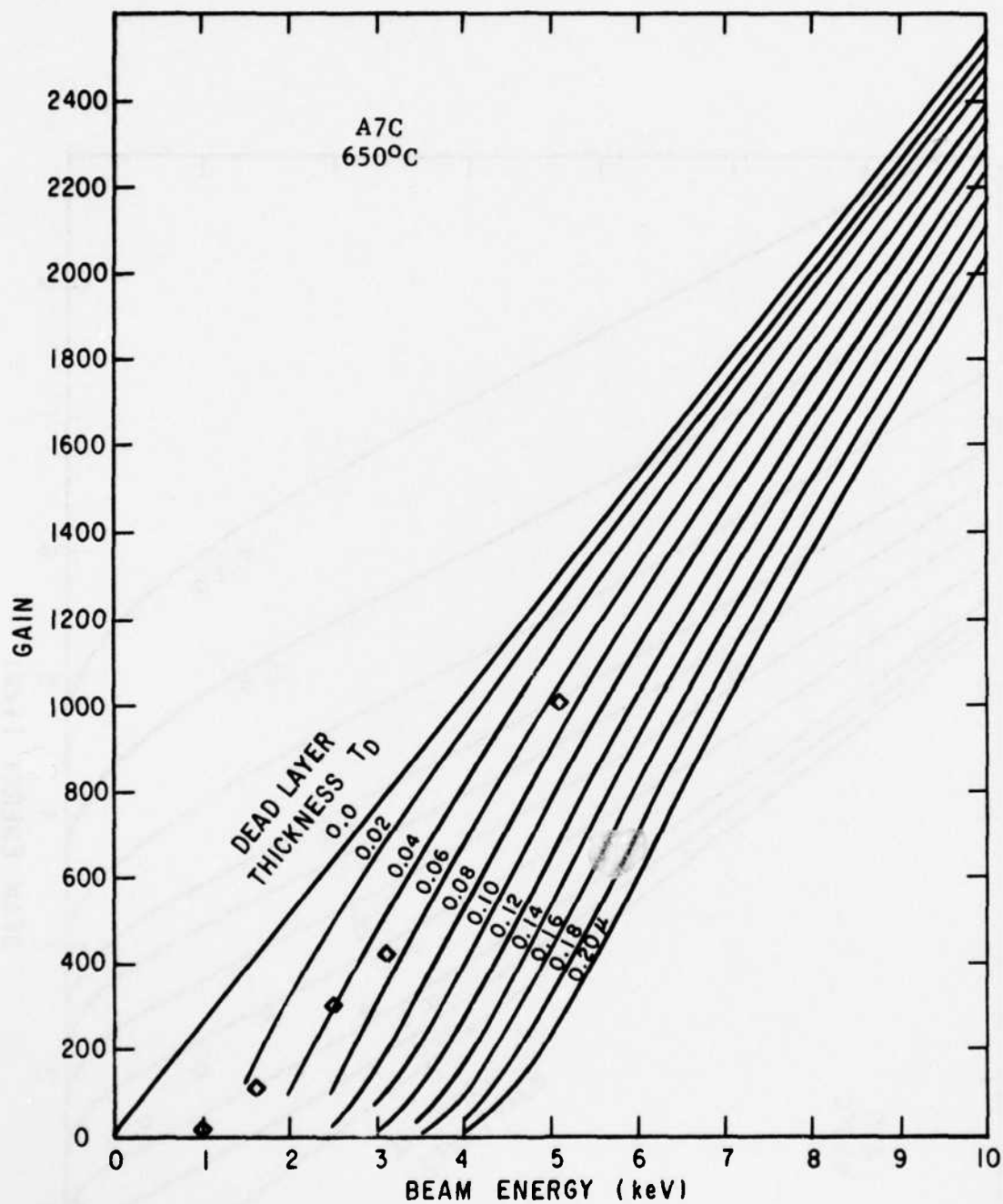
Figure 51b. Gain vs. voltage measurements for 12-18 ohm-cm, <111> p-Si, implanted at room temperature 7° off axis at 30 kV to a fluence of 10^{14} ions/cm².
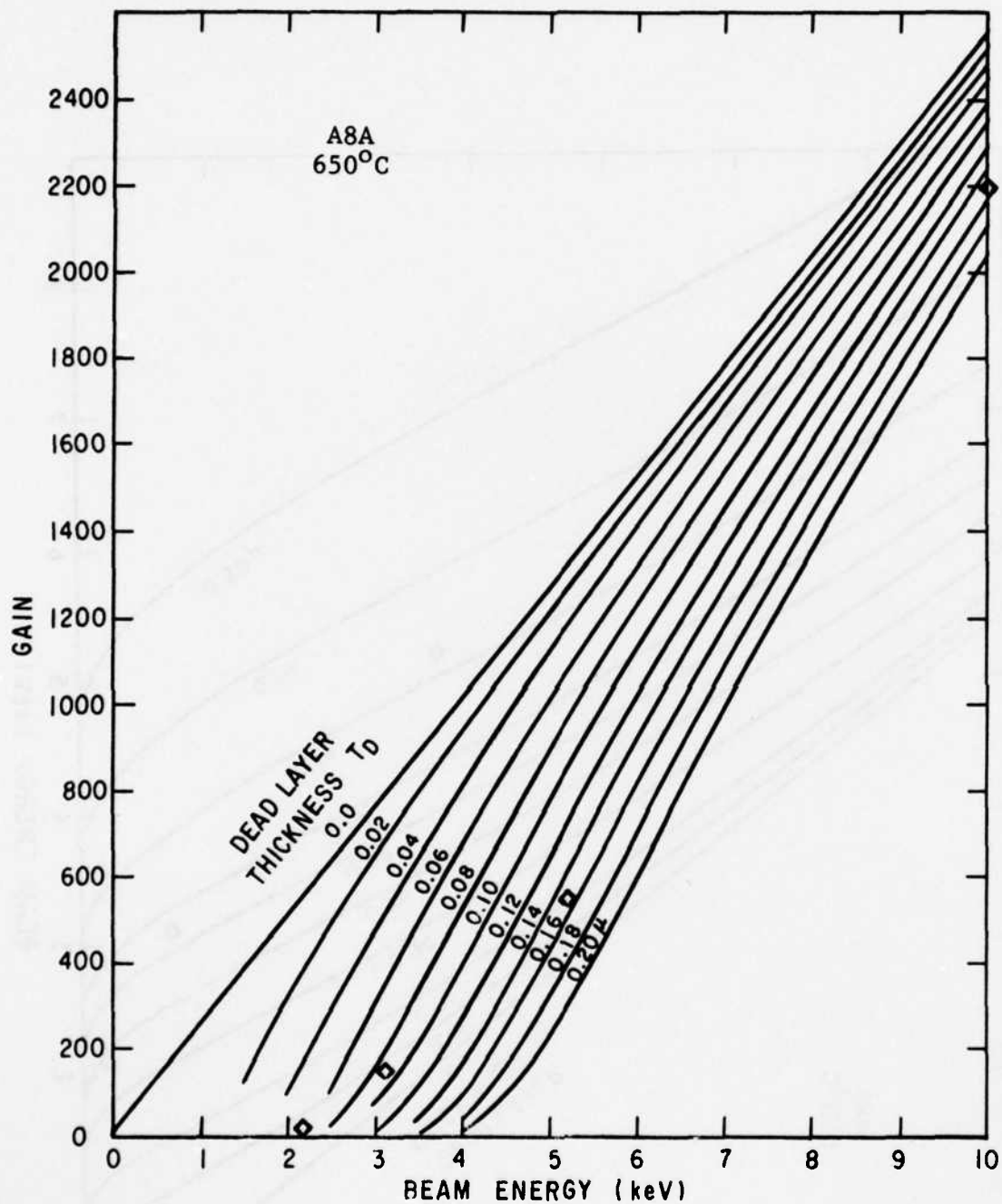
Figure 52. Gain vs. voltage measurements for 4.8-7.2 ohm-cm, <100> p-Si, implanted at room temperature 7° off axis at 100 kV to a fluence of 10^{14} ions/cm².
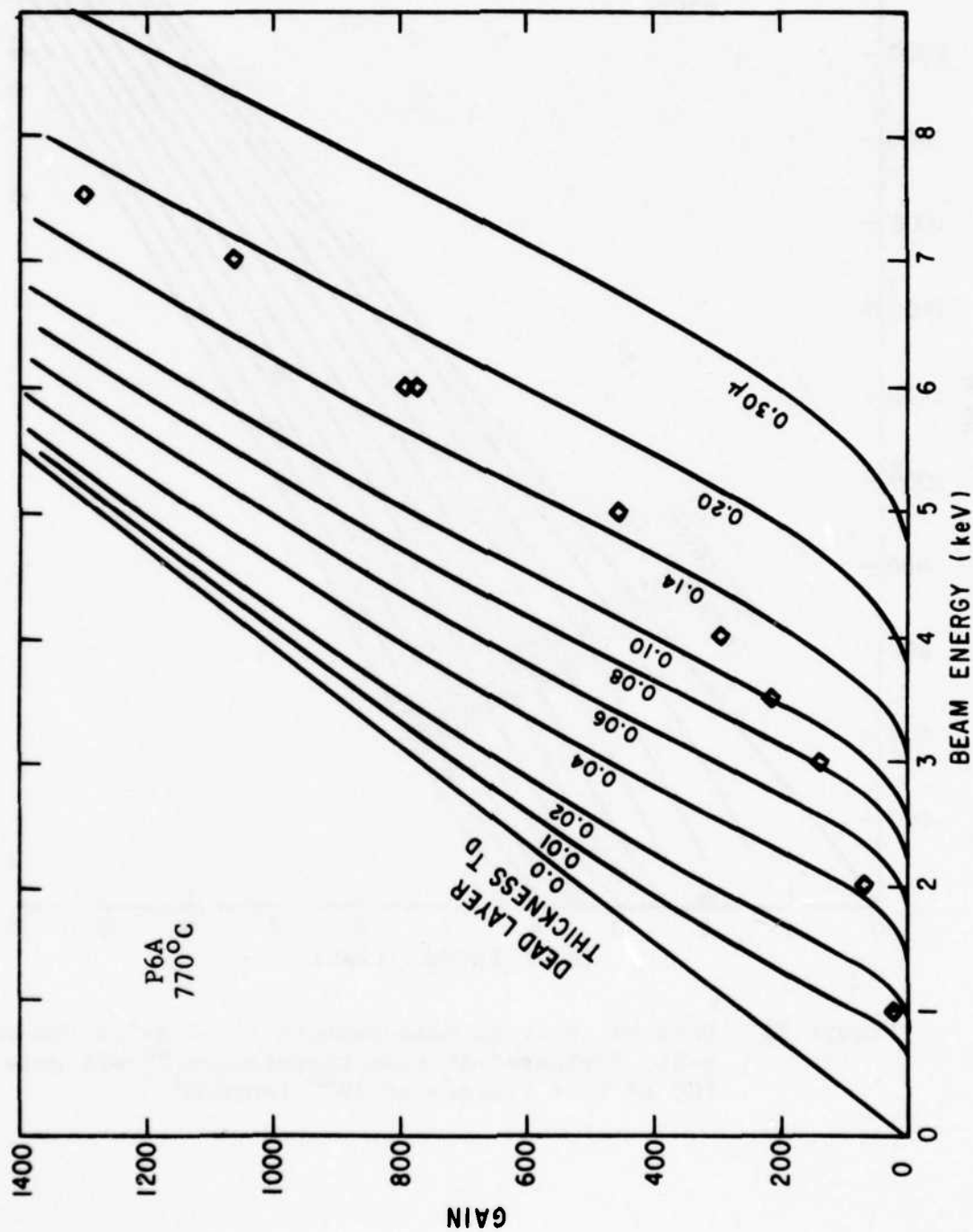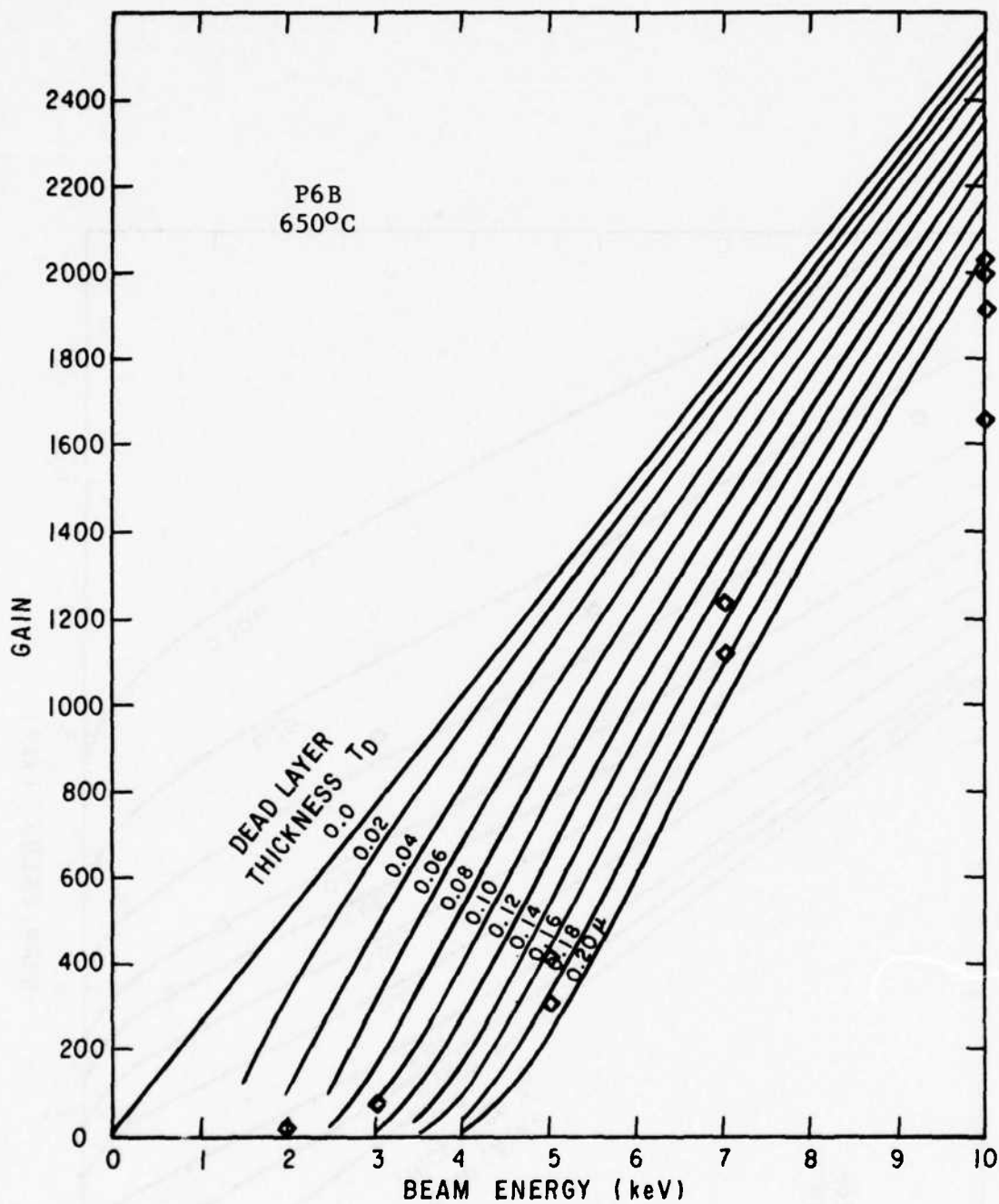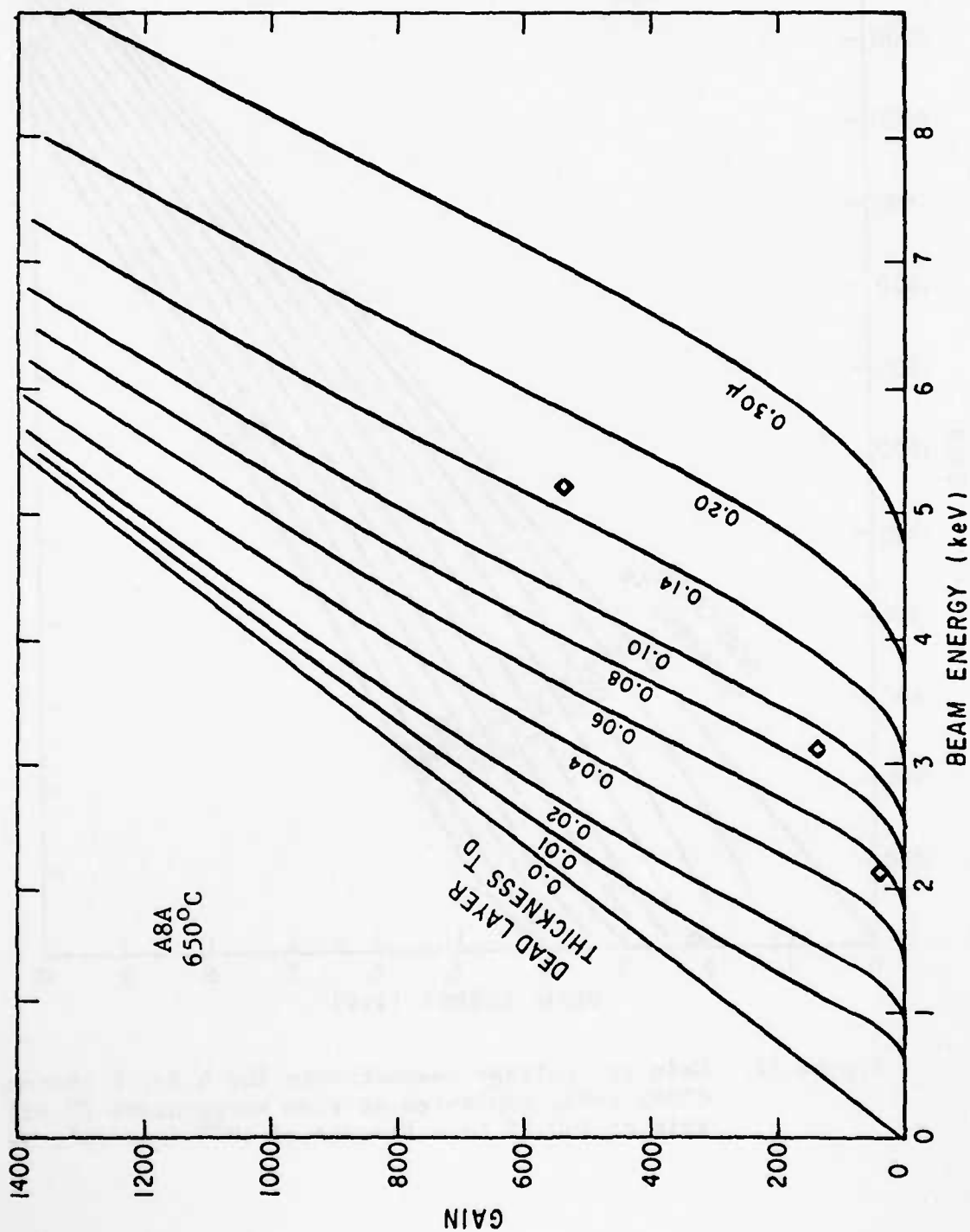
Figure 53. Gain vs. voltage measurements for 4.8-7.2 ohm-cm, ⟨100⟩ p-Si implanted at room temperature 7° off axis at 100 kV to a fluence of 10^{14} ions/cm^2.
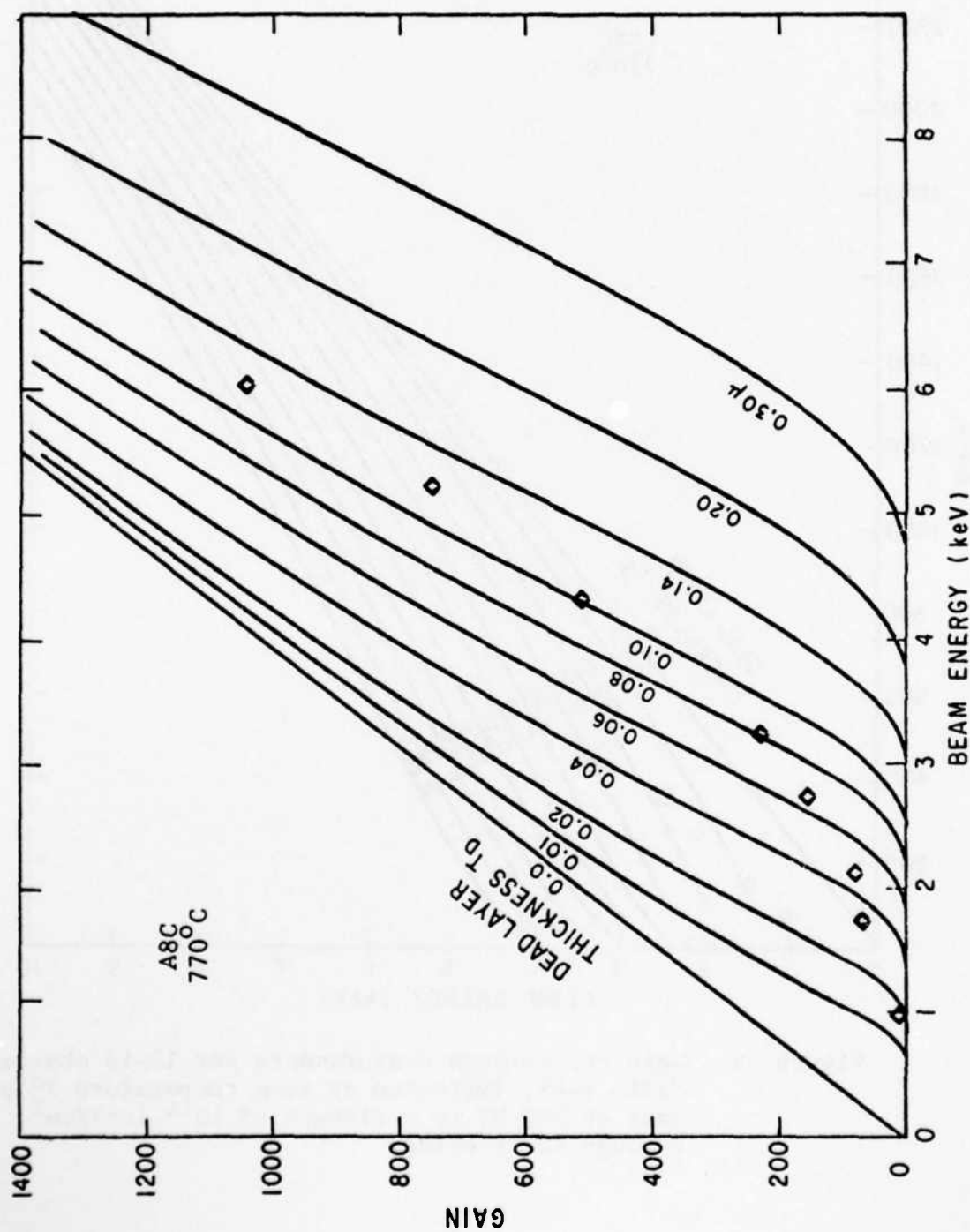
Figure 54. Gain vs. voltage measurements for 4.8-7.2 ohm-cm, <100> p-Si implanted at room temperature 7° off axis at 100 kV to a fluence of 10_{14} ions/cm².
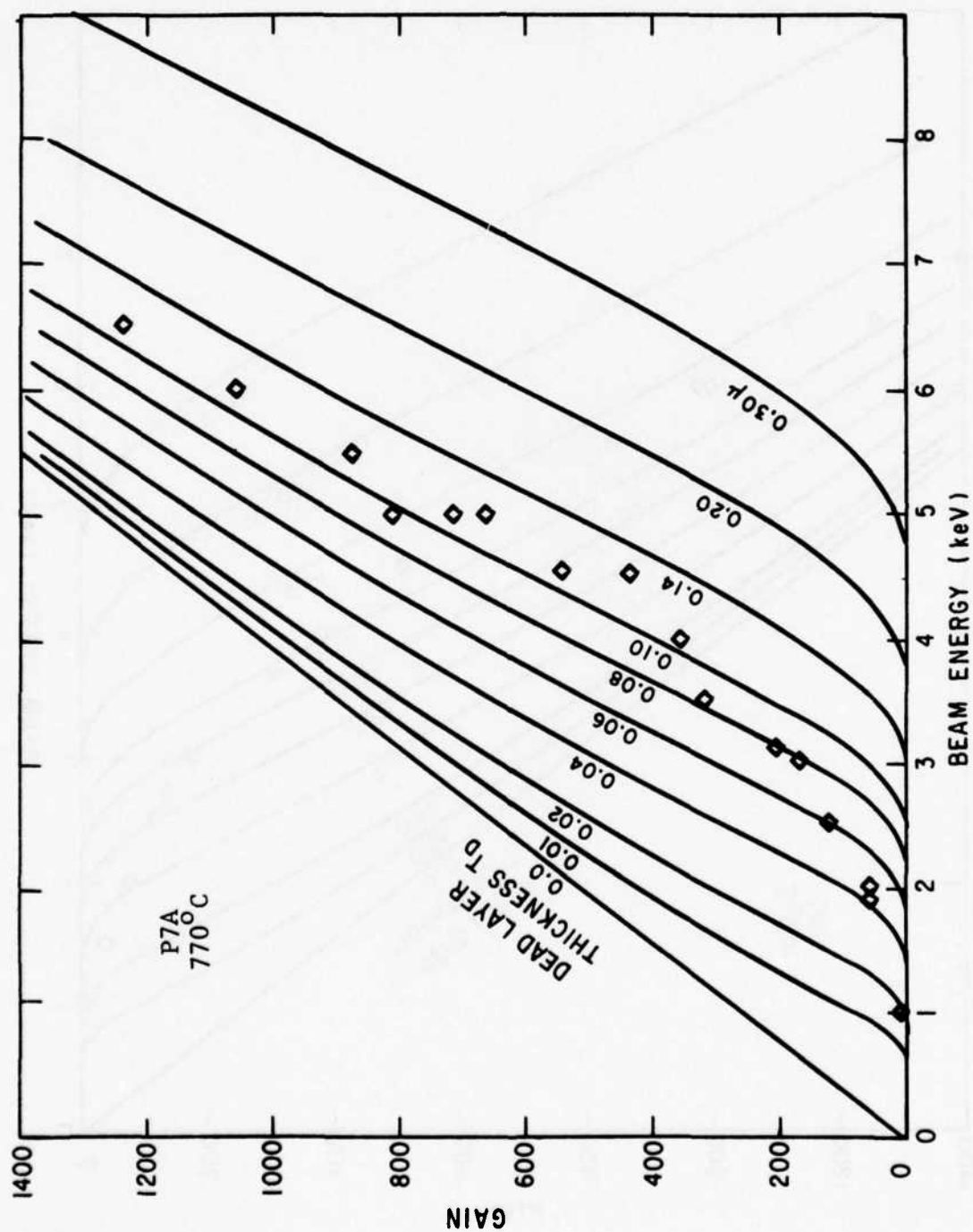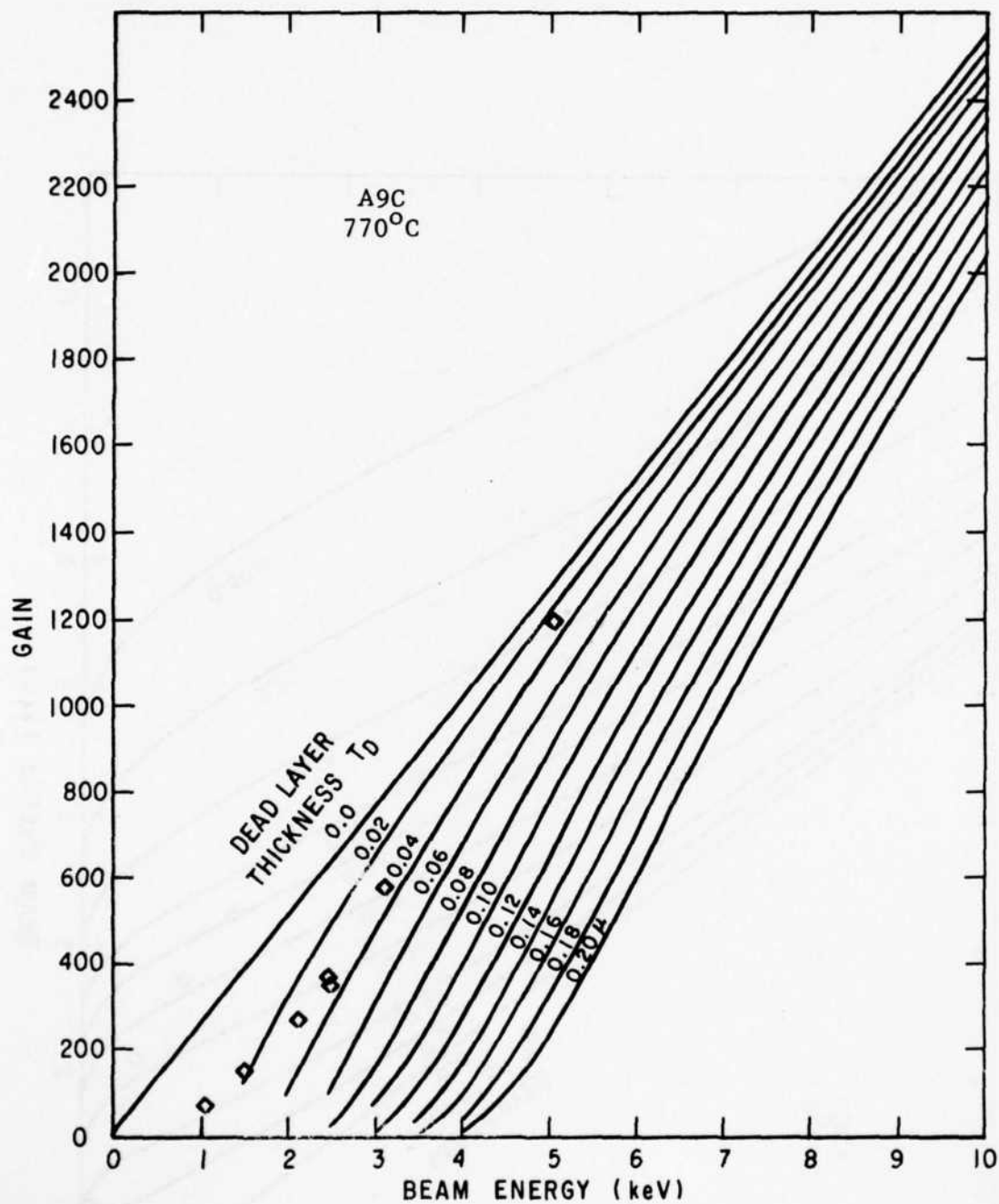
Figure 55.   Gain vs. voltage measurements for 12-18 ohm-cm,
             <111> p-Si, implanted at room temperature 7° off
             axis at 100 kV to a fluence of 10^{14} ions/cm^2,
             through 200 Å oxide.
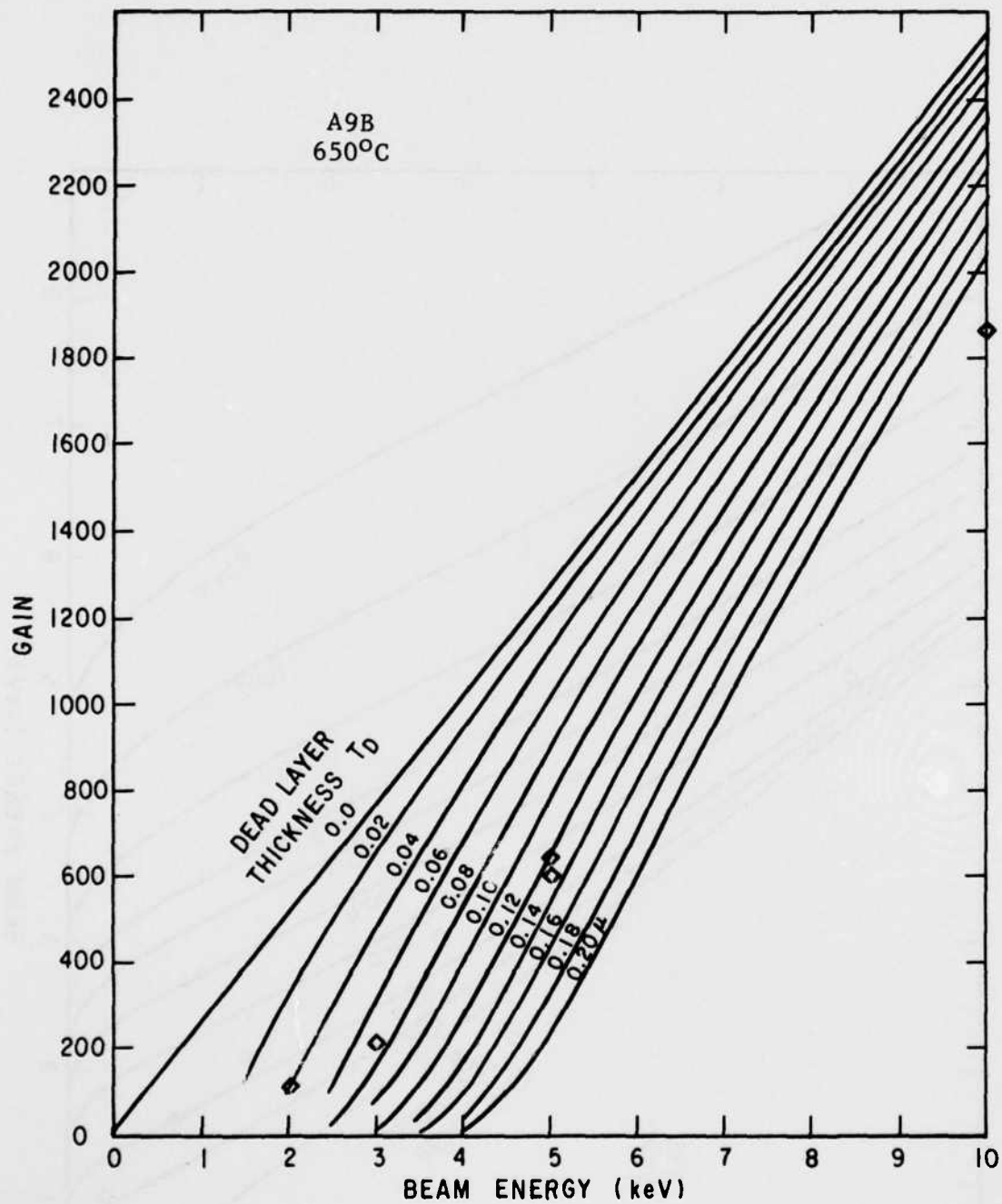
Figure 56. Gain vs. voltage measurements for 11-13 ohm-cm, <111> p-Si, implanted at room temperature 7° off axis at 100 kV to a fluence of 10^{14} ions/cm^2.
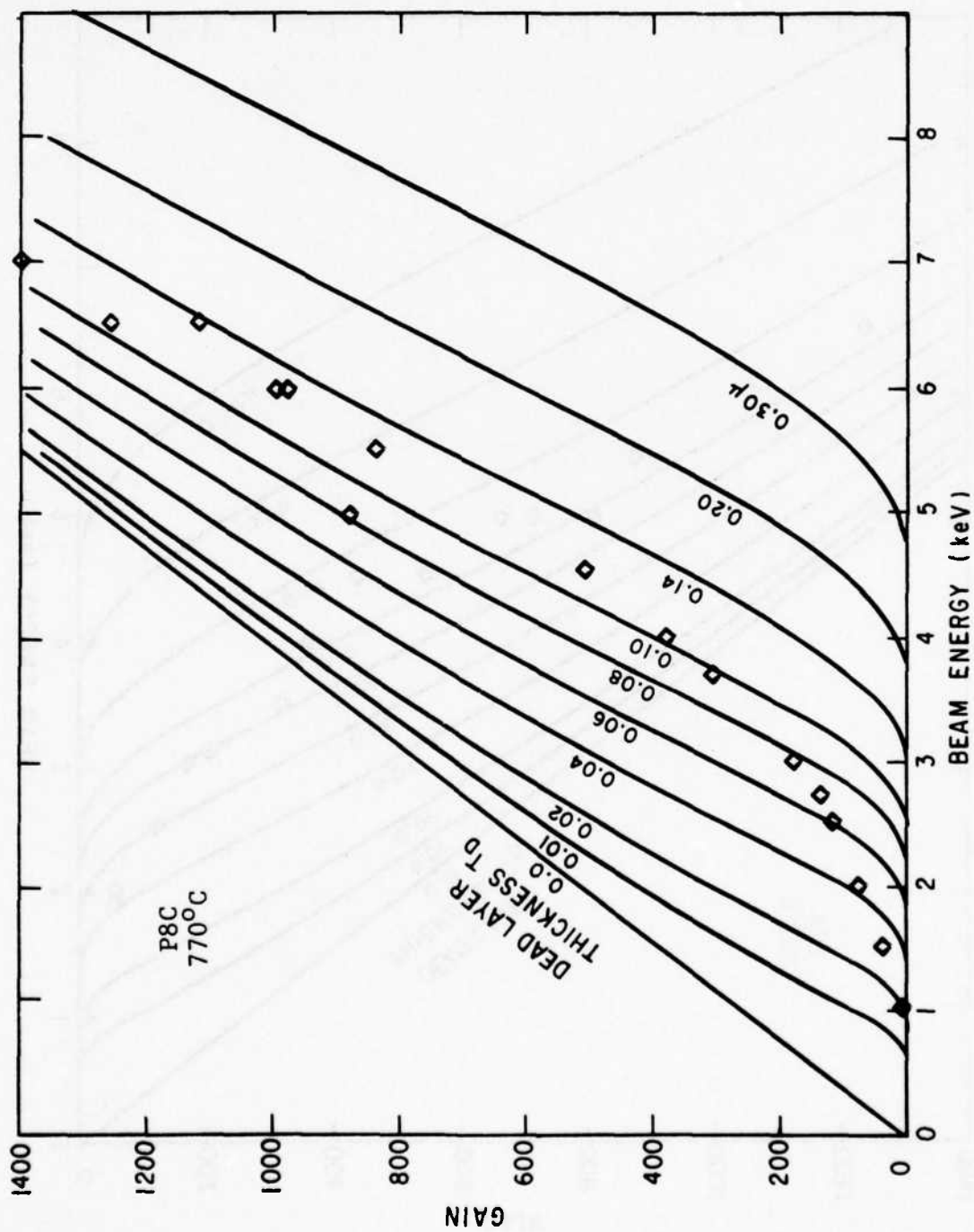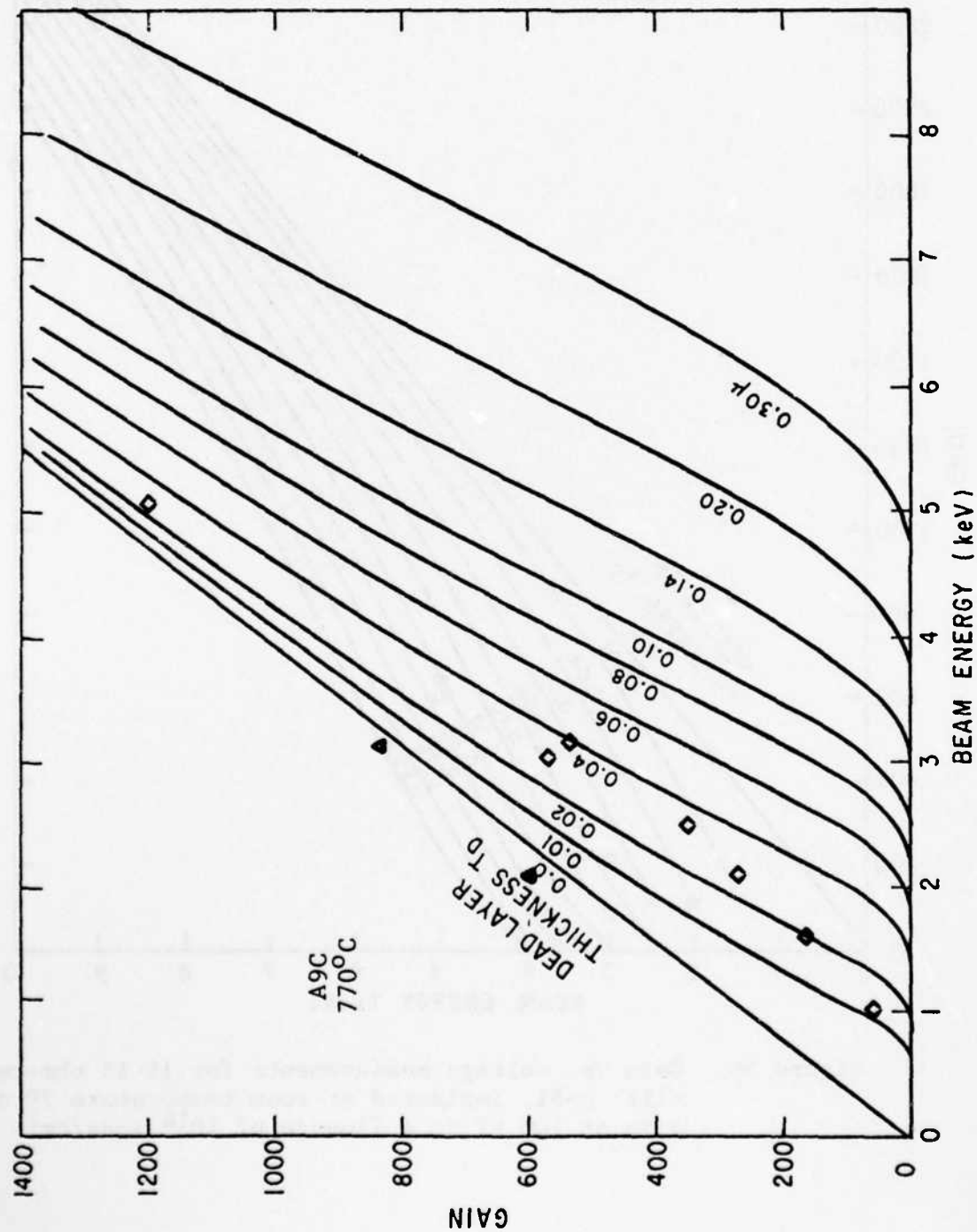
Figure 57. Gain vs. voltage measurements for 12-18 ohm-cm, ⟨111⟩ p-Si, implanted at room temperature 7° off axis at 100 kV to a fluence of 10^{14} ions/cm².
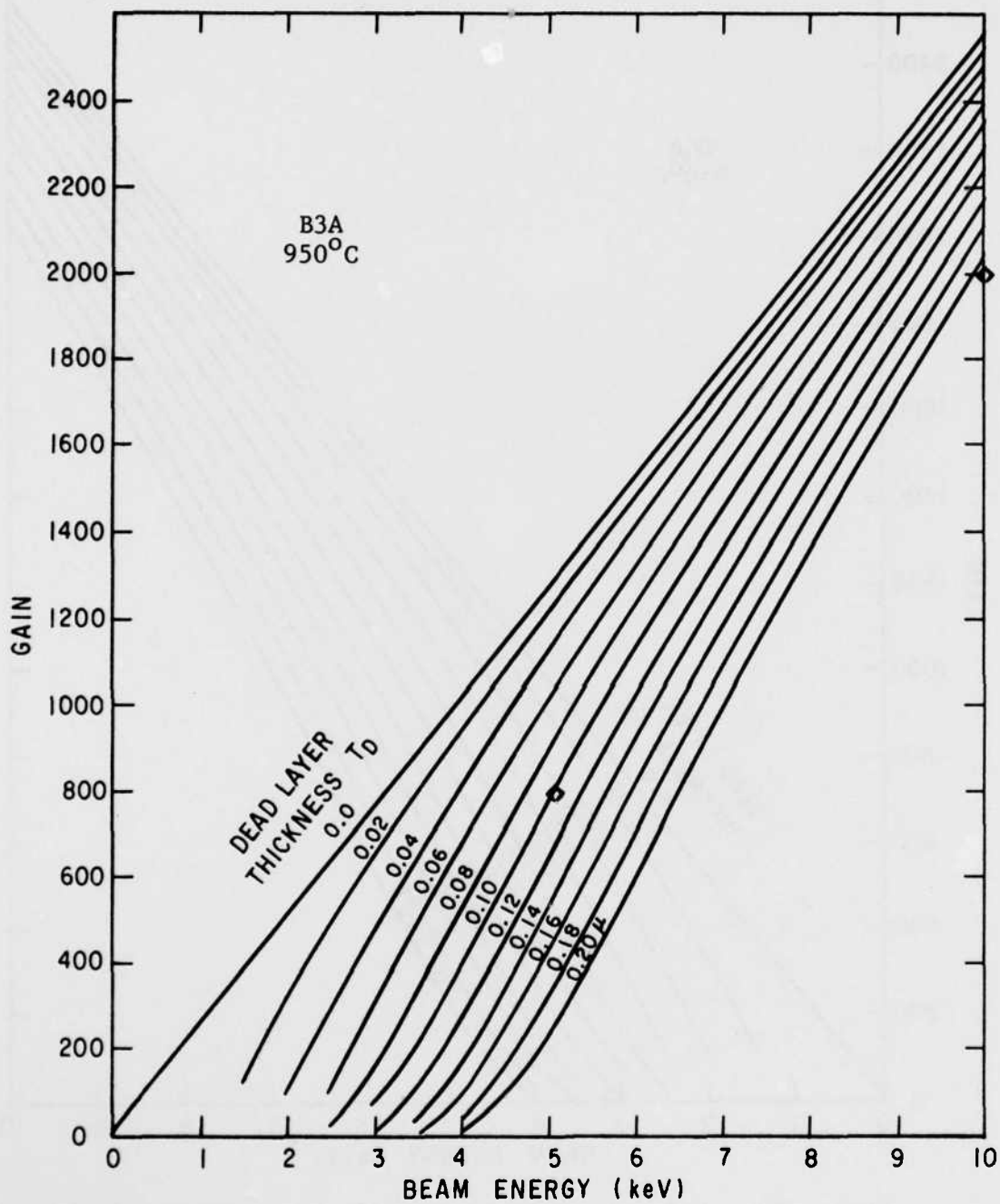
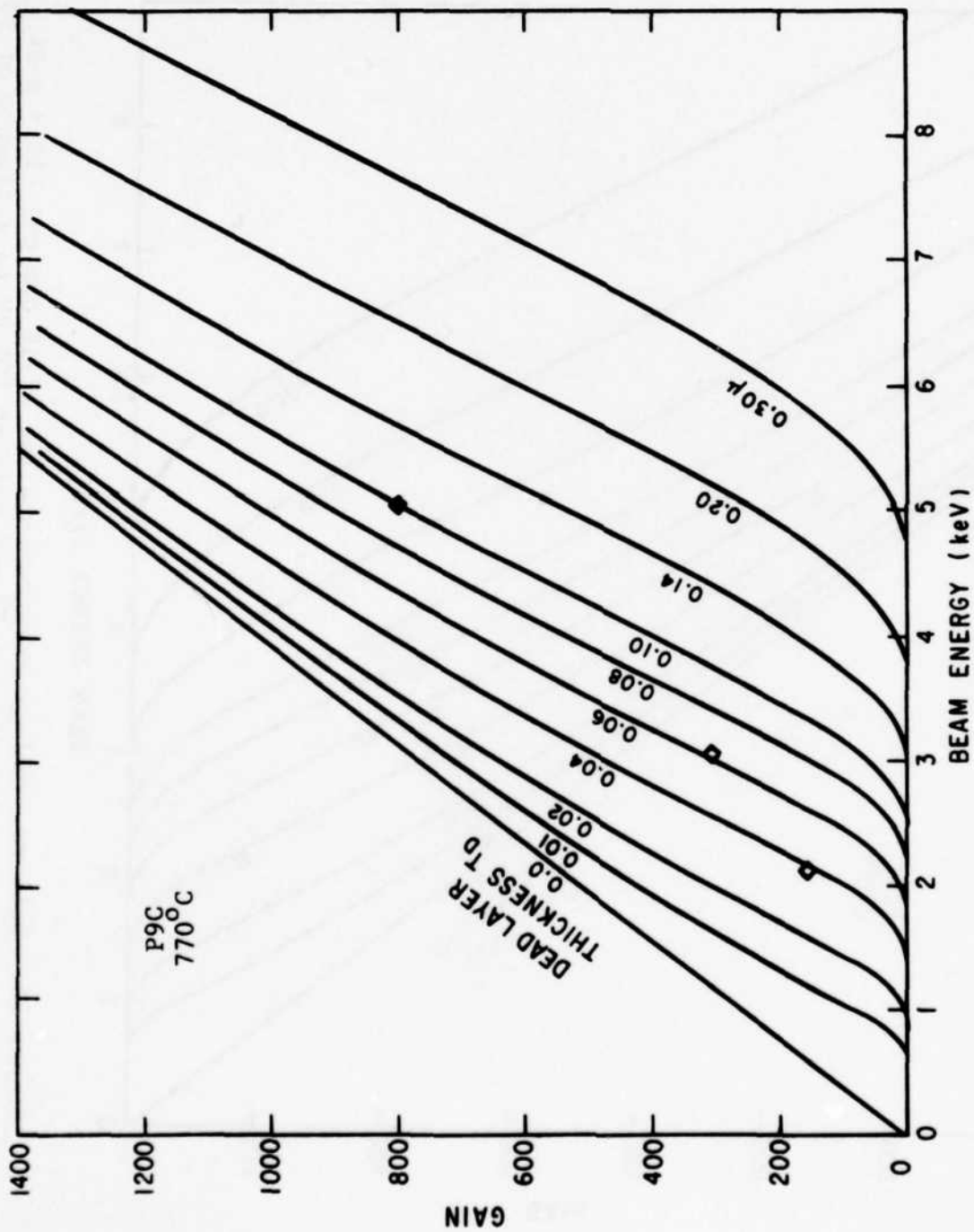Figure 58. Gain vs. voltage measurements for 11-13 ohm-cm,
⟨111⟩ n-Si, implanted at room temperature 7° off
axis at 100 kV to a fluence of 10^{14} ions/cm^2,
through 200 Å oxide.

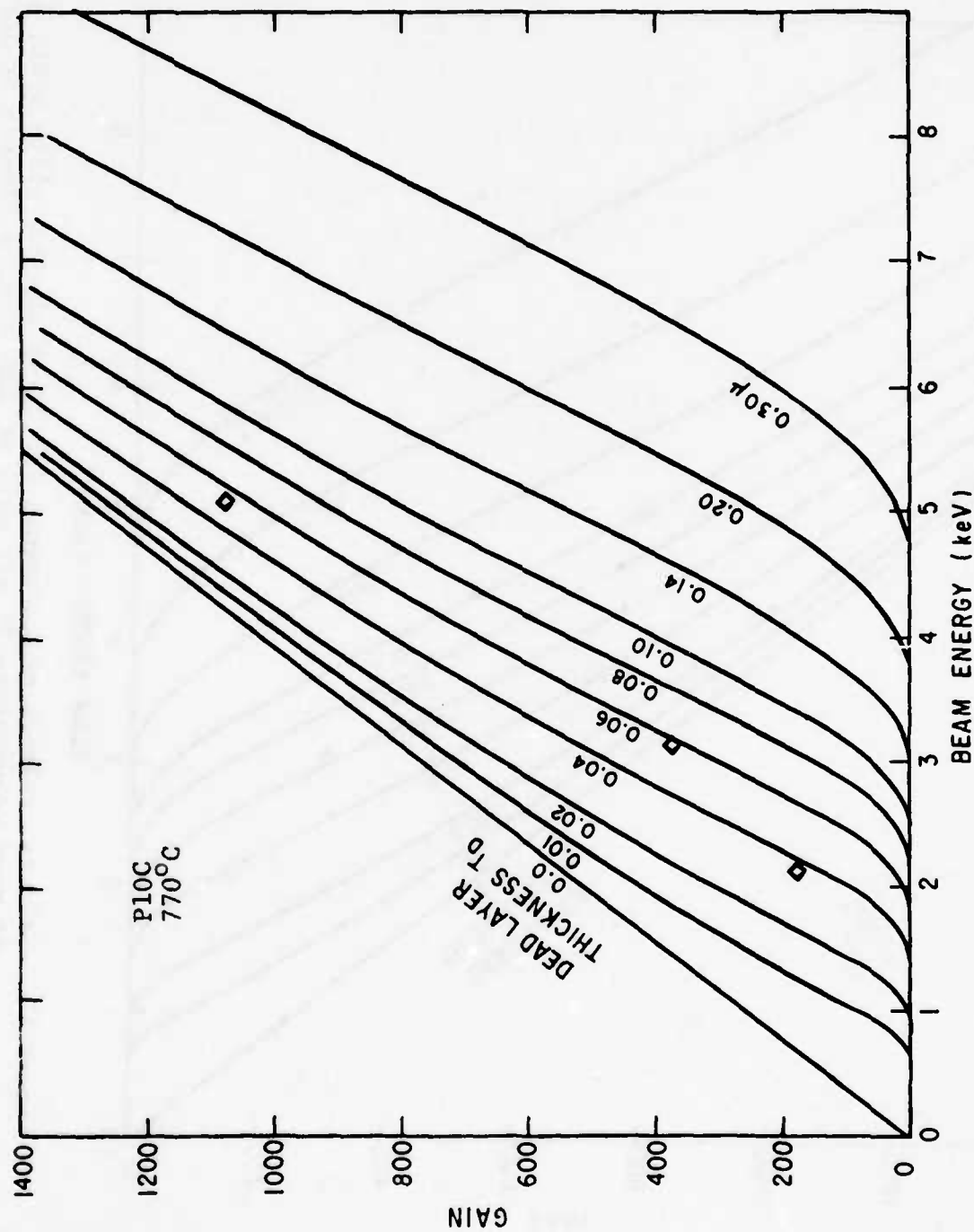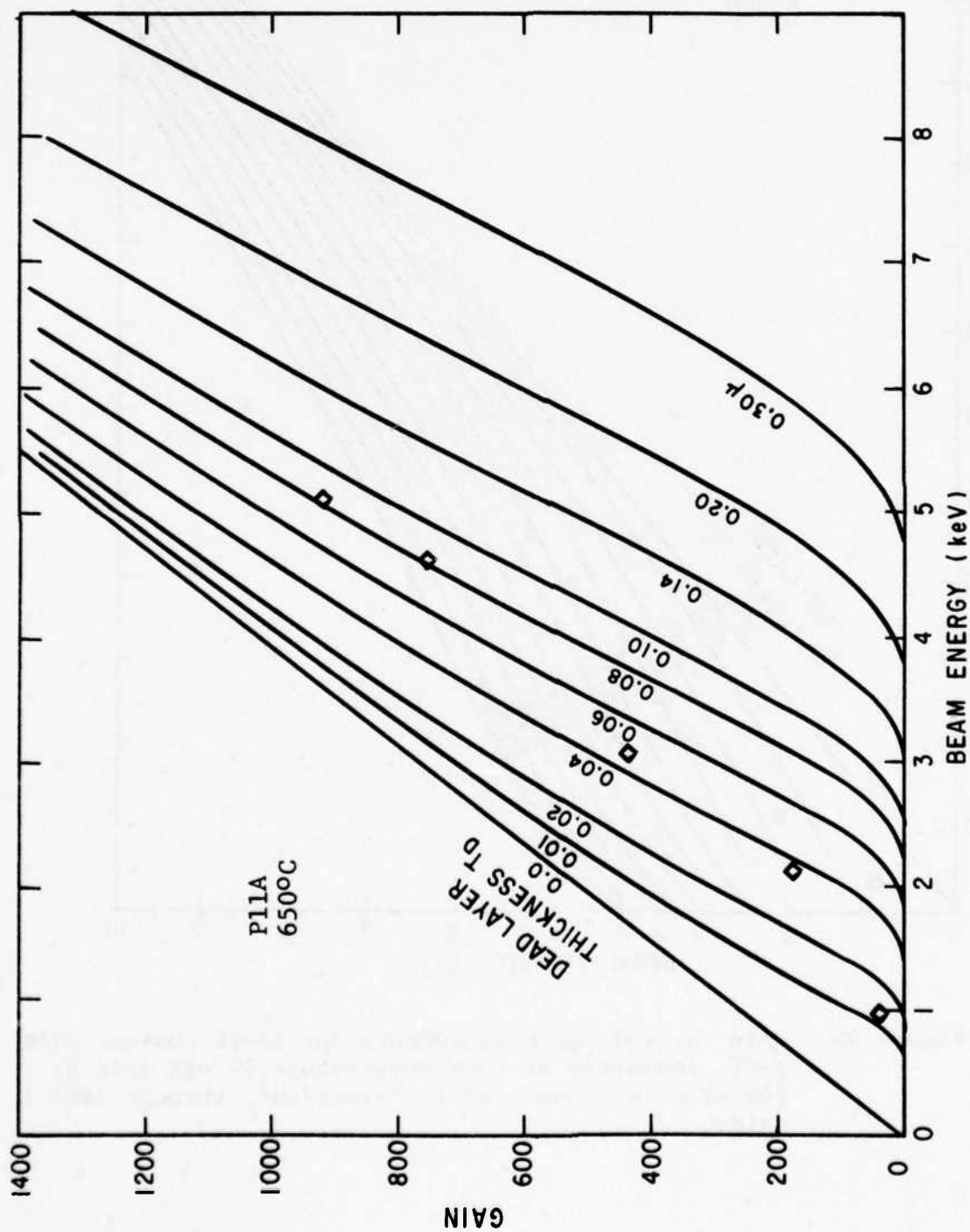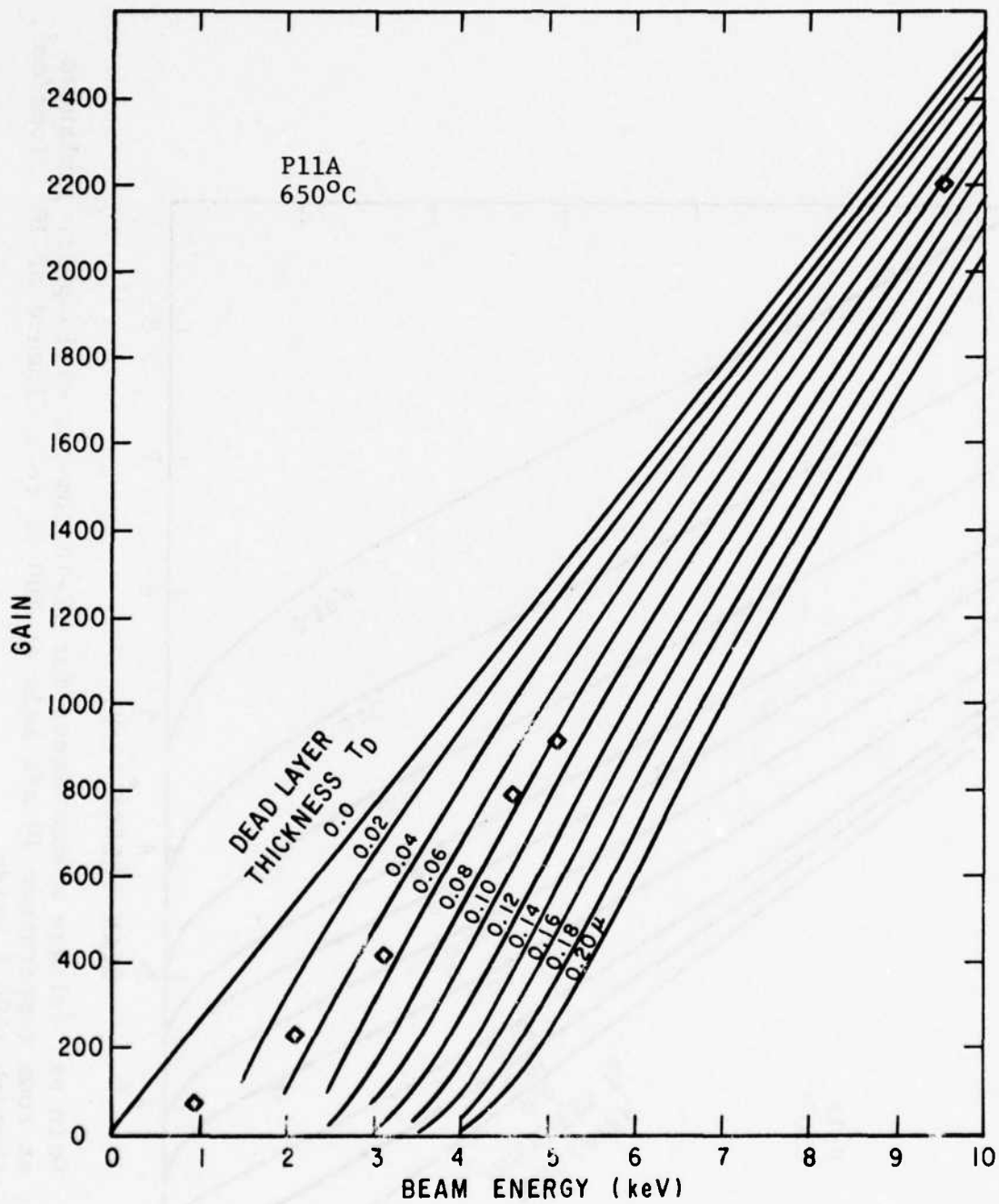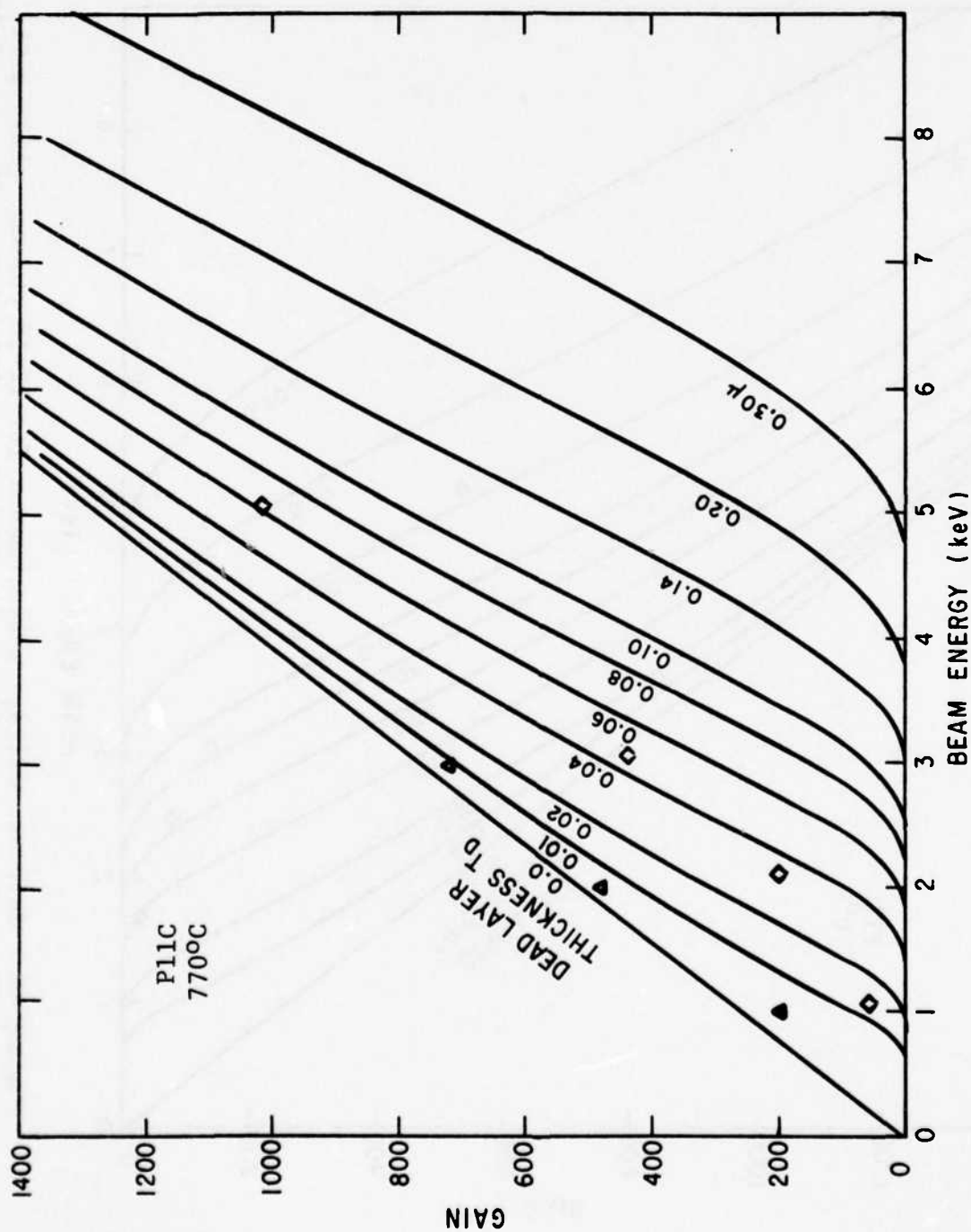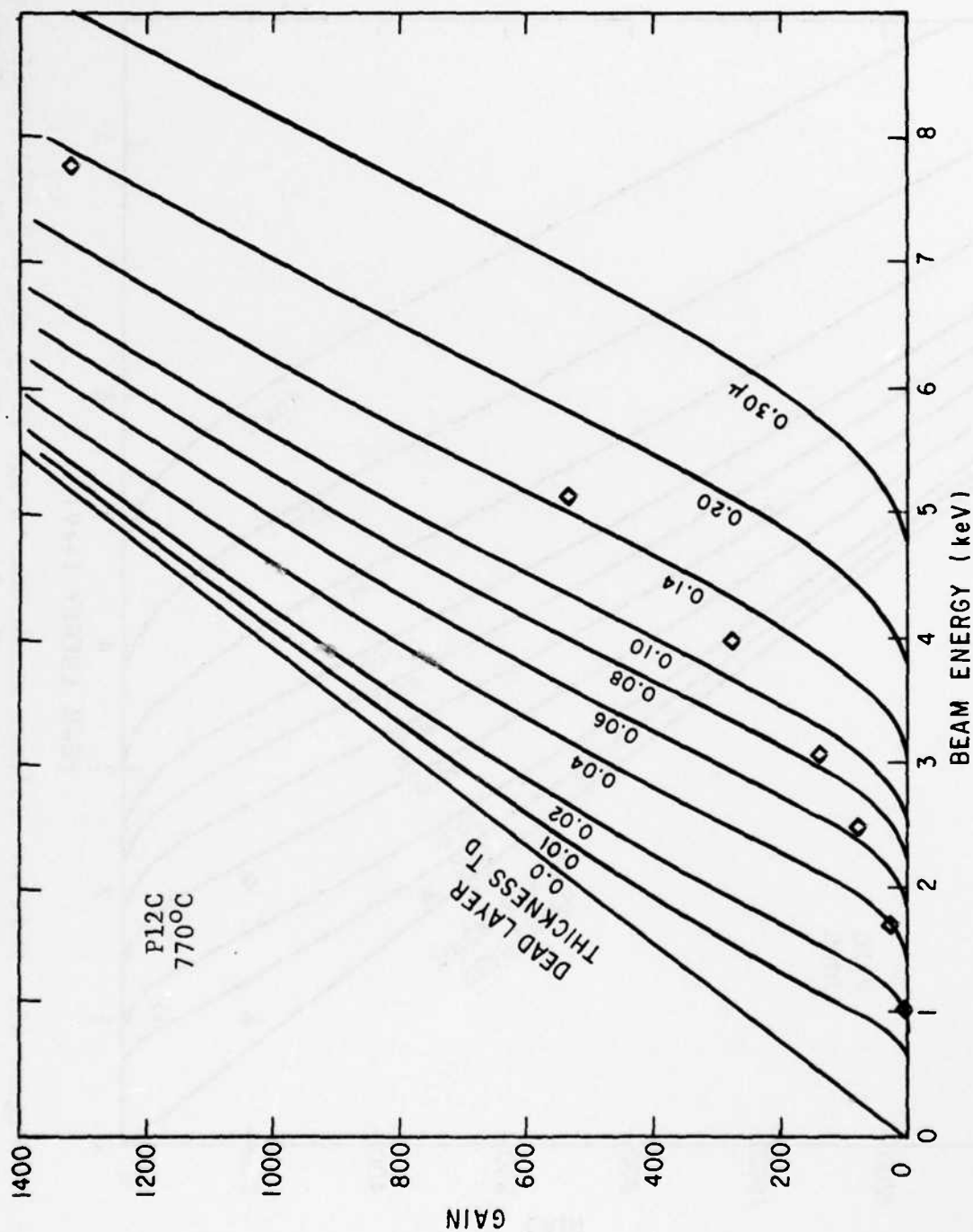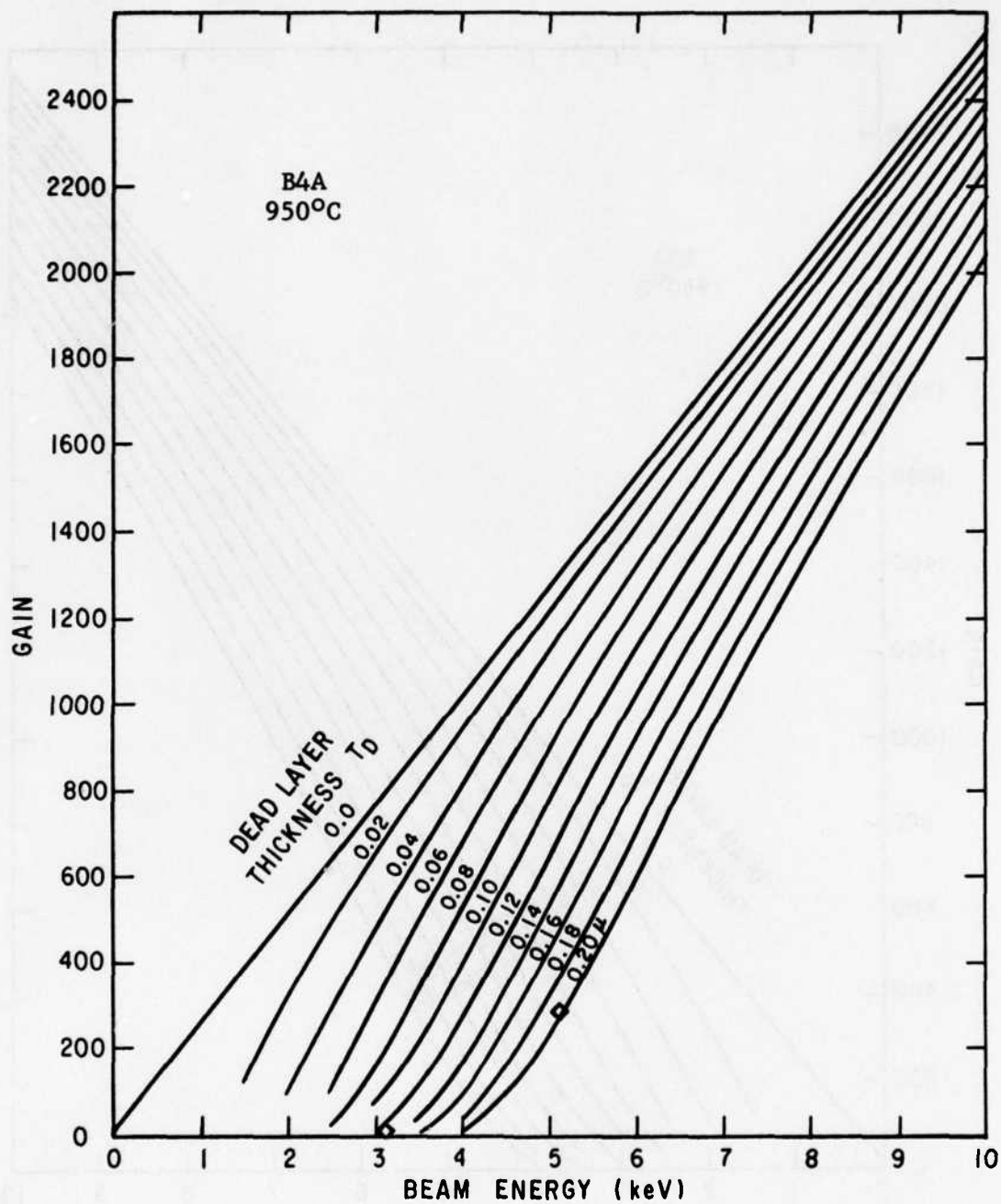Figure 59. Gain vs. voltage measurements for 11-13 ohm-cm, <111> n-Si, implanted at room temperature 7° off axis at 100 kV to a fluence of 10^{14} ions/cm².

and at 5 keV as though $T_D = 0.12$ microns. This provides a convenient method of comparing targets while at the same time giving some estimate of the thickness of the dead layers involved. To avoid confusion the term dead layer will be used in the generic sense of a phenomena which causes reduced electron beam gain from planar diodes. T_D will be used to describe the dead layer thickness in the first order model. T_D will generally require the measurement voltage to also be stated, when it is being used to describe experimental data.

In addition, many of the targets were scanned and photographed to search for gain irregularities. The gain irregularity was usually less than 5%. On some of the gain curves, the error bars are included indicating the amount of nonuniformity observed. Figure 60 shows such a gain photograph. The bright oval is the diode area and the dark central area is the area of the diode shadowed by the contact finger and Faraday cup. The upper part of the diode has 5% higher gain. This area had an oxide layer present during the anneal. Also note the gain variations over the entire diode. These are also less than 5%. These small variations show up clearly in this picture because the contrast is highly expanded.

Tables 1, 2 and 3 summarize the gain measurements on the targets examined so far. All samples were implanted at 7° off the crystal axis.

The best results were obtained for samples P11A and P11C (Figures 43, 44, 45) and A9C and A7B (Figures 50 & 57). For all of these samples the implantation peak is at or very near the

Figure 60. SEM Diode Signal Micrograph Showing Gain Difference For
            Substrate A9B After Anneal at 650° With Oxide Left on
            upper half of Mesa During Anneal Cycle and Removed
            Before Measurement.   Beam Energy 10 kV and Magnification
            ~ 17x.

Table 1

DEAD LAYER THICKNESSES MEASURED AT 2.5 and 5 keV FOR P^+ IMPLANTED p-Si. ALL ANNEALS 1 HR. IN Ar ATMOSPHERE. SUBSTRATE RESISTIVITIES PRIOR TO IMPLANT 5-18 Ω - CM.

Sample Number	Ion Energy (keV)	Ion Fluence (#/cm^2)	Crystal Orient.	Surface[+] Prep.	Anneal Temp. (°C)	Dead Layer Thickness (Å)	
						at 2.5 keV	at 5 keV
P1A	100	10^{13}	<111>		20 min. at 550	800	1400
P1B	100	10^{13}	<111>		770	650	1550
P3A	100	10^{14}	<111>		770	600	1200
P3B	100	10^{14}	<111>		575	800	1700
					675	660	1200
					770	660	1500
					860	660	1500
P3C	100	10^{14}	<111>		650	700	1250
P4C	100	10^{14}	<111>		770	660	1300
P4A	100	10^{14}	<111>		770	220	420 no trap
P4B	100	10^{14}	<111>		~1050	700	~2000
P5A	100	10^{14}	<110>		770	630	1300
P5B	100	10^{14}	<110>		650	700	1400
P6A	100	10^{14}	<100>		770	630	1400
P6B	100	10^{14}	<100>		650	NE	NE
P7A	30	10^{14}	<111>		770	600	1100
P7B	30	10^{14}	<111>		650	580	1300
P8C	100	10^{14}	<111>	200 Å	770	620	1150
P8B	100	10^{14}	<111>		650	NE	NE
P9C	100	10^{14}	<111>	1000 Å oxide	770	440	900
P9D	100	10^{14}	<111>	1000 Å oxide	650	NE	NE
P10C	100	10^{14}	<111>	1200 Å oxide	770	430	720
P10A	100	10^{14}	<111>	1200 Å oxide	650	NE	NE
P11C	100	10^{14}	<111>	1400 Å oxide	770	380	600

Table 1 (con't)

Sample Number	Ion Energy (keV)	Ion Fluence (#/cm^2)	Crystal Orient.	Surface[+] Prep.	Anneal Temp. (°C)	Dead Layer Thickness (Å)	
						at 2.5 keV	at 5 keV
P11A	100	10^{14}	<111>	1400Å oxide	650	400	800
P12C	100	10^{14}	<111>		770	660	1400
P13B	100	10^{14}	<111>		650	800	1800
	50 He	10^{15}	<111>				

NE = Not Evaluated

[+]All wafers are polished, bright etched and cleaned in BHF before implant (except oxide wafers)

Table 2

DEAD LAYER THICKNESSES MEASURED AT 2.5 AND 5 keV FOR As[+] IMPLANTED
p-Si. ALL ANNEALS 1 HR. IN Ar ATMOSPHERE. SUBSTRATE RESISTIVITIES
PRIOR TO IMPLANT 5 - 15$_\Omega$ - CM.

Sample Number	Ion Energy (keV)	Ion Fluence ($\#/cm^2$)	Crystal Orient.	Surface[+] Prep.	Anneal Temp. (°C)	Dead Layer Thickness (Å)	
						at 2.5 keV	at 5 keV
A3A	100	10^{14}	<111>		770	520	700
A3B	100	10^{14}	<111>		650	NE	NE
A4B	100	10^{14}	<110>		770	480	700
A4C	100	10^{14}	<110>		650	NE	NE
A7B	30	10^{14}	<111>		770	320	400
A7C	30	10^{14}	<111>		650	380	700
A8C	100	10^{14}	<100>		770	570	1100
A8A	100	10^{14}	<100>		650	700	1400
A9C	100	10^{14}	<111>	200Å oxide	770	320	400
A9B	100	10^{14}	<111>	200Å oxide	650	540	1200

NE = Not Evaluated

[+]All wafers are polished, bright etched and cleaned in
 BHF before implant (except oxide wafers).

Table 3

DEAD LAYER THICKNESSES MEASURED AT 2.5 AND 5 keV FOR B$^+$ IMPLANTED n-Si. ALL ANNEALS 1 HR. IN Ar ATMOSPHERE. SUBSTRATE RESISTIVITIES PRIOR TO IMPLANT 4 - 13$_\Lambda$ - CM.

Sample Number	Ion Energy (keV)	Ion Fluence (#/cm^2)	Crystal Orient.	Surface$^+$ Prep.	Anneal Temp. (°C)	Dead Layer Thickness (Å)	
						at 2.5 keV	at 5 keV
B3A	100	10^{14}	<111>	200Å oxide	950	--	2300
B4A	100	10^{14}	<111>		950	1200 (3 keV)	1900
B5C	100	10^{14}	<110>		950	NE	NE

NE = Not Evaluated

$^+$All wafers are polished, bright etched and cleaned in BHF before implant (except oxide wafers).

surface. P11 and A9 used implantation through oxide layers to
achieve a implant peak near the surface. A7 used 30 keV As^+
implantation to achieve a very shallow penetration of the ions (see
Figure 20). Note also that $650^{\circ}C$ annealing for the As samples gives
consistently poorer results than $760^{\circ}C$ anneals. Higher temperature
anneals are planned for the As samples. For the P samples 650 and
$760^{\circ}C$ anneals gave about the same results. The Boron implanted
samples had much too deep implant peaks for good results. Boron
implants through thick oxides to put the implant peak near the
surface are in progress. It is desirable to have processing tech-
niques for both n^+ and p^+ surface planar diodes so that both n and
p dopants can be used for writing. Also damage writing may give
better results in n or p surfaces depending upon the type of deep
traps introduced by the damaging ion beam. The extremely good
result for sample P4A (Figure 32) could not be reproduced and does
not fit the pattern of the rest of the samples. The only identifiable
difference is that it was annealed in pre-purified Ar without any
trapping. All other anneals used a dry ice and acetone trap to
additionally clean the Ar. One other sample, P3A, was also annealed
without a trap in an attempt to reproduce P4A. P3 and P4 are from
different but nominally identical silicon wafers implanted sequentially
in the same implantation run. Note also that P4B and P4C, which
received similar annealing treatments do not have dead layers nearly
as small as P4A. P4A was anamolous also in that it occassionally

gave much lower gain indicating a thicker dead layer. This occurred several times during separate measurements of the sample by different operators on different days. One of these data points is indicated in Figure 32a. These low gain data points could never be consistently reproduced.

The good results for the P11 and A7 and A9 samples show that acceptable dead layers can be achieved for n^+ surface planar diodes. These targets achieved gains in excess of 200 at 2 keV which is 50% of the maximum possible. Since it is expected that beam energies ~2 keV will be optimum for 0.1 micron bit spacing readout, these targets are very acceptable for ion implantation writing and readout. For the alloy junction writing method thinner dead layers may be necessary as discussed in the alloy junction section.

Figure 61 shows an interesting effect called a bright edge. This is a diode gain picture as in Figure 60. The high gain strip along the left edge of the picture corresponds to the edge of the mesa of the diode. The dark point is again the contact finger. Figure 62 shows schematically what is believed to be occurring. The electron beam generates carriers along the mesa edge and the minority carriers (electrons in this case) diffuse to the N^+P planar junction and are collected as signal current. This collection can also be aided by the existence of an inversion layer extending from the junction as shown in the right side of Figure 62. In some cases the bright edge extends 1 mm or more from the mesa,
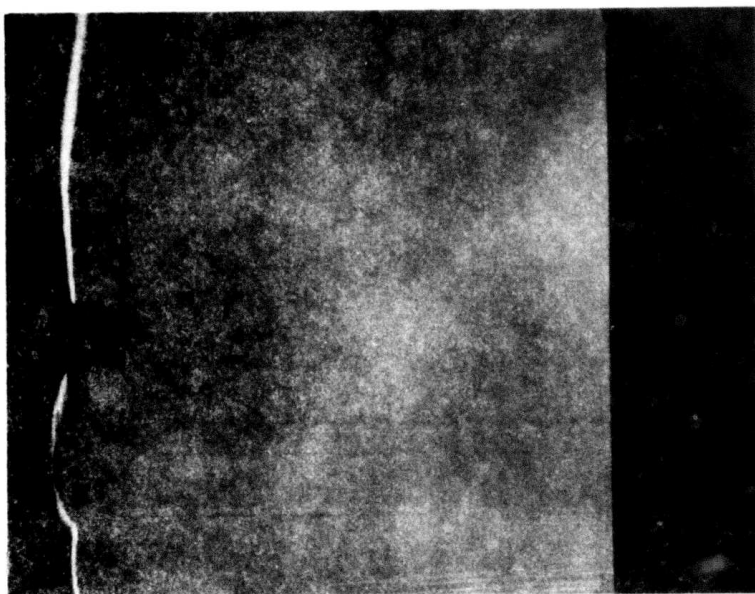
Figure 61. SEM Diode Signal Micrograph of Sample P10C After
One-Hour Anneal at 770° Showing Bright Edge (High
Gain Area) at Left.
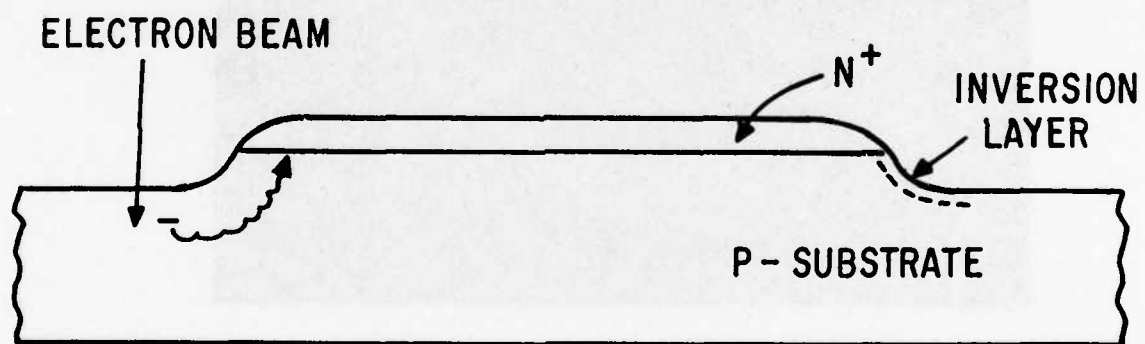
Figure 62.   Schematic of origin of high gain region at edge of
             diode mesa

however, usually it extends only 50 microns as in Figure 61. If no
inversion layer is present the extent of the bright edge is a measure
of the minority carrier lifetime in the substrate. A minority
carrier diffusion length of 100 microns is very typical for
average quality silicon. In several of the Figures (32, 35, 45,
50, 51, 57) the maximum gain in the bright edge is shown as open
circles. Note that in most cases this gain exactly follows the
$T_D = 0$ dead layer curve. This means that all the carriers generated
by the electron beam are being collected and none are lost in a
dead layer. This indicates that the dead layer phenomena is not
an intrinsic property of silicon surfaces but is related to the
introduction of dopant near the surface. Unfortunately high doping
levels near the surface are necessary to achieve high resolution as
discussed earlier so that ways to minimize the effect in the presence
of high doping must be found.

Dead Layer Models

For optimum performance of the surface diode targets it is
necessary to fabricate planar diodes with very thin dead layers.
This has been discussed earlier in this section. By a dead layer is
meant region in which carriers generated by the electron beam are
not collected by the diode. Figure 50 shows a typical electron beam
induced diode gain versus beam energy curve for a planar diode target.
The straight line labeled 0 microns is what would be expected if all
the carriers generated by the electron beam were collected by the

pn junction. The simplest explanation, for deviations from this
ideal curve is that a layer of the silicon near the surface has
a large amount of damage so that the minority carrier lifetime is
very short and the generated carriers recombine before reaching
the junction. Other explanations are possible as will be seen from
the following discussion.

1. First Order Dead Layer Model.

Figure 63 shows a first order model for the dead layer. We
will consider n on p diodes for definetiness. The n layer is
assumed to be uniformly doped and have a minority carrier lifetime
much larger than the duffusion time across the n-layer T_N^2/D_p where
T_N is the n-layer thickness and D_p the hole diffusion constant
($D_p \cong 10$ cm^2/sec). All carriers generated at $x < T_D$ are not collected
by the diode and all carriers generated for $z > T_D$ are collected.
This includes carriers generated at $z > T_N$. No assumptions need be
made about the reasons for these collection characteristics. The
generation of carriers by the penetrating electron beam is well
described by:

$$g(z,E) = \frac{(1-f)E}{e_i} \cdot \frac{1}{R(E)} \lambda\left(\frac{z}{R(E)}\right)$$

(4)

where $g(z,E)$ is the number of electron-hole pairs generated per
cm^3 per incident electron/cm^2, E is the incident electron beam
energy, f the fraction of electron beam energy backscattered by the
target, $\lambda(q)$ is the Grün generation function and $R(E)$ is the Grün

BEAM

DEAD LAYER

N
P

O
T_D
T_N
Z
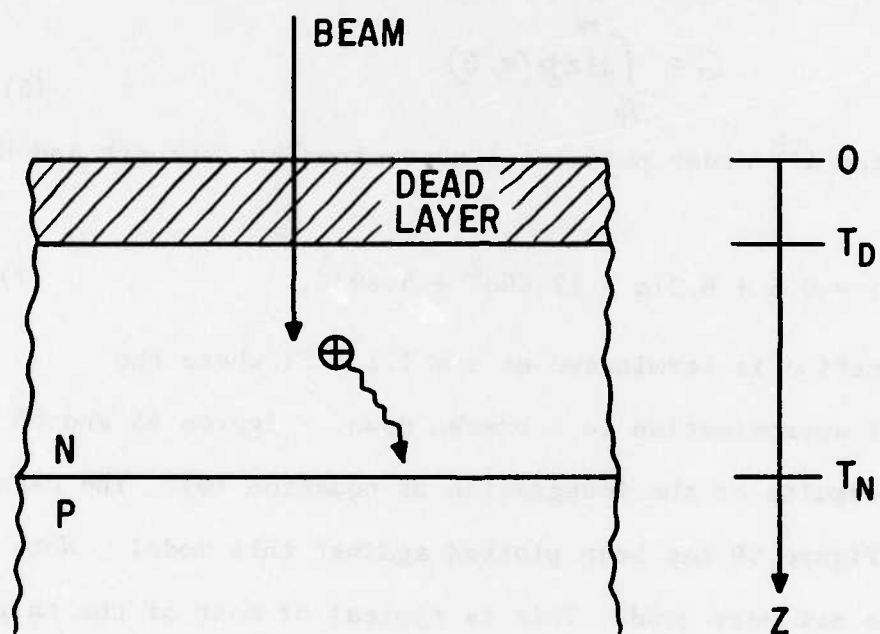
Figure 63   First Order Model for the Dead Layer

range (see Appendix II). For Al or Silicon f = 0.08. This should

be distinguished from the number backscatter coefficient which for

Al or Si is 0.13. For silicon or silicon dioxide:

$$R(E) = 0.019 \text{ microns x } E^{1.75} \tag{5}$$

where E is in keV, e_i is the average electron-hole pair generation

energy which is 3.65 ev/pair for silicon. The diode gain (G) or

number of holes collected per primary is given by:

$$G = \int_{T_p}^{\infty} dz\, g(z, E) \tag{6}$$

For $\lambda(q)$ the 4th order polynomial determined by Everhart and Hoff

is used:

$$\lambda(q) = 0.6 + 6.21q - 12.40q^2 + 5.69q^3 \tag{7}$$

The integration is terminated at z = 1.1 R(E) where the

polynomial approximation to λ breaks down. Figures 64 and 65

show the results of the integration of equation (6). The data

shown in Figure 50 has been plotted against this model. Note that

the fit is not very good. This is typical of most of the targets

discussed in this section, and is not surprising. Much of the

experimental data has been plotted against this model because it

gives some physical insight into the thickness of the dead like

target layer. For example in Figure 50 above about 3 keV the data

reasonably well follows the 0.04 micron dead layer curve. This

indicates that the thickness of the damaged region is about 0.04

microns. The deviations at smaller energy indicate that some but
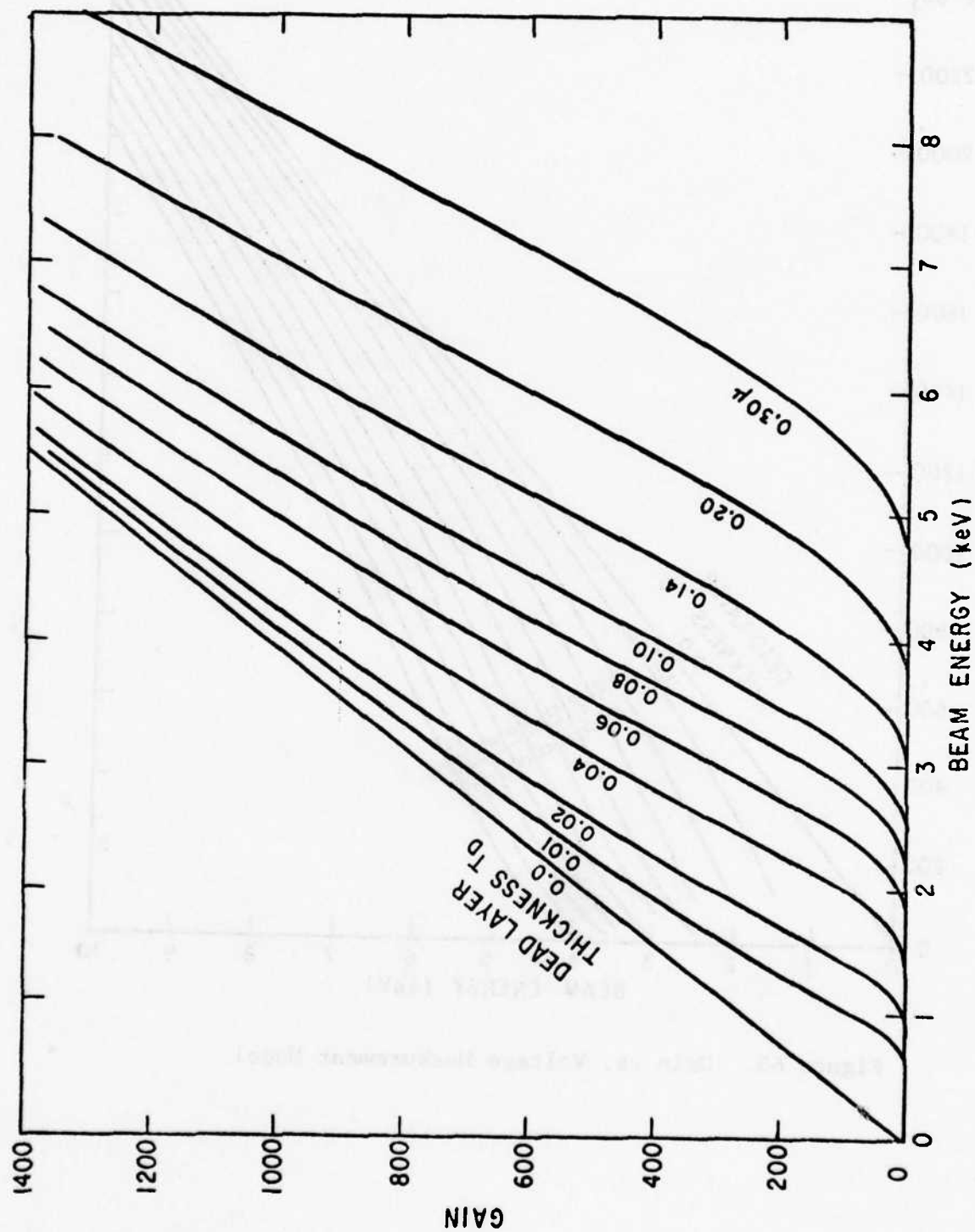
Figure 64. Gain vs. Voltage Model.
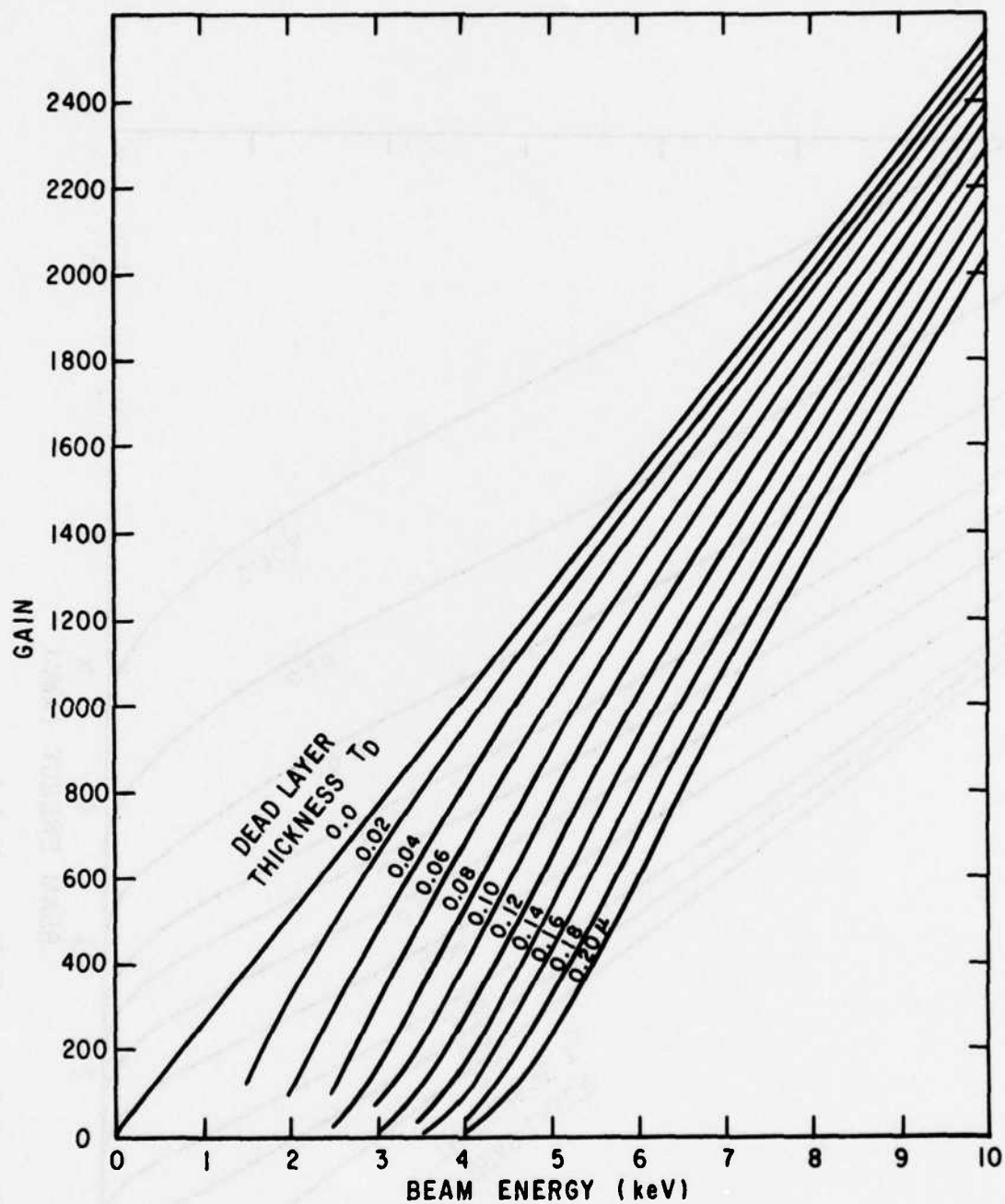
Figure 65.   Gain vs. Voltage Measurement Model

not all the carriers generated below 0.04 microns and even down to
0.01 microns are collected by the diode.

2. Derivation of the Collection Probability from gain versus energy
   data

The first order model can be improved by generalizing the
concept of a collection probability. The target gain can be
represented by:

$$G = \int_{0}^{\infty} dz \, P(z) \, g(z, E)$$

(8)

where $g(z,E)$ is the carrier generation function in equation (4), and
$P(z)$ is the collection probability for carriers generated at a depth
z. The first order model (equation (4)) is a special case of
equation (8) with $P(z) = 1$ for $z > T_D$ and 0 for $z < T_D$. Calculation
of $P(z)$ from models of the doping profiles and recombination rates
will be discussed in the following section. In this section the
problem of calculating $P(z)$ from measurements of gain versus energy
will be addressed. A least squares method will be used. Equation (8)
is rewritten as:

$$G = \int_{0}^{hR(E)} dz \, P(z) \, g(z, E)$$

(9)

where $h \cong 1.1$ so that the integral is cut off at the depth where
$g(z,E)$ becomes small. $\lambda(a)$ and $P(z)$ are written as:

$$\lambda(q) = \sum_{J=0}^{JM} b_j \left(q^j\right)$$

(10)

-105-

$$P(z) = \sum_{k=0}^{N} a_k z^k \tag{11}$$

where the coefficients b_j are given in equation (7). Using this notation equation (9) becomes:

$$G(E) = \frac{E}{\Theta_i} \cdot \frac{1}{R(E)} \int_0^{hR(E)} dz \left[\sum_{j=0}^{JM} b_j \left(\frac{z}{R(E)} \right)^j \right] \left[\sum_{k=0}^{N} a_k z^k \right] \left[1 - f \right] \tag{12}$$

Performing the integrations and interchanging summations gives:

$$G(E) = \sum_{k=0}^{N} a_k C_k (E)$$

where

$$C_k (E) = (1-f) \left(\frac{E}{\Theta_i} \right) \left[R(E) \right]^k \sum_{j=0}^{JM} \frac{b_j h^{j+k+1}}{(k+j+1)} \quad k = 0, 1, \cdots N \tag{14}$$

The experimental data is represented by a set of measurements of gain and energy and weight factors as G_i, E_i, W_i) $i = 1, 2, \ldots \ldots IM$. W_i are normally assigned according to the degree of fit desired at energy E_i. A logical choice is $W_i = 1/\sigma_i^2$ where σ_i is the estimated error or standard deviation of data point G_i. The least squares criteria is:

$$\sum_{i=1}^{JM} \left[G_i - G(E_i) \right]^2 W_i = minimum \tag{15}$$

-106-

Differentiating with respect to the N coefficients a_r in the standard fashion and assuming a unique minimum exists, yields N simultaneous equations in the N unknowns a_r ($r = 1,2,....N$).:

$$\sum_{K>0}^{N} B_{rk} \, a_k = D_r$$

(16)

where

$$B_{rk} = \sum_{i=1}^{IM} C_r(E_i) C_k(E_i) W_i$$

(17)

$$D_r = \sum_{i=1}^{IM} G_i \, C_r(E_i) W_i$$

(18)

A computer program written in ALGOL for performing this least squares fit and typical output is shown in Figure 66. This program calculates the best fit $P(z)$ and then recalculates the gain versus energy curve from the best fit $P(z)$ using direct integration of equation (8) and summation of equation (13). The simultaneous equation set (13) is solved by Crout Reduction (Ref. 11). Typical results of this program are shown in Figures 67 and 68. These figures show the effect of different orders of fit N. The order of fit must be chosen carefully, and be compatible with the number of data points. An order of fit comparable to the number of data points (e.g. $N = 6$ in this case) will result in large oscillations in $P(z)$ because it is possible to achieve almost an exact fit to the points while allowing large deviations between data points from the smooth curve that is physically expected. This is particularly

-107-

```
00010 BEGIN COMMENT CALCULATES THE COLLECTION PROBABILITY FROM
00020 MEASURED GAIN VERSUS ENERGY.  USES MODIFIED E AND H
00030 THIRD ORDER FIT TO GRUN FUNCTION AND LEAST SQUARES CRITERIA;
00040 REAL H,EG,SUM,DET,EMAX,Z,DEPI,DEPTH,DEPTHM,RR,ENI,EMAXP,ENERGY;
00050 INTEGER JM,I,OPT,N,R,K,Q,IM;
00060 REAL ARRAY BL[0:3],D,A[0:10],L[1:100,1:100],V,X[1:10];
00070 REAL ARRAY CA[0:100,1:100],B[0:10,0:10],G,E,W,ERROR[1:100];
00080 SWITCH S1-L1,L2,L3,L4; SWITCH S2-LL1,LL2,LL3,LL4;
00082 SWITCH S3-LX1,LX2;
00090 STRING FILE1,DESC;
00100 REAL PROCEDURE PROSUM(I,M,N,P);
00110 VALUE M,N; INTEGER I,M,N; REAL P;
00120 BEGIN
00130 REAL TSUM; TSUM-0;
00140 FOR I-M STEP 1 UNTIL N DO
00150    TSUM-TSUM +P;
00160 PROSUM-TSUM;
00170 END PROC PROSUM;
00180 REAL PROCEDURE INTEGRAL(F,X,X1,X2,N);
00190    !INTEGRATES BY WEDDLES RULE, N MUST BE MOD 6!
00200    VALUE X1,X2,N;
00210    INTEGER N;
00220    REAL X,X1,X2,F;
00230    BEGIN
00240    REAL SUM,DEL,DEL2,XI;
00250    INTEGER I;
00260    IF MOD(N,6)/=0 THEN PRINT(" INTEGRATION NOT MOD 6");
00270    DEL-(X2-X1)/N;   DEL2-2*DEL;
00280    XI-X1; SUM-0;
00290 AGAIN: FOR I-0 STEP 2 UNTIL 6 DO
00300    BEGIN X-I*DEL+XI; SUM-SUM+F; END;
00310    X-DEL+XI;   SUM-SUM+5*F;
00320    X-X+DEL2; SUM-SUM+6*F;
00330    X-X+DEL2; SUM-SUM+5*F;
00340    XI-6*DEL+XI;
00350    IF XI<X2-DEL THEN GO TO AGAIN;
00360    INTEGRAL-SUM*DEL*0.3;
00370    END WEDDLE INTEGRAL;
00380 PROCEDURE SOLVECROUT(N); VALUE N; INTEGER N;
00390 BEGIN COMMENT NEEDS MATRIX L, COEFF VECTOR V AND SOLUTION VECTOR X
00400    DECLARED EXTERNAL TO PROCEDURE;
00410 INTEGER JS,I,J,JSS;
00420 REAL ARRAY AL[1:N,1:N], AV[1:N];
00430 AL[1,1]-L[1,1]; AL[2,1]-L[2,1];
00440 AL[1,2]-L[1,2]/AL[1,1];
00450 FOR JS-1 STEP 1 UNTIL N DO
00460    BEGIN
00470    JSS-IF JS/=1 THEN JS ELSE 3;
00480    FOR I-JSS STEP 1 UNTIL N DO
00490       AL[I,JS]-L[I,JS]-PROSUM(Q,1,JS-1,AL[I,Q]*AL[Q,JS]);
00500    JSS-IF JS/=1 THEN JS ELSE 2;
00510    FOR J-JSS+1 STEP 1 UNTIL N DO
00520       BEGIN I-JS;
00530       AL[I,J]-(L[I,J]-PROSUM(Q,1,I-1,AL[I,Q]*AL[Q,J]))/AL[I,I];
00540       END;
00550    END;
```

**Figure 66a.   Computer program for calculation of best fit collection
probability from gain versus energy data.**

```
00560 AV[1]=V[1]/AL[1,1];
00570 FOR I=2 STEP 1 UNTIL N DO
00580   AV[I]=(V[I]-PROSUM(Q,1,I-1,AL[I,Q]*AV[Q]))/AL[I,I];
00590 X[N]=AV[N];
00600 FOR I=N-1 STEP -1 UNTIL 1 DO
00610   X[I]=AV[I]-PROSUM(Q,I+1,N,AL[I,Q]*X[Q]);
00620 END PROCEDURE CROUT;
00630 REAL PROCEDURE RANGE(E); REAL E;
00640   RANGE=1.1*(0.1*E)+1.75;
00650 REAL PROCEDURE C(K,E); REAL E; INTEGER K;
00660   BEGIN
00670   INTEGER J; REAL SUM; SUM=0;
00680   FOR J=0 STEP 1 UNTIL JM DO
00690     SUM=SUM+BL[J]*H+(J+K+1)/(K+J+1);
00700   C=E*RANGE(E)+K*SUM/EG;
00710   END PROC C(K,E);
00720 REAL PROCEDURE PROB(Z); REAL Z;
00730   PROB=PROSUM(Q,0,N,A[Q]*Z+Q);
00731 REAL PROCEDURE GAININT(E); REAL E;
00732   BEGIN REAL IN,RAN; RAN=RANGE(ENERGY);
00733   IN=INTEGRAL(PROSUM(Q,0,JM,BL[Q]*(Z/RAN)+Q)*PROB(Z),Z,0,H*RAN,36);
00734   GAININT=IN*E/(EG*RAN);
00735   END PRO GAIN BY INTEGRATION;
00736 REAL PROCEDURE GAINSUM(E); REAL E;
00737   GAINSUM=PROSUM(Q,0,N,A[Q]*C(Q,E));
00740 JM=3;
00750 H=1.05;
00760 EG=3.65E-3;
00765 I=0; FOR BL[I]=0.6,6.21,-12.4,5.69 DO I=I+1;
00766 L4:LL3: PRINT("OPTIONS: 1-TTY , 2-FILE INPUT");
00771 INPUT(OPT); GO TO S3[OPT];
00772 LX2: PRINT("FILE NAME"); INPUTF("(A)",FILE1);
00773 READ(FILE1,"(A50)",DEF,DESC);
00774 READ(FILE1,"(I3)",DEF,IM);
00775 FOR I=1 STEP 1 UNTIL IM DO
00776   READ(FILE1,"(3F6.2)",DEF,E[I],G[I],ERROR[I]);
00777 REWIND(FILE1);
00778 GO TO L5;
00780 LX1: FILE1="TTY"; DESC=" ";
00790 PRINT("INPUT ENERGY IN KEV,GAIN,ERROR - ENERGY=0 TERMINATES");
00800 FOR IM=1 STEP 1 UNTIL 1000 DO
00801   BEGIN INPUT(E[IM],G[IM],ERROR[IM]);
00802   IF E[IM]=0 THEN GO TO L5;
00803   END;
00820 DEF: PRINT("READING ERROR OF FILE"); GO TO LL3;
00920 L5: PRINT("OPTIONS: 1-PRINT DATA,2-SAVE DATA, 3-RUN, 4-NEW DATA");
00930 INPUT(OPT); GO TO S1[OPT];
00935 L1: PRINT("FILE NAME=",FILE1); PRINT(DESC);
00940 PRINT("  ENERGY   GAIN     ERROR"); PRINT("   KEV");
00950 FOR I=1 STEP 1 UNTIL IM DO PRINTF("(3F6.2)",E[I],G[I],ERROR[I]);
00960 GO TO L5;
00970 L2: PRINT("FILE NAME");
00980 INPUTF("(A6)",FILE1);
00982 PRINT("FILE DESCRIPTION"); INPUTF("(A)",DESC);
00984 WRITE(FILE1,"(A50)",DESC);
00990 WRITE(FILE1,"(I3)",IM);
01000 FOR I=1 STEP 1 UNTIL IM DO
01010   WRITE(FILE1,"(3F6.2)",E[I],G[I],ERROR[I]);
01015 ENDFILE(FILE1); REWIND(FILE1);
01020 GO TO L5;
```

Figure 66a (cont.)

-109-

```
01060 L3: PRINT("POLYNOMIAL ORDER FOR FIT TO PROB(Z)");
01070 INPUT(N);
01075 FOR I-1 STEP 1 UNTIL IM DO W[I]-1E-4*(ERROR[I]'(-2));
01080 FOR K-0 STEP 1 UNTIL N DO FOR I-1 STEP 1 UNTIL IM DO
01090   CA[K,I]-C(K,E[I]);
01100 FOR R-0 STEP 1 UNTIL N DO
01110   FOR K-R STEP 1 UNTIL N DO
01120   B[K,R]-B[R,K]-PROSUM(Q,1,IM,CA[R,Q]*CA[K,Q]*W[Q]);
01200 FOR R-0 STEP 1 UNTIL N DO
01210   D[R]-PROSUM(Q,1,IM,G[Q]*CA[R,Q]*W[Q]);
01260 COMMENT NOW READY TO SOLVE FOR COEFF. VECTOR A;
01261 FOR R-0 STEP 1 UNTIL N DO
01262   BEGIN V[R+1]-D[R];
01263   FOR K-0 STEP 1 UNTIL N DO L[R+1,K+1]-B[R,K];
01264   END; GO TO SOL;
01265 PRINT("CA[K,I]   K    I"); FOR K-0 STEP 1 UNTIL N DO FOR I-1 STEP
01266  1 UNTIL IM DO PRINTF("(E13.3,2I2)",CA[K,I],K,I);
01267 PRINT("B[K,R]   K    R"); FOR K-0 STEP 1 UNTIL N DO FOR R-0 STEP
01268  1 UNTIL N DO PRINTF("(E13.3,2I2)",B[K,R],K,R);
01269 FOR R-0 STEP 1 UNTIL N DO PRINT(D[R],R);
01270 SOL: SOLVECROUT(N+1);
01271 FOR R-0 STEP 1 UNTIL N DO A[R]-X[R+1];
01280 !DISPLAY RESULTS!
01290 PRINT("COEFFICIENTS ARE");
01300 PRINT("  A[R]          R");
01310 FOR R-0 STEP 1 UNTIL N DO
01320   PRINTF("(E14.7,I2)",A[R],R);
01330 EMAX-E[1];
01340 FOR I-2 STEP 1 UNTIL IM DO
01350   IF EMAX<E[I] THEN EMAX-E[I];
01360 LL5: PRINT("OPTIONS: 1-COLL PROB,2-GAIN VS E,3-NEW DATA,4-QUIT");
01370 INPUT(OPT); GO TO S2[OPT];
01380 LL1: PRINT("DEPTH INCREMENT AND DEPTH IN MICRONS");
01390 INPUT(DEPI,DEPTH);
01400 PRINT("COLLECTION    DEPTH");
01410 PRINT(  "PROB        MICRONS");
01420 DEPTHM-H*RANGE(EMAX);
01430 IF DEPTH<DEPTHM THEN DEPTHM-DEPTH;
01440 FOR DEPTH-0 STEP DEPI UNTIL DEPTHM DO
01450   PRINTF("(F9.5,F9.3)", PROB(DEPTH),DEPTH);
01460 GO TO LL5;
01470 LL2: PRINT("ENERGY INCREMENT AND MAX ENERGY");
01480 INPUT(ENI,EMAXP);
01490 IF EMAXP>EMAX THEN EMAXP-EMAX;
01500 PRINT("GAIN-I     GAIN-S  ENERGY-KEV");
01510 FOR ENERGY-ENI STEP ENI UNTIL EMAXP DO
01520   PRINTF("(3F9.2)",GAININT(ENERGY),GAINSUM(ENERGY),ENERGY);
01525 GO TO LL5;
01570 LL4:END


READY
```

Figure 66a (cont.)

```
FILE NAME=A7C

OPTIONS: 1-PRINT DATA,2-SAVE DATA, 3-RUN, 4-NEW DATA=1

FILE NAME=A7C
A7C 30KV AS 1E14 650 DEG 70-7-27-12:30
   ENERGY  GAIN     ERROR
    KEV
   10.00 2360.00   40.00
    9.00 2100.00   40.00
    8.00 1820.00   35.00
    7.00 1540.00   30.00
    6.00 1260.00   30.00
    5.10 1000.00   30.00
    4.00  700.00   30.00
    3.07  440.00   25.00
    2.48  300.00   20.00
    1.63  120.00   15.00
    0.93   24.00    4.00
    0.50    2.00    1.00
    0.      0.      1.00
OPTIONS: 1-PRINT DATA,2-SAVE DATA, 3-RUN, 4-NEW DATA=3

POLYNOMIAL ORDER FOR FIT TO PROB(Z)=5

COEFFICIENTS ARE
 A(R)          R


0.1908802E-01 0
0.1379112E+02 1


0.1018529E+03 2
0.2820855E+03 3


0.3363527E+03 4
0.1414359E+03 5
OPTIONS: 1-COLL PROB,2-GAIN VS E,3-NEW DATA,4-QUIT=1

DEPTH INCREMENT AND DEPTH IN MICRONS=0.05,1
```

Figure 66b.   Typical output of program showing data access from a stored
               file.

```
COLLECTION    DEPTH
PROB          MICRONS
-0.01969      0.
 0.54844      0.050
 0.79076      0.100
 0.84979      0.150
 0.82820      0.200
 0.79411      0.250
 0.78643      0.300
 0.82009      0.350
 0.89144      0.400
 0.98347      0.450
 1.07116      0.500
 1.12677      0.550
 1.12515      0.600
 1.04903      0.650
 0.89435      0.700
 0.67552      0.750
 0.43077      0.800
 0.22744      0.850
 0.16727      0.900
 0.39171      0.950
 1.08722      1.000
OPTIONS: 1-COLL PROB,2-GAIN VS E,3-NEW DATA,4-QUIT=2

ENERGY INCREMENT AND MAX ENERGY=.5,10

GAIN-I      GAIN-S     ENERGY-KEV
   2.38        2.38       0.50
  27.12       27.12       1.00-
  84.25       84.25       1.50
 175.16      175.16       2.00
 294.44      294.44       2.50
 432.41      432.41       3.00
 577.99      577.99       3.50
 721.69      721.69       4.00
 857.88      857.88       4.50
 966.05      986.05       5.00
1110.58     1110.58       5.50
1238.84     1238.84       6.00
1377.96     1377.96       6.50
1530.81     1530.80       7.00
1692.44     1692.44       7.50
1849.07     1849.06       8.00
1982.14     1982.14       8.50
2081.52     2081.51       9.00
2172.50     2172.49       9.50
2363.06     2363.04      10.00
OPTIONS: 1-COLL PROB,2-GAIN VS E,3-NEW DATA,4-QUIT=4
```

Figure 66b (cont.)
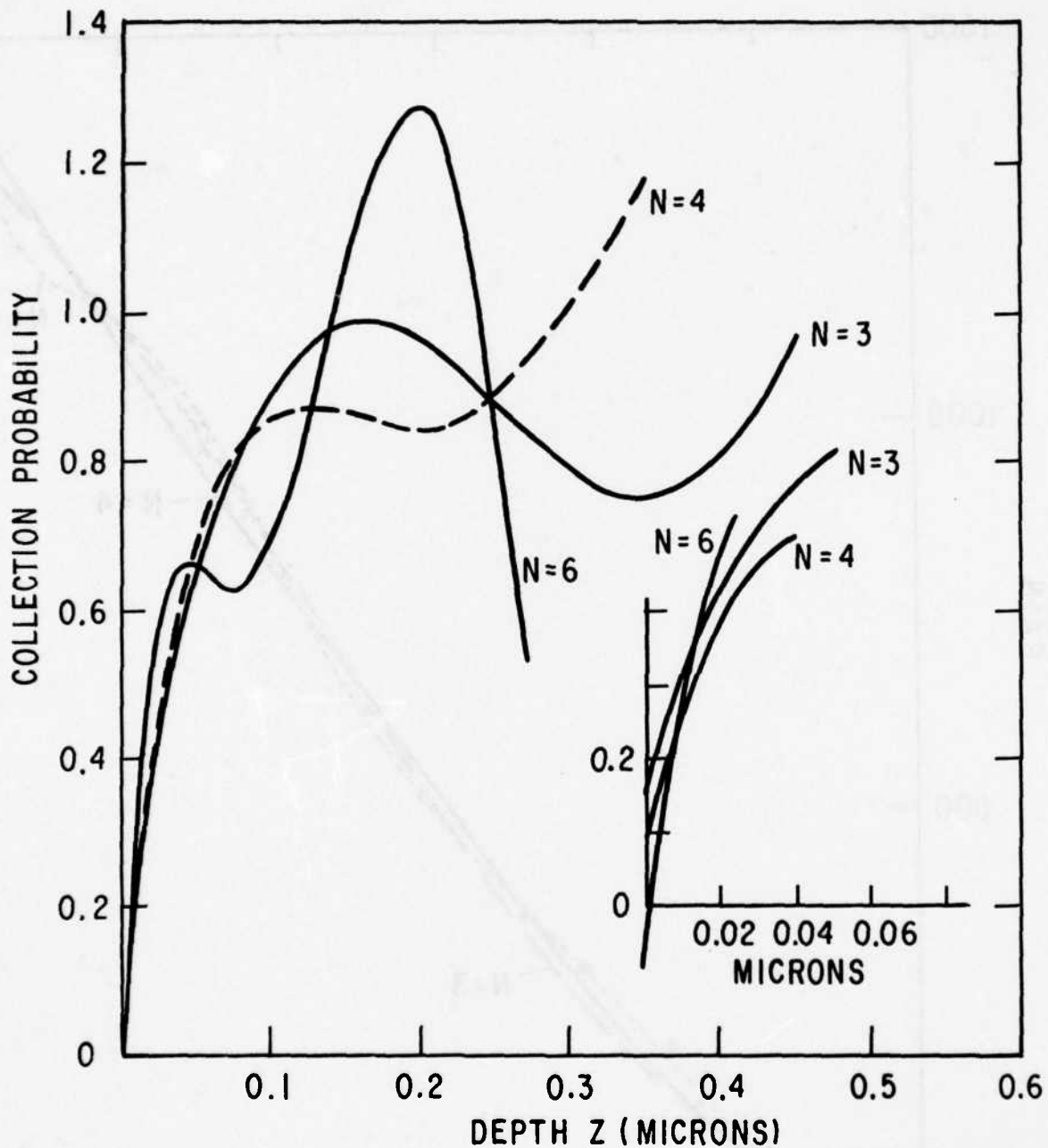
Figure 67. Examples of best fit collection probability for data from sample A7B. Gain versus energy data and gain curve calculated from collection probability data. N is order of fit.
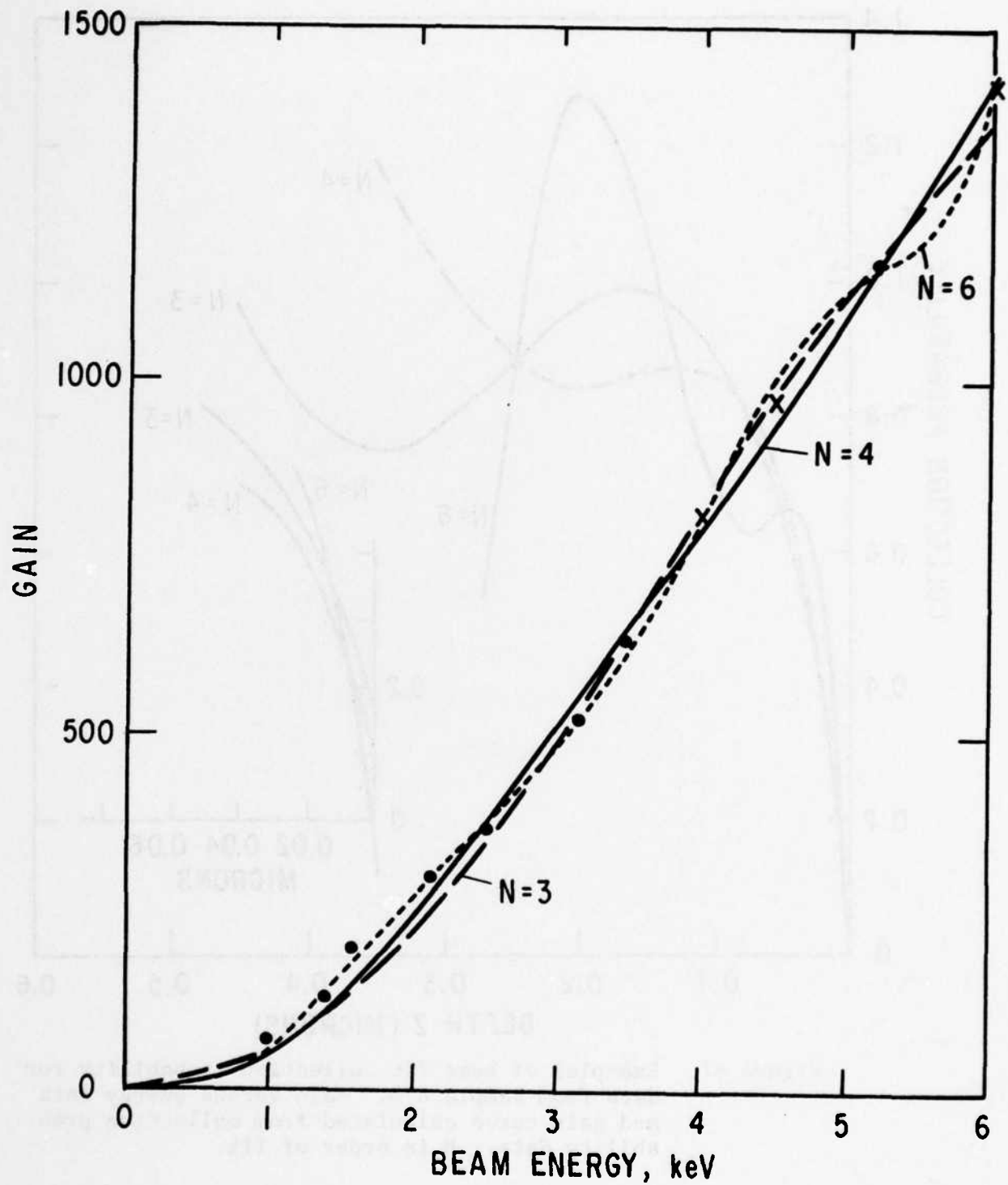
Figure 68.   Gain versus energy curve calculated from best fit
collection probability shown in Figure 67.   Solid
points are measured data.

a problem at the larger depths z where the gain versus energy curve

is insensitive to the exact shape of the P(z) curve. Since the

generation function is a very broad smooth function, the gain at an

energy E is a weighted average of P(z) over all z less than R(E).

For small z the fits obtained are essentially independent of the

order N as can be seen in Figure 67. Collection probabilities

greater than one are not physical unless avalanche is occurring

in the diode pn junction which is not possible for the low diode

bias of 1.5 volts used for these measurements. Hence the fit for

N = 3 or 4 is the most reasonable in this case. The solid points

shown in the gain versus energy curve are actual measured points.

To improve the fit, extra interpolated points indicated by crosses

are sometimes added. Figure 69 and 70 demonstrate the sensitivity

of the fit to the shape of P(z) at small z. Figure 69 shows the

collection probability from Figure 67 for the 3rd order fit

and the dotted line is an assumed collection probability which is

zero for z<0.04 microns. This corresponds to the first order dead

layer model with a 0.04 micron dead layer. Figure 70 shows the gain

versus energy curves determined by these two collection probability

functions by integration of equation (9). This clearly demonstrates

that the shape of the P(z) curve in this small z region is not an

artifact of the least squares fit. The finite intercept at z = 0

for the N = 3 fit is probably an artifact since there are no data

below 0.5 keV to determine the shape of P(z) in this region. Since

the derived gain for the N = 3 fit deviates from the assumed data
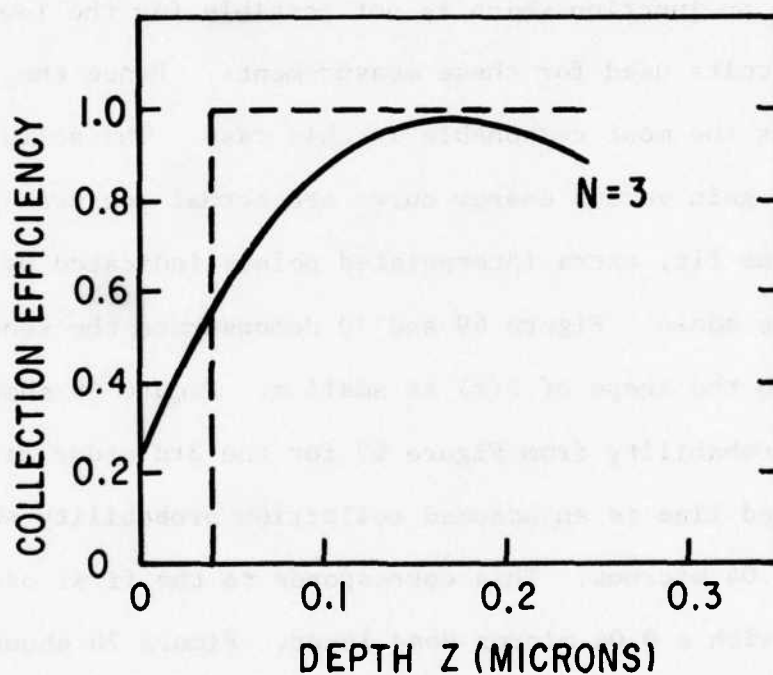
Figure 69.   Collection Probability P(z) from Figure
67 for N = 3 fit compared to T_D = 0.04μ
dead layer approximation (dotted curve).
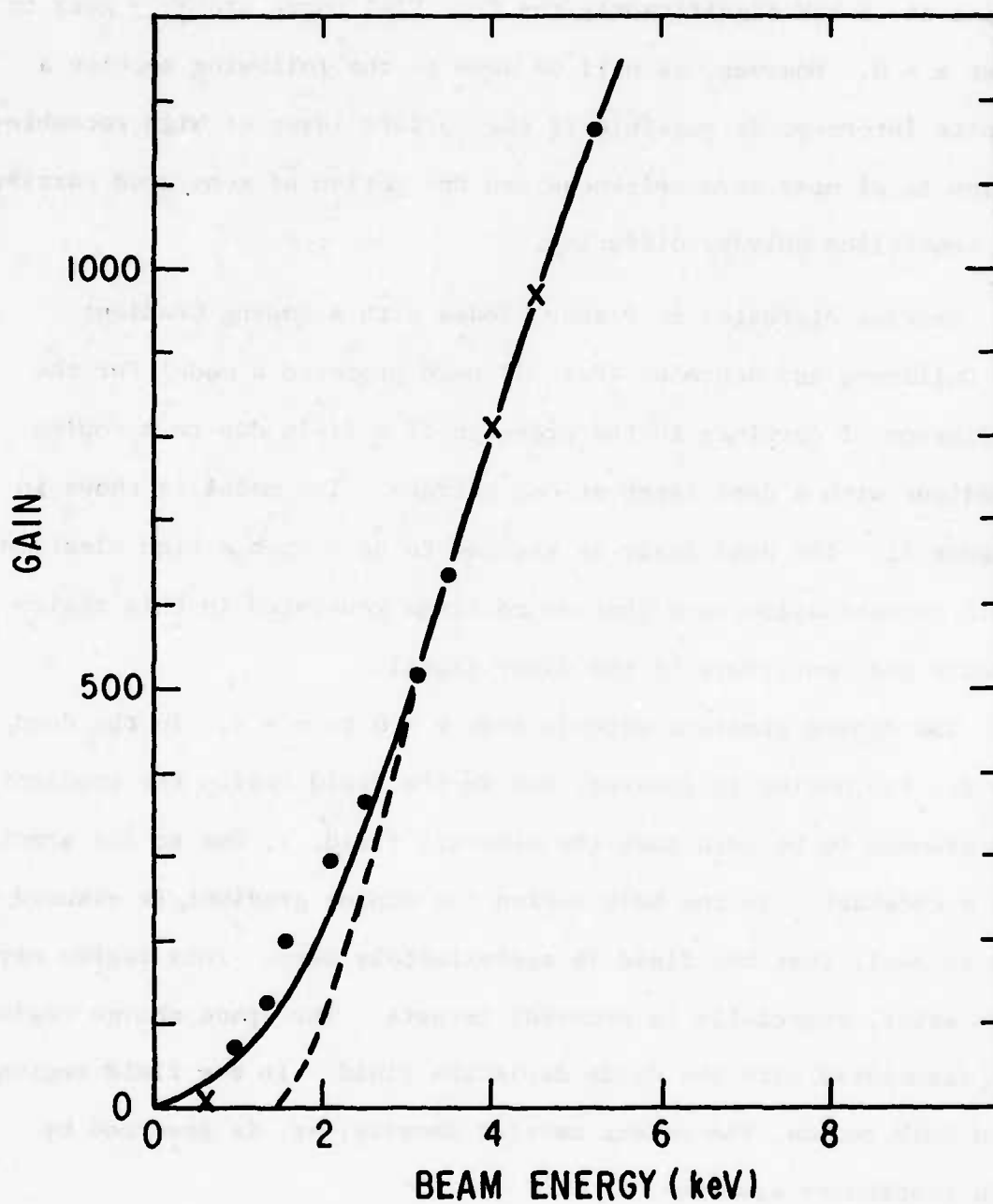
Figure 70. Gain vs. energy curves derived by direct integration of equation (9) for the P(z) curves in Figure 69.

point at .5 keV significantly the true P(z) curve probably goes to 0 at z = 0. However, as will be seen in the following section a finite intercept is possible if the surface layer of high recombination is of near zero thickness and the motion of generated carriers is controlled only by diffusion.

3. Carrier Diffusion in Planar Diodes with a Doping Gradient

Guildberg and Schroder (Ref. 3) have proposed a model for the diffusion of carriers in the presence of a field due to a doping gradient with a dead layer at one surface. The model is shown in Figure 71. The dead layer is assumed to have such a high electron hole recombination rate that no carriers generated in this region escape and contribute to the diode signal.

The doping gradient extends from z = 0 to z = δ. In the dead layer, any doping is ignored, but in the field region the gradient is assumed to be such that the electric field, ε, due to the gradient, is a constant. In the bulk region the doping gradient is assumed to be so small that the field is approximately zero. This region may not exist, expecially in archival targets. The space charge region is associated with the diode depletion field. In the field region and bulk region, the excess carrier density, δp, is governed by the continuity equation:

$$D\nabla^2 \delta p - \mu \vec{\varepsilon} \cdot \nabla \delta p - \delta p/\tau + g = 0 \qquad (19)$$
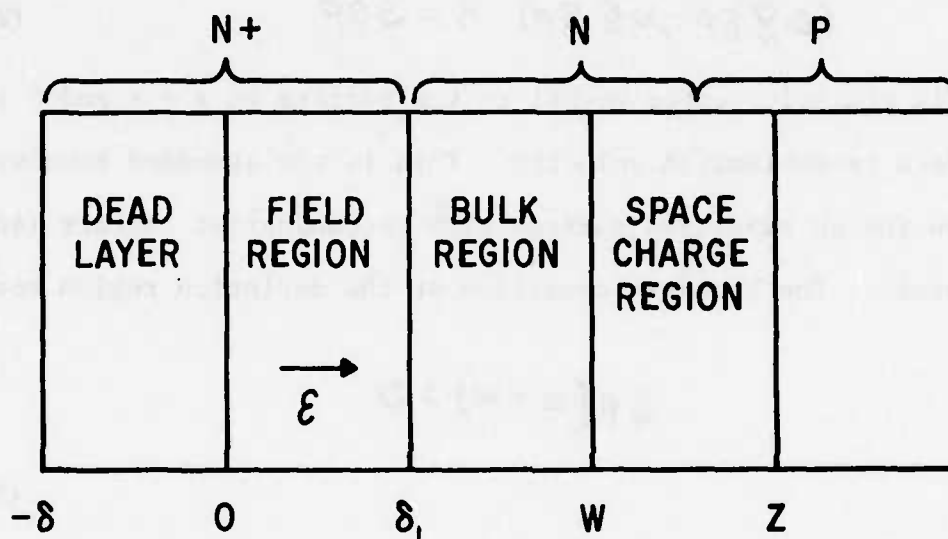
Figure 71.   Model for Diffusion of Carriers in Presence of Field

where D is the minority carrier diffusion constant, u is the mobility,
τ is the recombination time, and g is the generation rate of the
carriers. It is assumed that $\tau = \infty$ in the bulk and field regions.
The boundary condition at $z = \delta$ is:

$$(D \nabla \delta p - u \xi \delta p) \cdot \hat{n} = S \delta p \qquad (20)$$

where $\hat{n}$ is the unit vector normal to the surface at $z = \delta$ and S is
the surface recombination velocity. This is the standard boundary
condition for an idealized surface with recombination centers (inter-
face states). The boundary condition at the depletion region boundary
is:

$$\delta p (z = w) = 0$$

$$(21)$$

because the very high fields that exist in this region sweep out
carriers very rapidly. General solutions to Equation 19 in the field
region are of the form $C_o + C_1 \exp(Az)$ and in the field free region
$\alpha z + \beta$. The additional boundary conditions are carrier and current
continuity across boundaries where the minority current is:

$$\underset{\sim}{J} = -D \nabla \delta p + u \xi \delta p \qquad (22)$$

Using Equation 19 and these boundary conditions, the solutions in
each region can be found. In fact, any series of field regions, each
with different uniform fields, can be solved by this method, which

reduces to the solution of simultaneous linear equations. The electric field due to a doping gradient is:

$$\underset{\sim}{E} = -\left(\frac{KT}{q}\right)\frac{\nabla N(z)}{N(z)} = \frac{-KT}{q}\underset{\sim}{\nabla}\ln\left(N(z)\right)$$

(23)

where $N = N_D - N_A$. This assumes that charge neutrality exists, which is similarly required for Equation 19.

Because $N(x) \propto \exp(-d\varphi/kT)$, where φ is the electron potential, voltage drop between Z_1 and Z_2 is

$$\Delta V_{12} = \int_{z_1}^{z_2} \mathcal{E}(z)dz = \frac{KT}{q}\int_{z_1}^{z_2}dz\frac{\partial}{\partial z}\ln\left(N(z)\right) = \frac{KT}{q}\ln\left(\frac{N(z_1)}{N(z_0)}\right)$$

The model can be solved if the carrier generation $g = g_0 \delta(z - z_1)$; that is all carriers are generated in a plane at a depth z_0. A specific case solution of the model is for $Z_0 < \delta_1$. This is of most interest for the surface diode target, because the electron beam penetration will be shallow and will generate carriers only within the field region. The solution for the diode gain (signal current/beam current) normalized to the maximum possible gain, G_M, which occurs for $S = 0$ is:

$$\frac{G}{G_M} = \frac{\frac{S}{D}(1 - e^{-AZ_0}) + A}{\frac{S}{D}(1 - e^{-A\delta_1}) + A + \frac{S}{D}A(W - \delta_1)\exp(-A\delta_1)}$$

(24)

For the special case $W = \delta_1$ this reduces to:

$$\frac{G}{G_M} = \frac{1 + \frac{S}{D}\cdot\frac{1}{A}(1 - e^{-AZ_0})}{1 + \frac{S}{D}\frac{1}{A}(1 - e^{-AW})}$$

(25)

The constant $A = (q/kT) \varepsilon$ is proportional to the electric field. Because of the presence of at least a thin damaged surface layer, S is very large. The limiting maximum value for S is the thermal velocity, $\sim 10^7$ cm/sec, which is probably approached in most cases. To calculate the normalized gain for an arbitrary generation function, $g(z)$, Equation 24 or 25 can be integrated over $g(z)$ i.e.:

$$\frac{G}{G_M} = \frac{\int_{z_0=0}^{\delta_1} dz_0\, g(z_0 + \delta) \dfrac{\frac{S}{D}(1-e^{-Az_0})A}{\frac{S}{D}(1-e^{-A\delta_1})+A+\frac{S}{D}A(w-\delta_1)e^{-A\delta_1}}}{\int_{z=\delta_1}^{W} g(z_0 + \delta)\, dz_0} \tag{26}$$

assuming $g\,(z_0 > w + \delta_1) = 0$.

Figure 72 shows the dependence of the normalized gain or collection probability on A or the electric field for several values of surface recombination velocity. This figure is for $z_0 = 0$ and is valid if $AW > 3$ or for $A < 10^6$ cm^{-1} and $W > 0.03$ microns, which covers the range of values of A and W of interest.

Figure 73 shows the dependence of normalized gain or collection probability on generation depth z_0. This figure is for $S/D = 10^6$ cm^{-1} and again is valid for $AW > 3$. For $AW < 3$ it is specific to $W = 0.5$ microns. Note the condition $AW < 3$ includes all the curves for $A < 0$.

To apply this model to prediction of collection probabilities and gain versus energy curves it is necessary to know the doping profiles and recombination characteristics of the targets. As discussed in a following section, the second quarter will include
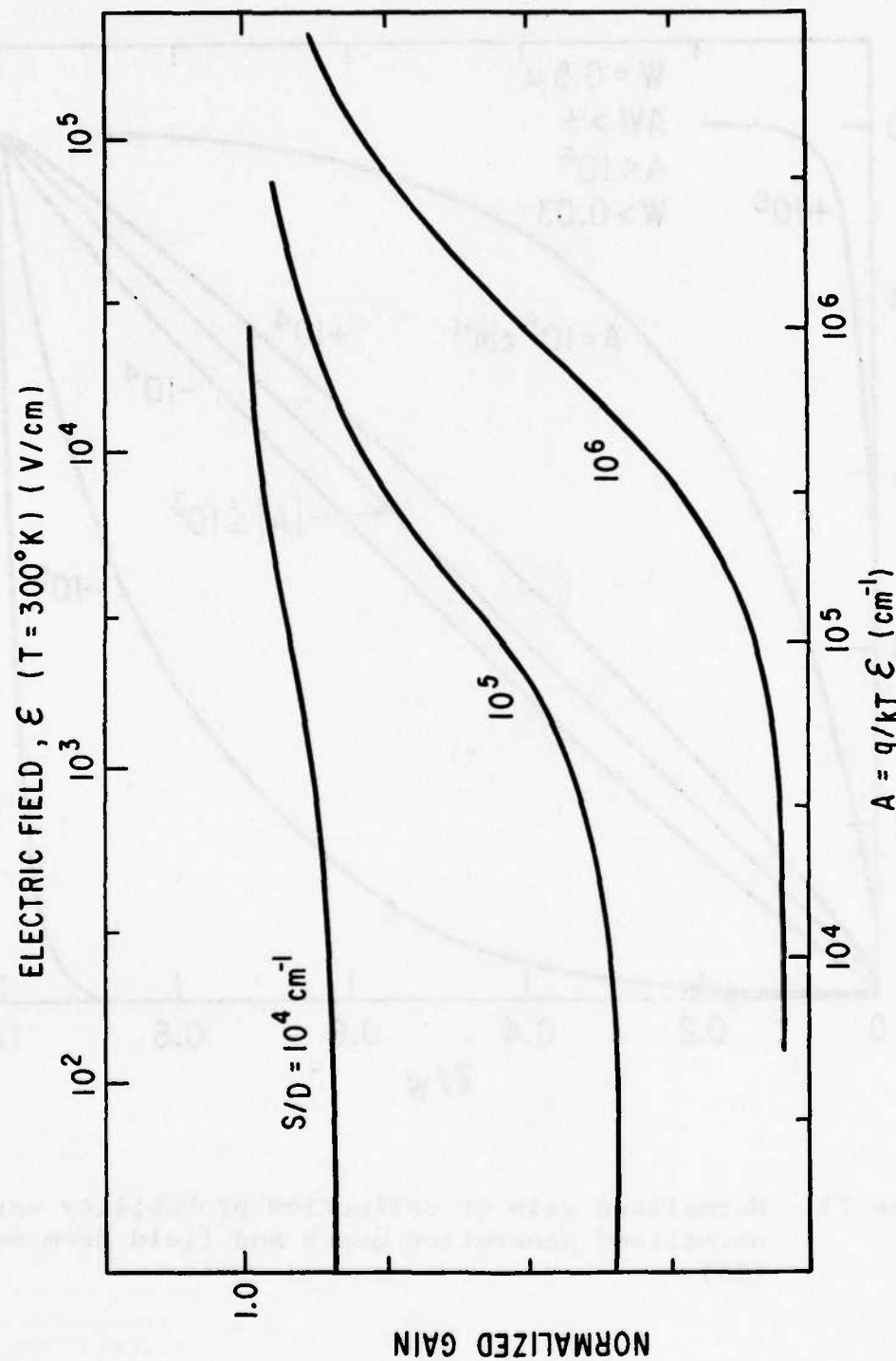
Figure 72. Dependence of Normalized Gain on Electric Field
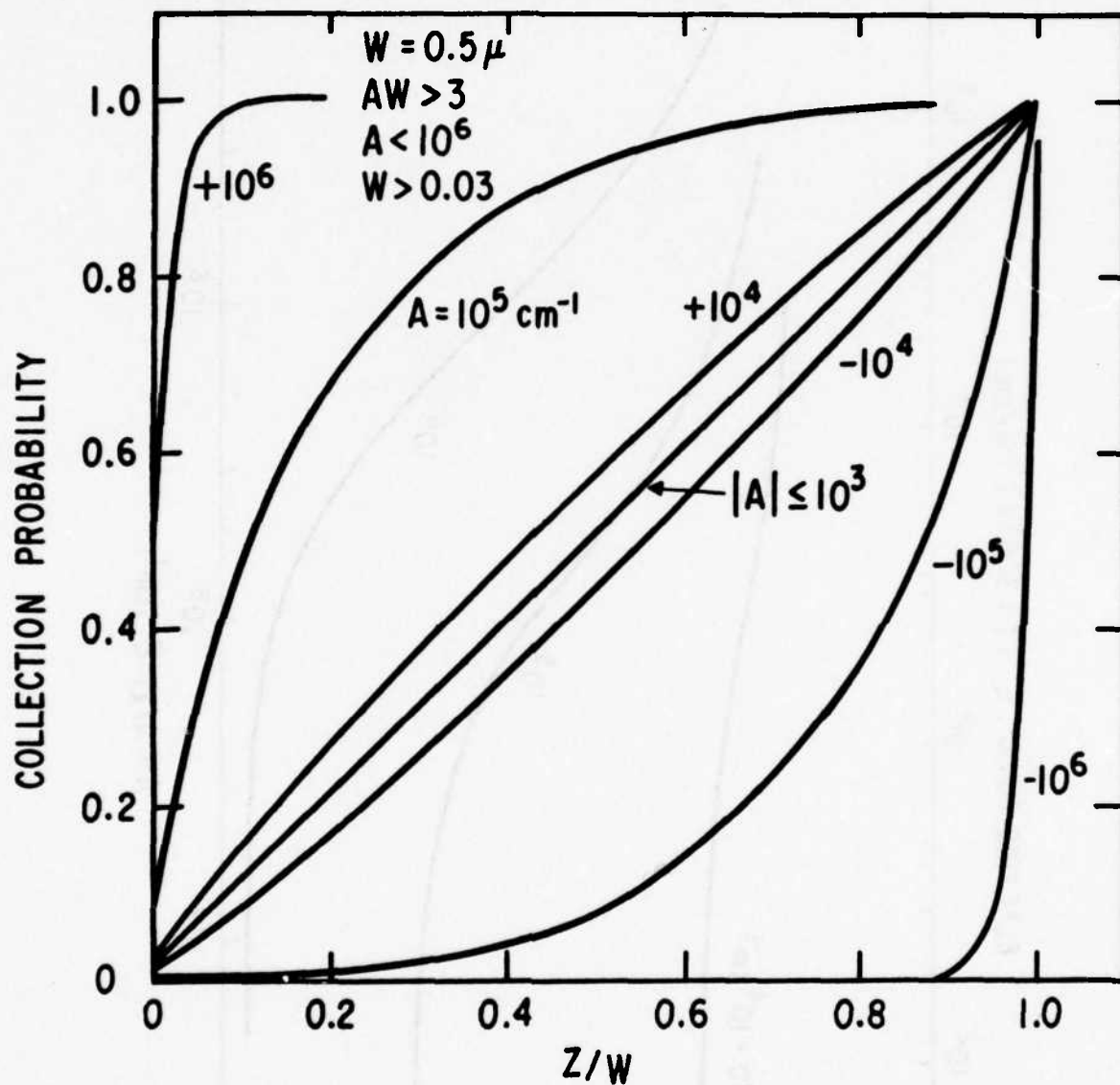
Figure 73. Normalized gain or collection probability versus normalized generation depth and field from equation (25).

work directed towards this end. However, based on the expected
implantation profiles coupled with some intuition it is possible
to make some predictions which agree qualitatively with the exper-
imental results.

Figure 74 shows the model to be used. Figure 74a is the
expected ion implantation profile which in LSS theory is a simple
gaussian. Assuming a gaussian profile:

$$N_p = 2F / (\sqrt{\pi} \, \Delta R_p)$$

(27)

and

$$N_D = N_p \, exp. \, (- (z-z_p)^2 / \Delta R_p^2)$$

(28)

where F is the implantation fluence (and ΔR_p the standard deviation
of the expected range (see Appendix I). The position of the center
profile is

$$z_p = R_p - d_{ox}$$

(29)

where R_p is the projected range (see Appendix I) and d_{ox} is the
thickness of the oxide layer present during implant. For the low
mass ions used in these studies so far the stopping powers of SiO_2
and Si are identical. The implantation tail shown will have to be
guessed at for now until the profiling measurements become available.
W_I is the ideal junction depth which is determined by:

$$N_D - N_A = 0 = N_p \, exp \, (- (W_I - z_p)^2 / \Delta R_p^2) - N_B$$

(30)

-125-

A.

$$N_D - N_A \cong N_P e^{-(Z-Z_P)^2/\Delta R^2}$$

NET DONOR DENSITY

$N_D + N_A$

IMPLANTATION "TAIL"

0

Z_P W_I W_A Z

B.

ELECTRIC FIELD

ACTUAL FIELD

UNIFORM APPROX.

E_R

E_L
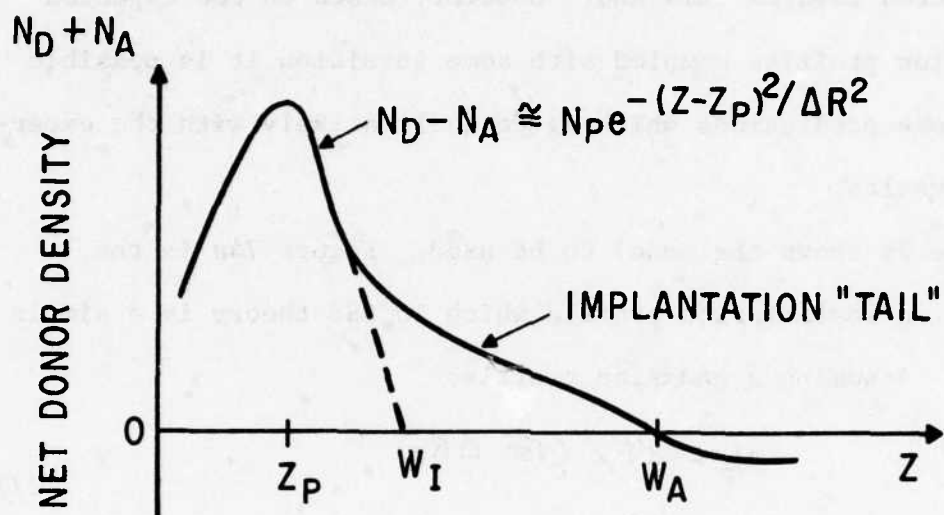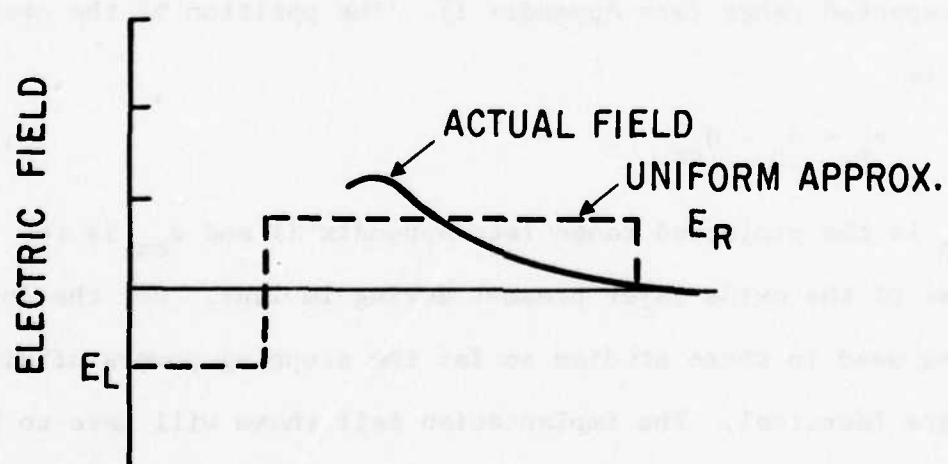
Figure 74.   Model Approximation of: (a) implanted doping profile
(b) Electric field distribution.
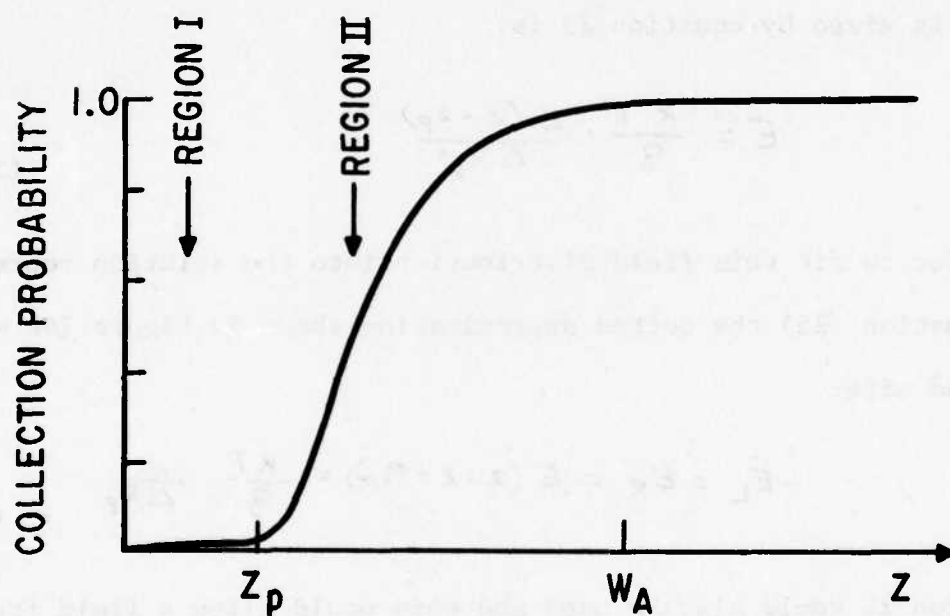
Figure 74c. Model Approximation of Collection Probability.

where N_B is the acceptor doping of the starting wafer. For most of the samples used so far $N_B \cong 10^{15}$ cm^{-3}. The effect of tailing can be quite severe (see Figure 22), and we will estimate that $W_A = W_I + 2(W_I - z_p)$.

Assuming that the doping profiles profile is given by equation 27 and 28 at least in the vicinity of the doping peak. The electric field is given by equation 23 is:

$$E = \frac{KT}{q} \cdot \frac{2(z - z_p)}{\Delta R_p^2} \tag{31}$$

In order to fit this field distribution into the solution represented by equation (25) the dotted approximation shown in Figure 74b will be used with:

$$-E_L = E_R = E(z = z + R_p) = \frac{KT}{q} \cdot \frac{2}{\Delta R_p} \tag{32}$$

Equation 24 could also be used and this would allow a field free region near the junction. In general, equation 19 can be solved for any number of uniform field regions to better approximate the actual field distribution. It is also possible to solve equation 19 by finite difference relaxation for any field and recombination distribution. This will be considered during the second quarter if it seems desirable.

Using figures 72, 73, and 74 predictions about the collection probability can be made. Table 4 shows the calculated values of $A_R = (q/kT) E_R$, z_p, W_A etc. for several fabricated planar diodes

-128-

Table 4

CALCULATED VALUES FOR ARSENIC AND PHOSPHORUS PLANAR DIODES

Sample	Species	Energy keV	d_{ox}	R_p	ΔR_p	F cm^{-3}	Z_p	E_R v/cm	A_R cm^{-1}	W_1	W_A
A7B	As	30	--	210	47	10^{14}	210	1.1×10^5	4.2×10^6	375	700
A8A	As	100	--	574	122	10^{14}	574	4.1×10^4	1.6×10^5	986	1810
P12C	P	100	--	1230	350	10^{14}	1230	1.4×10^4	5.7×10^5	2350	4600
P11C	P	100	1400	1230	350	10^{14}	170	1.4×10^4	5.7×10^5	950	3200

discussed in this section (see Tables I & II). Note that these are

calculated only from the implant conditions and not from measured

doping profiles. In some cases the values for A_R are extremely high

corresponding to electric fields $\sim 10^5$ v/cm. Such high fields are

not likely to actually exist in these samples because the doping

profile is not as sharp as assumed, equation 23 does not apply to

very steep doping gradients where the Debye length $\lambda = \sqrt{\dfrac{\epsilon\,(\kappa T/q)}{2q\,N_D}}$

is long compared to the distance over which the doping is changing.

For $N_D = 10^{17}$ cm^{-3}, $\lambda = 100$ Å. Hence we will assume $A \cong 10^5$ cm^{-1}

is a more realistic estimate of the built-in fields. From Figure 73

note that for $z < z_p$ (Region I) $A = -10^5$ cm^{-1} effectively constrains

all the carriers within that region and few escape past $z = z_p$.

That is, this region acts as a potential well which holds the carriers

until they recombine at the surface $z = 0$ which has high surface

recombination. In applying Figure 73 to region I it can be assumed

that region II $(z > z_p)$ acts as a collecting diode (i.e. $z_p = W$).

Hence the collection probability for carriers generated in Region

I is near zero as indicated in Figure 74c. Carriers on the other

side of z_p will have a collection probability somewhat like the

curve $A \cong 10^5$ cm^{-1} in Figure 73. For carriers generated in Region II

the boundary $z = z_p$ is a high recombination surface, since carriers

which pass this point to $z < z_p$ are effectively lost and recombine

as Region I. The shape of the curve in Region II (Figure 74c) does

not turn up as sharply as in figure 73 because the electric field

is zero at z_p and increases gradually rather than having a constant

large value from z_p to W_A as assumed in the calculation. The exact

shape of the curve in region II will depend on the electric field

distribution. As mentioned earlier it is possible to calculate

exactly the collection probability for any doping profile and this

will be considered during the following quarters if it seems approp-

riate. The curve shown in Figure 74c is a reasonable approximation

to the result of such an exact calculation.

Figure 75 shows the calculated collection probability curves

from the data described earlier in this section compared to the

estimated collection probability based on the model described by

Figure 74 and equations 27 through 32. As can be seen the predic-

tions are reasonably consistent. In particular the simple model

just discussed seems to predict the general trends of the probability

curves. This indicates that the basic concepts of a dead like region

due to a negative electric field and back diffusion of carriers

against the positive electric field can explain most of the dead

layer effects observed. It is possible that in carefully prepared

samples there is no dead layer effect in the sense of a high recom-

bination region. Further investigation will be necessary to resolve

this.

For reference the best fit collection probability curves and

gain energy curves for several additional samples discussed in the

planar diode fabrication and measurements sections are included in

the following figures 76 through 80. In each case the order of the

fit is indicated. Figure 78 again compares the first order dead layer
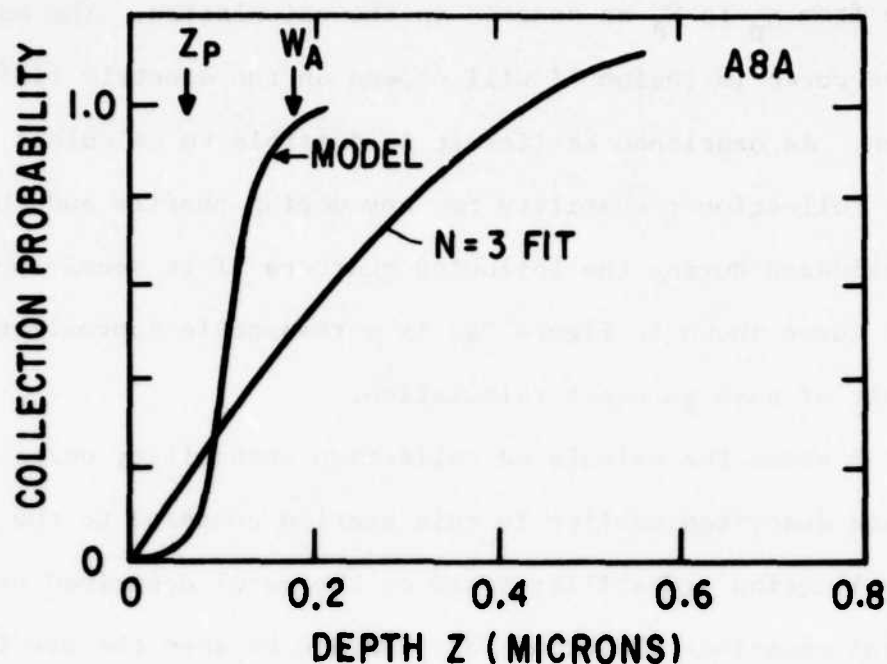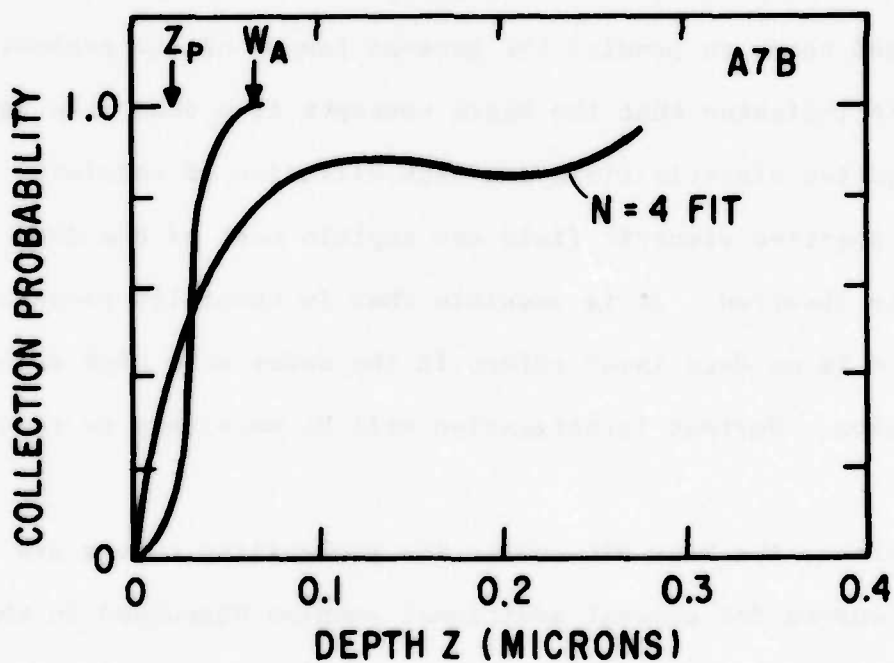
Figure 75. Comparisons of calculated collection probability by least squares fit with the model calculation based on figure 74 and Table IV. (a) Sample A8A, 100keV As at 10^{14} cm^{-2}, <100> orientation annealed for 1 hour in Ar at 650°C. (b) Sample A7B, 30 keV As at 10^{14} cm^{-2}, <111> orientation, annealed for 1 hour in Ar at 770°C.

-132-
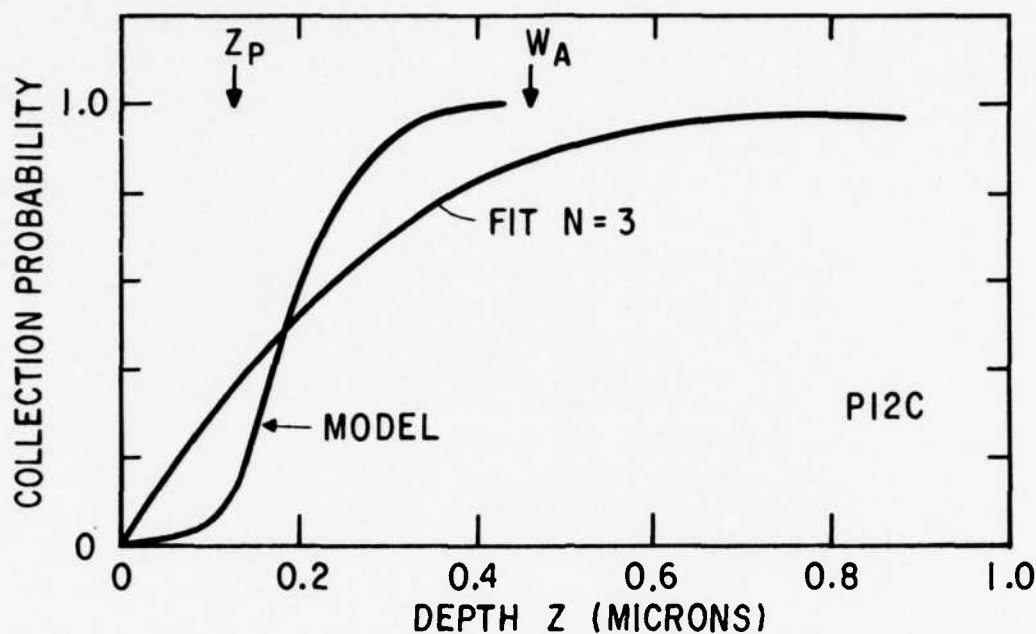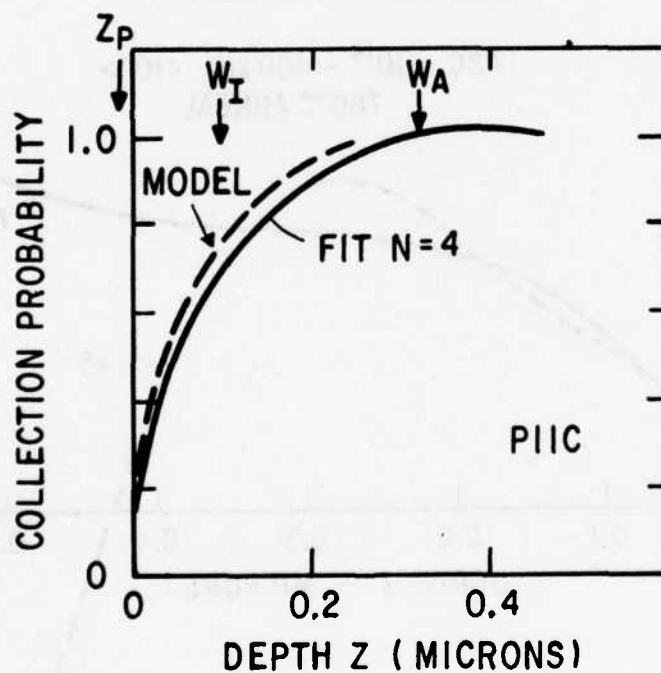
Figure 75 (Cont.) Comparisons of calculated collection probability by least squares fit with the model calculation based on figure 74 and Table IV. (c) Sample P12C, 100 keV P at 10^{14} cm^{-2}, <111> orientation annealed for 1 hour in Ar at 760°C. (d) Sample P11C, 100 keV P at 10^{14} cm^{-2}, <111> orientation annealed for 1 hour in Ar at 760°C.

A8C — 10^{14} — 100 keV <100>
760°C ANNEAL

N = 3

N = 5

COLLECTION PROBABILITY

DEPTH Z — MICRONS
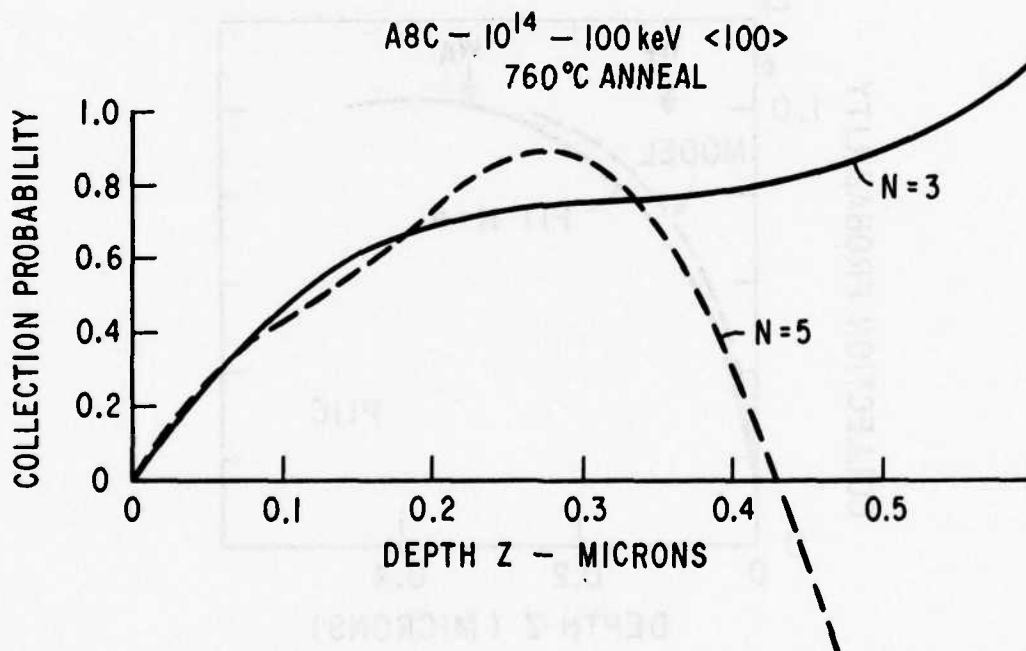
Figure 76a   Best Fit Collection Probability for Sample A8C,
10^{14} - As - 100 keV <100> after 760°C Anneal.
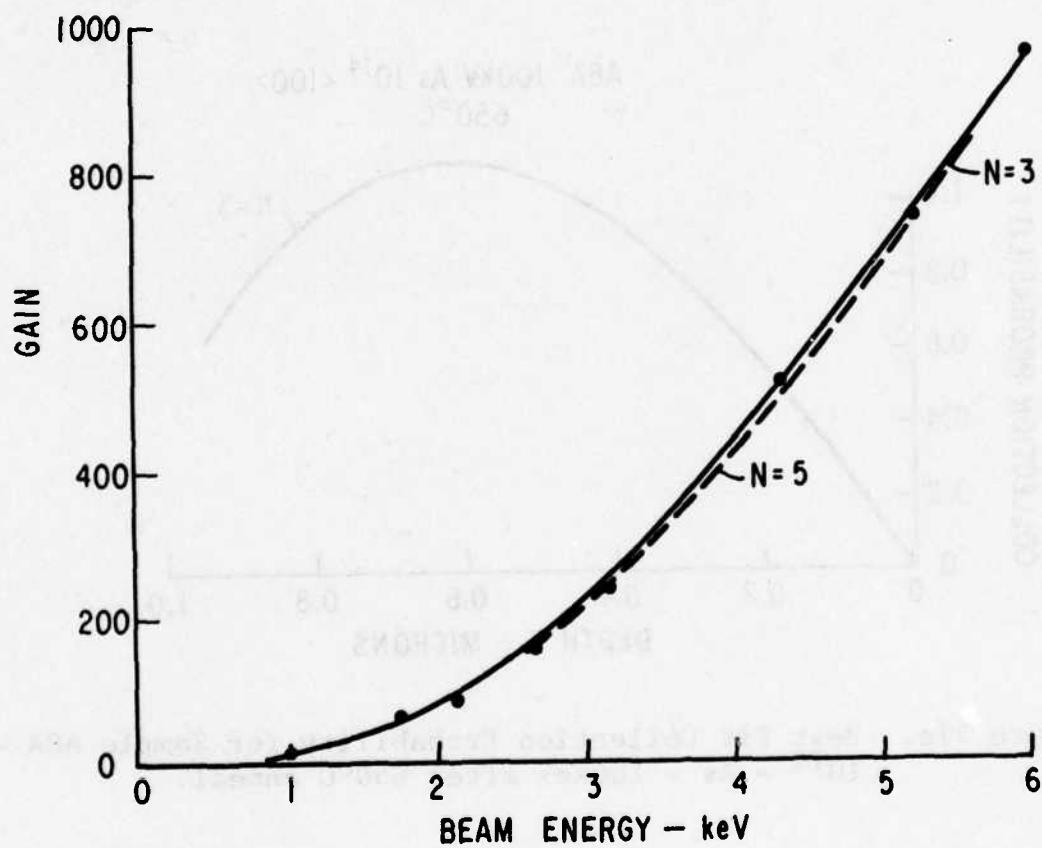
Figure 76b   Gain vs. Energy for Sample A8C, 10^{14} - As - 100 keV
⟨100⟩ after 760°C.
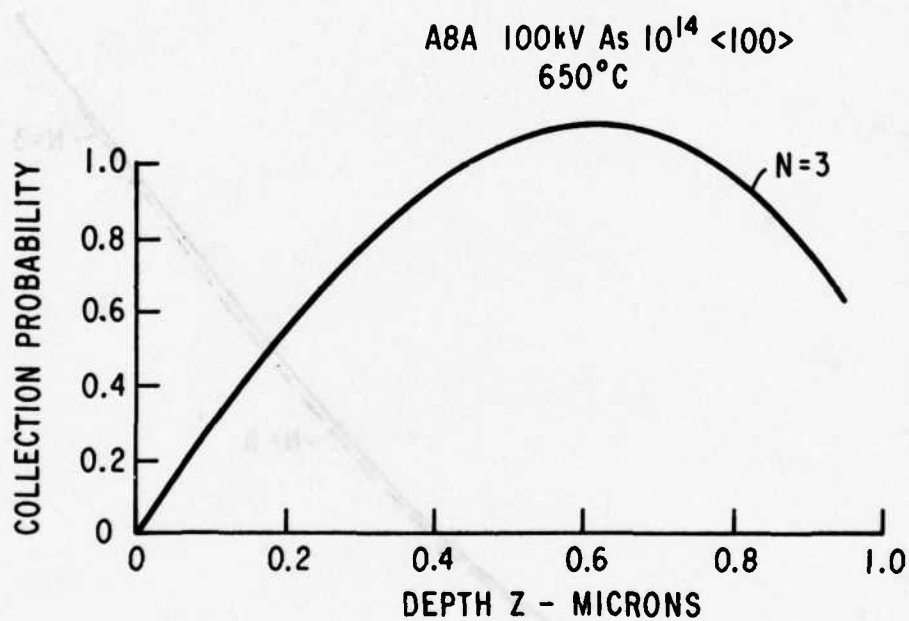
Figure 77a. Best Fit Collection Probability for Sample A8A - 10^{14} - As - 100keV after 650°C anneal.
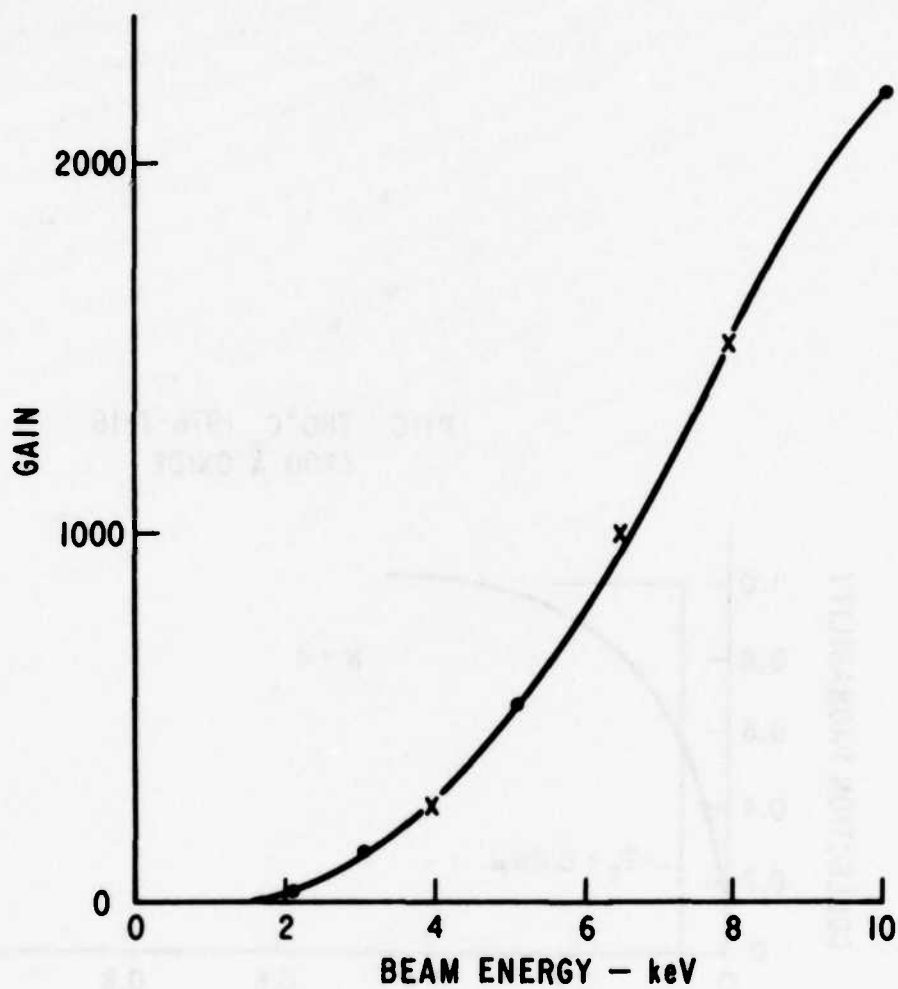
Figure 77b. Gain vs Energy for Sample A8A - 10^{14} - As - 100keV
after 650°C anneal.
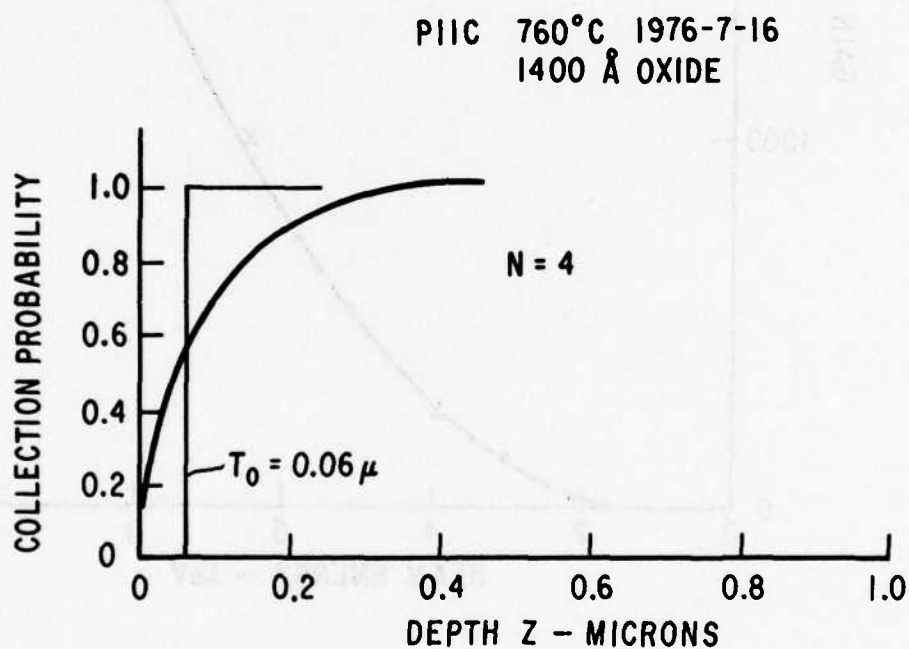
Figure 78a. Best Fit Collection Probability for Sample P11C - 10^{14} - P - 100keV - $\langle 111 \rangle$ through 1400 Å oxide. Curve labeled $T_D = 0.06\mu$ compare first order model approximation to Data.
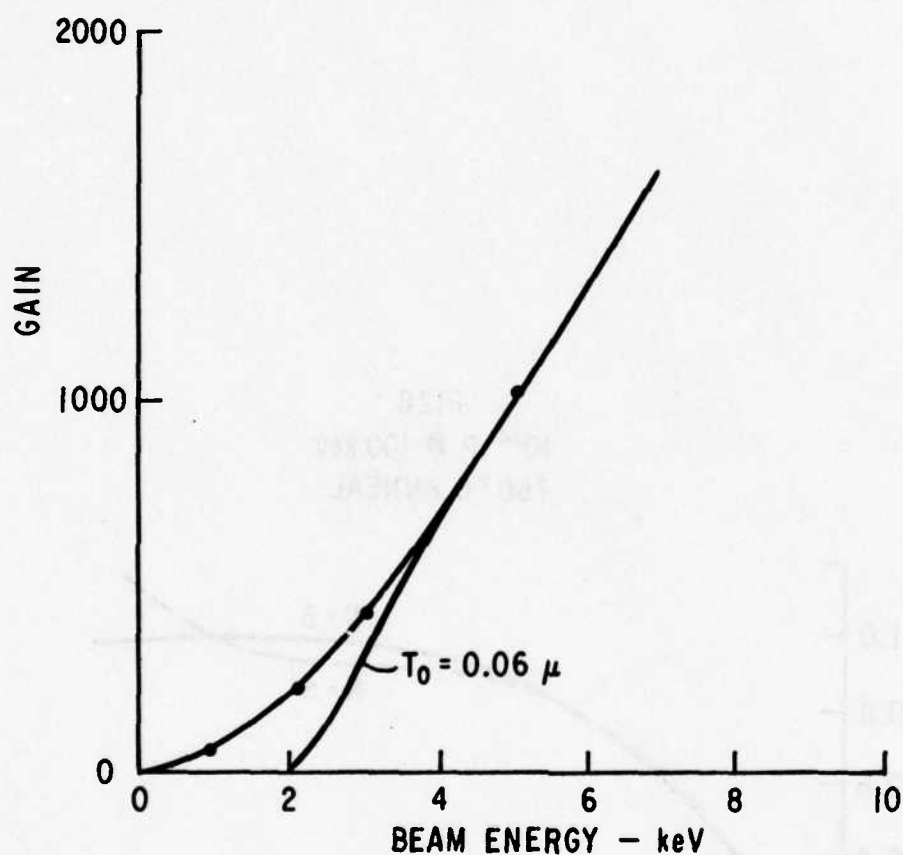
Figure 78b. Gain vs Energy for Sample P11C - 10^{14} - P-100keV- $\langle 111 \rangle$ through 1400 Å oxide. Curve labeled $T_D = 0.06u$ compare first order model approximation to Data.

-139-

P12C
10^{14} P @ 100 keV
760°C ANNEAL
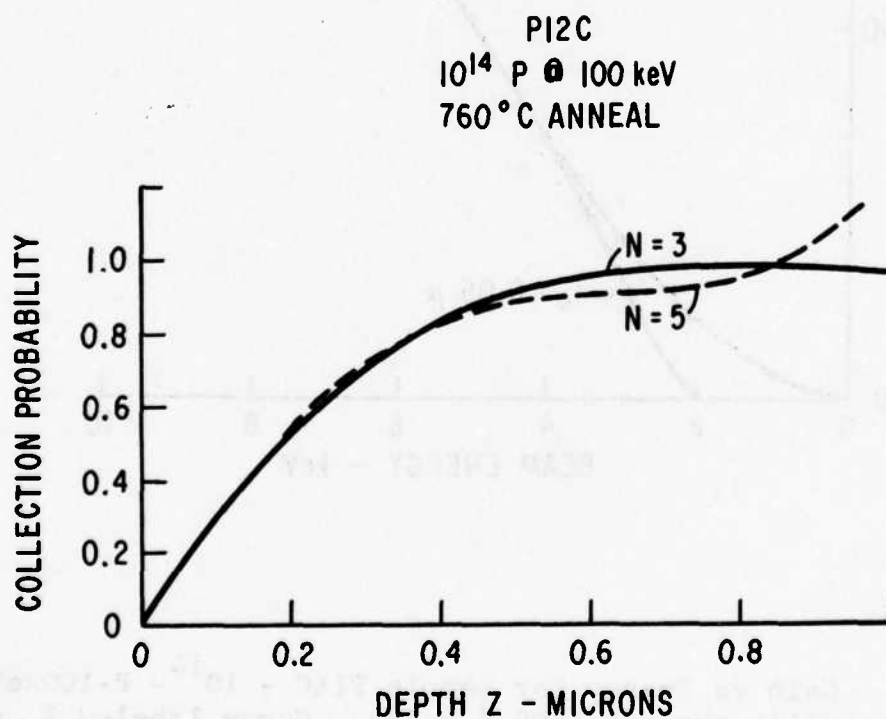
Figure 79a. Best Fit Collection Probability for Sample P12C - 10^{14}-
P - 100keV - <111> after 760°C anneal.
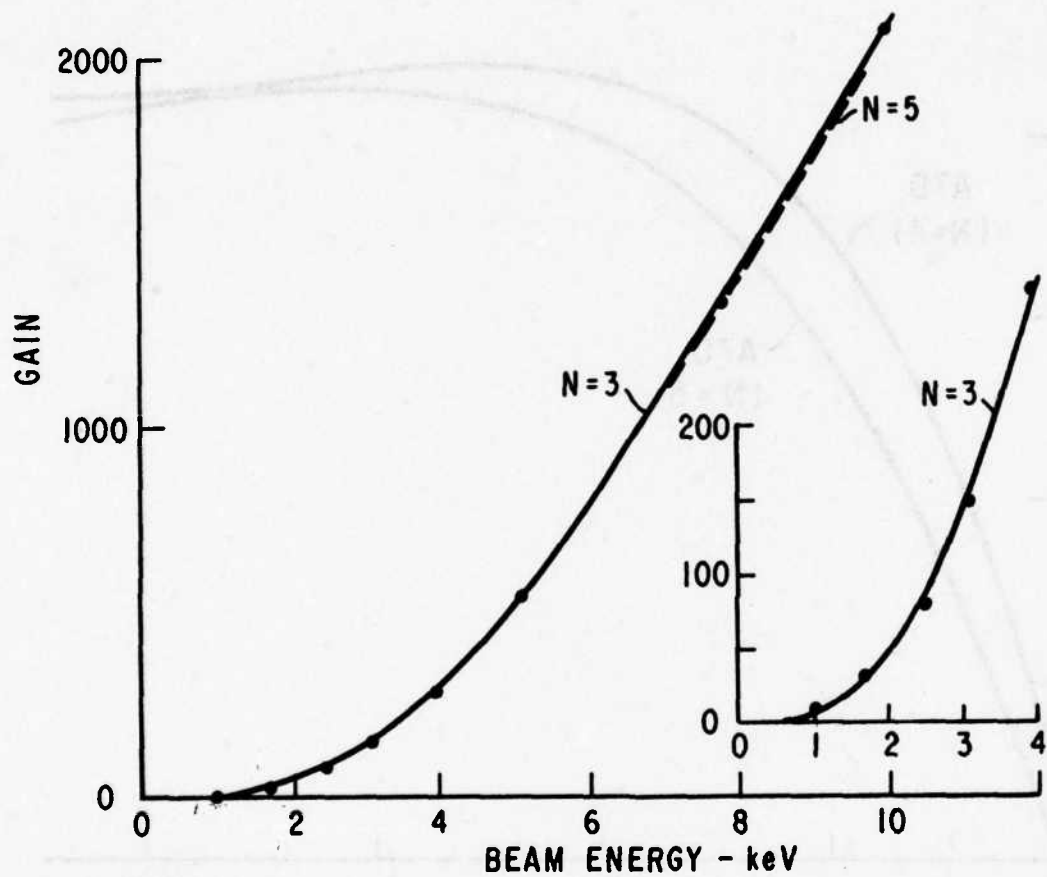
Figure 79b. Beam vs Energy for Sample P12C - 10^{14} - P - 100keV-
           <111> after 760° anneal.
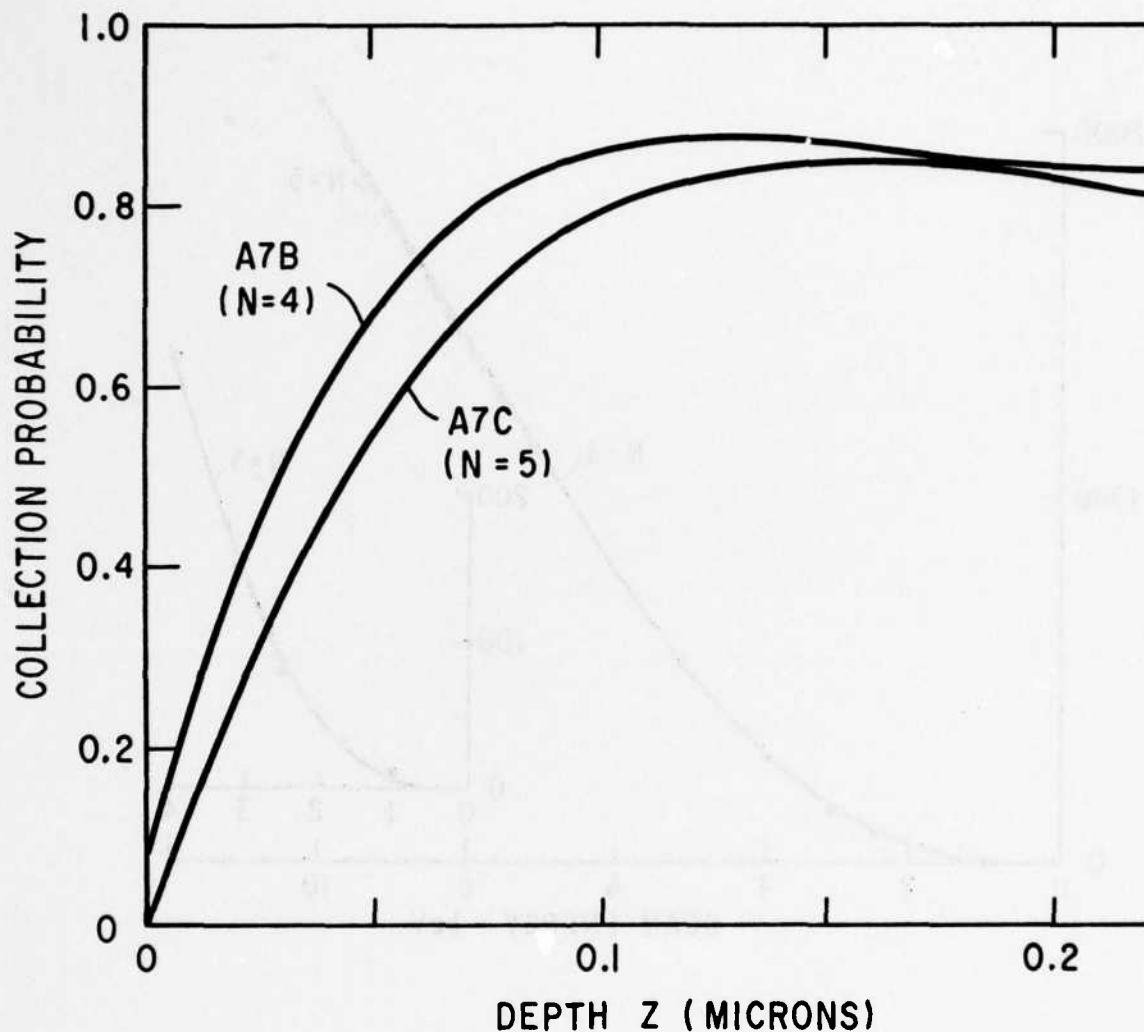
Figure 80a. Best Collection Probability for two implanted sample annealed at different temperatures. Both A7B and A7 are sections of the same wafer, implanted with 30 ke As$^+$ at 10^{14} cm^{-2} into <111> p type silicon. A7B was annealed at 760°C and A7C at 650°C for 1 hour in Ar. The difference for z<0.02 microns may not be real si there is no gain data below 1 keV. The electron ran at 1 keV is 200 Å. The differences for 0.02 microns microns are real. Comparison of these samples also some idea of the sensitivity of the gain curves to t collection probability.
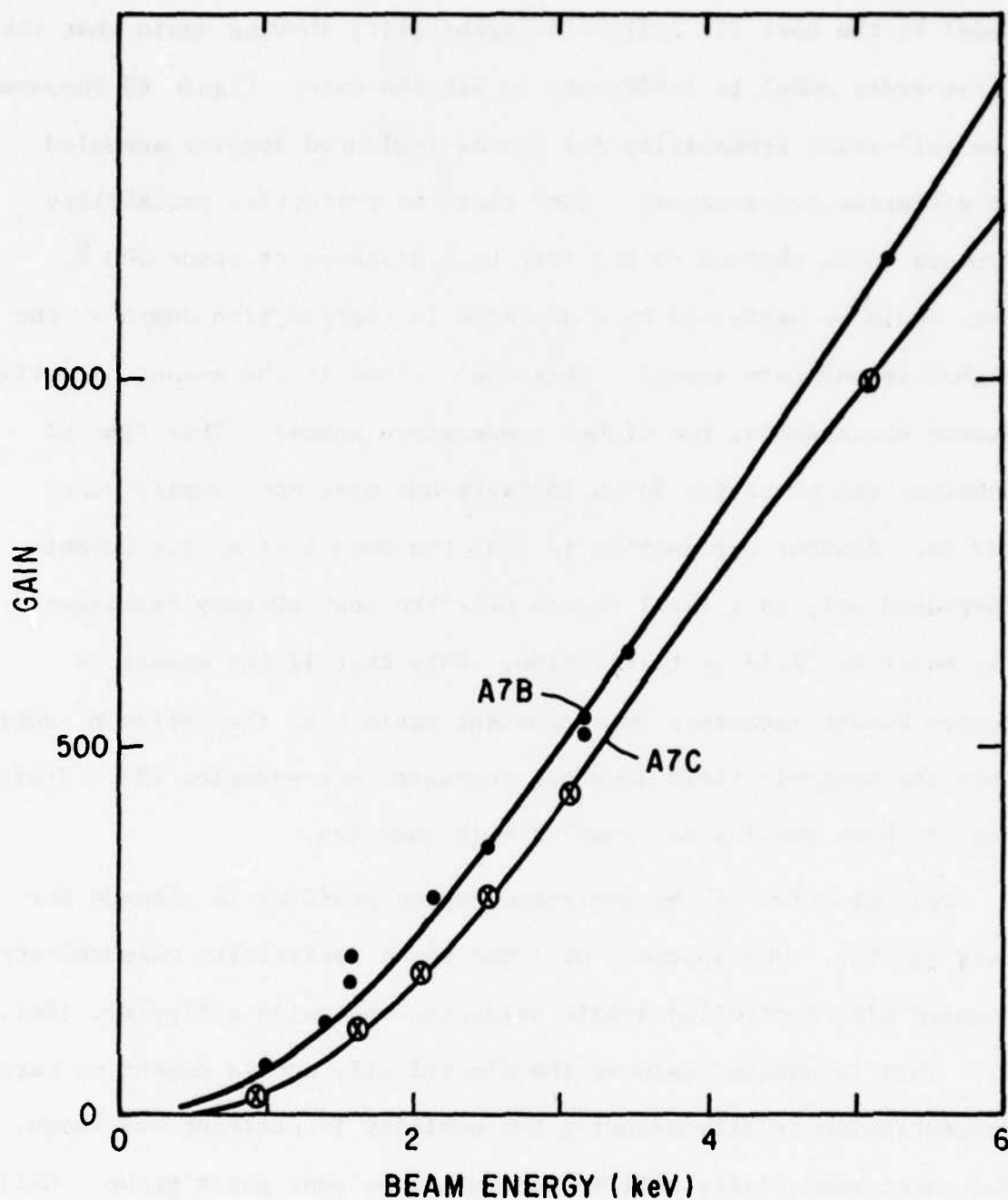
Figure 80b. The Gain versus Energy Data used for the fit and also the best fit gain curves calculated. Both A7B and A7C are sections of the same wafer, implanted with 30 keV As$^+$ at 10^{14} cm^{-2} into <111> p type silicon. A7B was annealed at 760°C and A7C at 650°C for 1 hour in Ar. The differences for z<0.02 microns may not be real since there is no gain data below 1 keV. The electron range at 1 keV is 200 Å. The differences for 0.02 microns<z<0.2 microns are real. Comparison of these samples also gives some idea of the sensitivity of the gain curves to the collection probability.

model to the best fit collection probability showing again that the first order model is inadequate to fit the data. Figure 80 compares the collection probability for two As implanted samples annealed at different temperatures. Note that the collection probability appears to be shifted to the left by a distance of about 200 $\overset{o}{A}$. This could be explained by a decrease in the junction depth at the higher temperature anneal. This could occur if the amount of active dopant decreased at the higher temperature anneal. This type of behavior can occur for Boron implants but does not usually occur for As. Another explanation is that the amount of active dopant increased only in a small region near the peak thereby increases the built-in field in this region. Note that if the amount on active dopant increases by a constant ratio over the entire n^+ region then the built-in field does not increase (see equation 23). Profiling of these samples may resolve this question.

Determination of the implanted doping profiles is planned for next quarter. One approach will use sheet resistivity measurements coupled with controlled anodic oxidation and oxide stripping. (Ref. 9). This technique measures the electrically active dopant or carrier concentration profile assuming the mobility is constant and known. The sheet resistivity will be determined by four point probe. Calibration of the oxide thickness will be carried out by ellipsometry (Ref. 10). Computer programs for all the necessary calculations and corrections (Ref. 10) have been acquired and developed.

The second technique will be secondary ion mass spectrometry (SIMS). This measures the total dopant profile (active plus inactive) and is complementary to the resistivity technique. Unless a SIMS unit is acquired by the Center, this will be done on a contract basis with outside laboratories.

Section IV

RESOLUTION MODEL I

Figure 19 shows a somewhat idealized model of the surface diode target. This can be even more idealized as shown in Figure 81. Radial symmetry is implied. The areas labeled P^+ are the written areas and should be thought of as the outer edges of the P^+N^+ diode depletion field in the case of surface diode writing or the boundary of the high recombination region in the case of damage writing. In either case the boundary condition along these surfaces is $V = 0$ where V is the excess minority carrier density.

The motion of generated excess carriers is governed by the continuity equation as discussed earlier in this section.

$$D\nabla^2 V - \mu \underset{\sim}{E} \cdot \nabla V - V/\tau + g = 0$$

(33)

where D is the minority carrier diffusion constant, μ is the mobility, τ the minority carrier recombination time and g is the generation rate of carriers. The boundary conditions can very generally be expressed as:

$$(D \underset{\sim}{\nabla} V - \mu \underset{\sim}{E} V) \cdot \hat{n} = SV$$

(34)
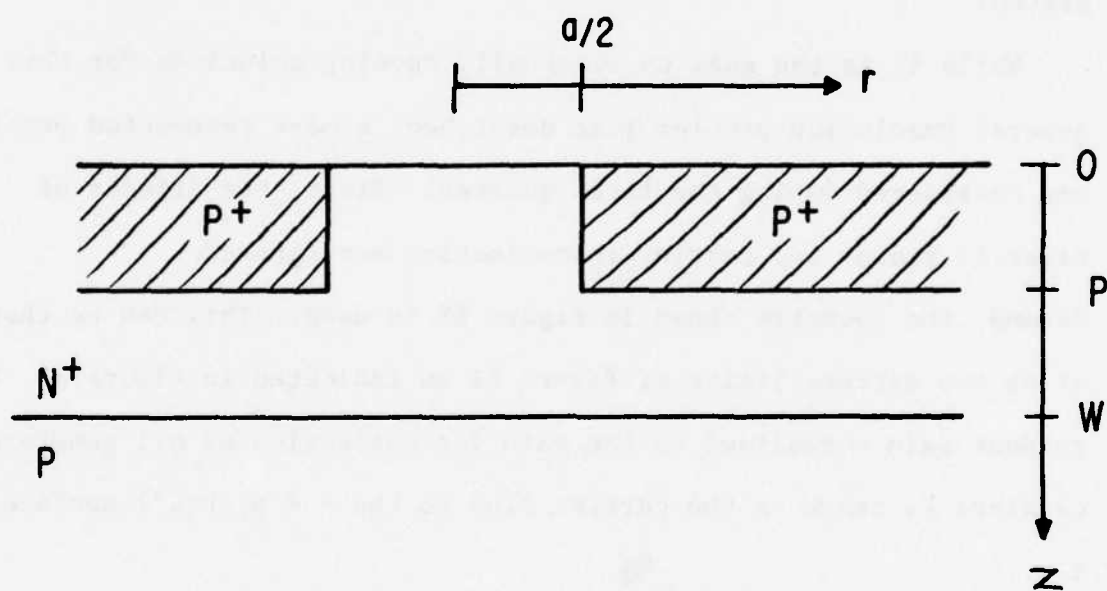
Figure 81   Idealized Written Surface Diode Target

where $\hat{n}$ is the unit vector normal to the surface and S is the sur-
face recombination velocity. For the edge of the written regions
S→∞ or equivalently V = 0 as previously mentioned. The boundary
condition at the z = 0 surface for r = a/2 is assumed to be S = 0.
This is equivalent to no carrier recombinations at the z = 0 surface,
or to no dead layer. The goal of the dead layer studies is to
produce targets approximating this boundary condition.

Carriers are assumed to be generated in the region z<d and
r<a/2 during reading. The readout gain is then the number of carriers
collected by the diode (z = W surface) normalized to the number gen-
erated.

While it is the goal to eventually develop solutions for this
general resolution problem just described, a more restricted problem
was considered during the first quarter. First, the effects of
electric fields and carrier recombination are ignored.
Second, the geometry shown in Figure 82 is used. This can be thought
of as two extreme limits of Figure 81 as indicated in Figure 83. The
readout gain normalized to the gain for collection of all generated
carriers is taken as the carrier flux to the z = p, r<a/2 surface
i.e.,:

$$ G = \int_0^{a/2} 2\pi r \, dr \left(-D \frac{\partial V}{\partial z} \right) $$

(35)

where it is assumed that the total carrier generation rate is 1 sec^{-1}.
If in Figure 82 we take T = P then the approximation being made is
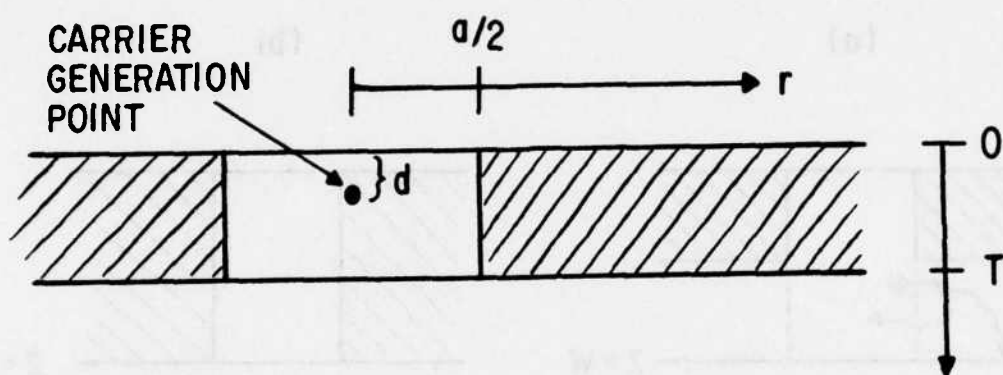
Figure 82. Model Approximation to Written Target
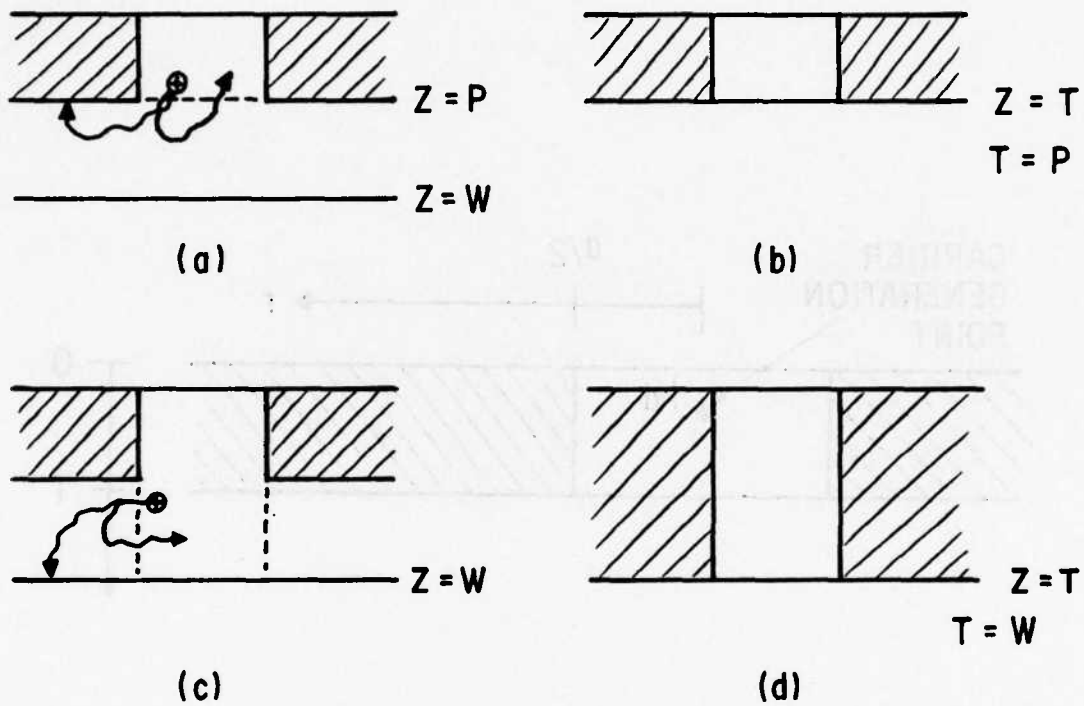
Figure 83. Limiting cases of model approximation in Figure 82
applied to figure 81 b) gives maximum readout gain
for (a) and (d) gives minimum readout gain for (c)

that carriers which cross the dotted boundary in Figure 83a are assumed to be collected by the N^+P diode (planar diode) and do not back diffuse into the $z<P$ region or recombine at the $z = P$ surface as indicated in Figure 83a. This approximation tends to give a higher readout gain than would actually be observed. If $T = W$ (Figure 83d) then the approximation being made is that the carriers that cross the dotted boundary in Figure 83c do not back diffuse into the $r<a/2$ region or to the collection junction at $z = W$ but recombine at the $z = P$ surface. If the readout gain is taken as the carrier flux to the $z = T = W$ surface in Figure 83d then some carriers which might have reached the diode will not be included and the readout gain will be lower for the Figure 83d approximation than for Figure 83c. Here the calculated gain for $T = P$ & $T = W$ brackets the actual gain for the model of Figure 81.

With the assumptions that $E = 0$ and $\tau = 0$ equation (33) reduces to the form of Poissons equation. This is the reason for the introduction of the notation V for δP with g equivalent to electric charge density. The boundary conditions are $V = 0$ for $r = a/2$, $V = 0$, for $z = T$ and $\frac{\partial V}{\partial z} = 0$ for $z = 0$. Hence the problem is equivalent to a conductive cylindrical box with an open end where the boundary condition at the open end is $\frac{\partial V}{\partial z} = 0$. Since closed form solutions are available for charges in cylindrical conductive boxes, the method of images can be used to yield the desired solution. This is summarized in Figure 84 along with the notation to be used. q is the strength of the point injection of carriers at points $z = d$ and $z = -d$. This
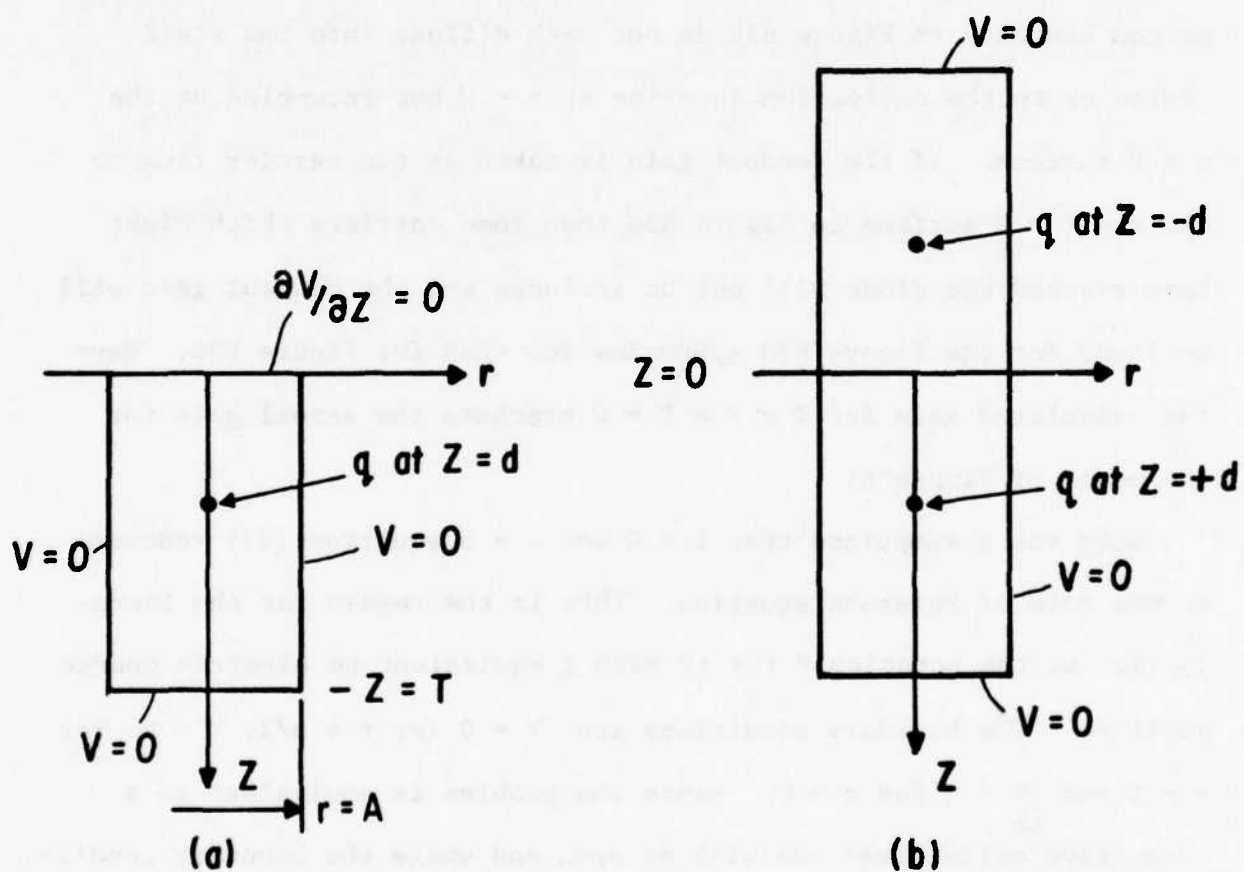
Figure 84. Application of known solutions of Poissons equation by method of images (b) to solution of boundary value problem (a)

is equivalent to $g = q \, \delta^3 \, (\underset{\sim}{r} - r_o)$ where $\delta^3 (\underset{\sim}{r})$ is the three dimensional delta function. The net rate of carrier generation is then q. By symmetry $\frac{\partial V}{\partial z} = 0$ at $z = 0$. That is, the net carrier flux across the $z = 0$ plane is zero.

Solutions of the potential problem shown in Figure 84b can be obtained by a series expansion in Bessel functions. See for example Smythe (Ref. 12) p. 189-90. The solution to Figure 84b is:

$$\frac{\pi D A^2}{8} V = \sum_{s=1}^{\infty} \frac{J_o (\mu_s r)}{\mu_s [J_1 (\mu_s A)]^2} \left\{ \frac{\sinh \mu_s (T-d) \sinh \mu_s (T-z) + \sinh \mu_s (z+T) \sinh \mu_s (T-d)}{\sinh \mu_s 2T} \right\}$$
$$-d < z < d \qquad (36)$$

$$\frac{\pi DA}{8} V = \sum_{s=1}^{\infty} \frac{J_o (\mu_s r)}{\mu_s [J_1 (\mu_s A)]^2} \left\{ \frac{\sinh \mu_s (T-z)}{\sinh \mu_s 2T} \left[\sinh \mu_s (T-d) + \sinh \mu_s (T+d) \right] \right\}$$
$$(37)$$

These are also solutions to Figure 84a since they satisfy the boundary conditions and are solutions of equation 33. Only the solution for $z > d$ is needed for the following calculations, the $-d < z < d$ is included for reference. Note that A is equivalent to a/2.

The normal derivative of the carrier density at $z = T$ is:

$$\frac{\partial V}{\partial z} \bigg|_{z=T} = \frac{-8}{\pi DA^2} \sum_{s=1}^{\infty} \frac{J_o (\mu_s r)}{[J_1 (\mu_s A)]^2} \left\{ \frac{\sinh \mu_s (T-d) + \sinh \mu_s (T+d)}{\sinh \mu_s 2T} \right\}$$
$$(38)$$

Integrating equation 38 according to equation 35 gives the normalized readout gain (with $q = 1$)

$$G = \frac{2}{A} \sum_{s=1}^{\infty} \frac{\sinh \mu_s (T-d) + \sinh \mu_s (T+d)}{\mu_s \sinh (\mu_s 2T) J_1 (\mu_s A)}$$
$$(39)$$

-153-

Equation 39 can be easily summed using a computer. Typically only 5 or 10 terms are necessary to give convergence $<10^{-5}$ unless $T - d/_T < 0.1$.

Figure 85 shows the result of evaluation of equation 39. As an example of the application of these results consider the model of Figure 81 with $P/_W = 0.5$, $P = 0.05$ microns and a generation depth $d = P/2$. Figure 86 shows the calculated normalized gain as a function of 2a which can be identified as the bit spacing in Figure 81 which is an isolated zero pattern. The actual gain for the model of Figure 81 will be between these two limiting curves as discussed earlier. Note that 2a/W should be larger than 2 for large readout gain. For bit spacings ~0.1 micron a junction depth W of ≤0.05 microns is therefore desired. Inclusion of electric fields in equation 33 will modify this result and should increase the gain for a given bit spacing relaxing the requirement on junction depth. Inclusion of these electric field effects will be considered during the following quarters. This preliminary model will then be useful as a limiting case check on the more sophisticated models.
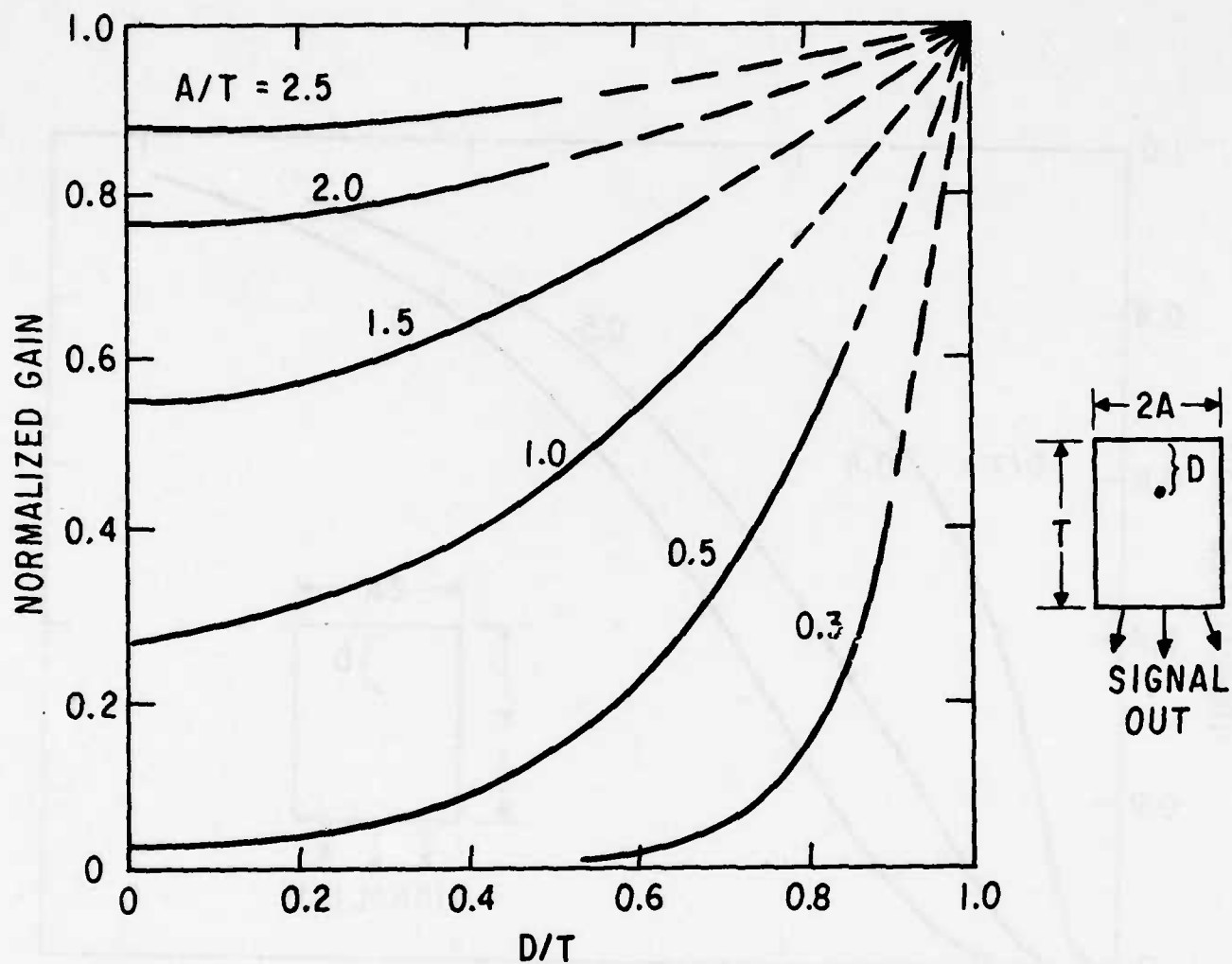
Figure 85a. Normalized readout gain form equation (39). D is the generation depth of the carriers, and T the thickness of the T and A the dimensions of the diffusion region (see Figure 82).
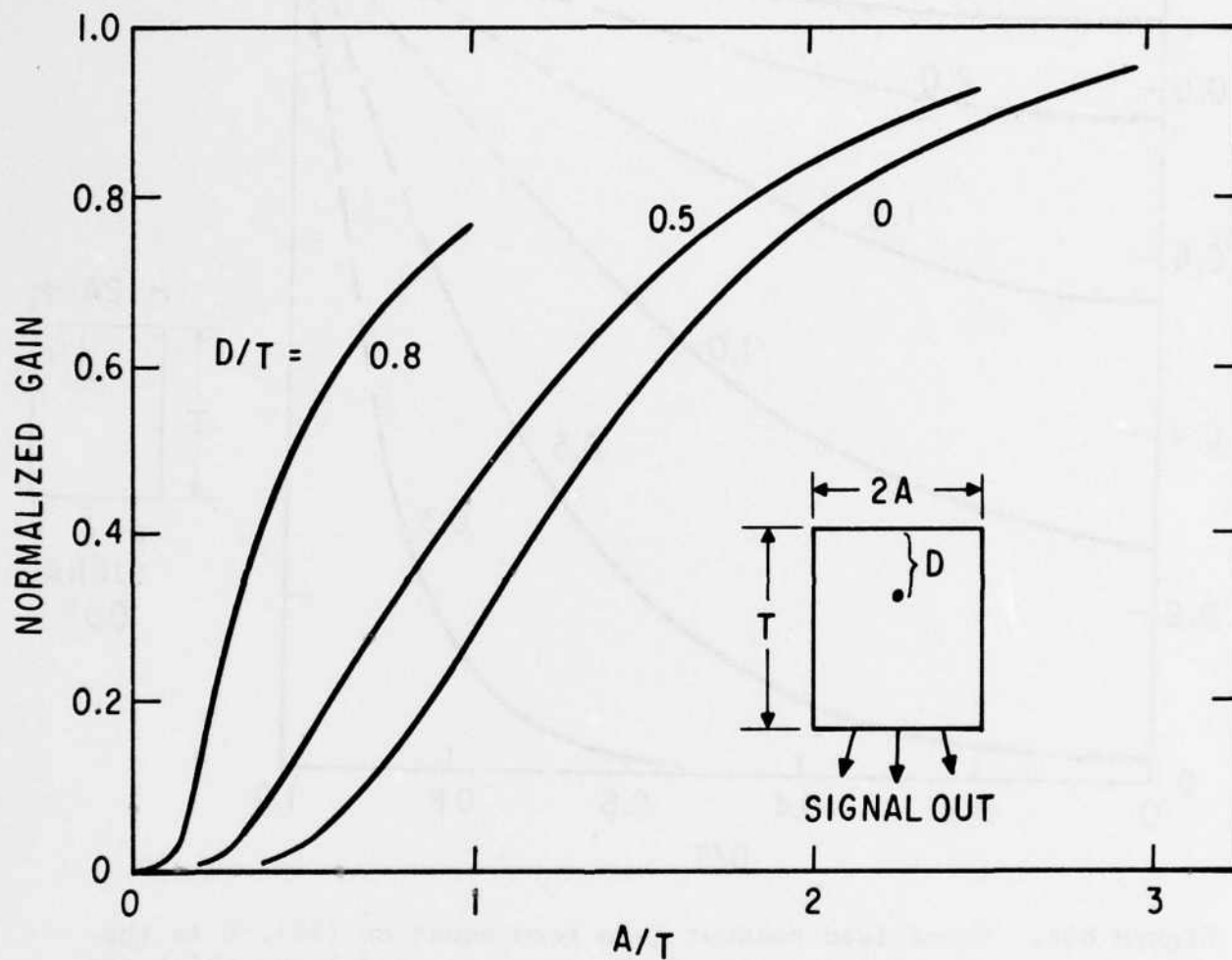
Figure 85b. Normalized readout gain form equation (39). D is the generation depth of the carriers, and T the thickness of the T and A the dimensions of the diffusion region (see Figure 82).
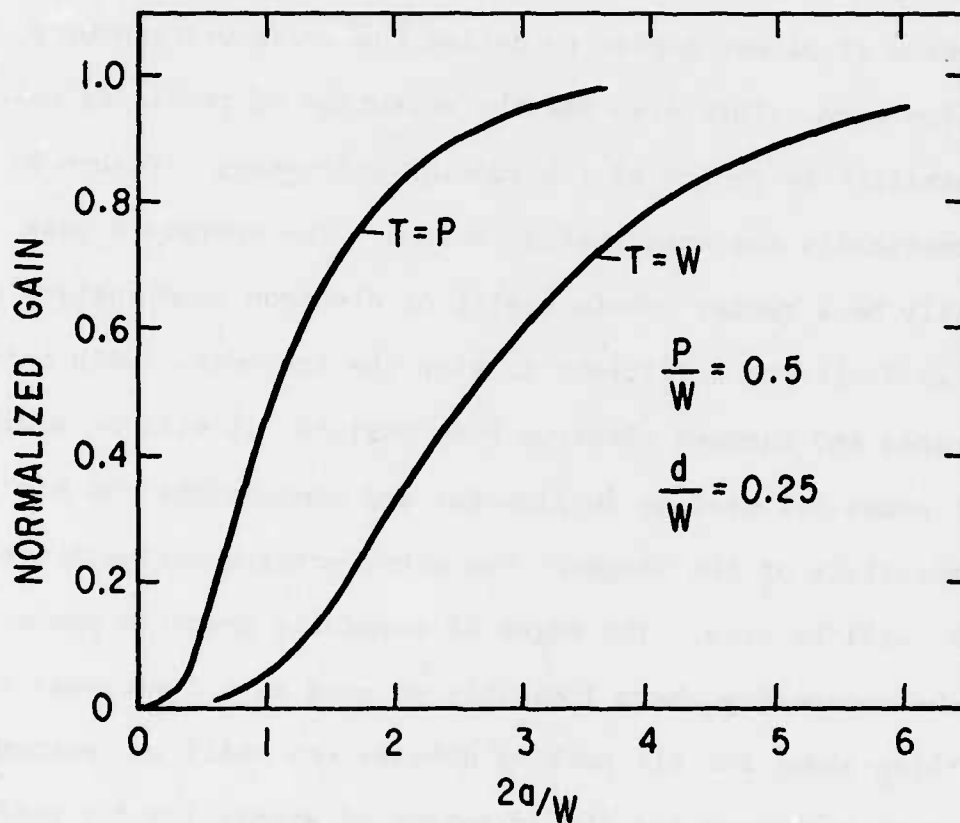
Figure 86. Normalized gain from equation (39) for $P/_W = 0.5$, $d/_W = 0.25$ (see Figure 81 and 82) for the limiting cases described by Figure 83 of $T = W$ & $T = P$.

Section V
ION IMPLANTATION WRITING

Since focused ion beam systems are not available, all ion beam writing experiments during the first phase will use aperature masks on the surface of planar diodes to define the areas written by a defocused ion beam. This also has the advantage of providing complete flexibility in choice of ion species and energy. Figure 87 shows schematically the experimental method. The aperature mask will normally be a resist (photo resist or electron beam resist) of thickness ≥0.2 microns sufficient to stop the ion beam. With carefully prepared and exposed electron beam resists, it will be possible to implant areas 0.1 microns in diameter and demonstrate the bit packing capability of the target. For other writing evaluation tests photo masks will be used. The edges of carefully prepared photo masks can be reasonably sharp (possibly as good as 0.1 microns) so that something about the bit packing density can still be learned . The photo mask technique has the advantage of simplicity for preliminary evaluation experiments.

An initial writing test was performed prior to the submission of the proposal. These early tests were performed using 40 ohm-cm, Boron doped <100> silicon. The N^+ surface was formed using $900^{\circ}C$ $POCl_3$ gas diffusion. The surface doping level was calculated to be $\sim 10^{19}$ cm^{-3}. The sheet resistance of the N^+ layer after deposition

WRITING DEMONSTRATION

20 keV BORON IMPLANT

7×10^{12} #/cm^2

ELECTRON BEAM
PATTERENED PMM RESIST

0.1μ

N^+-Si

P - Si
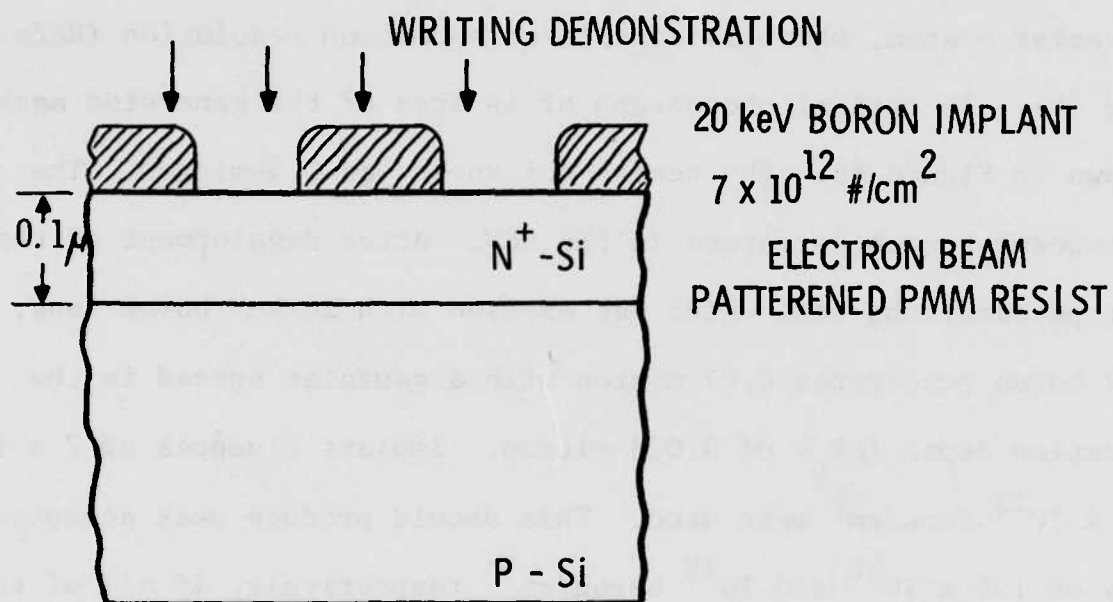
Figure 87. Aperature Mask Ion Beam Writing

and drive-in was 100 ohms/square. The depth of the N^+ surface is estimated as 0.5 microns.

A mask was formed on the target surface using electron beam exposure of polymethyl methacrylate (PMM) and development in isopropyl alcohol and methyl isobutyl ketone. This is a standard electron beam resist system, which is capable of submicron resolution (Refs. 13 and 14). An optical photograph of an area of the generated mask is shown in Figure 88. The resist thickness was 0.3 micron. The mask exposures were performed in the SEM. After development of the resist pattern, the test wafer was exposed with 20-keV boron ions. 20 keV boron penetrates 0.07 micron with a gaussian spread in the penetration depth (ΔR_p) of 0.028 micron. Implant fluences of 7×12^{12} and 5×10^{13} ions/cm^2 were used. This should produce peak acceptor levels of 1.4×10^{18} and 10^{18} boron/cm^3, respectively, if all of the boron is active. Very little difference was noted in the behavior of the two implant fluences.

Figures 89 and 90 show diode current readout signals from this target, using a 3 keV electron beam. The modulation in the video pictures is the diode signal current.

Figure 91 shows the signal levels from recorded bit and bar patterns of various dimensions as a function of the reading beam current. Ones are the signals between the implanted regions in Figure 89. Zeros are the signals from the implanted region. Note that the resolution is relatively independent of beam current at least up to
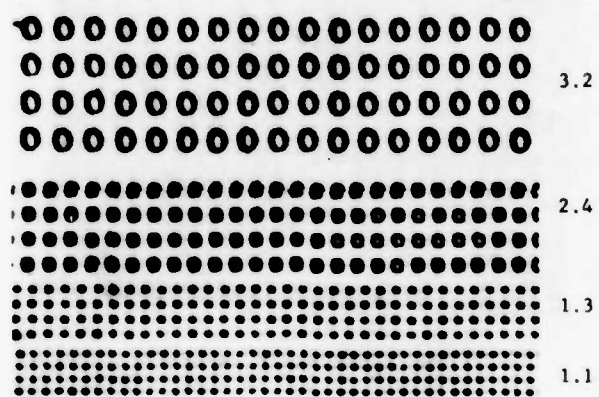
Figure 88.   Optical Micrograph Resist Pattern Used as
Ion Mask.
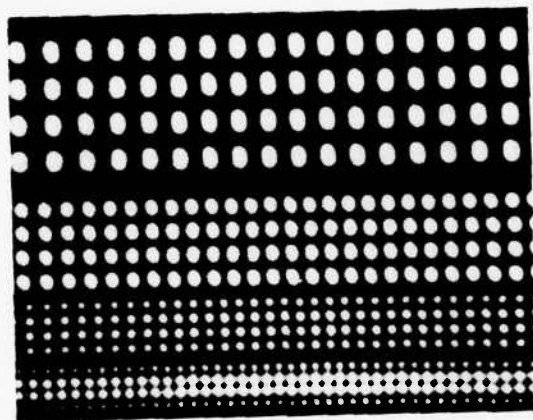
Figure 89.   SEM Micrograph Showing Implanted Diode Patterns
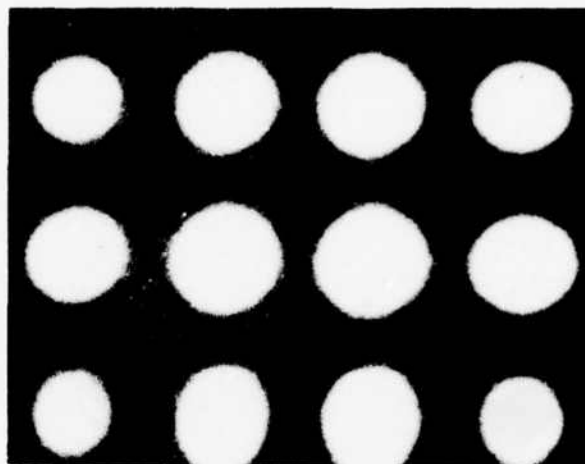
SEM Micrograph Showing
Implanted Diode Pattern.
Diodes on 1.3 Micron
Centers.
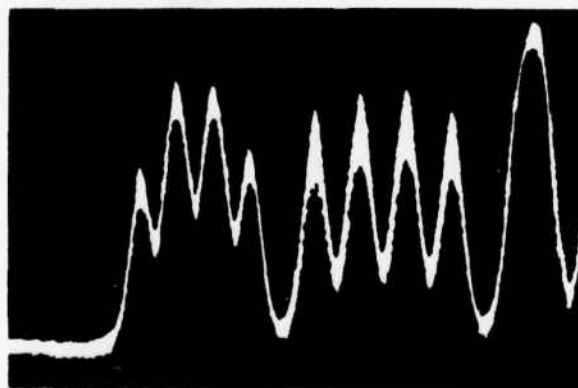
Readout Waveform
1.1 and 1.3 Micron
Spaced Implanted Diodes.

Figure 90. Implanted Diode Archival Memory Readout
(The largest gain modulation is 100 times
the reading beam current.)
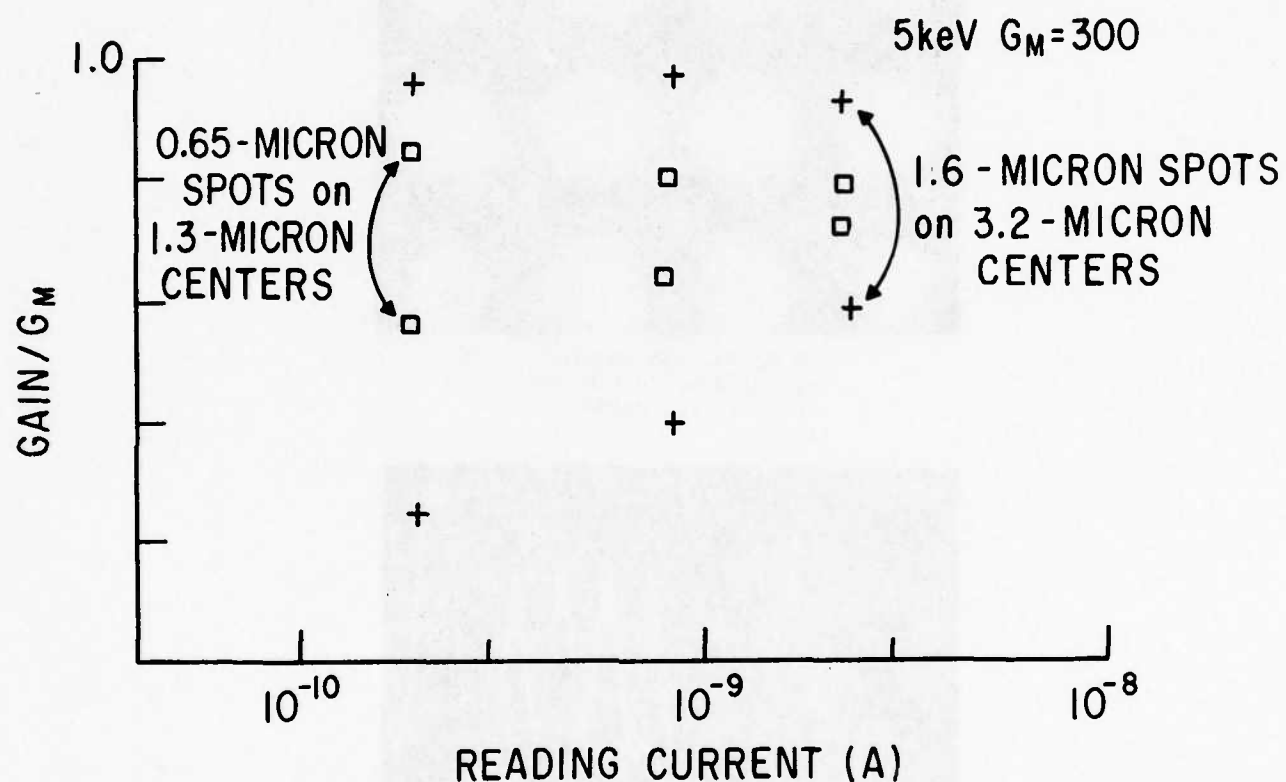
Figure 91. Effect of Reading Beam Current and Bit Spacing on Readout Signal Levels (The upper set of data points (ones) are for the unimplanted area between the implanted spots. The low sets of points (zeros) are for implanted spots of the indicated size.)

~0.5 nA. Without more careful additional work, it is difficult to separate the effects of increasing the electron beam spot size, as the beam current is increased, from any saturation effects on the resolution, but all of the resolution degradation can be attributed to increasing the electron beam spot size. Figure 92 shows the normalized signal levels at a low reading current, where the spot size is smallest (~0.5 micron), versus bit size. As can be seen, the recorded patterns are well resolved down to at least 0.6-micron bit size. An actual signal trace at the 0.6-micron bit size is shown in Figure 90. The zeros (implanted areas) show resolution degradation at the smaller sizes, as would be expected if most the resolution degradation is due to electron beam spot size effects. Because of depletion field spreading, implanted areas should always appear larger than expected in the readout signal and should not show this gain increase at smaller sizes. However, if the read electron beam spot size is too large during reading, then some ionization is always created outside the implanted zero, and the effect seen in these readout signals occurs. An alternate explanation for the resolution degradation at 0.5 micron is the lack of edge sharpness in the PMM mask. This would produce a tapered implant distribution that could also explain the observed result.

It has been tacitly assumed that this writing evaluation demonstrates the surface diode type of writing mechanism. However it is possible that the readout observed depended only upon the damage done
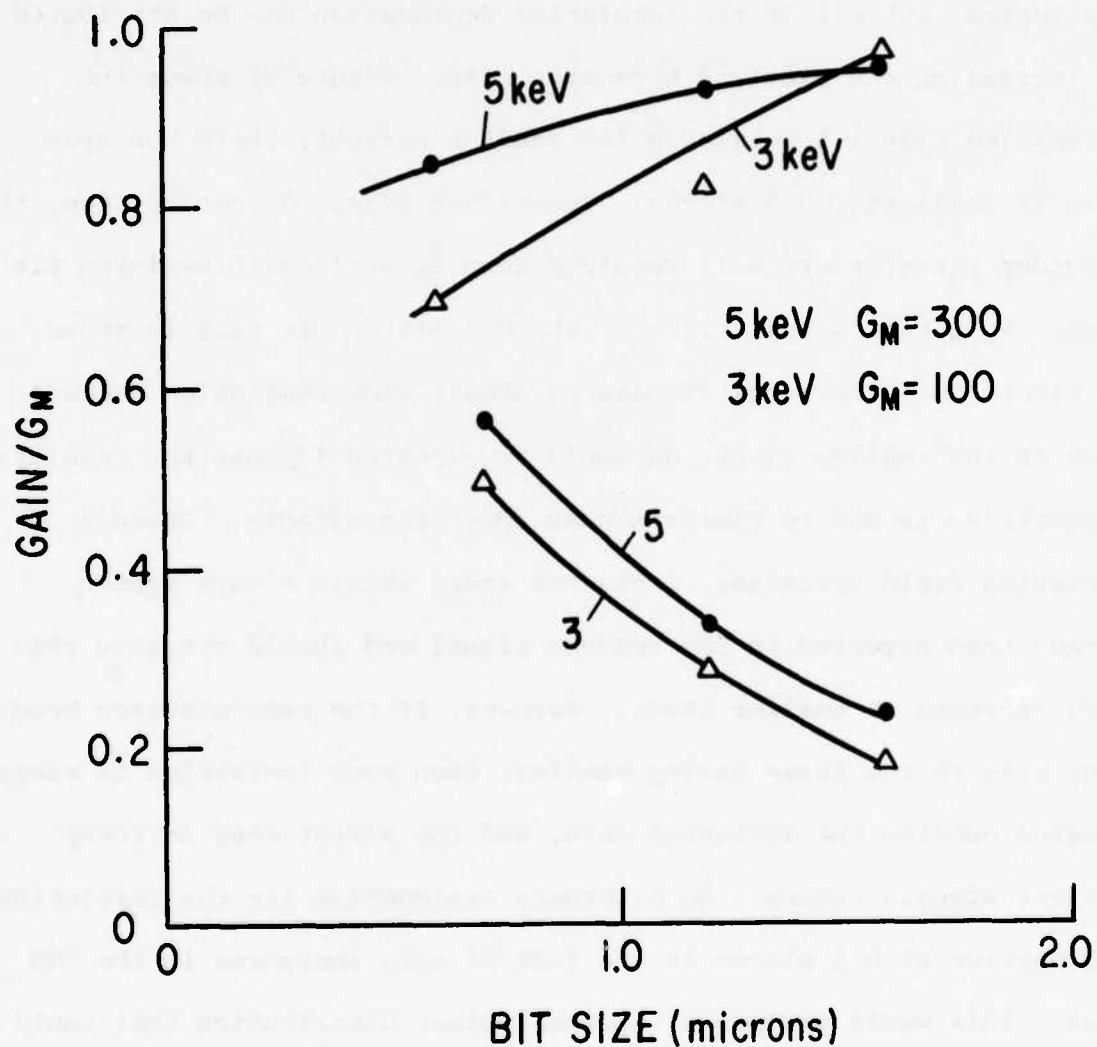
Figure 92. Dependence of Readout Resolution on Written Bit Size
Upper Set Ones and Lower Set Zeros. (Degradation of
zero resolution indicates the reading resolution
degradation is due to electron beam spot size effects.)

to the silicon by the P^+ ion beam. Writing studies were not planned
until the second quarter of the contract but it seems desirable to
settle this question by an exploratory writing experiment. He^+ ions
were chosen as the writing ions. Being an inert gas with no known
doping effects in silicon they seem appropriate as a test of the
damage writing method. A planar diode target (P12B) was fabricated
from <111>, 12-18 ohm-cm P-Si by implantation of P^+ ions at 100 keV
at room temperature, 7° off axis to a fluence of 10^{14} cm^{-2}. The
target was annealed for 1 hour in Argon at 760^oC. (This target is
identical to P12C). The target was then coated with resist and
patterned with a relatively coarse bar mask (Air Force Resolution
Chart). The patterned wafer was then exposed to a 30 keV room temp-
erature He^+ implant, 7° off axis to a fluence of 10^{13} cm^{-2}. Figure
93 is a secondary emission image from the SEM of a part of the exposed
resist. Figure 94 and 95 are SEM micrographs using diode signal modul-
ation after stripping of the resist. Figure 96 shows scope traces of
line scans across the edge of one of the bars. The edge sharpness of
the diode signal is about 0.6 microns at 5 keV beam energy and 1.2
microns at 7 keV. Secondary emission pictures of indicated that the
spot size of the SEM was ~0.4 microns at 5 keV and ~0.2 microns at 7
keV. In addition the broadening of the electron beam by scattering
in the substrate is ~0.3 microns at 5 keV and ~0.6 microns at 7 keV
(Figure 17). The total width of the traces in Figure 96 will be
approximately twice the effective spot size in the target including
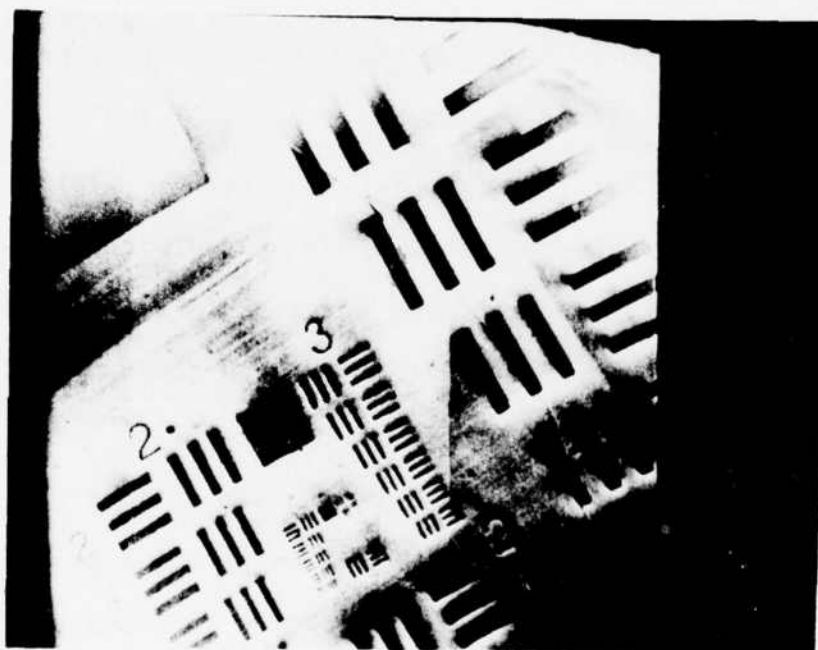
Figure 93.   Secondary Emission Micrograph of resist pattern
used as mask for the Ion Beam.   Dark Square between
2 and 3 is 590 Microns on a side.
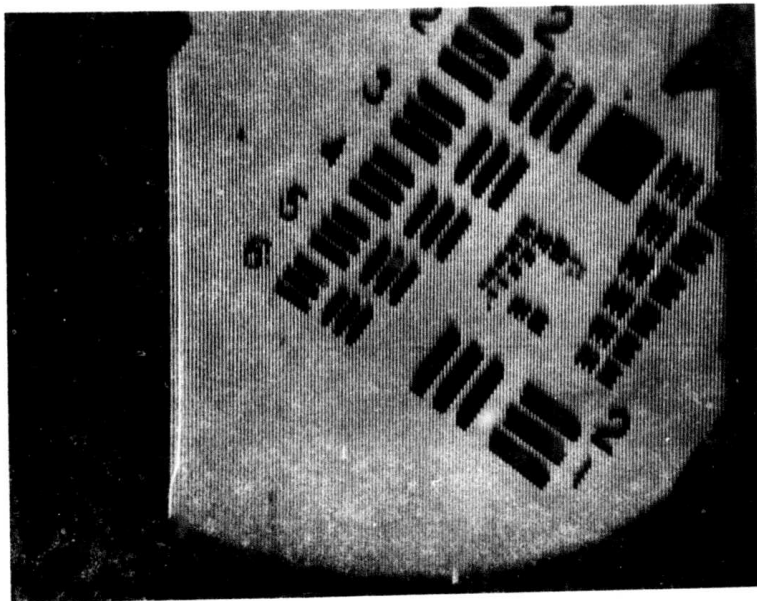
Figure 94. Scanning Electron Micrograph using Diode Current
Modulation Readout showing He Implanted Archival
Target P12B. Electron Beam Energy 3keV.
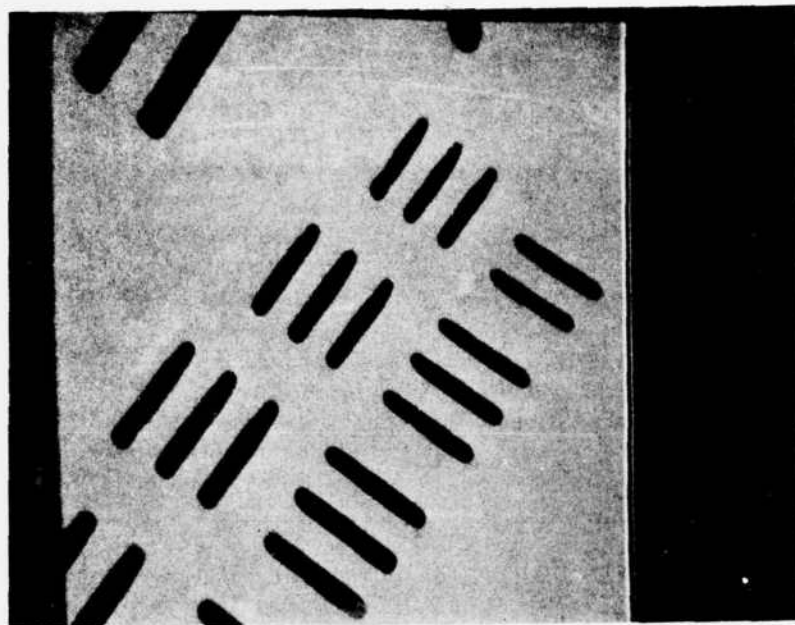
Figure 95. SEM Micrograph using Diode Signal Modulation showing He-Implanted Bar Pattern in Target P12B. Electron Beam Energy 3keV. Spacing of Finest Bar Patterns is 38 Microns.

(a)

⊢——→| |←—— 0.52 Microns

(b)

——→| |←—— 0.45 Microns
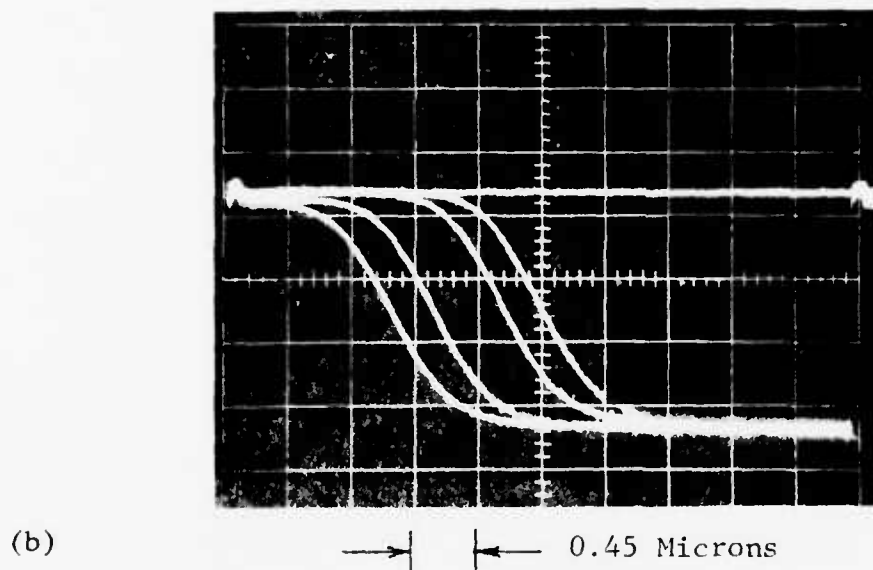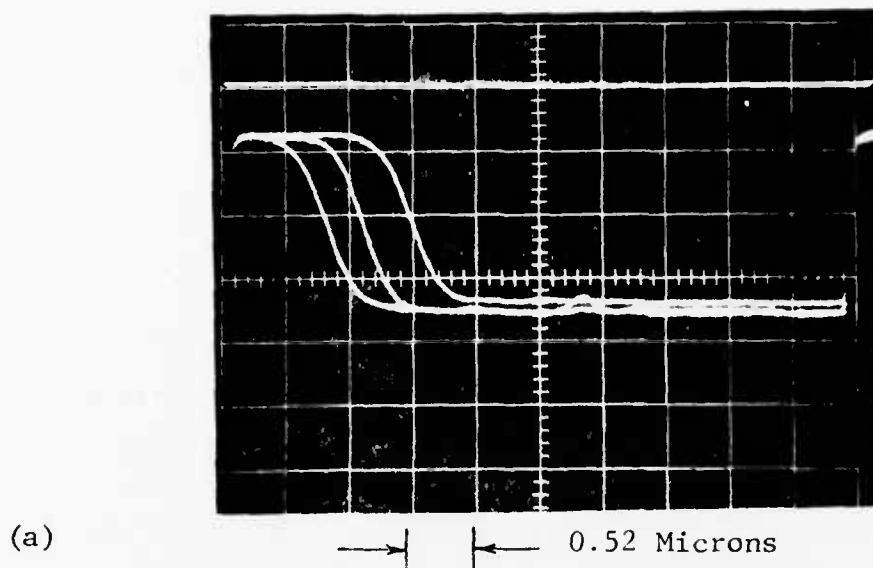
Figure 96   Single line scope traces across the edge of one of
the wide bars on He implanted target P12B. Multiple
traces at random positions along the bar are shown
to indicate uniformity. Top flat line is zero signal
or beam off trace. Scope sensitivity 0.2 uA/cm target
current. (a) Beam energy 7 keV, horizontal distance
scale 0.52 microns/div as indicated, beam current ~6 x
10^{-10}A (b) Beam energy 5 keV, horizontal distance scale
0.45 microns/div as indicated, Beam current ~1.5 x 10^{-9}A.

-171-

scattering and incident spot size. This gives an estimated edge

sharpness comparable to that observed so all the resolution degrad-

ation can be accounted for by spot size and scattering effects.

Readout of this pattern with a smaller spot size at lower beam energy

will be very interesting when the new Coates & Welter SEM under

order by General Electric becomes available later in the year.

Figure 97 shows the measured gain versus beam energy energy

curves and best fit collection probability for the He written target

areas, unwritten areas and the control sample. Note the very large

gain differences between the written and unwritten areas and the

good reproducibility between the two identically processed targets

P12C and P12B. Readout at 2.5 keV would be possible with this

target and writing method. Low voltage readout is important because

it minimizes beam scattering during readout. Figure 97a shows the

collection probability calculated from the data of figure 97b. The

expected region of He damage between $z = R_p \pm \wedge R_p$ is indicated. The

collection probability is significantly reduced in this area and at

smaller z. It is reduced at smaller z probably because of the block-

ing effect of the damaged region. This also shows that as expected

the writing was very deep in this experiment. Clearly 0.1 micron

resolution will be difficult to achieve with this energy He ions.

Lower energy or heavier mass ions are preferred.

This preliminary test indicates that damage writing is possible

in the planar diode target. Damage writing depends on a reduction

Figure 97.   Comparison of the calculated collection probability and
             Gain versus energy for the He written sample and control.
             Wafers P12C and P12B were implanted at 100 keV at 10^{14} P
             into <111> 12-18 ohm-cm n type silicon and annealed for
             1 hour in Ar at 760°C.   P12B was written in selected areas
             with He at 10^{13} cm^{-2} and 30 keV.   (a) shows the best fit
             collection probability for the written area of P12B and
             target P12C which functions as a control.   (b) shows the
             gain versus beam energy data and the best fit gain curves
             calculated from the collection probability in Figure (a).
             The solid circles are the data from P12C and the open
             circles from the unwritten area of P12B.   The triangles
             are the data from the written areas of P12B.   In (a)
             the calculated position of the He implant peak R_p and the
             standard deviation in the projection range ΔR_p are
             indicated.   The damaged region should coincide with the
             implanted region.   Note that the region of reduced collec-
             tion probability agrees well with the predicted region
             of damage generated by the He.

             (See pages 174 & 175)
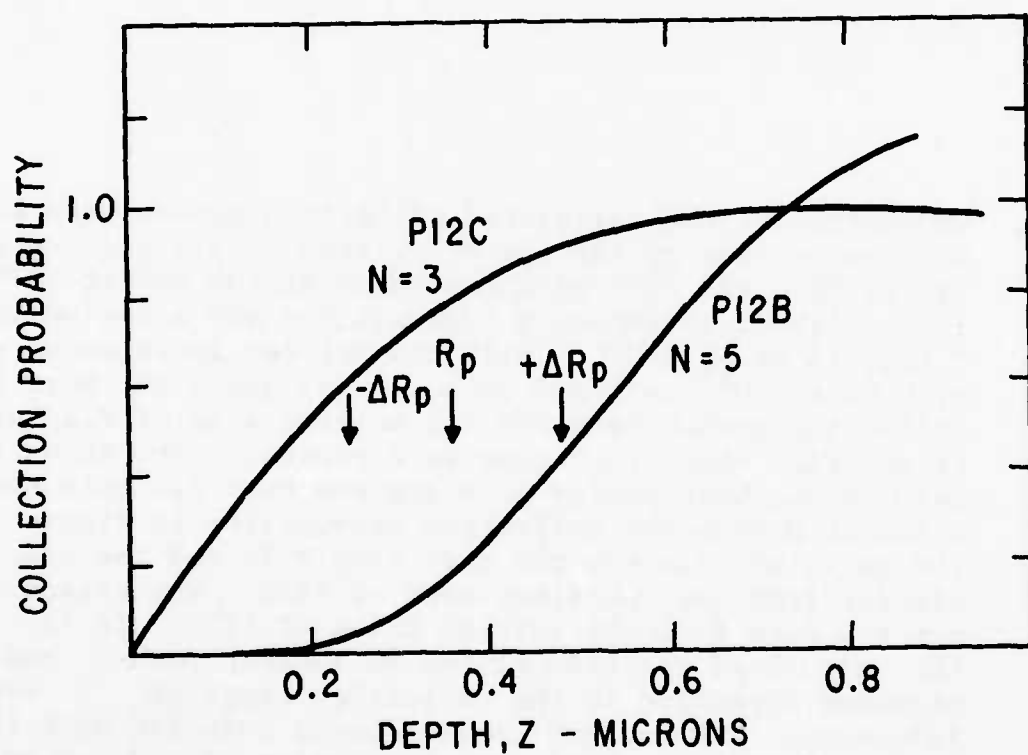
Figure 97a. Comparison of best fit collection probability for Samples P12C and He written sample P12B.
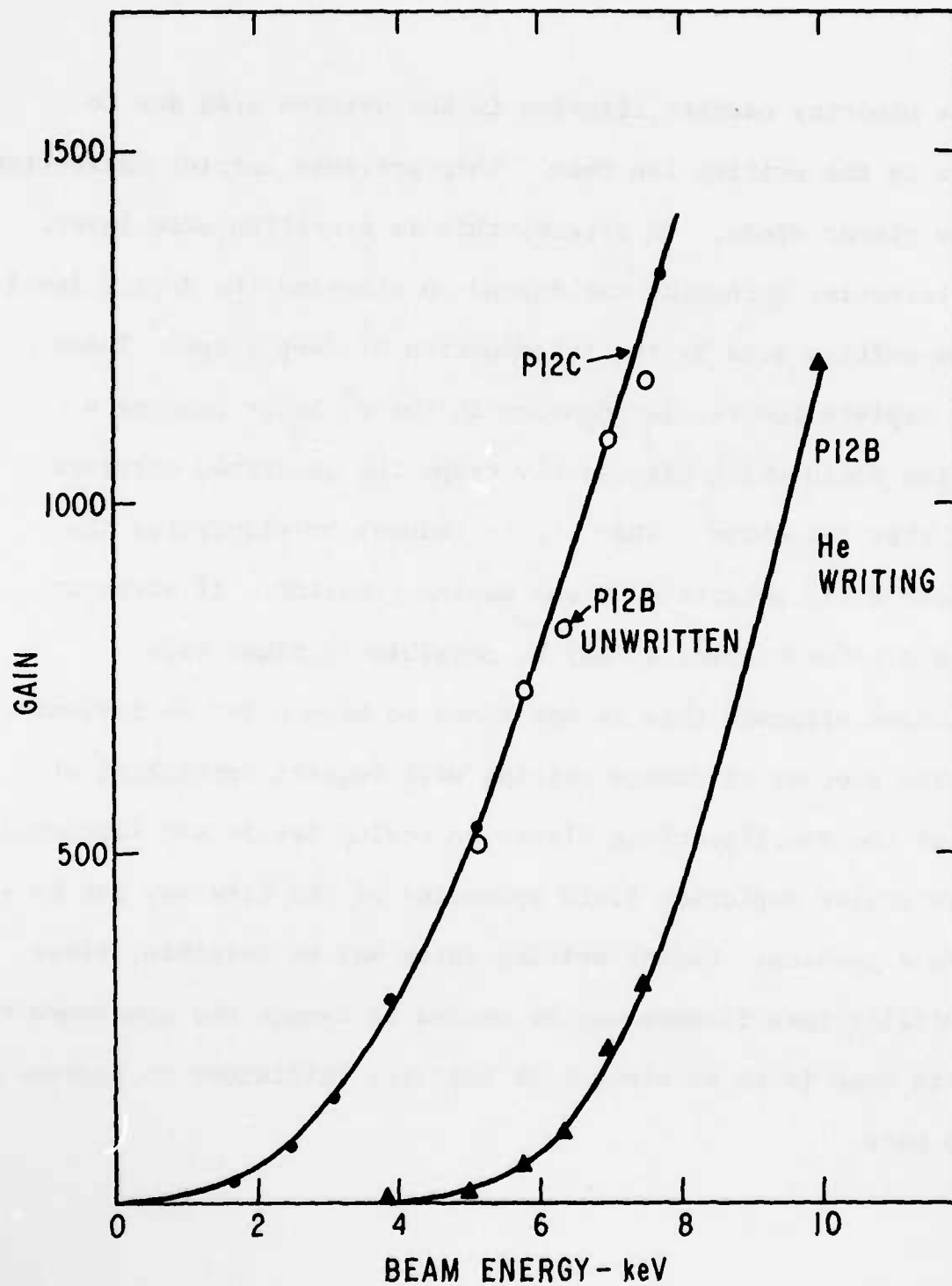
Figure 97b. Gain curves calculated from best fit collection
probability in Figure 97(a) and gain versus
energy data.

in the minority carrier lifetime in the written area due to damage by the writing ion beam. This prevents carrier collection by the planar diode. In effect, this is a written dead layer. An alternative mechanism may depend on altering the doping level of the written area by the introduction of deep traps. These traps deplete the carrier density in the n^+ layer causing a negative field which effectively traps the generated carriers until they recombine. That is, it reduces or eliminates the electric field generated by the doping gradient. If acceptor levels are introduced, it may be possible to cause type conversion although this is not known to happen for He implants.

The success of damage writing will require rethinking of some of the specifications placed on doping levels and fabrication. In particular depletion field spreading of the bits may not be as severe a problem. Higher writing rates may be possible, since potentially less fluence may be needed to damage the semiconductor than to dope it to an electrical activity sufficient to produce diode bits.

Future Plans: The writing effects of other ions, particularly
the inert gas ions will be explored, as well as the limitations
on writing fluence. Degradation mechanisms will also be explored
including readout fatigue of the stored patterns and room tem-
perature annealing of the damage writing. The doping levels in
the planar structure will be changed as well.

Section VI

ALLOY JUNCTION WRITING

Selection of Metal Semiconductor Systems for the Alloy Junction Target

An alloy junction target is shown in cross section in Figure 98. To write, an area is heated locally by an electron beam (or laser beam in evaluation tests) to cause local alloying of the metal-semiconductor. In the idealized concept, the heated region forms a pn junction. This can then be read by the electron beam because of its effect on the generated carriers. This section discusses the criteria for the choice of the best semiconductor metal combinations and identifies the most promising binary systems.

Alloy Junction Formation

Figure 99 shows the motion of carriers during readout of a written bit. When the beam impinges on the written area, there should be only a small readout signal (i_s) generated in the main pn junction circuit. For this to occur the carriers generated by the electron beam must either recombine in the local region where they are generated or not be generated at all. Local recombination can occur if the written area is actually a pn junction as shown in Figure 99a. In this embodiment electron-hole pairs are trapped by the diode depletion field until they recombine by some process, for example, recombination at an ohmic contact across the top of the structure. The ohmic contact or short could be a metal contact or just a heavily doped semiconductor layer.

-178-
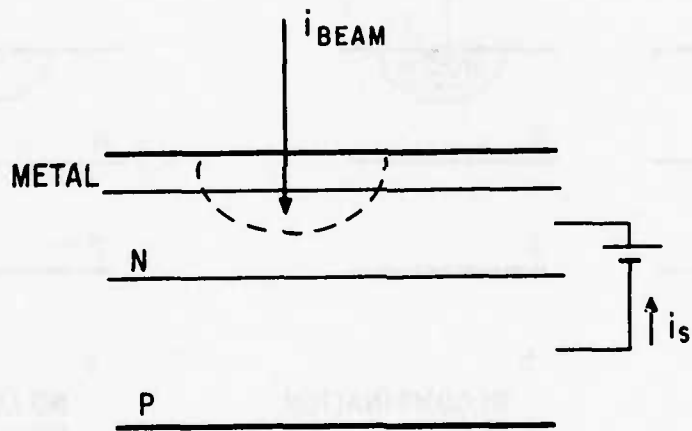
Figure 98. Alloy Junction Target
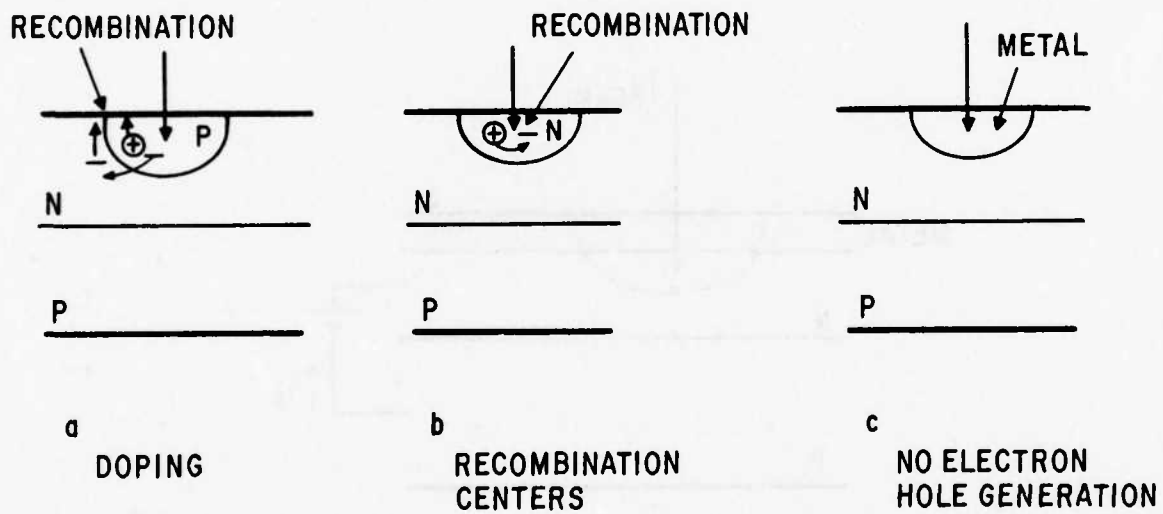
Figure 99.   Writing Methods

Another way to cause local recombination is to cause the written region to have a very short minority carrier lifetime (Figure 99b). This could be accomplished by damage to the lattice (introduced, for example, by the rapid regrowth of the semiconductor from the semiconductor-metal melt or by a heavy concentration of dissolved metal.

An alternative writing and readout method would depend on preventing electron-hole pair generation in the written region because the area is actually a metal or ⟨ metal with semiconductor crystallites imbedded (Figure 99c).

All of these writing methods depend upon the formation of a liquid metal-semiconductor melt. The solubility of the semiconductor in the melt must be large for good writing. Figure 100 shows the formation of the melt above some critical temperature T_E. The solubility by weight (w) of the semiconductor in the melt is:

$$w = \left(\frac{\rho_s t_s}{\rho_M t_M + \rho_s t_s} \right) \tag{41}$$

Where t_s is the thickness of the dissolved semiconductor, t_M the initial metal layer thickness and ρ_s and ρ_n the mass densities of the semiconductor and metal, respectively. Equation 41 can be solved for the ratio thickness of dissolved semiconductor

$$t_s/t_M = (\rho_M/\rho_s)(\frac{w}{1-w})$$

$$\tag{42}$$
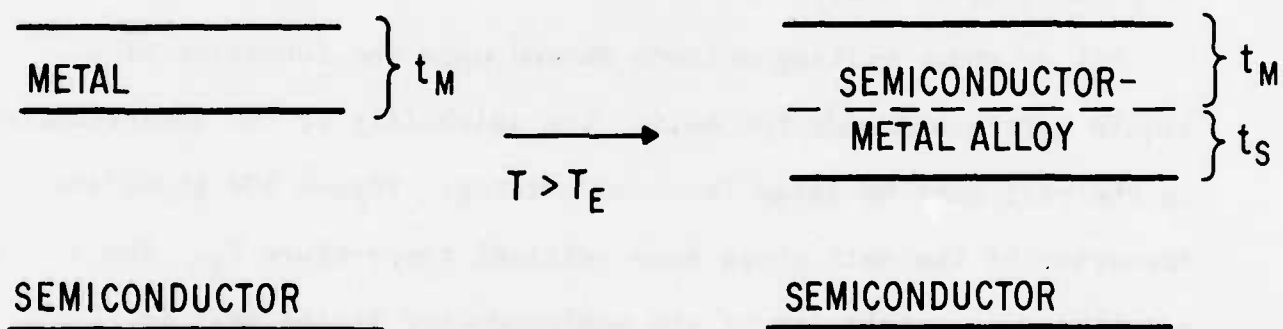
Figure 100. Calculation of Dissolved Semiconductor Layer Thickness

During cooling of the written region the melt will solidify leaving an affected region of depth t_s in the semiconductor.

During cooling any of the situations shown in Figure 99 could occur depending upon the material properties and cooling rates. However, for all three cases the thickness of the affected region t_s should be large to produce a large reduction in readout diode gain. (It is, of course, possible that none of the three situations occurs if the semiconductor regrows with very little damage or doping. This is unlikely, expecially because of the rapid cooling rates.) It is therefore important to choose metal-semiconductor pairs where t_s is large. Tables 5 and 6 summarize the properties of a large number of metal-Ge and metal-Si pairs. All of these pairs (except As which is not really a metal) have simple eutectic phase diagrams. As an example, the phase diagram for Al-Si is reproduced in Figure 101. All of the data in Tables 5 and 6 is taken from Hansen and its supplements (Refs. 15, 16, 17). This collection is believed to represent all of the eutectic pairs for Ge and Si with eutectic temperatures below 700°C. III-V and II-IV semiconductors might also be considered but these are less well characterized and are of course trinary systems which are more complicated. They need not be reviewed unless none of the Ge and Si systems are successful.

Note that only a few pairs have t_s/t_M greater than even 1%. For most pairs it is much less and was not even calculated. Based on the criteria of large t_s/t_M only 8 pairs are candidates: Al-Ge, Al-Si, Au-Ge, Au-Si, Ag-Ge, Ag-Si, Sb-Ge, and Zn-Ge.

-183-

Table 5

PROPERTIES OF METAL-SI PAIRS

	Eutectic Temp. T_E °C	Atomic % Si in Eutectic	Weight % Si in Eutectic = W_E	t_s/t_M	Solubility of Si in Metal at $T \gtrsim T_E$ Atomic %	Diffusion Coeff. of Metal in Si at $T = T_E - 50°C$ cm^2/sec
Si-Al	577	12.7	11.7	0.15	1.59%	10^{-20} (extrapolated)
Ga	29.8	2 x 10^{-8}				
In	156	~0				
Tl	no alloys					
As	not simple eutectic, compounds and eutectics formed at ~740 °C					
Sb	629	0.3				
Bi	271	10^{-8}				
Ag	840	10.6	3			
Au	370	31	6			3 x 10^{-10}
Sn	231.9	10^{-5}				10^{-13}
Pb	327	9 x 10^{-8}				
Cd	no alloys					
Zn	419	~0				

Table 6

PROPERTIES OF METAL-GE PAIRS

	Eutectic Temp. T_E °C	Atomic % Si in Eutectic	Weight % Si in Eutectic = W_E	t_s/t_M	Solubility of Ge in Metal at $T \lesssim T_E$ Atomic %	Diffusion Coeff. of Metal in Ge at $T = T_E - 50$ °C cm^2/sec
Ge-Al	424	30.3	53	0.57	2.5	10^{-20} (extrapolated)
Ga	29.8	5×10^{-3}				
In	157	0.5				
Tl	302	~0				
As	not simple eutectic, compounds and eutectics formed at $T \lesssim 730$°C					
Sb	590	17	11	0.15	2.5?	10^{-14}
Bi	271	~0				
Ag	651	25.9	19	0.46	9.6	$\sim 2 \times 10^{-12}$ (if like Au)
Au	356	27	12	0.49	3.2	3×10^{-19} (extrapolated)
Sn	232	~0				
Pb	327	~0				
Cd	320	0.2				
Zn	398	~5	~6		small	$\sim 10^{-20}$
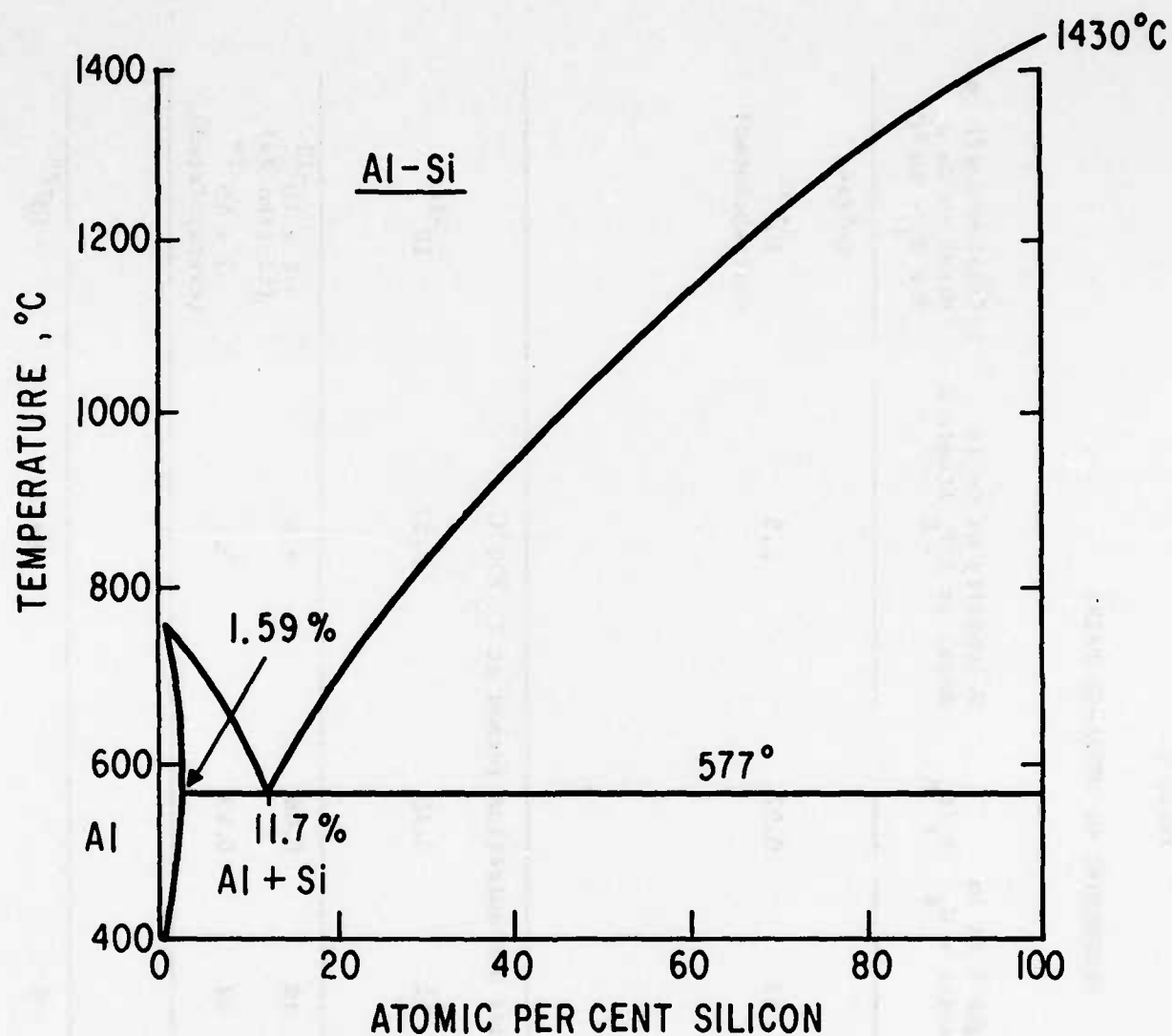
Figure 101.   Typical Eutectic Phase Diagram

Thermal bias of the target will probably be necessary because of the limited power of the electron beam and the high thermal conductivity of the semiconductors. Since a minimum of several hours is required to write a 10^{11} bit memory chip, the target will have to tolerate extended periods (hours or days) at a temperature tens of degrees below the eutectic temperature and probably several cycles between the thermal bias temperature and room temperature. Hence any pair where the diffusion or solid-phase reactions can occur is less attractive.

Diffusion

The diffusion constants $30^{\circ}C$ below the eutectic temperature are tabulated in Tables V and VI. In many cases these are very extended extrapolations of much higher temperature data and so may be grossly in error. In 10^4 seconds (2.8 hours) a diffusion constant of 10^{-16} cm^2/sec would result in a 100 Å diffusion depth. This could begin to cause some spontaneous writing so $D < 10^{-16}$ cm^2/sec is unattractive. Based on this criteria Ag-Ge, Ag-Si, and Sb-Ge can be clearly eliminated. The diffusion constants are fairly well known for these pairs because the eutectic temperatures are so high. The high temperatures these systems have also makes them less attractive. Au-Si would also appear to be ruled out. However, because the diffusion constant is not as well known at this temperature, it should not be completely eliminated.

Solid-Solid Reactions

Solid phase reactions are another potential problem. It is known

that Al-Ge and Al-Si (Refs. 18 - 23) films will dissolve and migrate at temperatures much below the reaction temperature until the solid solubility of the semiconductor in metal is reached. For Al-Ge[20], a 3000 Å Al film reacts completely in 20 min. at less than 300°C, even though the eutectic temperature is 424°C. For Al-Si the reaction is affected by impurities [21] and is aided by the presence of poly-crystalline [22] or amorphous silicon but the reaction does occur on single crystals.[22] For Sb-Ge[19] the reaction apparently does not occur after 1 hour at 280°C. The addition of an amorphous Ge layer inside the Sb layer causes the reaction to occur[19].

Solid-solid reactions are generally undesirable for this application. The solid solubility of semiconductor in the metal is generally low as shown in Tables V and VI. Upon cooling a doped semiconductor layer will regrow or the semiconductor may precipitate out in the metal. If the solid solubility is large, the regrown doped region can be large and produce an entirely written target. If the dissolution and regrowth are nonuniform, each cycle between room temperature and thermal bias temperature will cause greater nonuniformity and eventually permanent damage to the storage surface. Hence, it will be necessary to find methods to prevent solid-solid reactions or at least ensure that they occur uniformly. This points to the desirability of a diffusion barrier which breaks down or melts near the eutectic temperature of the metal-semiconductor pair. It will be necessary to study these solid-solid reactions since they are not well

characterized except for the Al systems. Since the solubility is low (<3%) for all the candidate systems, there is no reason to rule out any pair until more is known about the reactions. Solubilities $\lesssim 5\%$ should not prevent feasibility demonstrations.

Electron Beam Penetration

During readout, the electron beam must penetrate through the metallization. The metallization could be stripped before readout, but this is undesirable because verification of the written data would be impossible until the entire plate was written and stripped of metal. The beam energy can be increased to penetrate through the metal layer, but this will increase the lateral scattering of the beam in the semiconductor. This effect is sketched schematically in Figure 102. To a first approximation, the electron range and lateral scattering is proportional to the mass density for a given beam energy. If the beam has sufficient energy to penetrate into the semiconductor then the penetration and lateral scattering in the semiconductor will be approximately
$$t_p = R_s - \frac{\rho_M}{\rho_s} t_M \qquad (45)$$
as shown in Figure 102, where R_s is the electron range in the semi-conductor. This is only a reasonable approximation if $t_p/R_s \gtrsim 1$ (46) so that lateral scattering in the metal is negligible. To achieve a bit spacing B, the lateral scattering in the semiconductor must be less than B/2 so that:
$$R_s - (\rho_M/\rho_s) t_M = t_p \leq B/2 \qquad (47)$$
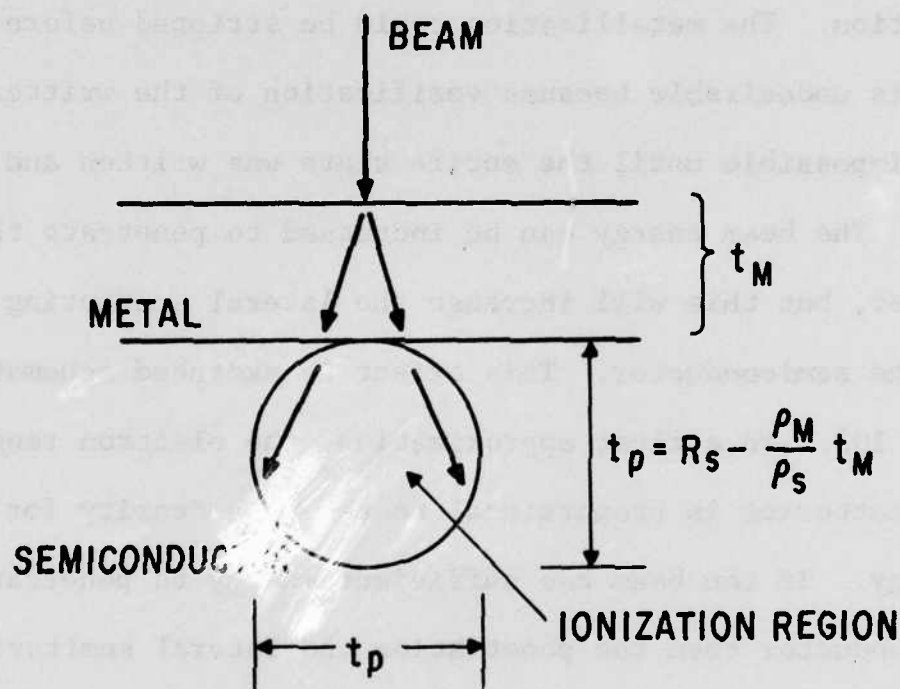
Figure 102. Electron Scattering

$$t_\rho = R_S - \frac{\rho_M}{\rho_S} t_M$$

To satisfy equation 46 and assure a significant amount, beam energy
is dissipated in the semiconductor. It is assumed that:

$$R_s = 2t_p \qquad (48)$$

Solving equations 42, 45, 47, and 48 for t_s yields:

$$t_s \leq B/_2 \left(\frac{w}{1-w}\right) \qquad (49)$$

Note that equation 49 is independent of the mass density of the
metal. The reason is that for the same solubility a thinner layer
of a dense metal can dissolve more semiconductor and compensate for
the thinner metal layer required to permit adequate beam penetration
into the semiconductor.

To assure a large modulation, t_s should be as a significant
fraction of the electron penetration into the semiconductor and must
also be larger than the dead layer thickness. For both of these
reasons $t_s \gtrsim 0.02$ microns is a reasonable requirement. Hence for a
bit spacing of 0.1 microns, equation 49 can be solved for the minimum
required solubility. This gives $w \geq 30\%$; this calculation is only
a rough approximation but it points to solid solubilities much less
than 10% as very undesirable. Based on this criteria the Al-Ge is by
far the most favorable with Au-Ge, Al-Si the next most favorable
choices, of the remaining uneliminated pairs.

Choice of the Most Favorable Pairs

Based on the above discussion the metal-semiconductor pairs
listed in Tables V and VI can be reduced to Al-Ge, Au-Ge and Al-Si

with Al-Ge by far the most attractive. Au-Si should be considered
if the diffusion constant of Au in Si is smaller than predicted. The
In-Ge system (Ref. 21, 22) does not look attractive. Sb-Ge is also
possible although the diffusion constant of Sb in Ge is too large
based on published data.

Alloy Junction Laser Diode Experiments

An established method for producing p-n diodes involves alloying
metal dopant material on an oppositely doped semiconductor. For
example heating of an indium (p-type dopant) on n-type germanium
forms a local alloy melt as the temperature reaches approximately
160°C, in which the proportion of indium to germanium exceeds the
solid solubility of indium in germanium (Figure 103). Upon cooling,
indium doped germanium regrows at the alloy-germanium interface by
a process similar to liquid epitaxy, resulting in a junction between
the p- and n-type germanium. Such junctions are often produced under
conditions that inhibit oxidation of the semiconductor and the alloy
during heating, such as a reducing atmosphere, so that oxide at the
interface does not hinder alloying.

This technique has been proposed as a writing method for the
surface diode archival memory concept to form the tiny p-n diodes
in the surface of a planar n-p junction structure as shown in Figure
104.

The writing method for producing alloy surface diodes is illus-
trated in Figure 105. In this process the surface of the n-p planar
structure is coated with a thin layer of the desired metal, and a

In PELLET ON n- Ge

In-Ge MELT FORMS DUE TO HEATING

p-Ge PRECIPITATE

p-Ge REGROWN REGION
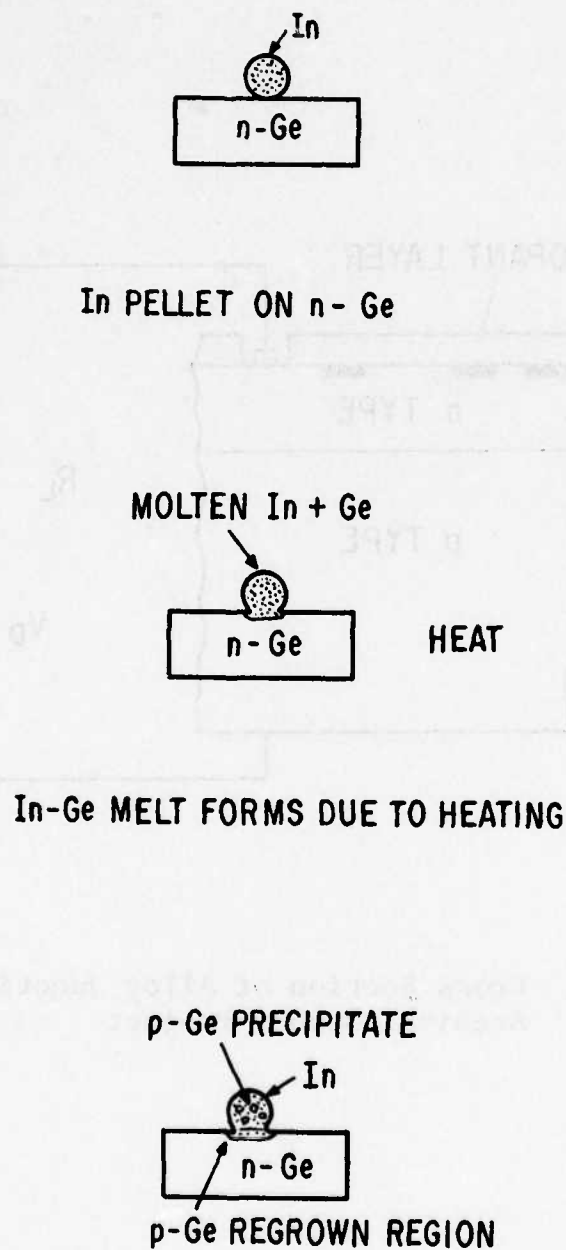
Figure 103. Formation of Alloy Junction with Indium on N-Type Germanium
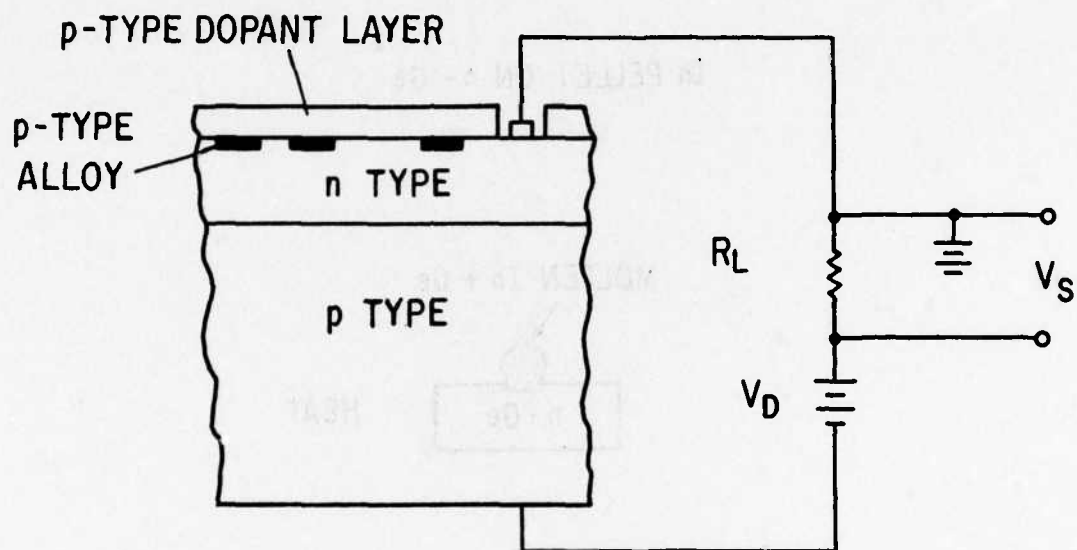
Figure 104.   Cross Section of Alloy Junction Diode
Archival Memory Project
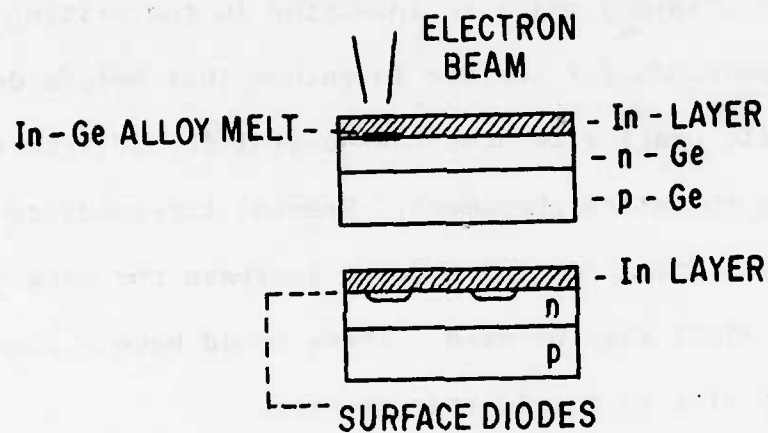
Figure 105. Focused Electron Beam Method for Formation of Alloy Junctions

focused electron beam is used to locally heat a bit region to the
temperature required for alloy action. The entire structure is
thermally biased to a temperature near the eutectic temperature,
so that less local heating by the electron beam would be required
for alloy formation, thus reducing the writing beam requirements.

The metal coated n-p diode blanks can be prepared using well
established processing techniques (e.g. ion implantation or diffusion
of an n or p layer) prior to insertion in the writing station. Clean-
ing the semiconductor surface in vacuum just before deposition of
the metallic coating reduces the possibility of interface oxidation
inhibiting the alloy phenomena. Special intermediate layers to
reduce oxide formation and thereby increase the rate of eutectic
formation might also be used. These would have a function similar
to that of flux in a soldering process.

A number of III-V dopant-semiconductor systems exist that might
be applicable to this alloy writing technique, for which the roles
of the n and p regions could be interchanged. The most promising
of these, due to their relatively low eutectic temperatures are:

System	Eutectic Temperature (^{o}C)
Indium-Geranium	156
Antimony-Germanium	590
Thallim-germanium	302
Aluminum-germanium	424
Aluminum-silicon	577
Antimony-silicon	630
Indium-silicon	156

Germanium systems have the advantages of a thermal diffusivity one-third that of silicon and surfaces less prone to oxidation.

To estimate the amount of beam current necessary to heat a local volume of the alloy junction target, the simplified model shown in Figure 106 is used. The beam energy is assumed to be completely dissipated within a hemisphere of radius a. Radius a is determined by the electron scattering in the material and by spot size b. A reasonable approximation to a is:

$$2a = b + R_G \qquad (50)$$

where R_G is the Grün range which is a measure of electron penetration into solids. Figure 107 shows the dependence of R_G on beam voltage for several materials of interest.

The solution of the heat diffusion equation for a uniformly heated hemisphere at the surface of a semiinfinite medium has been solved by Goldenberg. Figure 108 shows the temperature distribution in a target at various times as a function of radial distance r. Temperature and time are normalized as follows:

$$\Delta T_0 = 3P/4\pi Ka \qquad (51)$$

$$\tau = a^2/k \qquad (52)$$

where k = thermal diffusivity of the medium, K = thermal conductivity, and P = total thermal power into the hemisphere of radius a. The thermal parameters of silicon, germanium, aluminum, and indium are given in the Table VII. Note that the parameters for indium and

METAL

N – SEMICONDUCTOR

P – SEMICONDUCTOR
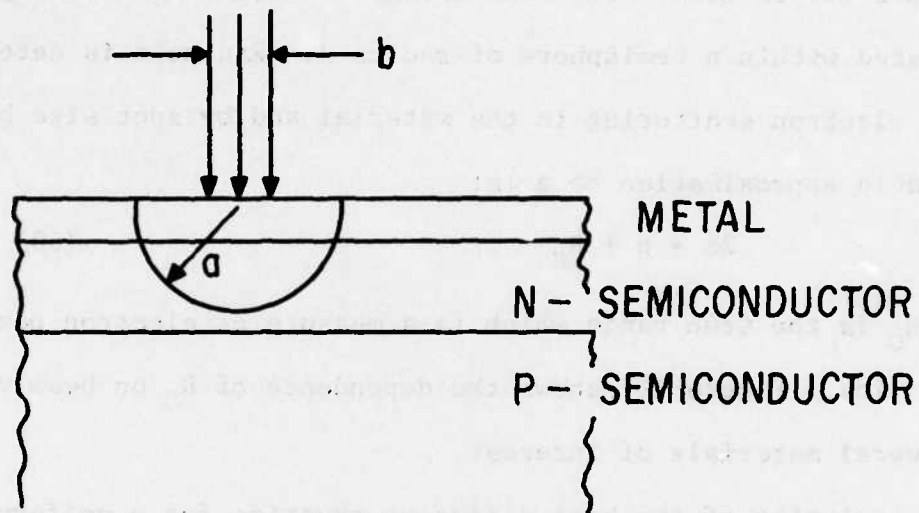
Figure 106. Thermal Writing Model for Alloy Junction Writing
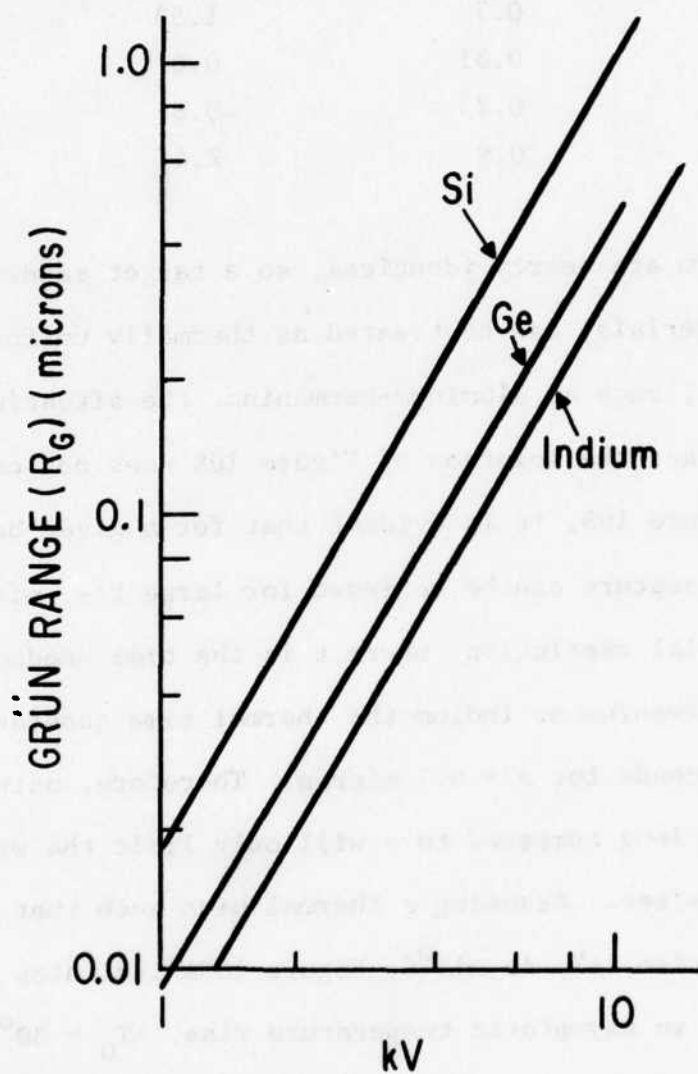
Figure 107. Dependence of Grün Range of Beam Voltage
for Several Materials

Table VII
THERMAL PARAMETERS

Element	Specific Heat (Cv j/g°C)	Thermal Condition (K(W/cm°C)	Thermal Diffusivity (K cm²/sec)
Silicon	0.7	1.53	0.9
Germanium	0.31	0.6	0.36
Indium	0.23	~0.8	0.29
Aluminum	0.9	2.4	0.38

and germanium are nearly identical, so a target sandwich constructed of these materials, can be treated as thermally uniform. For other combinations, such as aluminum-germanium, the situation is more complicated and the solution of Figure 108 does not exactly apply.

From Figure 108, it is evident that for a given beam power the highest temperature can be achieved for large t/τ, without very much loss in spatial resolution, where t is the time needed to write one bit. For germanium or indium the thermal time constant, τ, is 3×10^{-10} seconds for a = 0.1 micron. Therefore, using a beam dwell time that is long compared to τ will only limit the writing rate to <300 Mbits/sec. Assuming a thermal bias such that the desired temperature rise, ΔT, is >15°C, Figure 109a indicates the beam power required for an asymptotic temperature rise, $\Delta T_0 = 30°C$, at the center of the spot, as a function of hemisphere radius a. Bit spacing B as identified with hemisphere diameter 2a. The approximate size of the heated area will exceed the alloy temperature if the thermal bias is chosen $\Delta T_0/2$ below the alloy temperature (Figure 108).
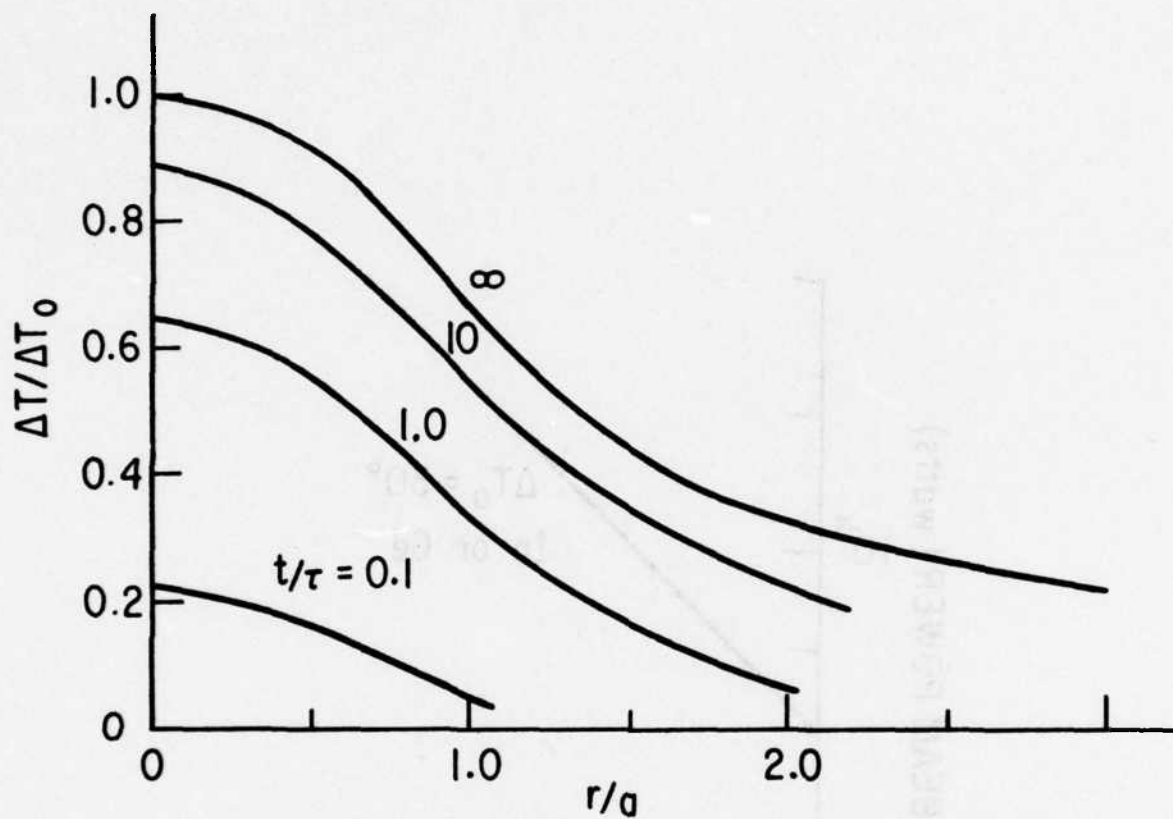
Figure 108. Normalized Temperature Distributions
at Various Times t
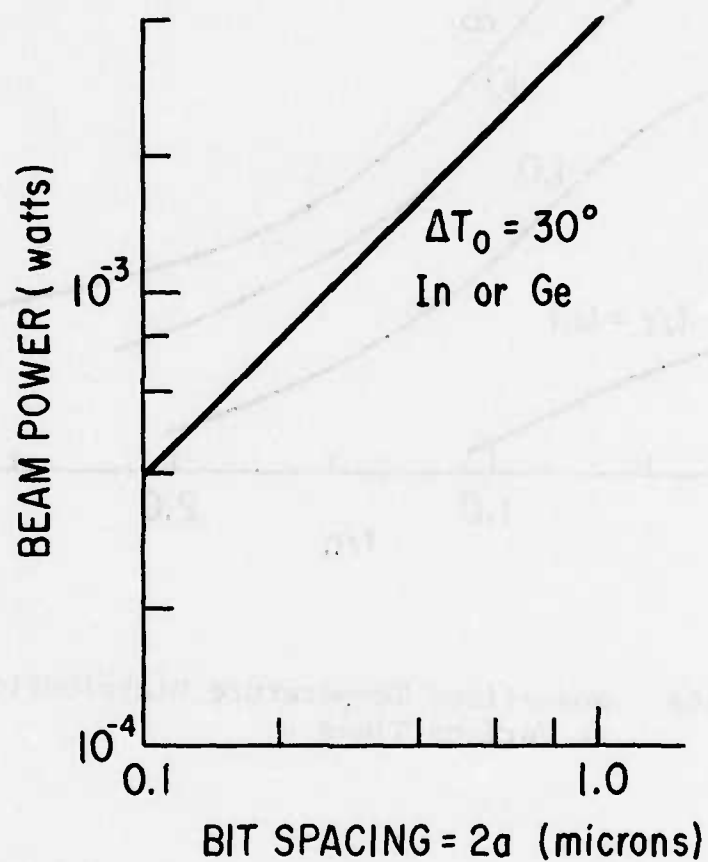
Figure 109a. Beam Power Required for Asymptotic Temperature Rise of 30°C Versus Bit Spacing for Germanium Alloy Diode Target
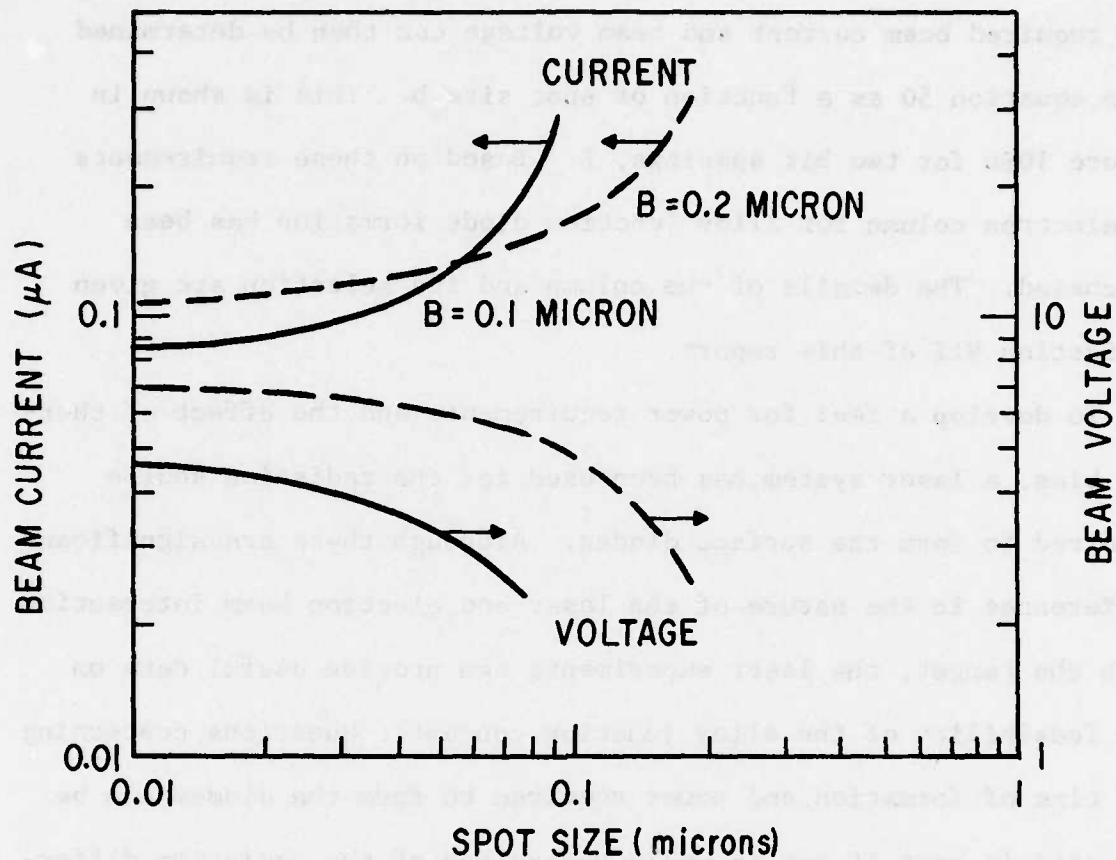
Figure 109b.   Predicted Beam Current and Beam Voltage
Requirements for Alloy Junction Writing on
Indium-Germanium Target at 0.1-micron and
0.2-micron Bit Spacing

The required beam current and beam voltage can then be determined from equation 50 as a function of spot size b. This is shown in Figure 109b for two bit spacings, B. Based on these requirements an electron column for alloy junction diode formation has been purchased. The details of the column and its selection are given in Section VII of this report.

To develop a feel for power requirements and the effect of thermal bias, a laser system has been used for the radiation source required to form the surface diodes. Although there are significant differences in the nature of the laser and electron beam interaction with the target, the laser experiments can provide useful data on the feasibility of the alloy junction concept. Questions concerning the time of formation and power required to form the diodes can be answered in part if not in whole regardless of the radiation differences. The details of the laser experiments performed thus far are discussed in the following paragraphs.

Laser System

The laser system used for the alloy junction experiments is an Electro Scientific Industries Model 25 laser trimmer. The system uses a continuously pumped Nd doped YAG laser with an acousto-optic Q-switch. It is capable of delivering at least 3.0 watts C.W. in the TEM_{00} mode and up to 30 watts C.W. multimode in Q-switched operation. The Q switch modulator itself is powered by a 50 Mhz. RF driver unit. The Q switch frequency or pulse repetition rate is continuously variable from 1 to 20 KHz with a typical pulse time of

150 ns. The laser can be apertured between the reflecting surfaces
to limit the higher order modes. These apertures also influence
the final spot size since the optics are diffraction limited. Various
optical configurations are possible:

- 2 lens system-condensor and
  objective $\approx$ .8 mil final spot;
  $\pm$10 mil depth of focus.

- 3 lens system-condensor, projector
  and objective $\approx$2-3 mil final spot;
  $\pm$30 mil depth of field

- 3 lens system-condensor and
  projector lens switched - final
  spot less than 1 mil.

For the alloy junction diode experiments   the optics des-
cribed last above were used exclusively. Final output power is a
function of lamp current, limiting aperture, optical chain and Q
switch frequency.

The system is equipped with a manually operated two-position
handler. Each position has vacuum hold down for securing chips up
to 2 1/4 by 2 1/4 inches in size. The two position handler allows
the operator to load or unload substrates while a second substrate
is being exposed to the laser in the other next. The handler has
positional repeatability of $\pm$0.001 inch.

The laser beam is positioned on the sample by mirrors and lenses
mounted on an X-Y table which is actuated by linear motors. In
moving over the substrate area the laser beam remains perpendicular

to the work surface resulting in no change in focus or beam energy.
Position of the laser beam can be either manual or under the process
control computer (Digital Equipment Corporation PDP8 series).

Targets

Alloy junction target blanks were fabricated from BEAMOS memory
planes. The basic BEAMOS target structure that was used is shown in
crossection in Figure 110. It consists of a p substrate with an
expitaxially grown n layer covered with an oxide and aluminum layer.
Typical parameters are:

> Al layer thickness
> Oxide thickness
> n epitaxi   ~2.0 um
> n layer resistivity .9 $_\Lambda$ - cm
> p layer resistivity 100 $_\Lambda$ - cm

The BEAMOS target structures were modified slightly. First, the
aluminum layers were removed with aluminum etch and the oxide strip-
ped with hydroflouric acid. The silicon target surfaces were then
plasma etched and sputter coated with a thin aluminum layer. These
last two steps were done sequentially under vacuum to prevent oxide
growth on the silicon surface. Targets with sputtered aluminum
layers of 500 Å, 1000 Å, and 2000 Å were fabricated. All tests to
date have been performed on the targets with 1000 Å layers.

Laser Writing Experiments

As a first step the laser experiments were aimed at determining
the operating conditions for diode formation. The process control
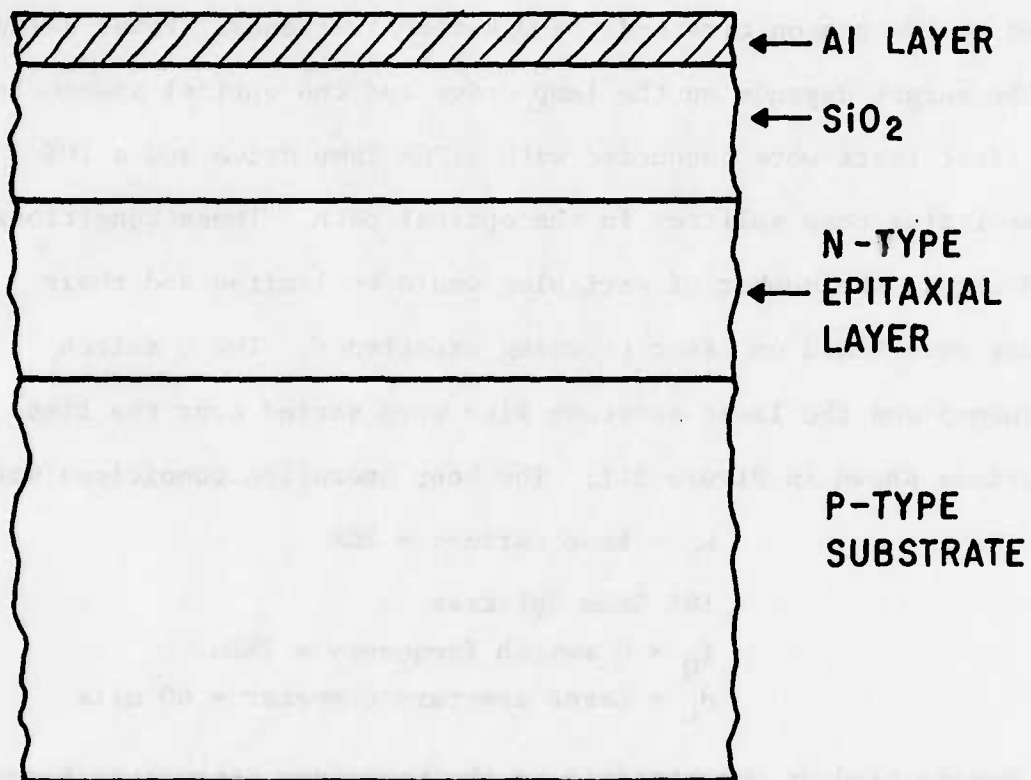
Figure 110. Cross Section of BEAMOS Target

computer was programmed to produce the test patterns shown in Figure 111. The laser is held stationary at each spot and gated on for the time duration indicated above each dot on the figure. Lamp drive current, Q switch frequency and laser apertures were manually changed variables. The number of pulses delivered to each spot is determined by the gate on time and the Q switch frequency. Power delivered to the target depends on the lamp drive and the optical aperturing. The first tests were conducted with a 20A lamp drive and a 10% transmitting beam splitter in the optical path. These conditions were set so the number of variables would be limited and their values were based on laser trimming experience. The Q switch frequency and the laser aperture size were varied over the time durations shown in Figure 111. The best operating conditions were:

$$L_L = \text{lamp current} = 20A$$

10% Beam Splitter

$$f_Q = \text{Q switch frequency} = 2kHz.$$

$$d_L = \text{Laser aperture diameter} = 60 \text{ mils}$$

Memory readout was obtained on the Cambridge Stereoscan Scanning Electron Microscope. The target planar diode signal was used for readout as shown in Figure 112. Memory readout from a laser irradiated spot before removal of the 1000 $\overset{o}{A}$ Al layer is shown in Figure 113. Figure 114 shows readout of the same area after the aluminum layer was etched off. These two figures verify the initial belief that readout could be achieved with or without removal of the

-208-

Figure 111. Laser Test Patterns showing Gate on Time
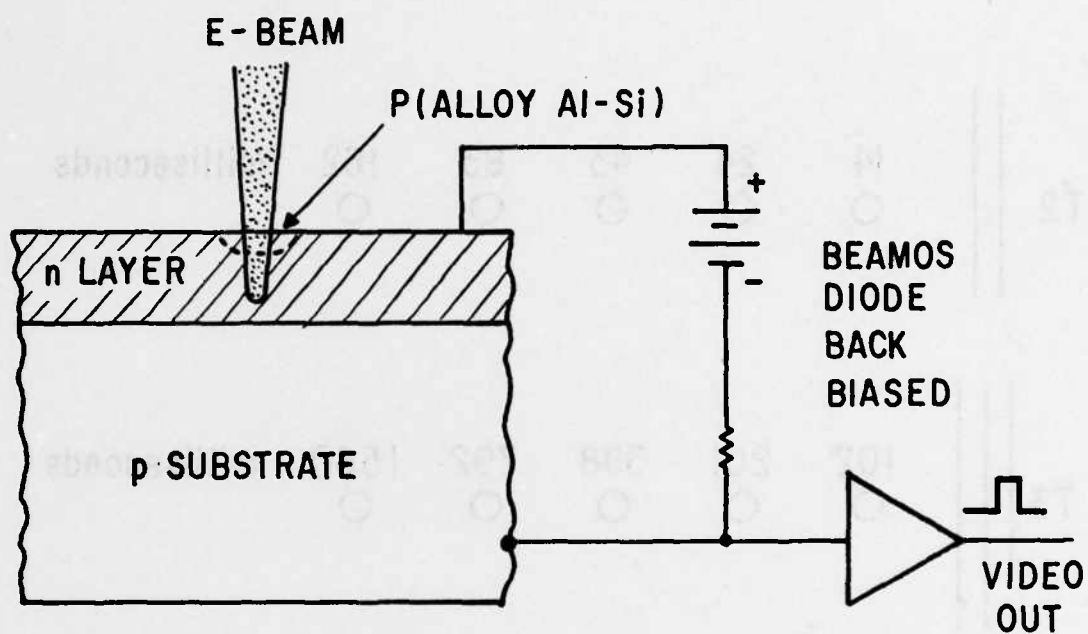
ALLOY JUNCTION TARGET READOUT

Figure 112. Readout Configuration

Figure 113.   Planar Diode Signal Showing Laser Alloyed
Region on Si Substrate Coated with 1000 Å Al.
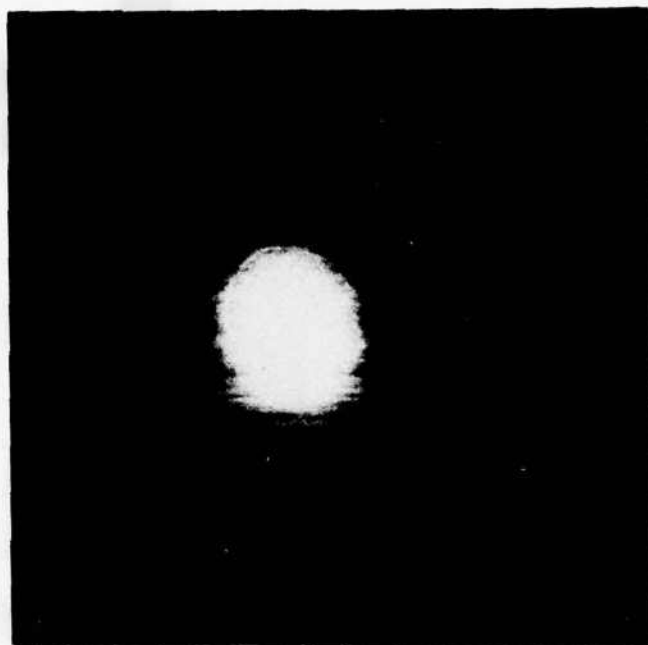
Figure 114. Planar Diode Signal Showing Laser Alloyed Region on Si Substrate After Removal of 1000 Å Al Layer.

aluminum layer. A secondary electron surface scan showing the top-

ography of this irradiated area is shown in Figure 115. The indented

crater with raised center as indicated by this figure seemed to be

characteristic of areas with good readout. The existence of aluminum

within the laser irradiated area was verified by scanning electron

microscope nondispersive x-ray analysis. The results of this analysis

within the irradiated area are shown in Figure 116. Here the marker

at 1.74 keV denotes the Silicon peak. At the lower value of 1.49

keV the much smaller aluminum peak is found. The same type of analy-

sis from the area just outside the irradiated spot is shown in Figure

117. As seen here only the marker at 1.49 keV remains indicating

the absence of aluminum outside of the irradiated area. Although

not conclusive proof the results from the diode read and x-ray analy-

sis give strong indications that an alloy junction surface diode was

formed. The actual crater area from which memory readout was obtained

was on the order of 15 um across. For this particular spot the laser

was gated on for 1.56 seconds corresponding to 3120 pulses at the

Q switch frequency of 2kHz. The memory readout and the video wave

form for two spots written with fewer pulses is shown in Figure 118.

Here the laser gate on time was 0.083 and 0.162 sec for the spot on

the left and right respectively. At the 2kHz. Q switch rate these

correspond to 166 and 324 pulses. The video waveform corresponds to

1.0 volt/cm and demonstrates good discrimination between written and

unwritten areas.
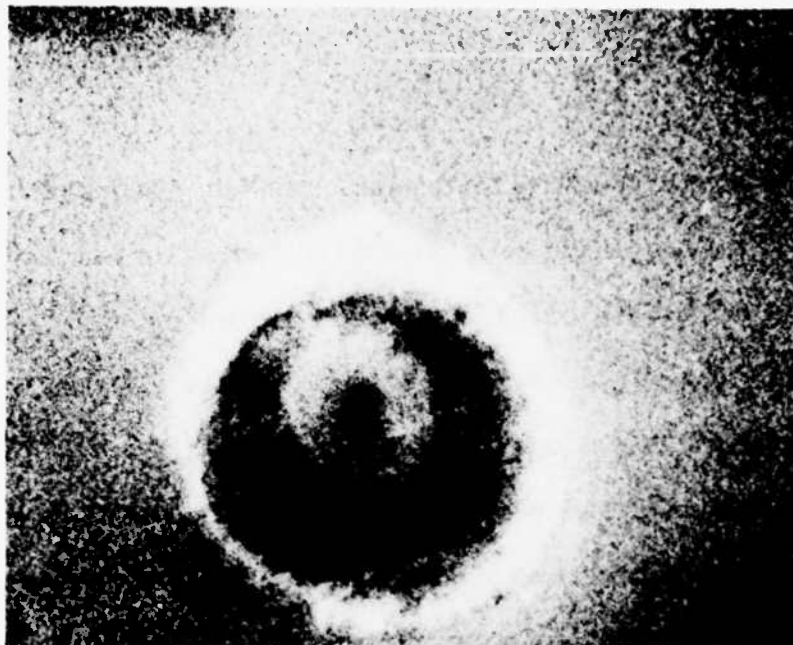
Figure 115.   Secondary Emission Scan of Laser Alloyed Region on Si Substrate after removal of 1000 Å layer.
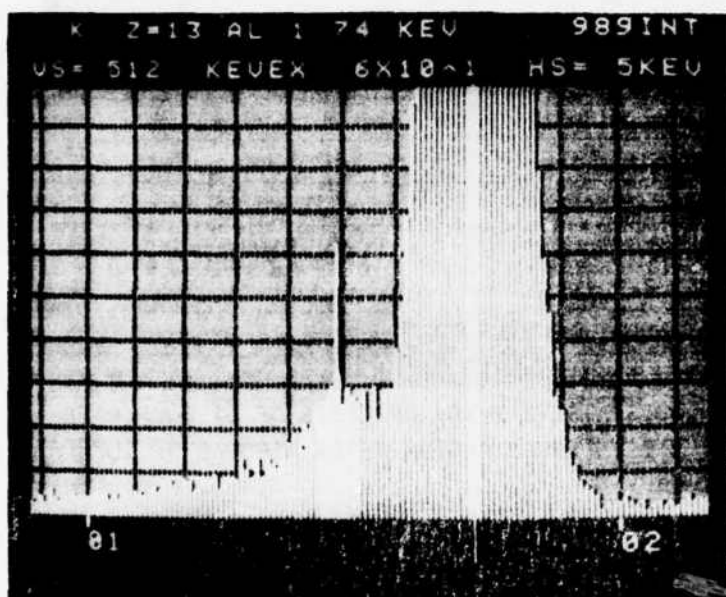
Figure 116. SEM Nondispersive X-Ray Analysis of Laser Alloyed
Region on Si Substrate after removal of 1000 Å
Al layer.
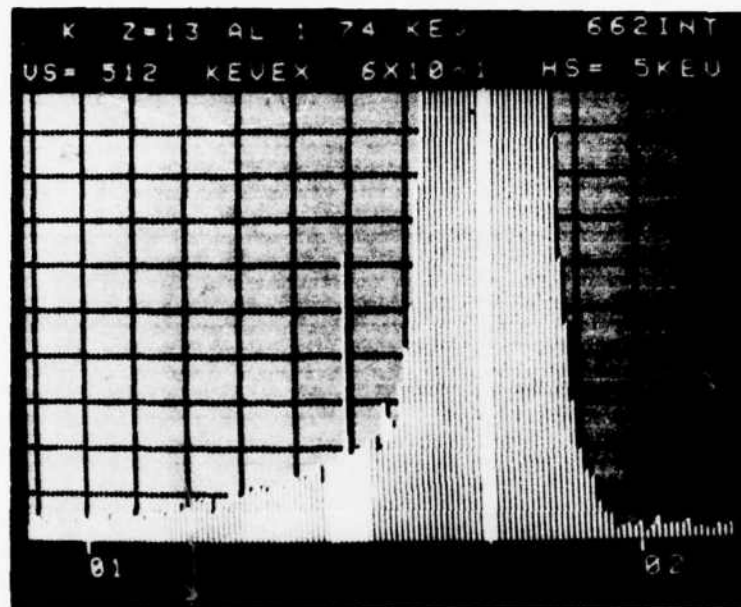
SEM NONDISPERSIVE X-RAY ANALYSIS OF Si SUBSTRATE
NEAR LASER ALLOYED REGION AFTER REMOVAL OF 1000 Å
AL LAYER

Figure 117. SEM Nondispersive X-Ray Analysis of Si Substrate
near Laser Alloyed Region after removal of 1000 Å
Al layer.
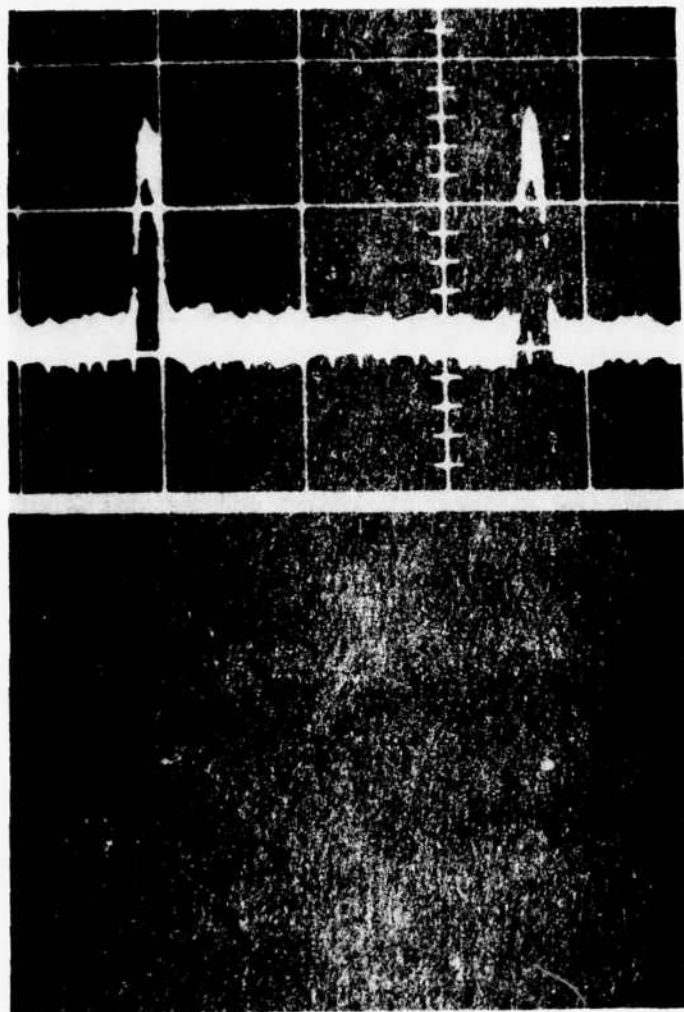
Figure 118. Video Waveform and Planar Diode Signal from two adjacent Laser Alloyed Regions.

One of the purposes of the laser experiments was to demonstrate that alloy diodes could be formed on a short time scale (i.e. 10 MHz writing rate). The preceeding experiments did not do this because of the large number of pulses involved. However, the model used for the alloy junction formation in the introduction to this section indicates that the diodes should form in one pulse if they form at all. Hope is added to this concept due to the fact that diode read-out was just as good from an area irradiated with 166 pulses as one irradiated with 3120 pulses. Therefore, the next experiments were dedicated to reducing the number of laser pulses per spot with the final goal of writing with one pulse.

As a starting point for this goal the process control computer was reprogrammed to write an NxN array. The size of the array, in terms of spot to spot center distance and number of spot N as well as the laser "gate on" time per pulse were programmable inputs. A new laser operating mode was sought using the 40 mil aperture so that the spot size would be smaller. With this aperture it was found that diodes were formed with a lamp drive current of 18 A and a Q switch frequency of 2kHz. The 10% transmissive beam splitter was also removed from the optical system.

Planar diode readout of a 10^4 spot array formed with these oper-ating conditions and 10 pulses per spot is shown in Figure 119. Considerable variability from point to point and even the absence of readout at some points can be seen. A magnified scan of part of
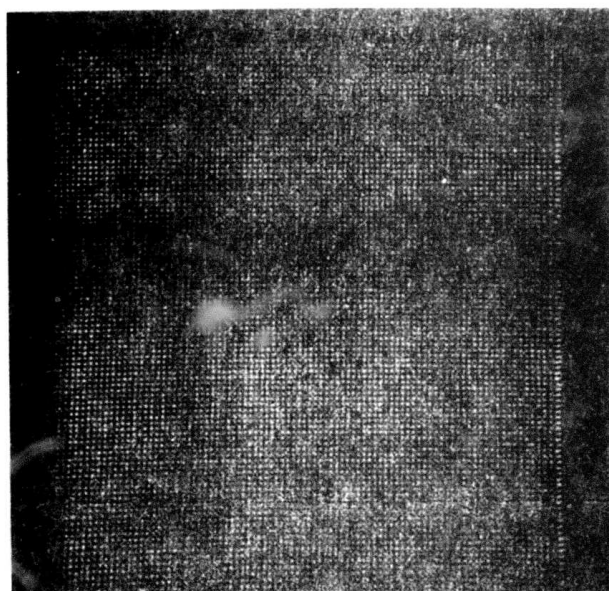
Figure 119. Diode Current Signal - 10^4 Spot Array - SEM Readout 50X - Laser Irradiated - 10 pulses per spot - 1000 Å Al on Si.

this array showing a missing location and the variability from point to point more clearly is given in Figure 120. A secondary emission surface scan of this same area is shown in Figure 121. With this figure the variability in the diode signal can be linked directly to surface nature variations of the irradiated spots. Note that at the missing signal location there was apparently no laser pulse as the surface scan shows no radiation damage. All of these variations are attributed to variations in the laser output due to a poorly regulated power supply and an aging lamp. More will be said about this when the laser power measurements are discussed.

Figure 122 shows the planar diode signal of a portion of this array at still higher SEM magnification. The spots are on 20 μm centers indicating an irradicated spot size which is typically 10 μm in diameter. The secondary emission surface scan of the same 3 x 3 spots is shown in Figure 123. At this magnification the granularity of the sputtered aluminum layer is clearly visible in this figure. This same granularity shows up but at a lesser degree, in the planar surface diode output of Figure 122. The reason for this is that the beam is stopped at some points and therefore no electron hole pairs are generated and hence no diode signal. As far as planar diode signal this result is the same as at an irradiated spot where the excess minority carriers experience enhanced recombination. Finally a video waveform, or the actual planar diode current for the center three spots of this portion of the array is shown in Figure 124.
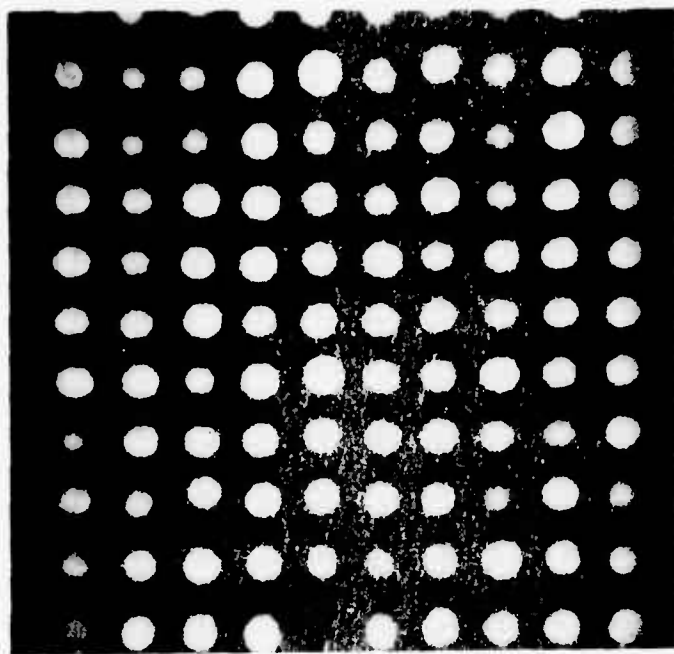
Figure 120. Diode Current Signal from 10^4 Spot Array - SEM
Readout 500X - Laser Irradiated - 10 pulses per
spot - 100 Å Al on Si.
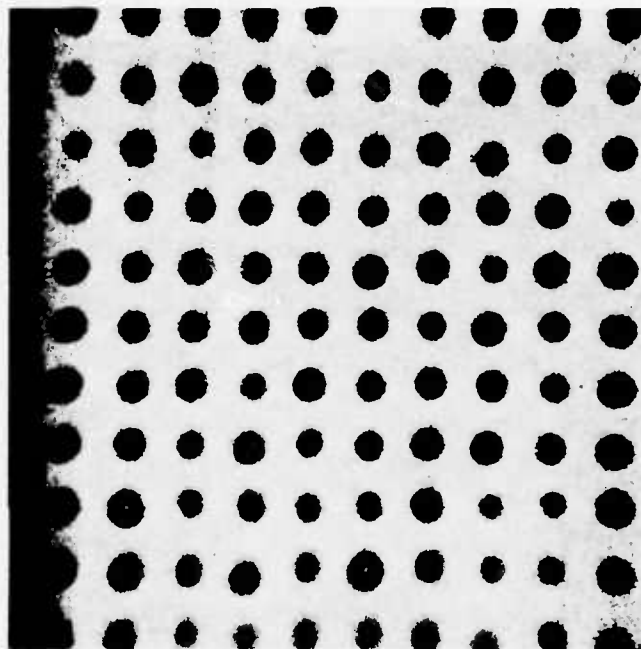
Figure 121. Secondary Emission Surface Scan from 10^4 Spot
Array - SEM Readout 500X - Laser Irradiated -
10 Pulses per Spot - 1000 Å Al on Si.
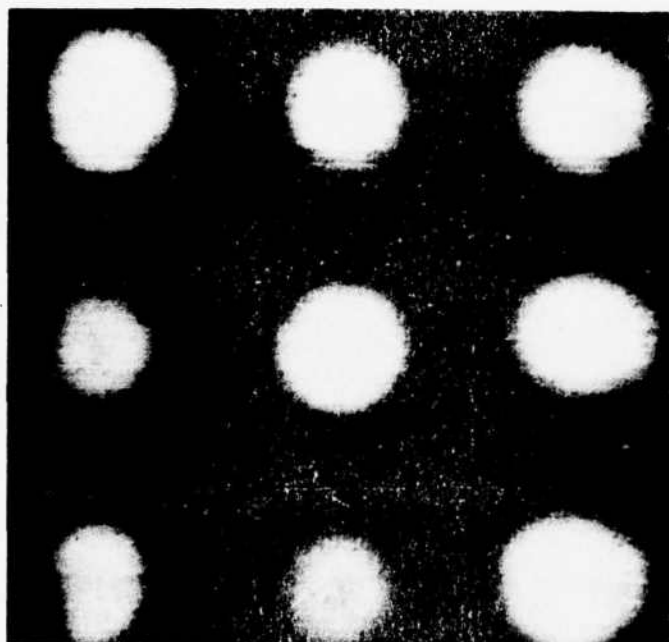
Figure 122. Diode Current Signal of 3 x 3 Laser Irradiated
Spots from 10^4 Spot Array - SEM Readout 2000 X
- Laser Irradiated - 10 Pulses per Spot - 1000 Å
Al on Si.
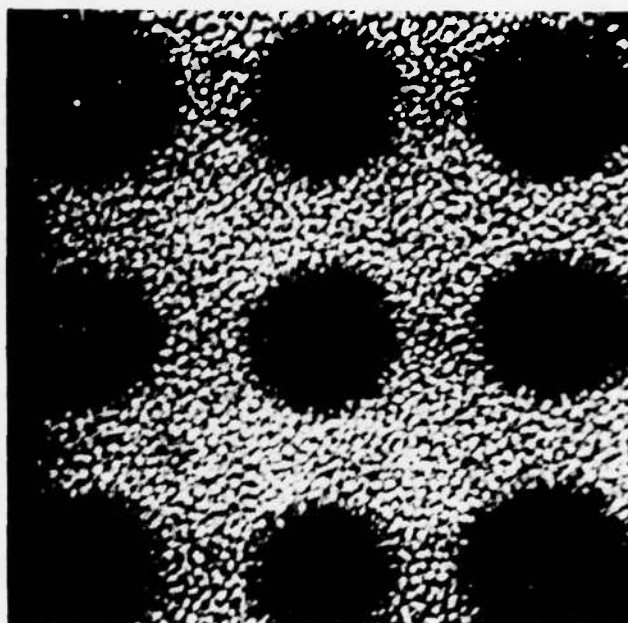
Figure 123.   Secondary Emission Surface Scan of 3 x 3 Spots
from 10^4 Spot Array - SEM Readout 2000X - Laser
Irradiated - 10 Pulses per Spot - 1000 Å Al on Si.
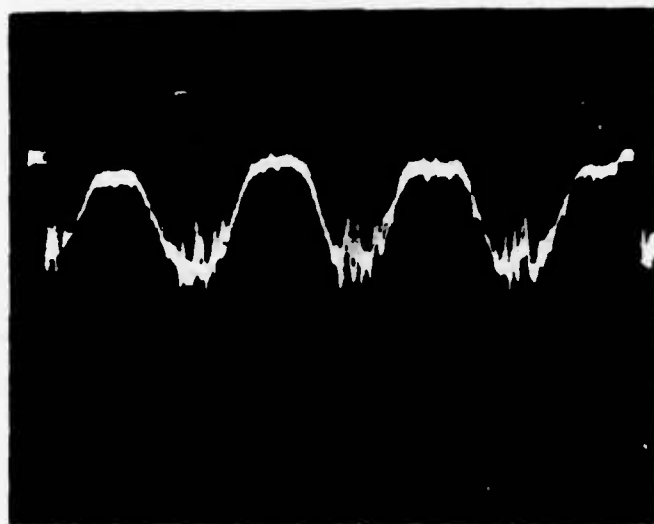
Figure 124. Video Waveform from 3 Adjacent Alloy Junction Diodes -
Laser Irradiated - 10 Pulses per Spot - 1000 Å Al on
Si.

The noise between diode signals if just the result of the granularity of the sputtered aluminum in this presentation.

The 10 pulses per spot shown in the preceeding figures was the minimum number of pulses that could be programmed. The next step was to try single pulses and therefore a program change had to be made. The process control computer was reprogrammed so that the table moved with a constant velocity. Based on the 10 um spot size, as long as the table velocity was greater than 20 mm/sec, single pulses at a 2kHz rep rate would be resolved. Figure 125 shows readout through the planar diode of three successive single pulse irradiated areas. The laser operating conditions were the same as the preceeding experiment; i.e. 40 mil aperture, 18 A lamp current, 2kHz rep rate and the table velocity was 50 mm/sec. The irradiated spots are on 25 um centers and have a typical diameter of 7.5 um. The difference in spot size between these and the 10 pulse per spot results is attributed to the changing surface conditions and increased damage effects due to multi pulses. The planar diode current signal or video waveform from a scan through the three pulses is shown in Figure 126.

Laser Power Measurements

The beam power delivered to the target in the model 25 system was measured for various operating conditions. This data is needed in order to obtain a calibration on the temperature rise achieved in the preceeding experiments as well as for future experiments. Of course the full power delivered to the target is not utilized and

-226-
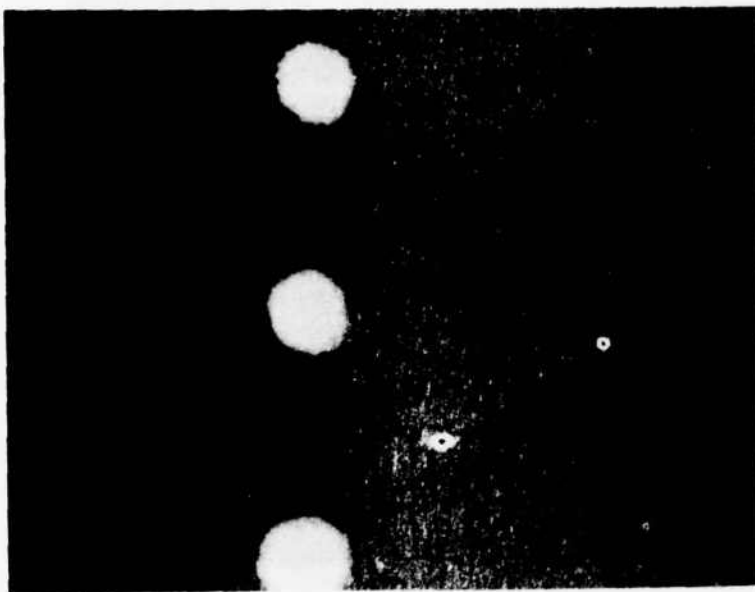
Figure 125. Readout Through Planar Diode of Three Single Pulse
Irradiated Areas.
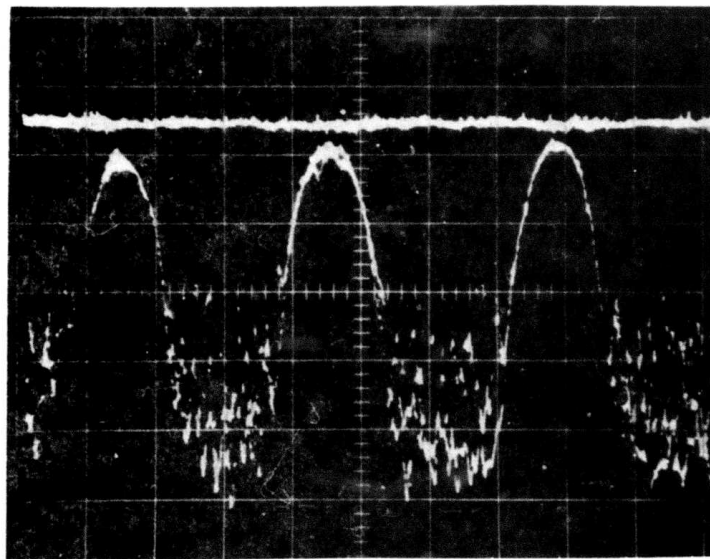
Figure 126.   Waveform Scan Through Three Irradiated Areas.

must be modified by the reflectance of the surface. The reflectance data is still under investigation. At present we have determined the power delivered to the target as a function of the laser system parameters.

Average power was measured at the target plane with a Coherent Radiation model 205 power meter. The model 205 consists of a direct absorption, convection-cooled head and a control-indicator unit. The instrument is specified for CW laser measurements covering the broad wavelength range of .3 to 30 microns. A relative measure of peak pulse power was obtained from a photo diode that looks at the laser beam in the model 25 laser system. The signal from this photo diode was displayed on a high speed Tektronix storage scope, model-7633, and photographically recorded.

Power measurements were made for the full range of lamp drive currents with aperture diameters of 40 and 60 mils at 2kHz Q switch frequency. Power versus Q switch frequency was also measured at 18 A lamp drive and with a 60 mil aperture. The peak power per pulse was obtained from graphical integration of the normalized to unity photo diode signal as:

$$P_{peak} = \frac{P_{AV} \, \Upsilon_c}{\int f(t)dt} \tag{53}$$

where P_{AV} = average power

Υ_c = Q switch cycle time

$f(t)$ = normalized photo diode signal.

The average and peak powers at the target plane as a function of lamp current at 2kHz are shown in Figure 127. Curves showing the peak and average power as a function of Q switch frequency are shown in Figure 128. The data used in plotting these curves is also summarized in Table VIII.

TABLE 8

POWER SUMMARY ND:YAG LASER

Lamp Current amps	Q switch freq - kHz	Average Power - watts	Peak Power kilowatts	Laser Aperture
12	2	.24	.53	60
14	"	.43	1.175	"
16	"	.55	1.52	"
18	"	.70	1.95	"
18	4	1.03	1.20	"
18	6	1.17	.887	"
18	8	1.25	.627	"
18	10	1.36	.468	"
20	2	.83	2.38	"
22	"	.96	2.99	"
18.	"	.02	.034	40
18.5	"	.04	.097	"
20	"	.09	.308	"
22	"	.20	.966	"

The photo diode output pulse used to obtain the peak power is shown for the two operating conditions used in the laser diode experiments in Figure 129 a and b. Considerable variation in the output waveform and hence the output power is noticeable at both operating

-230-
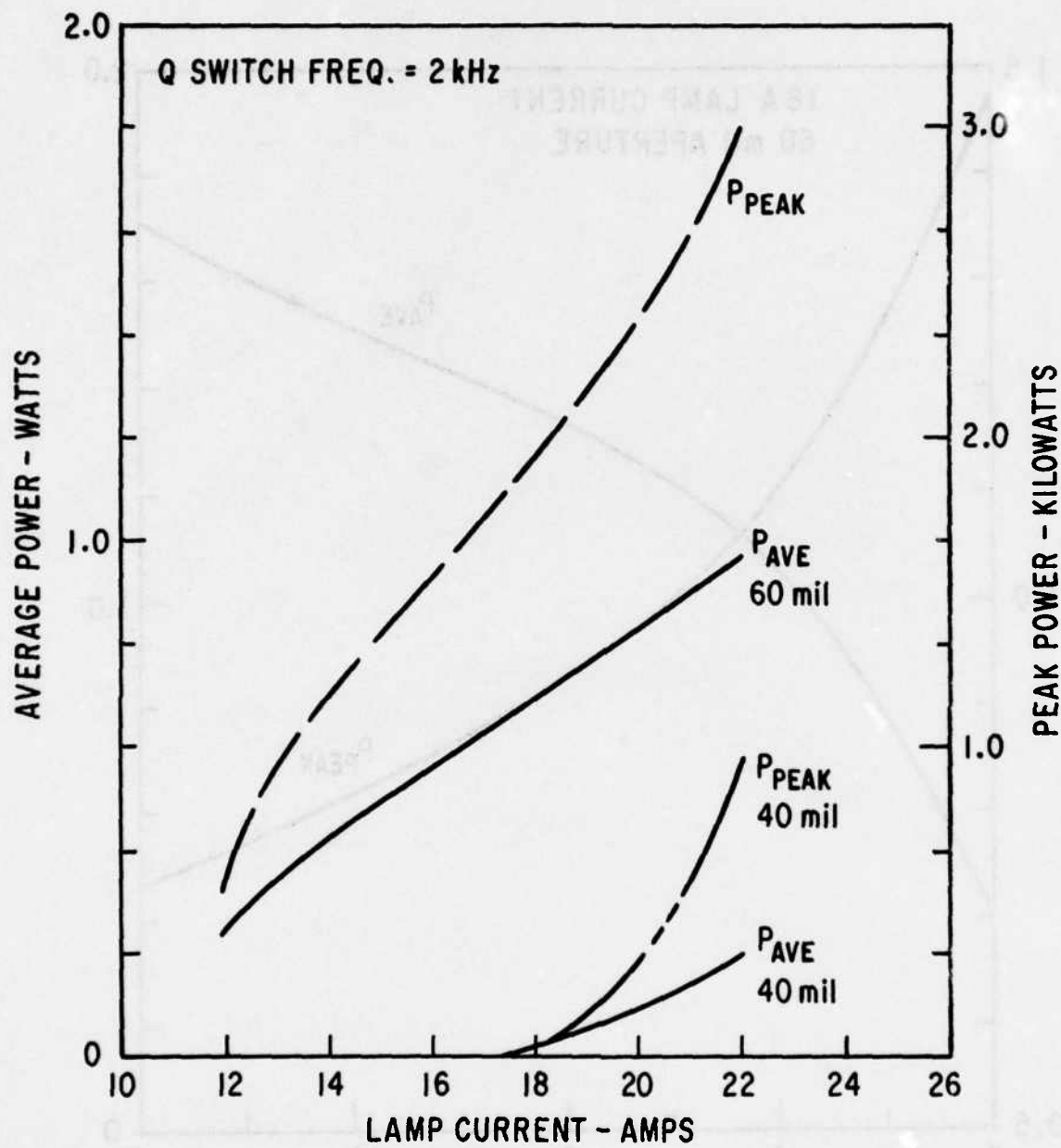
Figure 127.   Laser Power as a Function of Lamp Current
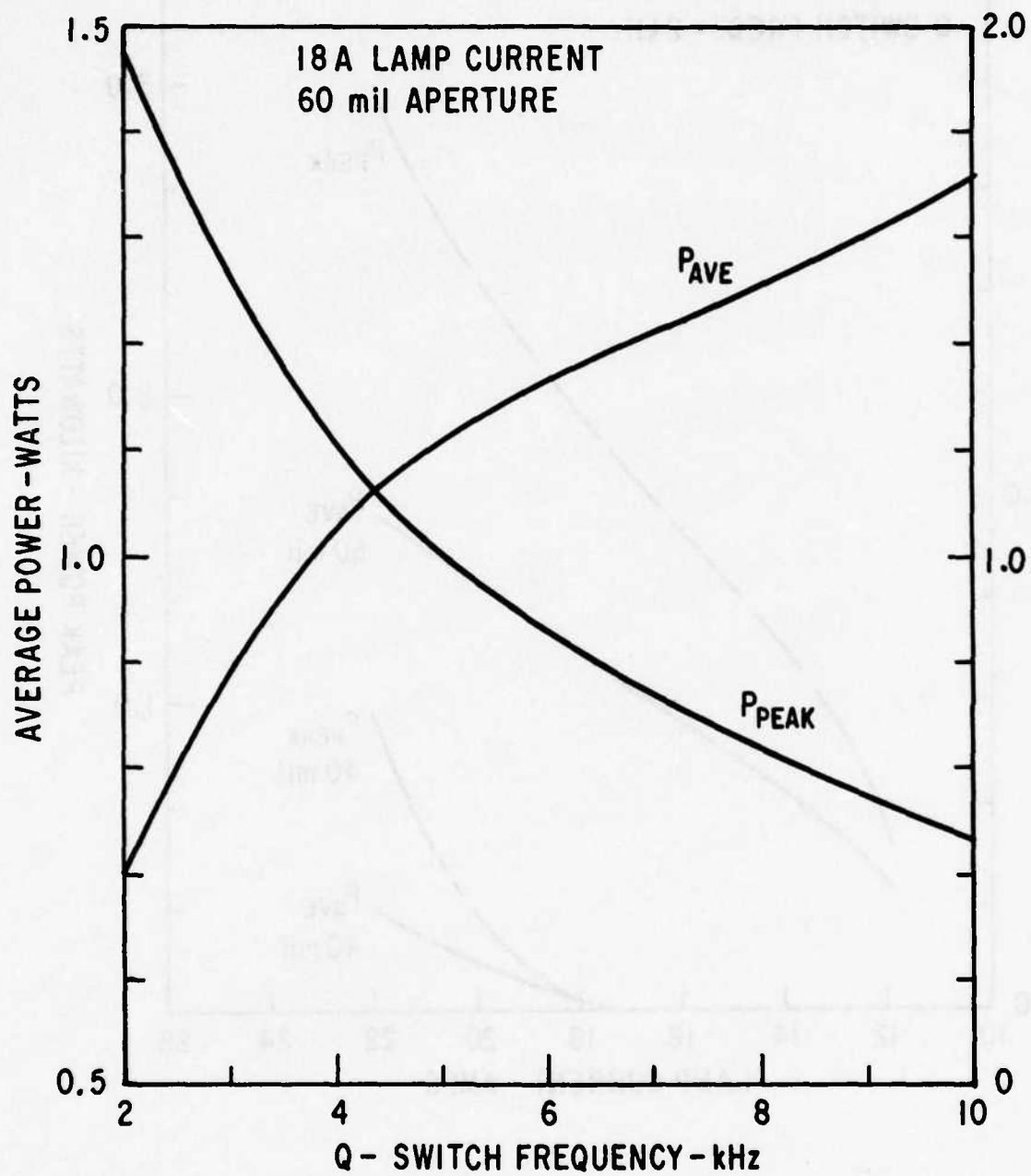
Figure 128. Laser Power as a Function of Q Switch Frequency
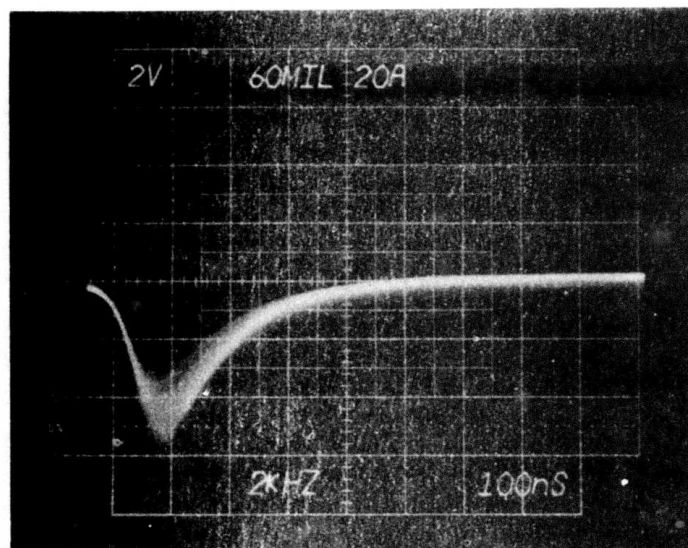
Figure 129a. Photo diode signal - 20 A Lamp drive 60 mil aperture 2kHz.
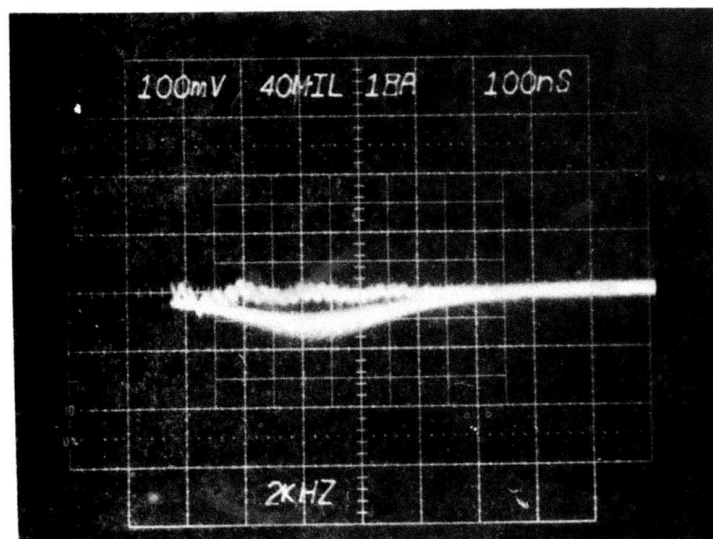
Figure 129b. Photo diode signal - 18 A Lamp drive 40 mil aperture 2kHz.

points. This power variation is believed to be the cause of the laser

spot variation noted previously in the discussion of the 10^4 array

experiments.

This power data will be used in the near future to get a feel

for the temperature rise required for diode formation. Before this

can be done the reflectance of the sputtered Al film must be known.

However, the power density per pulse delivered to the target can be

determined from the present data. Diodes were formed with 20 A lamp

current and a 60 mil aperture at 2kHz. With this system a 10% beam

splitter was also used. Power was measured with and without the

beam splitter and the actual transmission was found to be 6.67%.

Therefore using this value and the peak power of 2383.35 watts and

a typical irradiated spot size of 15 µm the calculated power density

per pulse is 8.99×10^7 watts/cm^2. The 40 mil aperture 18 A lamp

current operating conditions did not use a beam splitter in the optical

path. Therefore, with a peak power of 33.87 watts and a typical diode

size of 7.5 µm the calculated power density per pulse is 7.67×10^7

watts/cm^2. The power densities used to form the diodes under different

operating conditions are therefore in reasonably good agreement.

Lap Stain of Written Junctions

In order to further investigate the diodes, or damaged areas,

formed by the laser, a sample target was angle lapped and stained.

Figure 130 shows a photomicrograph of the lapped section. This photo-

graph reveals that the aluminum dissolved in the silicon (or vice
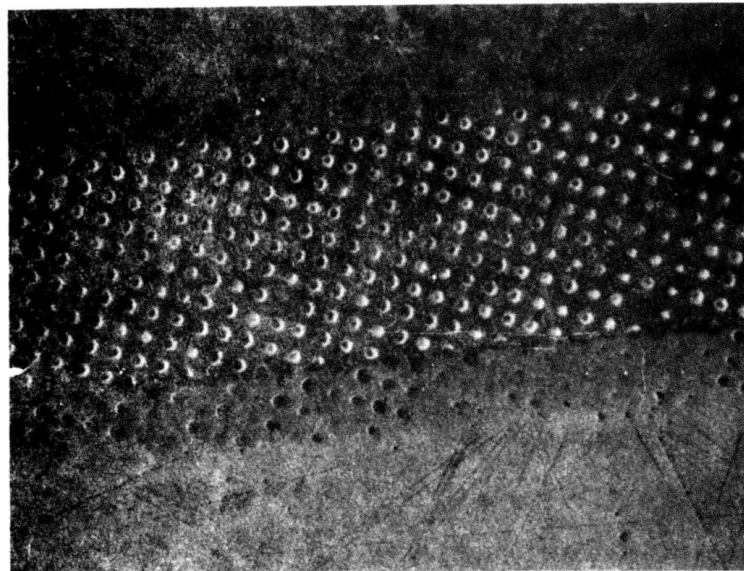
Figure 130   Angle Lapped (5°40') and Stained
              Section of a Prototype Archival
              Memory on a BEAMOS Substrate.
              Pattern is 10μm Spots on 20μm
              Centers.

versa) and that the bit pattern went to a depth of 5 to 6 microns. It also shows that the "write-in" was nonuniform across the wafer. This method investigation probably will not be adequate for junctions of 0.2 micron depth.

Section VII

ALLOY JUNCTION EXPERIMENTAL
WRITE COLUMN

Introduction

Alloy junction surface diodes are formed by locally heating
two suitable materials. As described in Section VI, junctions of
this type have been produced using an imaged laser beam. The laser
is capable of delivering far more energy than necessary to form the
diodes. For a memory system, however, it is more desirable to
use an electron beam for writing, since it can be deflected more
easily over the desired field of view. Additionally, an electron
beam will be used to read-out the stored information. Part of this
phase of the advanced Archival Memory Contract will determine if an
electron beam system can be structured with the beam characteristics
necessary for alloy-junction writing. As part of these studies, and
as an aide in determining the beam requirements, an electron beam
writing column will be set-up and experimental studies conducted.

Unfortunately, the analysis to determine the optimum configur-
ation for such a column is dependent in large measure on the stor-
age target studies. The laser beam experiments will be helpful
in determining power levels, but the manner in which the beam energy
heats the localized areas will be different when an electron beam
is employed. For this reason, an electron beam system, that will
come as close as possible to meeting the theoretical and analytical

-238-

estimates available at this time, will be assembled and electron

beam studies conducted. The method of selection and specification

of such a column will be discussed in the following paragraphs.

Column Specifications

The amount of beam current necessary to heat a local volume

of the alloy junction target was estimated for the advanced Archival

Memory proposal. For these purposes the simplified model shown in

Figure 131 was used. The beam energy is assumed to be completely

dissipated within a hemisphere of radius a given by

$$a = \frac{1}{2} (b + Rg) \qquad (54)$$

where b, is the beam diameter and Rg is the "Grün" range. The "Grün"

range depends on the material and is a measure of electron penetrat-

ion into the material which is proportional to beam energy raised

to the 1.75 power. The beam requirements to locally raise the

temperature of an Indium Germanium system $30^{\circ}C$ above a thermal bias

for selective alloying have been determined using this model. The

resulting beam current and voltage as a function of incident beam

spot size for 1000 and 2000 $\overset{o}{A}$ bit sizes are shown in Figure 132.

The possibility of meeting these beam requirements with an

electron column as shown schematically in Figure 133, has also

been estimated. A magnetic final lens is used because of the ext-

remely short focal lengths achievable. Since the target is non-

magnetic it can be brought close to the lens and even inside the

b

METAL

N – SEMICONDUCTOR

P – SEMICONDUCTOR

a
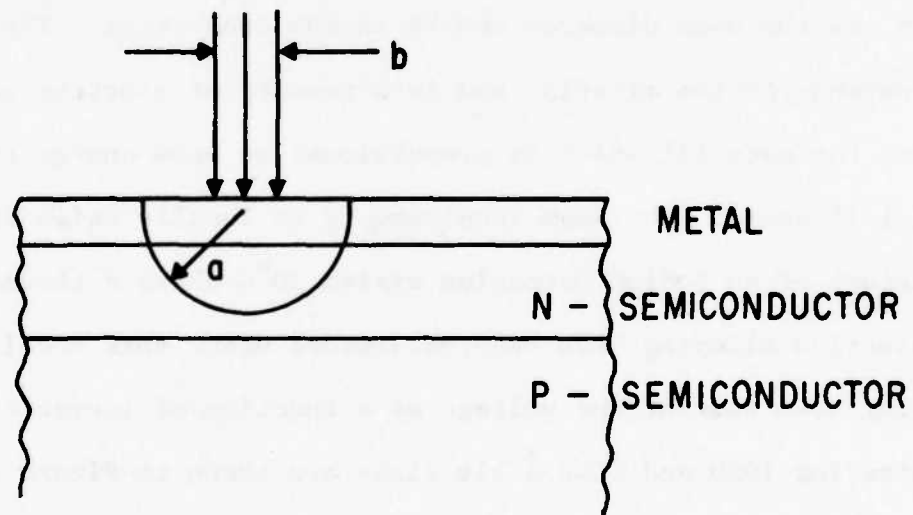
Figure 131   Thermal Writing Model for Alloy Junction Writing
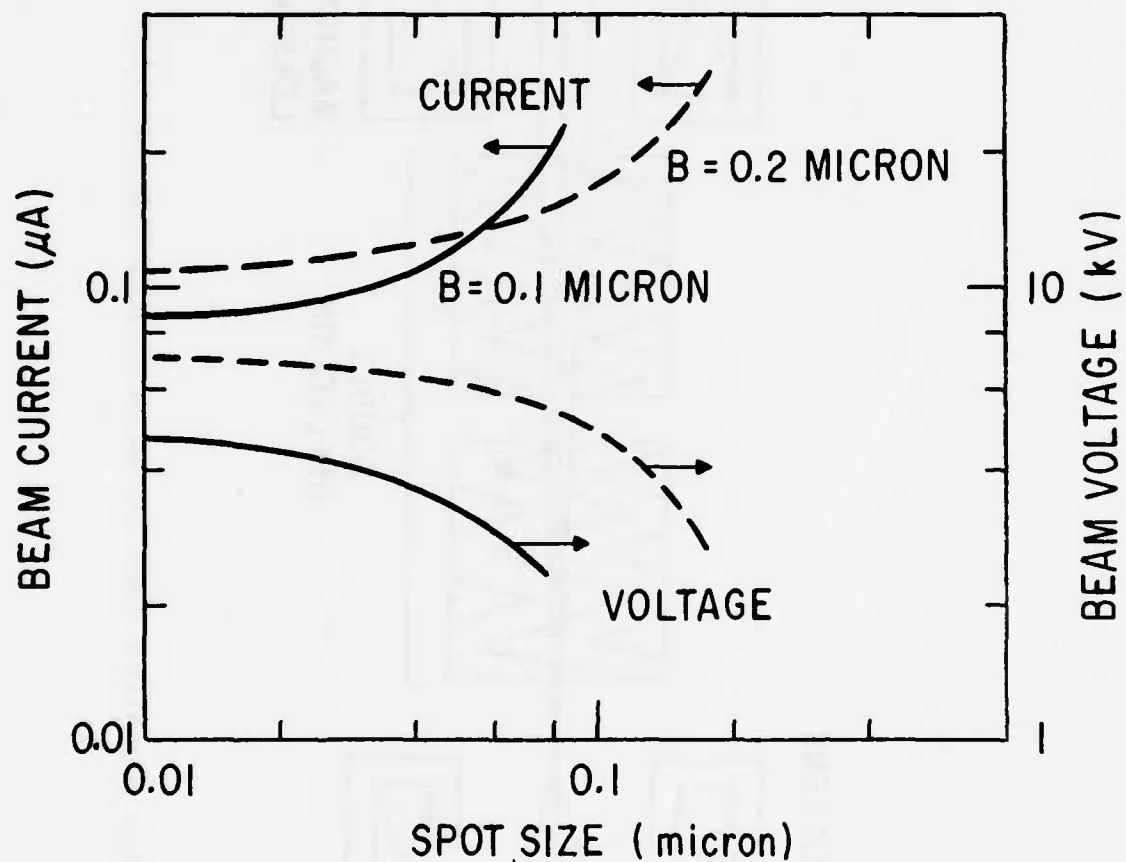
Figure 132. Predicted Beam Current and Beam Voltage Requirements for Alloy Junction Writing on In-Ge Target at 0.1 micron and 0.2 micron Bit Spacing.
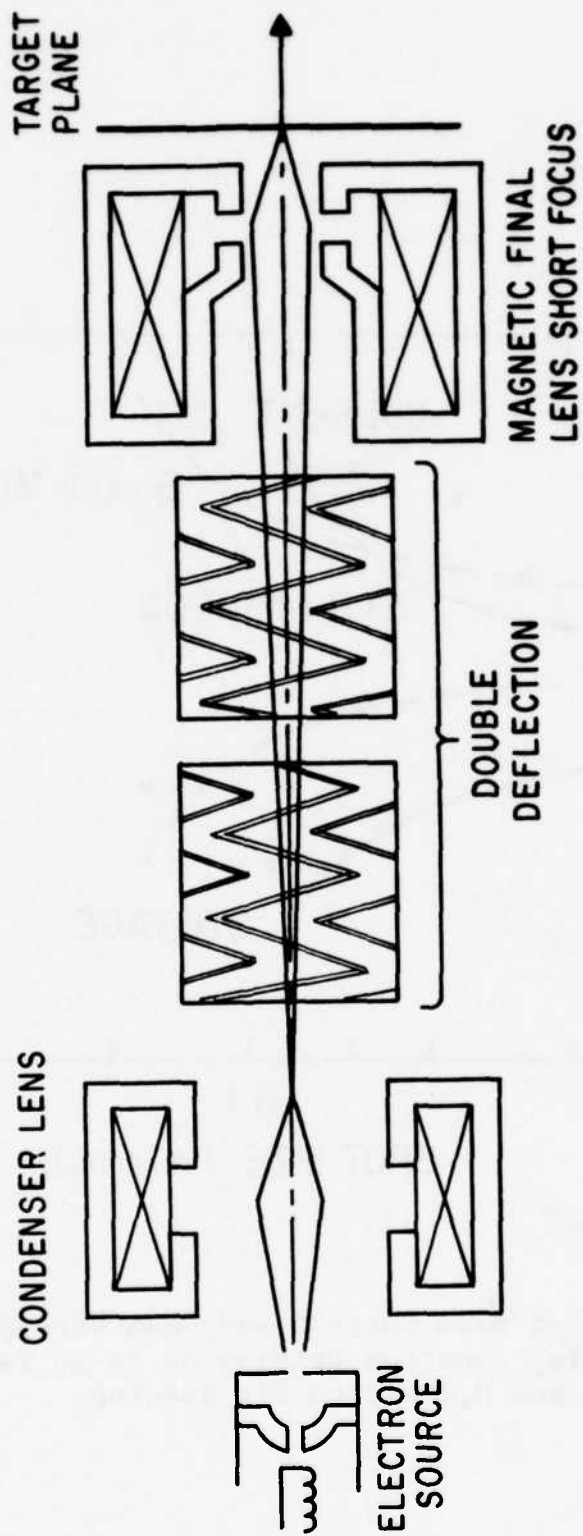
Figure 133. Optics for Alloy Junction Experimental Write Station

pole pieces without distorting the focusing field. Hence the lens can operate with an extremely short focus and small spherical aberration which results in larger beam currents. However, operation of the final lens at such a short focal length leaves no room for deflection between the lens and target. Therefore, a double deflector preceding the final lens similar to that used in SEM optics is used. The two stage deflector is arranged so that the deflected beam always passes through the optical center of the lens. Final deflection over the field-of-view results from varying the angle with respect to the optical axis of the principal ray as it passes through lens center.

The expected beam current from this type of column was estimated assuming a thermionic emission Radley Pierce source with a 10 A/cm^2 cathode loading and a much higher birghtness temperature aided field emission (TFE) source. High quality magnetic lenses with a spherical aberration coefficient of .13 cm of a type previously built at General Electric's Research and Development Center were also assumed. The results of this preliminary analysis showing the beam current capabilities of the column and the beam current requirements (from Figure 132) are shown in Figure 134. From this figure it appears as though a field emission type source is required.

Column Selection

Making use of the above background, the specifications for a column were determined. The specifications are:

-243-
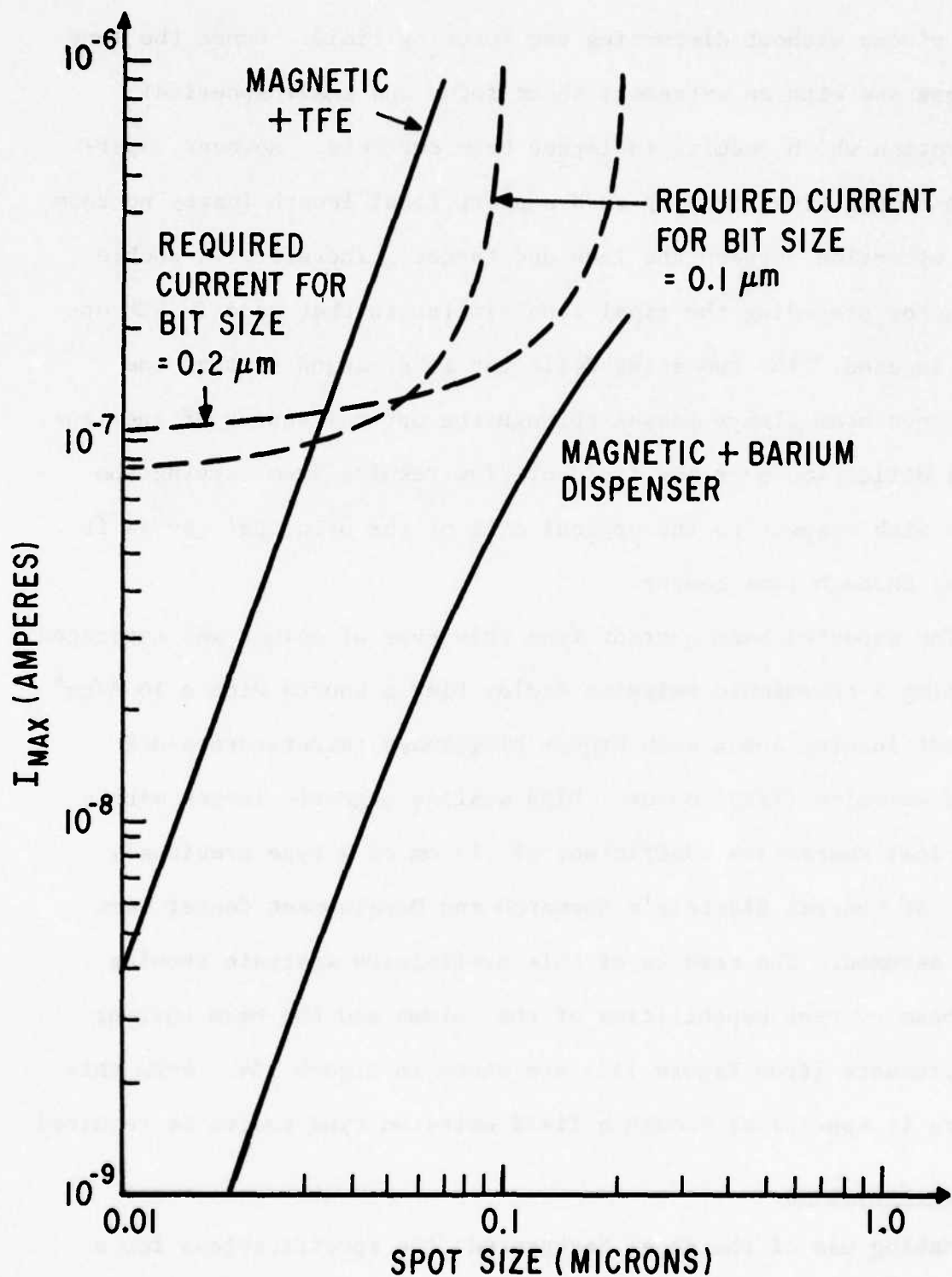
Figure 134. Predicted Beam Current vs. Spot Size for
Experimental Alloy Junction Write Optics

I_b = beam current $\geq$ 150 nA

d_s = spot size $\leq$ 1000 Å

V_1 = Landing potential = 3Kv $\leq V_1 \leq$ 5kV

In order to make use of experimental data gained from writing
experiments, a decision on how to quickly set-up such an equipment
was necessary. Several possibilities existed.

- Design and construct ourselves

- Purchase component parts from various vendors and
  assemble in house.

- Locate a manufacturer who could build a system capable
  of meeting the specifications.

This latter approach was selected since it was found that the Coates
and Welter Company could assemble a complete column that would
meet these specifications. After obtaining Contracting Office's
approval for the purchase of the equipment, it was ordered with
delivery promised during the second quarter.

The purchased Coates and Welter column is conceptually similar
to the column of Figure 133 as shown in Figure 135. The column has
a field emission electron source housed in an ultra high vacuum
region that is both internally and externally pumped to a pressure
of 10^{-10} to 10^{-9} Torr. The gun chamber is differentially pumped
through a conductance limited aperture so that the main column
pressure can be approximately 1000 times poorer than the gun chamber.
The gun chamber can be closed off with an isolation valve to allow
rapid changing of target samples. The first lens is a specially

Field Emission Tip

Internal UHV Pump

Extraction Electrode
Limiting Aperture

Electrostatic First Lens

Magnetic Double Deflector

Gun Isolation Valve

Magnetic Second Lens

Target

External UHV Pump

Extraction Voltage

Protect

Accelerating Voltage

Scan Amplifier

Vacuum Pump
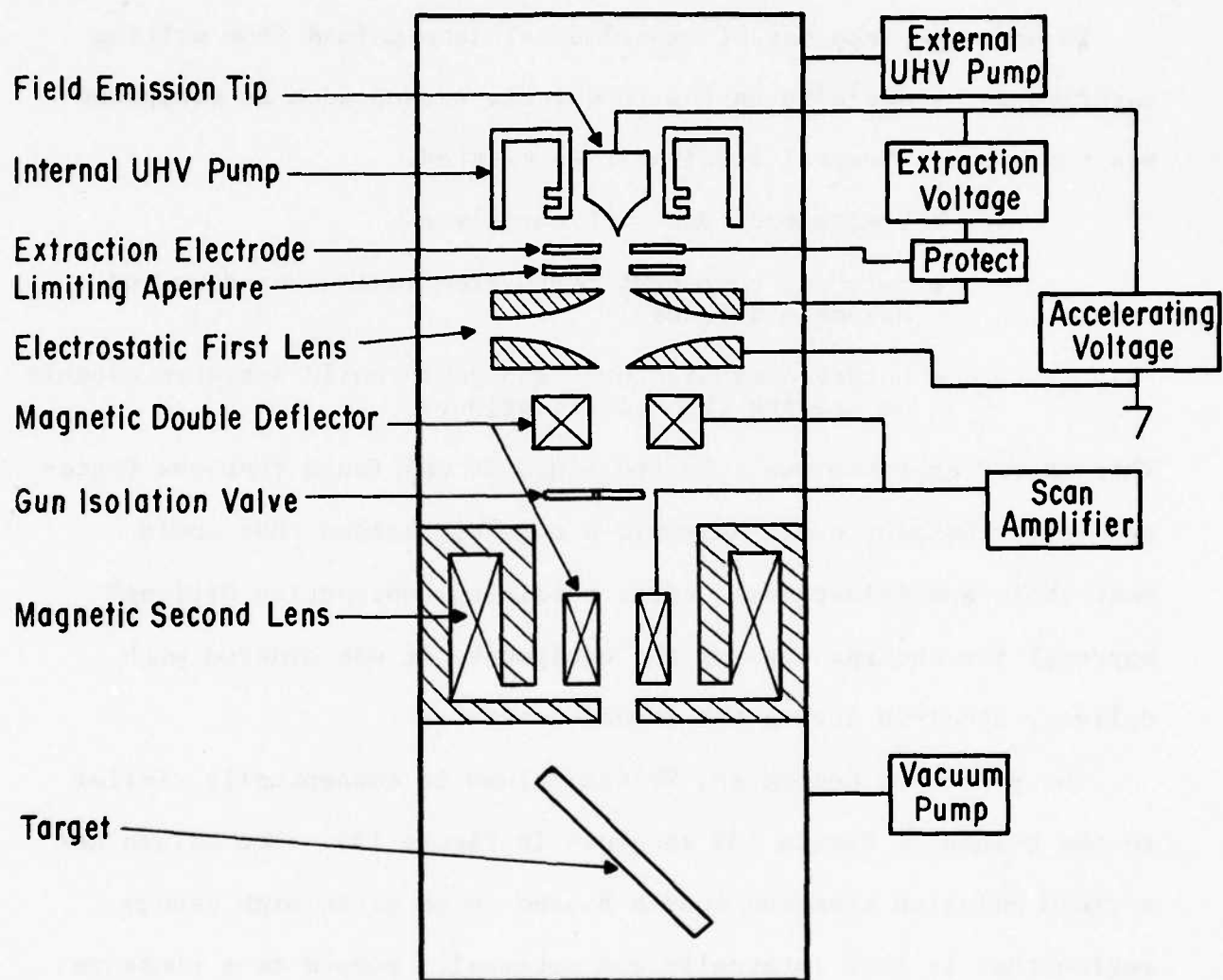
Figure 135.   Schematic of Purchased Alloy Junction Write Optics

designed low aberration electrostatic lens and the final lens is

a high quality magnetic lens as assumed in the preliminary analysis.

Magnetic prelens deflection, similar in concept to the electrostatic

prelens deflection shown in the column of Figure 133, is used.

Appendix A
ION IMPLANTATION

Ion implantation is a technique for placing atoms in the surface
layer of a solid material by bombarding the substrate with energetic
(keV to MeV) ions. This is a particularly valuable tool in semi-
conductor work, because a number of solid-state properties are sen-
sitive to small concentrations of foreign atoms. With implantation,
a wide range of ions can be introduced in specified concentrations
in the desired location.

Because of its potential in device fabrication, there is consid-
erable interest in the ion implantation process. This process
provides an attractive alternative to thermal diffusion for intro-
ducing atoms into the lattice. Dopant ions can be implanted at
temperatures considerably lower than those required for typical
diffusions. Impurity concentrations are not limited by the usual
thermodynamic solubility rules, and dopants that cannot be added by
conventional means can be used with implantation. By adjustment of
parameters such as ion energy and target crystal orientation, the
desired profile of the dopant in the substrate can be achieved as
well.

Range of Implanted Ions

As the ion being implanted penetrates a solid, it loses energy
through collisions with the nuclei and electrons in the target mater-
ial. The actual total path length the ion travels as it slows down

is called the range (R), and the projection of the range along the incident direction of the ion beam is referred to as the projected range (R_p) (Figure A-1).

The amount of energy lost per collision and the number of collisions are random variables, so all of the ions in a given implant do not come to rest in the same spot. Instead, there is a distribution or standard deviation in the ion range, which can be calculated and measured. The result is a Gaussian shaped profile of implanted ions in the substrate (Figure A-2).

For an amorphous target, this range distribution depends on such parameters as the ion energy, ion mass and atomic number, target atomic mass and atomic number, target atomic density, target temperature during implantation, and ion dose. In single crystal targets, surface conditions and crystal orientation relative to the ion beam are also important influences on the range.

As the ions come to rest they lose energy by two major mechanisms (Figure A-3):

- Inelastic collisions with the target atoms, which result in excitation of the orbital electrons of the ion and substrate atoms.

- Elastic collisions, involving the screened nuclei of the ion and target atoms.

As an approximation, these processes can be considered independent of each other for calculation of energy losses and the ion range. Thus, for an incident ion, the rate at which energy is lost with distance can be given as
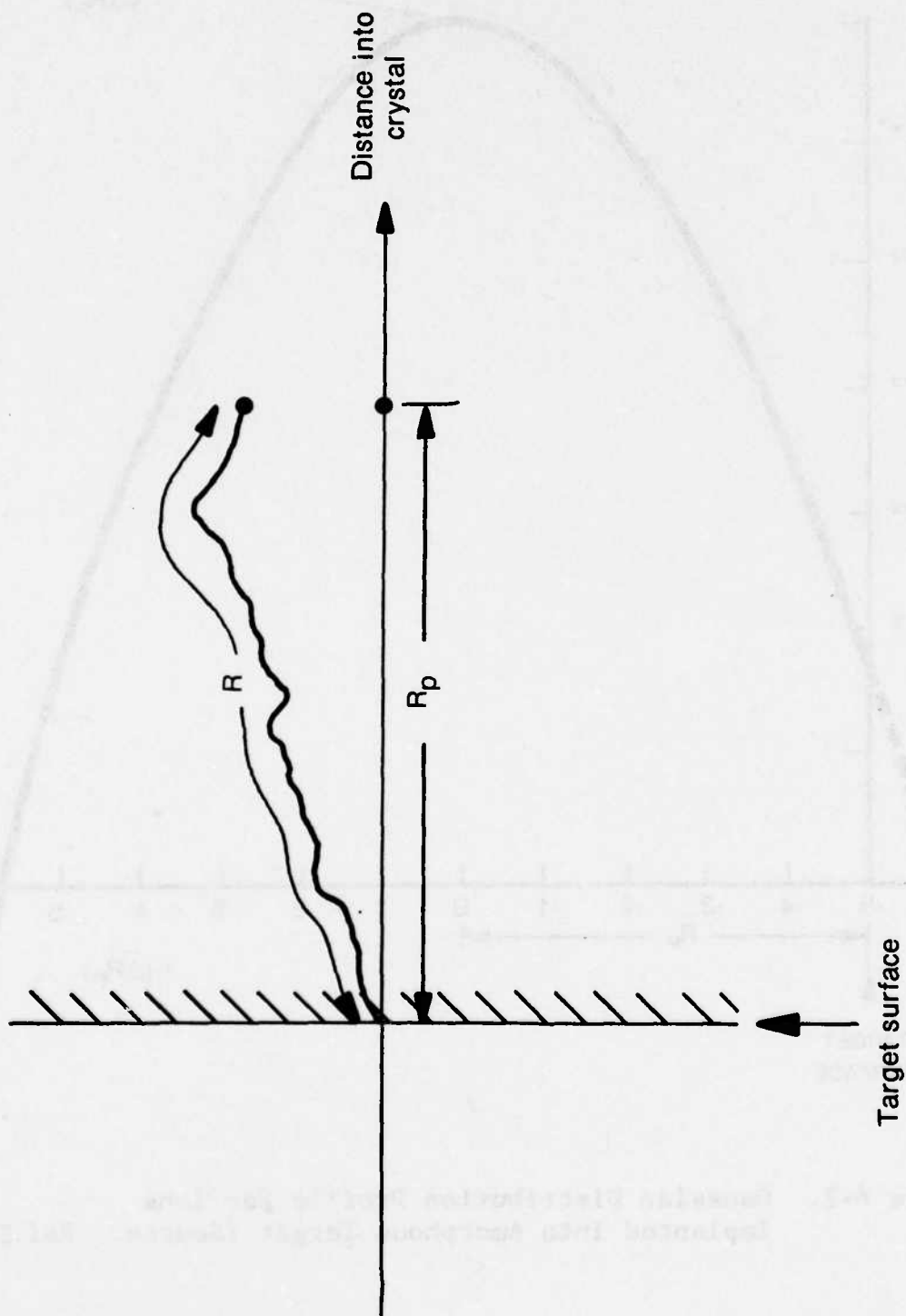
Figure A-1 Total Path Length R Traversed by Implanted Ion and Projected Range R_p, Actual Penetration Depth into Substrate (Source: Ref. 24)
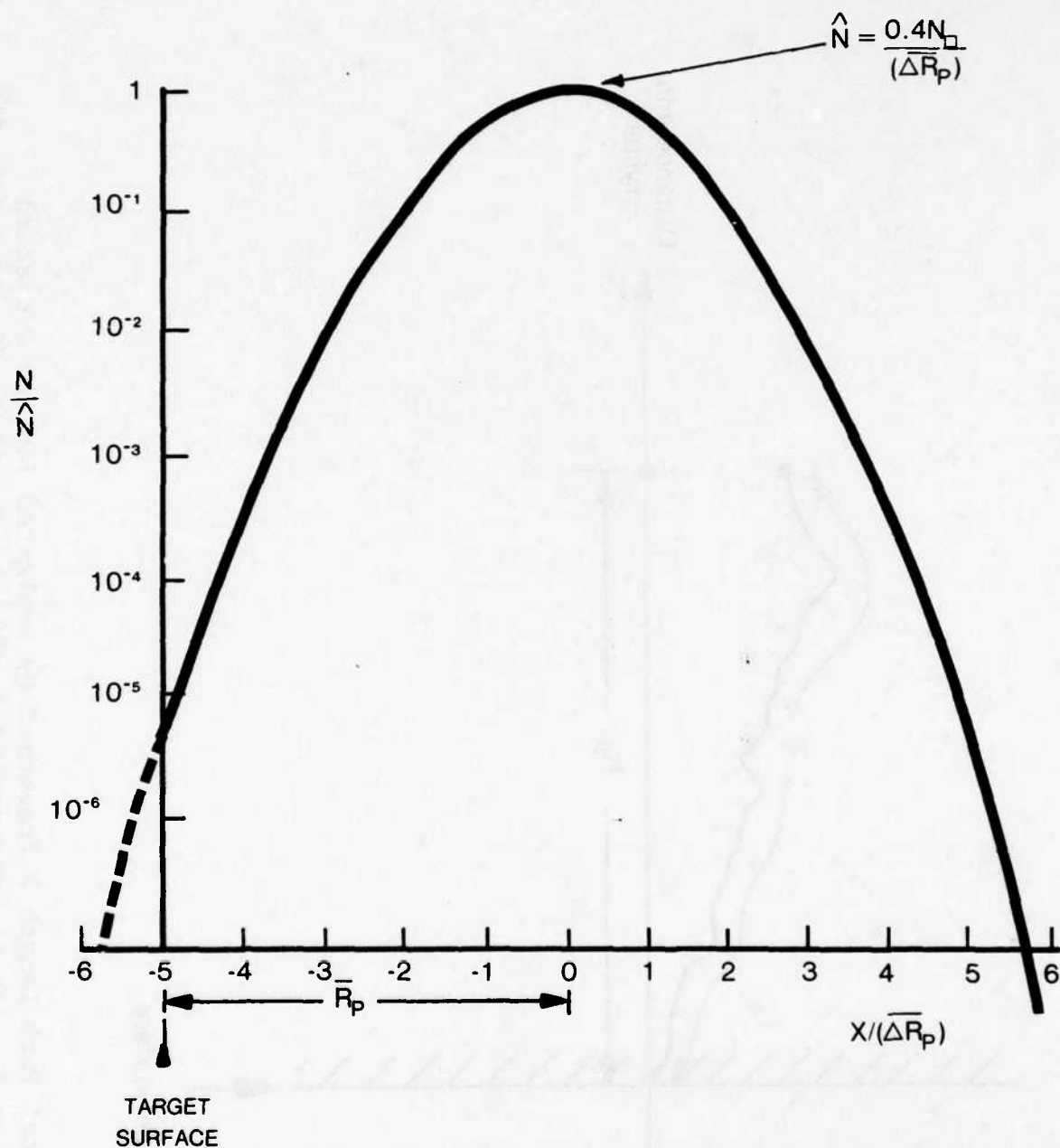
Figure A-2. Gaussian Distribution Profile for Ions
            Implanted Into Amorphous Target (Source: Ref.24)
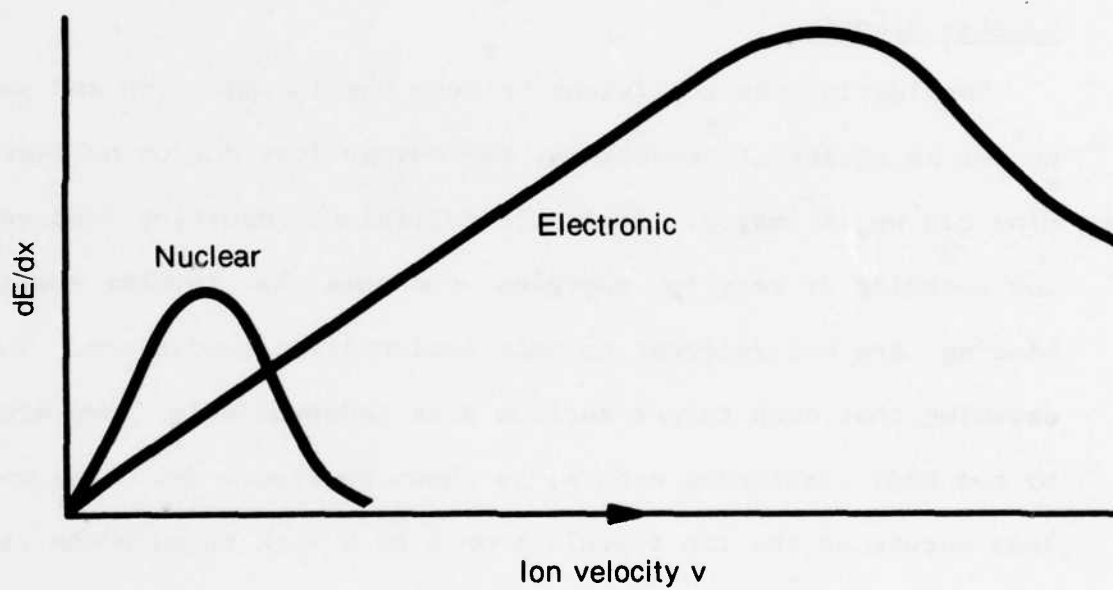
Figure A-3. Nuclear and Electronic Energy Loss dE/dx as Function of Ion Velocity V (Source: Ref.25)

$$- \frac{dE}{dx} = N \left[S_n(E) + S_e(E) \right] \tag{A-1}$$

where:

N = Average atomic density

$S_n(E)$ = Nuclear stopping power

$S_e(E)$ = Electronic stopping power

Integrating Equation A-1, range R for an ion with initial energy E can be written

$$R = \int_0^R dx = \frac{1}{N} \int_0^{E_0} \frac{dE}{S_n(E) + S_e(E)} \tag{Ref.25} \tag{A-2}$$

Nuclear Stopping

Considering the collisions between the incoming ion and substrate nuclei as elastic interactions, the energy loss due to nuclear stopping can be estimated. Inelastic collisions resulting from very high ion energies or very low energies, the ones that involve chemical binding, are not relevant to most implantation conditions. Thus, assuming that each target nucleus acts independently, ions are slowed by two body scattering events, as shown in Figure A-4. The energy loss occurs as the ion travels from x to x + $\wedge$x through the target material, passing within distance p of $N\triangle x\, 2\pi p\, dp$ target nuclei, giving up an energy $T(p_1, E)$ to each (Figure A-5).

The energy lost, $\wedge E$, due to nuclear interactions can then be found by integrating over all possible impact parameters

$$\Delta E = -N \Delta x \int_0^\infty T_n(p, E)\, 2\pi p\, dp \tag{A-3}$$
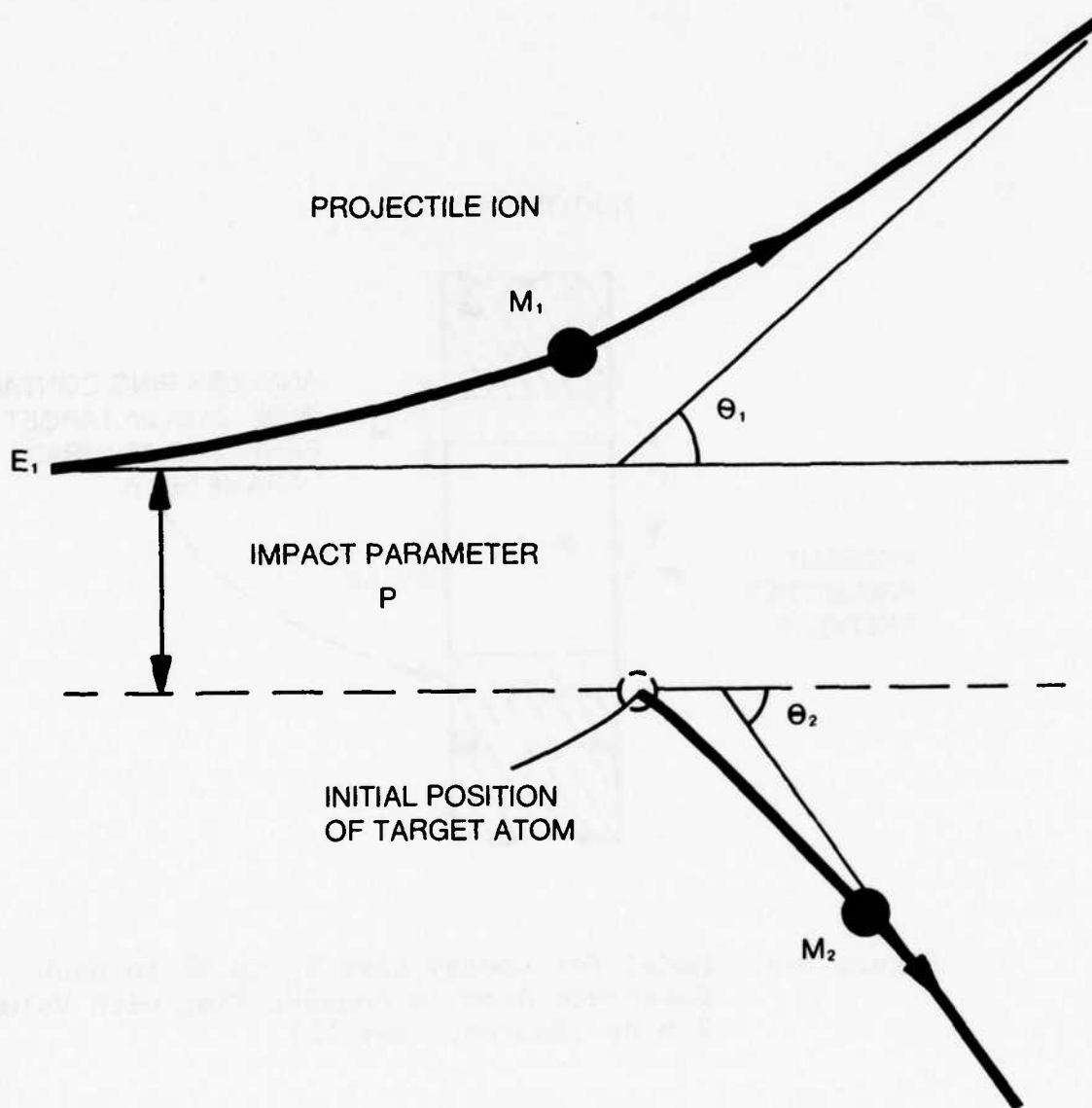
Figure A-4. Two Body Scattering Events in which Ion with Mass M_1 and Energy E_1 passes within Distance p of Stationary Substrate Atom with Mass M_2 (Source: Ref.25)
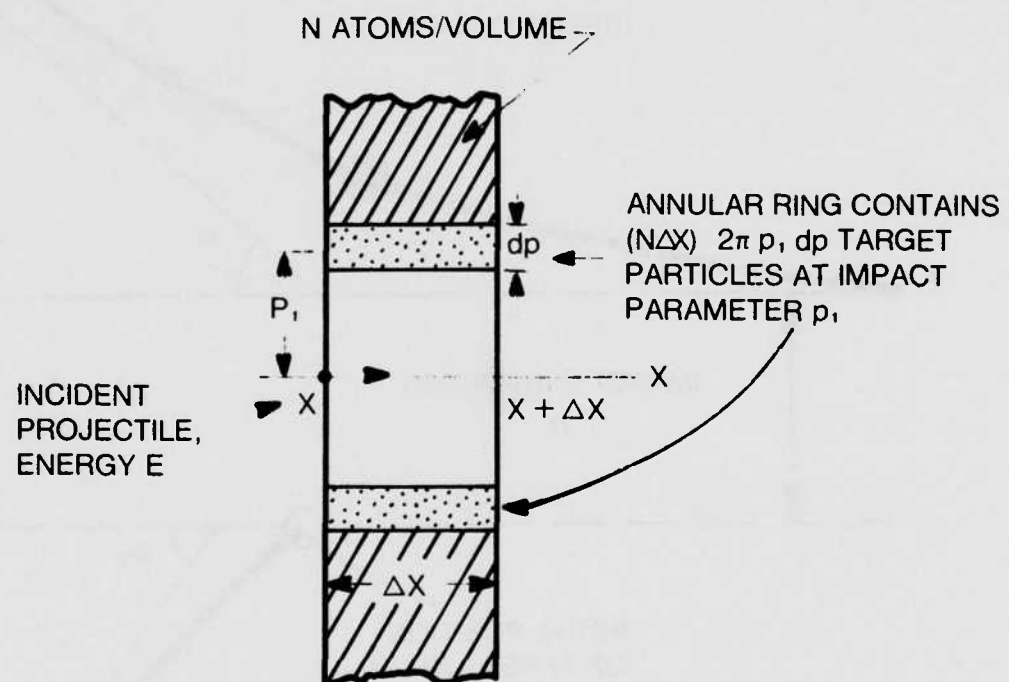
Figure A-5. Model for Energy Loss $T_n(p,E)$ to each Substrate Atom in Annular Ring with Volume $2\pi p_1 dp$ (Source: Ref.25)

where $\wedge E << E$ (Ref.25). Dividing by Δx and taking the limit as Δx 0, the average rate of energy loss is

$$-\frac{dE}{dx} = N \int_0^\infty T_n (\rho, E) 2\pi \rho d\rho \qquad (A-4)$$

$$= N S_n (E) \qquad (A-5)$$

For this type of scattering interaction, as the incident ion passes within distance b of a target atom, it is deflected through an angle θ as it gives up energy T (b,E), which can vary from

$$T (p = \infty, E) = 0 \qquad (A-6)$$

to

$$T \left(\rho = 0, E \right) = \frac{4 M_1 M_2}{(M_1 + M_2)} E \qquad (Ref.24) \quad (A-7)$$

Therefore, knowing T (p,E), S_n can be calculated. The solution of this elastic collision problem is obtained using classical mechanics and a change of coordinates, switching from the laboratory coordinates of Figure A-4 to a system in which the origin of the coordinates travels with the center of mass (Figure A-6). The incident ion energy, E, then becomes

$$E_{cm} = \frac{E u}{M_1} , \qquad (A-8)$$

where $\qquad u = \dfrac{M_1 M_2}{(M_1 + M_2)} = $ reduced mass. $\qquad (A-9)$

From conservation of energy and angular momentum considerations

$$E_{cm} (1-p^2 u^2_{max}) = V (u_{max}) \qquad (A-10)$$

-257-
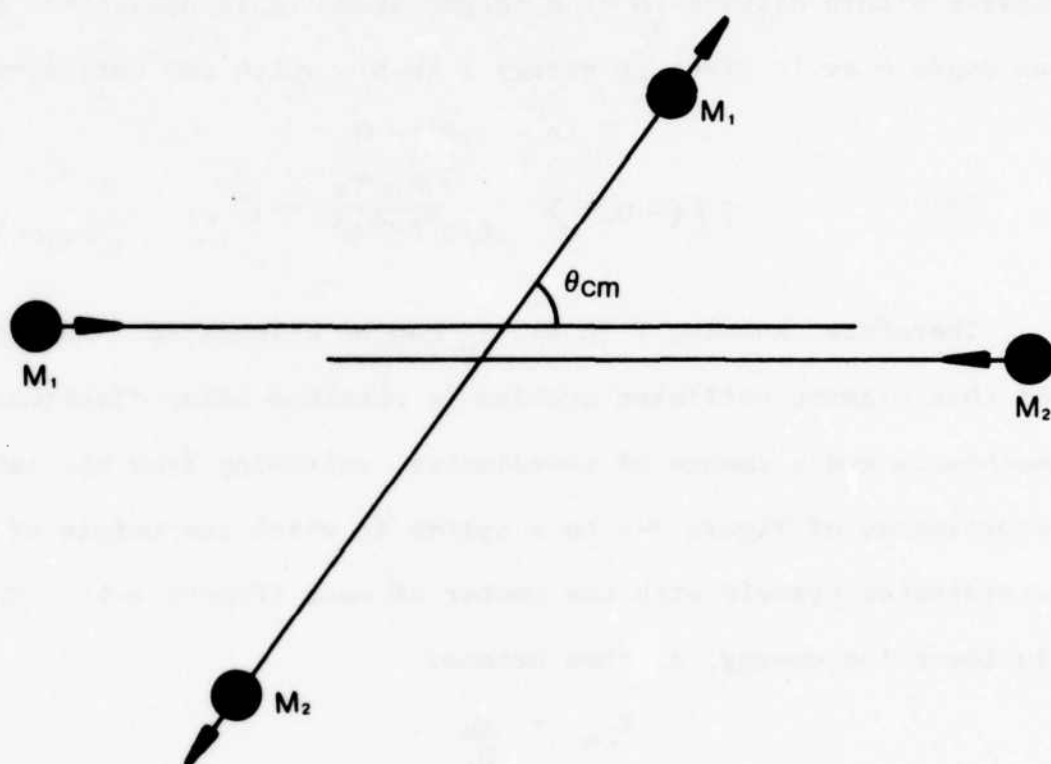
Figure A-6. Two Body Scattering Events in Center of Mass Coordinates (Source: Ref.25)

where $u = 1/r$, and

$$\dot{u}^2 + u^2 = \frac{1}{p^2}\left(1 - \frac{V(u)}{E_{cm}}\right)$$

(A-11)

Using this basis, the center of the mass deflection angle can be derived:

$$\theta_{cm} = -2p \int_0^{u_{max}} \frac{du}{\left(1 - \frac{V(u)}{E_{cm}} - p^2 u^2\right)^{1/2}}$$

(Ref.26) (A-12)

For a given E_{cm}, p, and interaction potential, $V(u)$, this integral can be evaluated. A general form for this potential is

$$V(r) = \frac{Z_1 Z_2}{4\pi\epsilon_o r} f\left(\frac{r}{a}\right)$$

(A-13)

where

Z_1 = Atomic number of implanted atom,

Z_2 = Atomic number of target atom,

and

$f\left(\frac{r}{a}\right)$ = Screening function with screening parameter a

For reasonably accurate numerical calculations, an approximation to The Thomas-Fermi potential (Figure A-7) is useful

$$f\left(\frac{r}{a}\right) = \frac{(r/a)}{\left[(r/a)^2 + C^2\right]^{1/2}}$$

(A-14)

where

$$a = 0.885\, a_o\, (Z_1^{2/3} + Z_2^{2/3})^{-1/2}$$
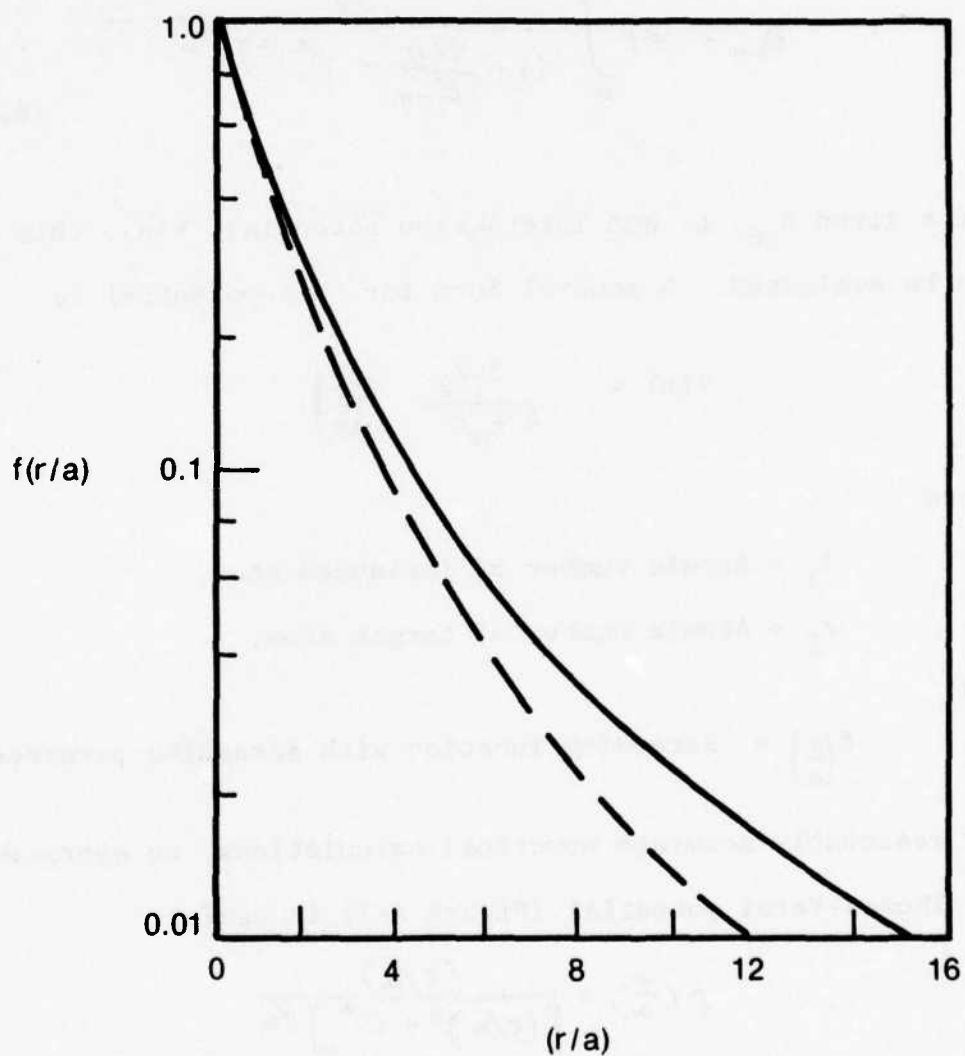
Figure A-7   Thomas-Fermi Screening Function (Solid Line) and
Approximation (Dashed Line) (Source: Ref. 24)

and $C = \sqrt{3}$ (Ref.27). After evaluation of the integral, θ_{cm} can be transformed back to the laboratory frame with

$$\tan \theta_1 = \frac{\sin \theta_{cm}}{\cos \theta_{cm} + M_1/M_2} \qquad \text{(A-15)}$$

and T calculated using

$$\cos \theta_1 = \frac{1 - \left(\frac{1 + M_2 M_1}{2}\right) \frac{T}{E}}{\sqrt{1 - T/E}} \qquad \text{(A-16)}$$

Thus T can be estimated from p using the sequency p θ_{cm} θ T, and therefore S_n. Assuming energy loss due to a series of small angle scattering processes, θ_{cm} is small, and using Equation A-15 and A-16

$$S_n \rightarrow T \; 2\pi p \; dp \qquad \text{(A-17)}$$

$$= T \; d\sigma \qquad \text{(A-18)}$$

$$= \frac{K_d T}{T^{1/2}} \qquad \text{(A-19)}$$

As a crude approximation, the nuclear stopping power in silicon can be given in the form

$$S_n = 2.8 \times 10^{-15} \frac{Z_1 Z_2}{(Z_1^{2/3} + Z_2^{2/3})^{1/2}} \frac{M_1}{M_1 + M_2} \quad \text{eV} \cdot \text{cm}^2 \quad \text{(Ref.24)(A-20)}$$

Electronic Stopping

Several models can be used to calculate the energy lost through electronic interactions, the Lindhard, Scharff, and Schiøtt (LSS) and Firsov models being the most prominent.

In the LSS model the ion is considered to be stopped by a free electron gas through close electron collisions and plasma resonance excitation away from the ion path. For an ion velocity less than the electron velocity (the electron has a Fermi energy E_F)

$$S_e (E) = cv = kE^{1/2} \tag{A-21}$$

The constant, k, in Thomas-Fermi terms is

$$k = \frac{k' C_R}{C_E^{1/2}} \tag{A-22}$$

where

$$K' = Z_1 \frac{\gamma_0 \, 0.0793 \, Z_1^{1/2} \, Z_2^{1/2} \, (A_1 + A_2)^{3/2}}{(Z_1^{2/3} + Z_2^{2/3})^{3/4} \, A_1^{3/2} \, A_2^{1/2}} \tag{A-23}$$

$$C_R = \frac{4\pi a^2 M_1 M_2}{(M_1 + M_2)^2} \tag{A-24}$$

$$C_E = \frac{4\pi \epsilon_0 \, a \, M_2}{Z_1 Z_2 \, q^2 (M_1 + M_2)} \tag{A-25}$$

A_1 = Atomic weight of implanted ion

and

A_2 = Atomic weight of substrate atom (Ref.27).

The Firsov model considers the overlap of electronic orbitals during the collision between an ion and a substrate atom. The transfer of electrons from one to the other results in a momentum transfer, which slows the ion (Ref.28). If the target is considered amorphous, S_e can be estimated by a scheme similar to that used for

S_n, where T_e, the energy lost due to electronic interactions in a two body event is calculated and a random distribution function is employed to result in

$$NS_e(E) = N\int_0^\infty T_e(p, E)\, 2\pi p\, dp$$

(A-26)

Considering the situation shown in Figure A-8, the ion and target atom form a sort of molecule, and as the ion comes near, the outer less tightly bound electrons can be exchanged. Electrons going from the moving ion over to the stationary target atom lose momentum, whereas those transferred to the ion must gain, with these energy exchanges taking a toll from the ion's energy. Thus as the ion travels from $-\infty$, near a traget atom, to $+\infty$, it loses an amount of energy

$$T = \frac{4.3\times 10^{-8}(z_1+z_2)^{5/2}\,v}{\left[1 + 3.1\times 10^{-7}(z_1+z_2)^{1/3}\,p\right]^5}\,(ev)$$

(A-27)

where v is given in cm/sec and p is given in cm. providing v < orbital electron velocity. Therefore S_e can be found using T in Equation A-26

$$S_e(V) = 2.34 \times 10^{-23}\,(Z_1 + Z_2)\,v\ (eV - cm)$$

(A-28)

In this view, all of the electrons are considered to take part in energy exchanges; however, in actuality, shielded inner electrons do not participate, and a reduced atomic number should be used to account for this fact.
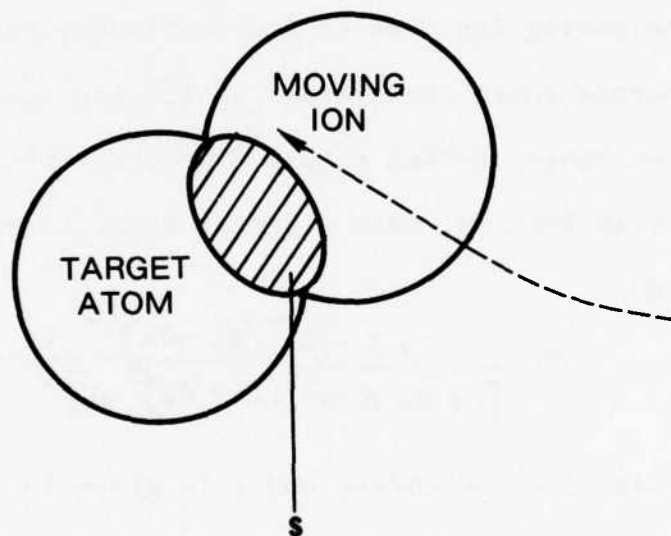
Figure A-8. Model for Electronic Stopping, Indicating Firsov Quasimolecule that Forms as Electronic Orbitals Overlap (Source: Ref.25)

Projected Range and Distribution

Knowing S_n and S_e, Equation A-1 can be used to calculate the range or total path length traveled by the ion. However, for practical applications this is not as relevant a statistic as the actual penetration depth into the substrate. To obtain the Gaussian distribution shown in Figure A-1, R_p and $\triangle R_p$ are the calculations of interest. Lindhard and his coworkers have done extensive work on this, formulating the LSS theory for atomic stopping. By noting that integration of the probability that an ion has a range between R and R + dR, integration from 0 to ∞ is 1, analogous integral equations can be written for R_p and other lengths indicated in Figure A-9, which can be converted to differential equations. Thus the integral equation for R_p is

$$1 = N \int d\sigma \left\{ \bar{R}_p (E) - \bar{R}_p (E-T) \cos \theta_1 \right\} \tag{A-29}$$

where:

$d\sigma$ = Differential cross section for energy transfer T

θ_1 = Scattering angle in laboratory system

N = Atomic density.

After the application of several useful approximations, this equation has as its solution in terms of stopping powers,

$$\bar{R}_p = \int_0^E \frac{dE'}{\beta_1 (E')} \, exp \left[\int_E^{E'} \frac{\sigma_1 (E'') \, dE''}{\beta_1 (E'')} \right] \tag{A-30}$$
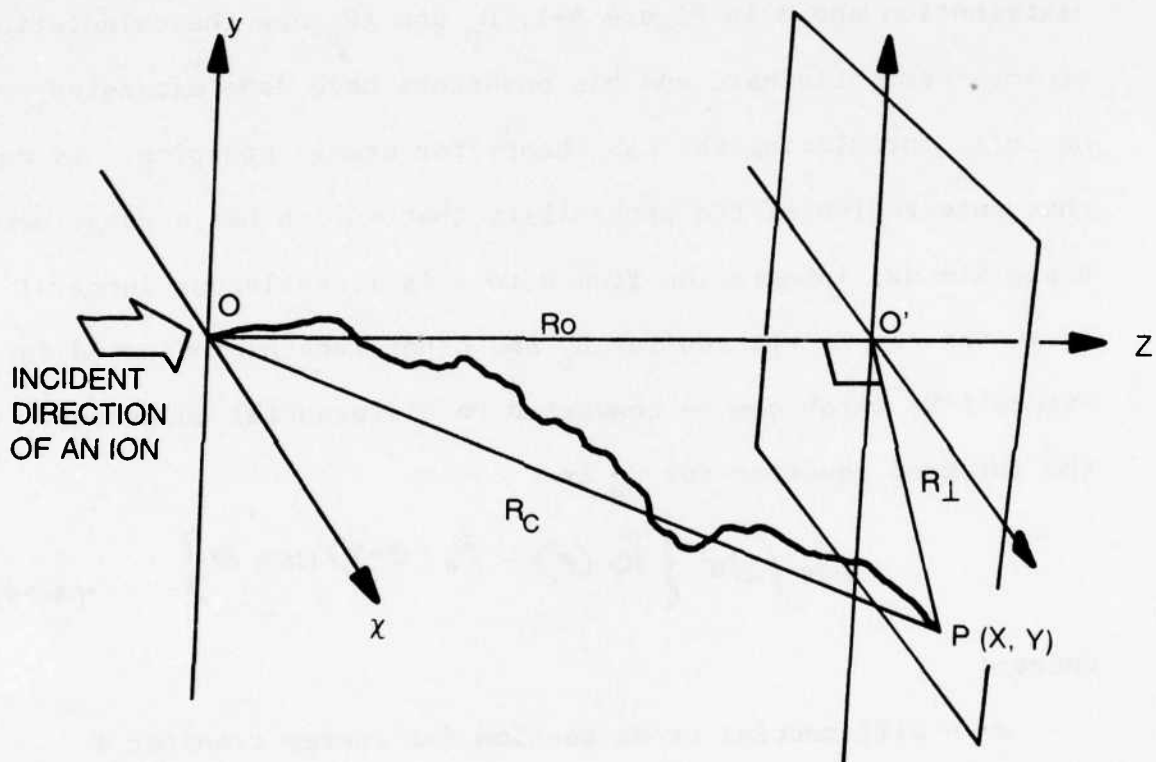
Figure A-9. Coordinate System for Distances R_p, R_c, and $R_\perp$ for Ion Entering Substrate at 0 and Coming to Rest at 0' (Source: Ref.29)

-266-

$$\alpha_1(E) = \frac{M_2}{M_1} \frac{N}{2} \frac{S_n(E)}{E} \qquad \text{(A-31)}$$

$$B_1(E) = N\left[S_N(E) + S_e(E) - \frac{M_2}{M_1} \frac{\Omega_n^2(E)}{2E}\right] \qquad \text{(A-32)}$$

$$\Omega_n^2(E) = \int_0^\infty T_n^2 \, d\sigma \qquad \text{(A-33)}$$

Under the same energy restriction, $R_r^2 \ (R_r^2 = R_p^2 - 1/2R_\perp^2)$ and $R_c^2 \ (R_c^2 = R_p^2 + R_\perp^2)$ have solutions:

$$\overline{R}^2(E) = \int_0^E \frac{2 R_p(E) \, dE'}{B_2(E')} \exp\left[\int_E^{E'} \frac{3\sigma_2(E'')}{B(E'')} dE''\right] \qquad \text{(A-34)}$$

and

$$\overline{R}_c^2(E) = \int_0^E \frac{2 R_p(E') \, dE'}{N\left[S_n(E') + S_e(E)\right]} \qquad \text{(A-35)}$$

where

$$\alpha_2(E) = \frac{\alpha_1(E)}{2} \qquad \text{(A-36)}$$

and

$$B_2(E) = B_1(E) - N\frac{M_2}{M_1} \frac{\Omega_n^2(E)}{E} \qquad \text{(A-37)}$$

Thus the straggling can be found using

$$\left(\Delta \overline{R}_p\right)^2 = \frac{2 \overline{R_r^2}(E) + \overline{R_c^2}(E)}{3} - \left(\overline{R}_p\right)^2 \qquad \text{(A-38)}$$

Numerical techniques involving the use of a Thomas-Fermi potential or stopping powers with

$$\Omega_n^2(E) = \frac{4 M_1 M_2}{3(M_1 + M_2)} S_n^o(E) \qquad \text{(A-39)}$$

where S_n^o = constant total stopping power approximation, enable

calculation of the straggling. Table A-1 indicates the results of computer calculations of R_p and $\wedge R_p$ for various ions and energies (Refs.24 and 30).

As a rough extimate for intermediate energies, the approximation of Nielsen is sometimes convenient to use (Ref.31)

$$R(\mathring{A}) = \frac{60 \, E \, (keV)}{g} \cdot \frac{M_2}{z_2} \cdot \frac{M_1 + M_2}{M_1} \cdot \frac{(z_1^{2/3} + z_2^{2/3})^{1/2}}{z_1} \qquad (A\text{-}40)$$

where g = density (gm/cm^3):

$$\simeq \frac{130 \, E \, (keV)}{g} \cdot \frac{1 + M_2/M_1}{z_1^{2/3}} \qquad (A\text{-}41)$$

For ions heavier than the substrate atoms, an approximate value for R_p is given by

$$\simeq \frac{R}{1 + M_2 (3M_1)} \qquad (A\text{-}42)$$

and

$$\Delta R_p \simeq 1.1 \, R_p \times \frac{2 \, (M_1 M_2)^{1/2}}{(M_1 + M_2)} \qquad (A\text{-}43)$$

$$\simeq R_p. \qquad (A\text{-}44)$$

As shown in Figure A-10, the more energetic an ion, the deeper it penetrates the substrate. Similarly, lighter ions have longer ranges.

The maximum in the ion distribution profile thus occurs at distance R_p into the substrate, as shown in Figure A-1, with a

-268-

Table A-1

PROJECTED RANGE (R_p) AND STANDARD DEVIATION IN R_p (ΔR_p) IN $\overset{\circ}{A}$
FOR COMMON IONS IMPLANTED IN SILICON AT VARIOUS ENERGIES
(Source: Ref. 24)

Projected Range, R_p ΔR_p ($\overset{\circ}{A}$)	Energy (keV)									
	20	40	60	80	100	120	140	160	180	200
Boron	714	1413	2074	2695	3275	3802	4289	4745	5177	5588
	276	443	562	653	726	793	855	910	959	1004
Nitrogen	491	961	1414	1847	2260	2655	3034	3391	3728	4046
	191	312	406	479	540	590	633	672	710	745
Aluminum	289	564	859	1141	1438	1737	2036	2335	2633	2929
	107	192	271	344	412	476	535	591	644	693
Phosphorus	255	488	729	976	1228	1483	1740	1998	2256	2514
	90	161	228	291	350	405	459	509	557	603
Gallium	155	272	383	492	602	712	823	936	1049	1163
	37	64	88	111	133	155	176	197	218	238
Arsenic	151	263	368	471	574	677	781	885	991	1097
	34	59	81	101	122	141	161	180	198	217
Indium	133	223	304	381	456	529	601	673	744	815
	23	38	51	63	75	86	97	108	119	129
Antimony	132	221	300	376	448	519	590	659	728	797
	22	36	49	60	71	82	92	102	112	122

Figure A-10   Ion Range Profiles Indicating Variation of Shape and Depth of Distribution with Energy (Source: Ref. 32)

concentration

$$N = \frac{0.4 \, N_D}{2(\Delta R_p)} \quad (\text{atoms/cm}^3) \qquad (A-45)$$

where N_D = ion fluence (atoms/cm^2) and ΛR_p is given in centimeters
(Ref.24).

Lateral Spreading

The lateral spread of implanted ions becomes of particular
concern as interest in very well defined doped regions grows.   In
addition to the standard deviation of the projected range, ΔR_p, the
lateral standard deviation can be calculated similarly.   Noting from
Figure A -9 that

$$\overline{R_p^2} = \overline{X^2} + \overline{Y^2}$$

$$\overline{X^2} = \overline{Y^2}$$

for an amorphous solid substrate the lateral standard deviation is

$$\overline{\Delta X_l} = \sqrt{\frac{\overline{R_p^2}}{2}}$$

$$(A-46)$$

Assuming a Gaussian distribution in three dimensions, the spatial
probability distribution for the point where an implanted ion comes
to rest is given by (Ref.32)

$$f(x,y,z) \propto exp\left\{ -\frac{x^2 + y^2}{2\overline{\Delta X_\perp}^2} - \frac{(z - \overline{R_p})^2}{2\Delta R_p^2} \right\} \quad (Ref. 32) \ (A-47)$$

Using the LSS computer calculation techniques for boton implanted in
silicon, for example, the curves of Figure A-11 are generated.
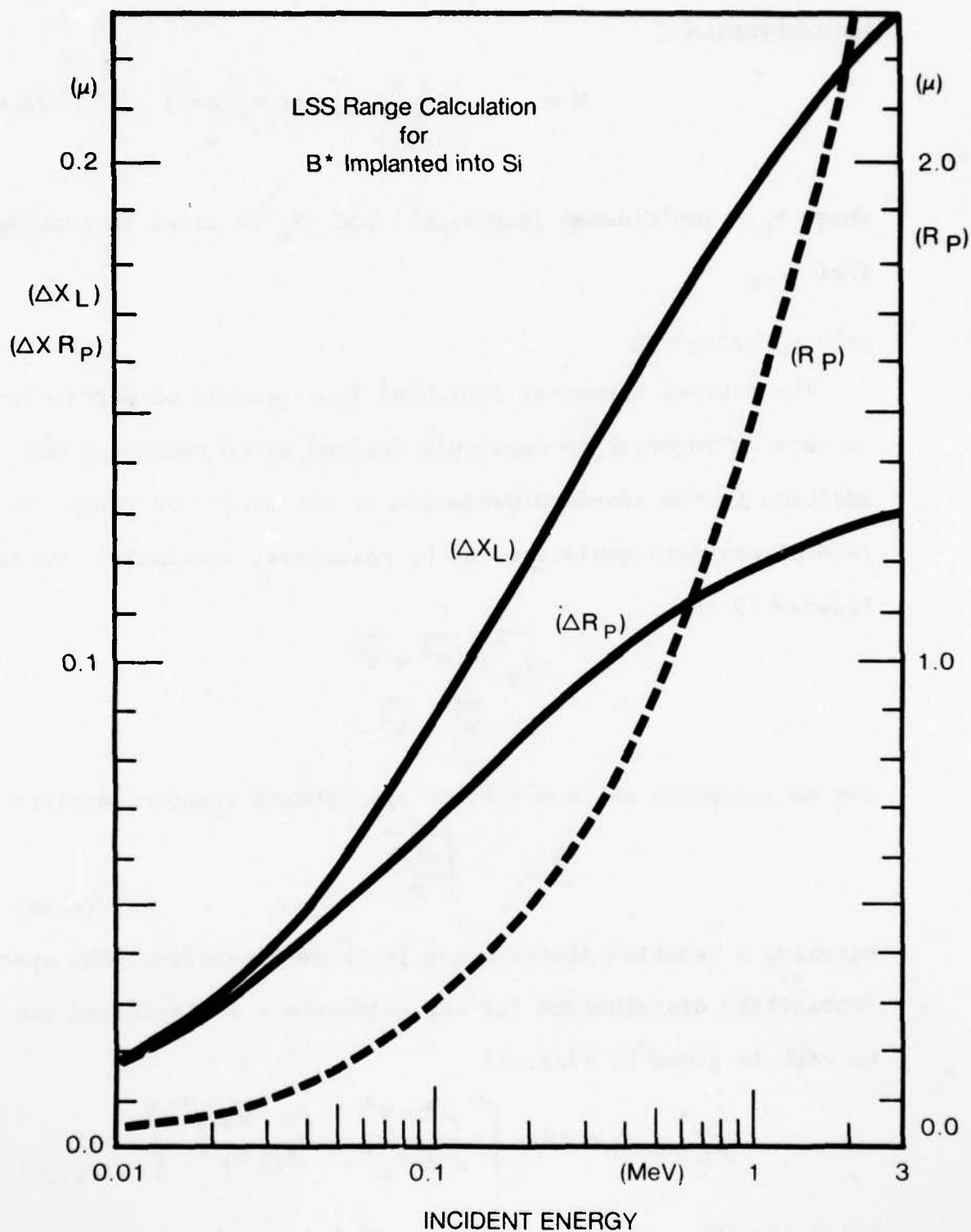
Figure A-11. Standard Deviation ΔR_p in Projected Range and Lateral Standard Deviation $\Delta \perp$ as Functions of Ion Energy (Source: Ref. 29).

Particularly for low-implantation energies, the predicted lateral scatter appears small.

The few experimental studies of lateral spreading support standard deviations predicted in this manner. Figure A-12 presents the results observed for boron implanted in silicon, and Table A-2 indicates both theoretical and experimental work for Kr and Ar into Si.

Channeling

The preceding predictions of the implanted ion's ranges and straggling were based on the premise that the substrate lattice appears amorphous to the incoming ion. However, in a single-crystal lattice resulting in deep ion penetration and less radiation damage. Providing the ion beam enters the crystal within a critical angle of a crystallographic axis, the repulsive force between the screened Coulomb fields of the ions and substrate atoms acts to steer the ions between the atomic rows so that they lose little energy to nuclear interactions (Figure A-13).

This critical angle, ψ_c, can be estimated by considering the ion's incident energy, E, to be composed of two components, $E_{\parallel}$ and $E_{\perp}$, parallel and perpendicular to the atomic rows (Figure A-14). If $E_{\perp}$ is less than the repulsive potential energy from the substrate atoms, the ion undergoes channeling. Approximating the configuration to a line of charge, the shielded potential can be written using the screening function of Equation A-13. Setting $U(r_{min}) = E_{\perp} = E \sin^2 \psi$ allows the minimum approach distance to be calculated. Because

-273-
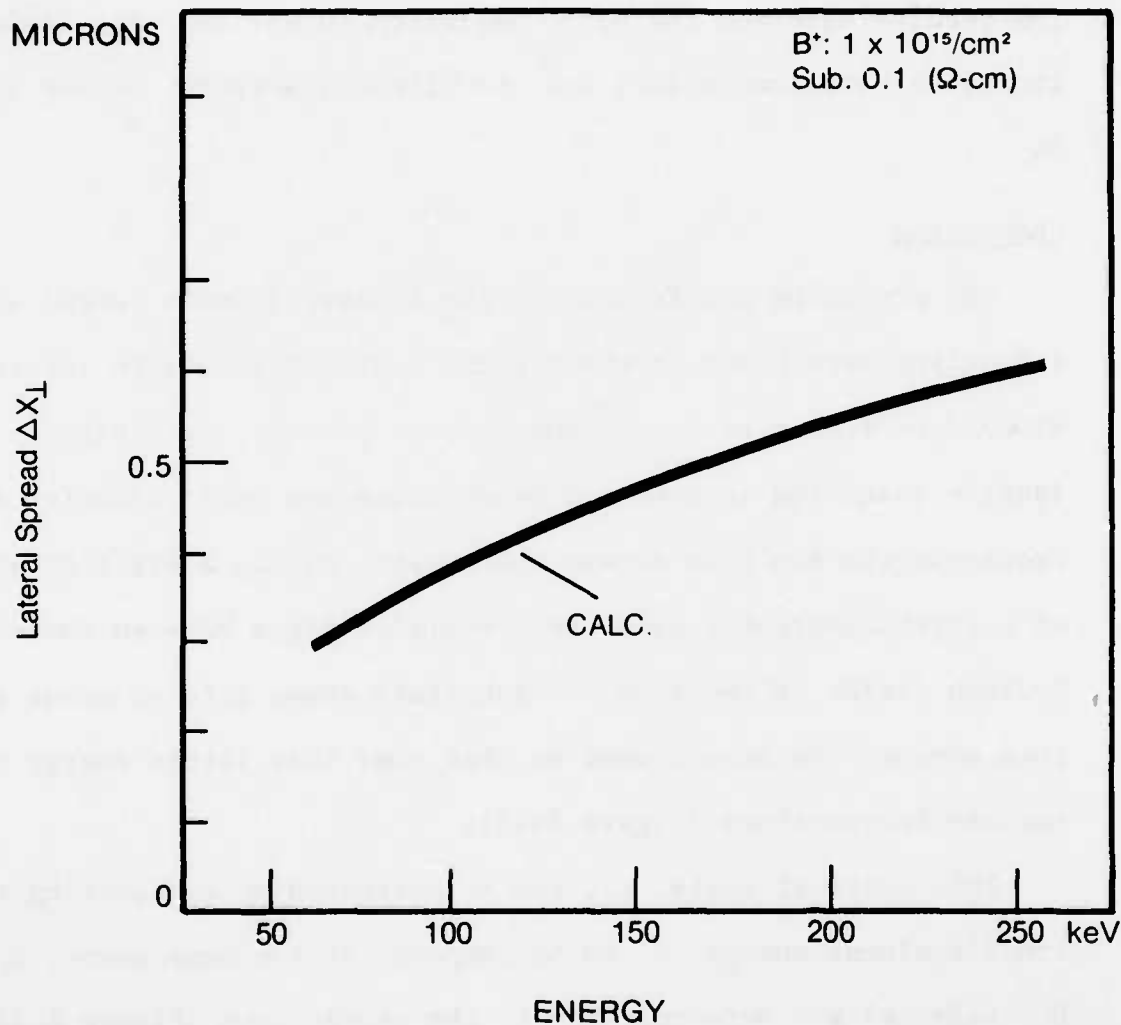
Figure A-12.   Lateral Spread of Boron Implanted in Silicon
              as a Function of Energy (Source: Ref. 33)

Table A-2

STANDARD DEVIATION AND LATERAL SPREAD VALUES
FROM THEORY AND EXPERIMENTS
(Source: Ref. 29)

Experiment	Type	$\langle R_p \rangle$ (angstroms)	$\langle \Delta R_p \rangle$ (angstroms)	$\langle \Delta X_L \rangle$ (angstroms)	$\dfrac{\langle \Delta R_p \rangle}{\langle R_p \rangle}$	$\dfrac{\langle \Delta X_L \rangle}{\langle R_p \rangle}$
Krypton into Silicon with 180 keV	Theoretical	929	305	219	0.33	0.24
	Experimental, by Thompson	1170	420	302	0.36	0.26
	Experimental, by Eisen	1024	368	265		
Krypton into Silicon with 100 keV	Theoretical	543	186	132	0.34	0.24
	Experimental, by Thompson	683	286	162	0.42	0.24
	Experimental, by Eisen	598	250	142		
Argon into Silicon with 50 keV	Theoretical	504	201	163	0.40	0.32
	Experimental, by Thompson	580	296	151	0.51	0.26
	Experimental, by Eisen	510	260	133		
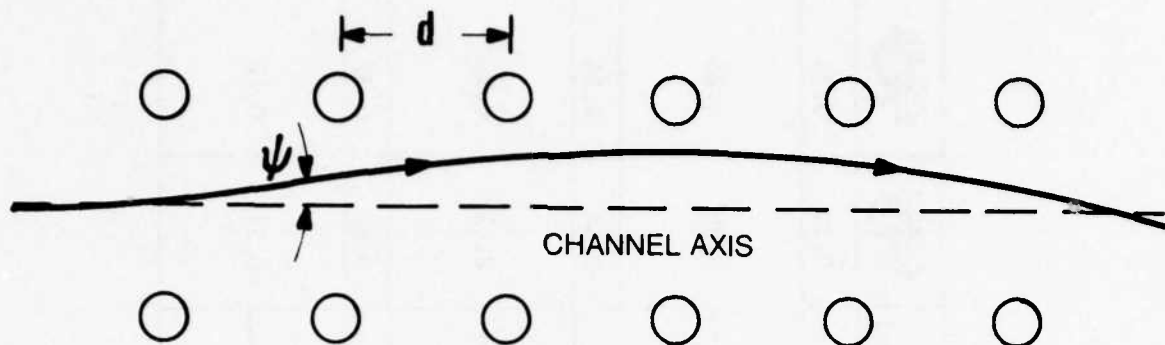
Figure A-13. Steering of Implanted Ion Along Channel Formed by
Rows of Substrate Atoms with Spacing d (Source: Ref. 24)
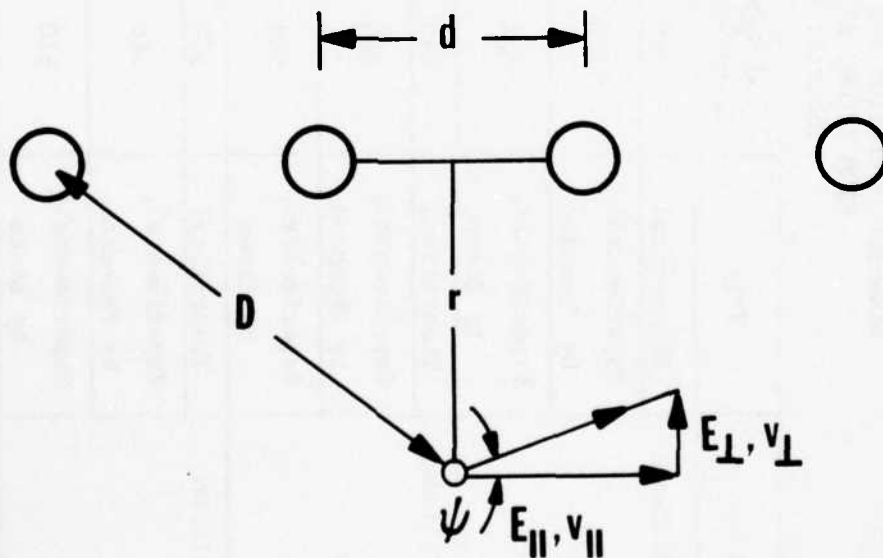
Figure A-14. Division of Energy into Components for Calculation
of Critical Angle ψ_c, which Determines Whether
Channeling Occurs (Source: Ref. 24)

$$U(r) = \frac{Z_1 Z_2 q^2}{4 \pi \epsilon_0 d} \cdot \ell_n \left[\left(\frac{C_a}{r} \right)^2 + 1 \right]$$

(A-48)

an atom could penetrate the channel walls, since they are not really continuous walls of charge, a requirement that the ion pass many substrate ions while traveling near the middle of a channel is imposed as an additional condition for channeling:

$$\frac{r_{min}}{v_\perp} > \frac{d}{v_{||}}$$

(A-49)

where $v_{||}$ and $v_\perp$ are parallel and perpendicular ion velocity components. Thus:

$$r_{min} \geq d \frac{v_\perp}{v_{||}} = d \tan \psi \simeq d \psi$$

(A-50)

for small ψ. Using this r_{min}, the critical angle can be estimated. For:

$$E \geq E_0 = \frac{Z_1 Z_2 q d}{2 \pi \epsilon_0 a^2} \ (eV)$$

(A-51)

then:

$$\psi \leq \psi_1 = \sqrt{\frac{E_1}{E}}$$

(Refs. 24 and 27) (A-52)

with

$$E_1 = \frac{Z_1 Z_2 q}{2 \pi \epsilon_0 d} \ (eV)$$

(A-53)

However, if $E \leq E_0$ (Refs. 24 and 27)

$$\psi \leq \psi_2 = \left(\frac{C_a}{\sqrt{2}d}\,\psi_1\right)^{1/2}$$

(A-54)

Table A-3 indicates critical angles for channeling for several common ions implanted at different energies along the major crystallographic axes. The fraction that are channeled can be estimated, as well, by the model that ions approaching within r_{min} of a substrate atom are scattered out of the channel. Assuming a surface density, Nd, in the substrate, the fraction of the random beam (portion scattered out) is

$$f_{random} = \pi\,(r_{min})^2 N\,d(cm^{-2})$$

(A-55)

However,

$$r_{min} \simeq d\,\psi c$$

(A-56)

for small ψc, and thus the channeled fraction is $(1 - f_{random})$.

Although the range distribution for the random fraction may be calculated, the path length traversed by a channeled ion is not as predictable. Due to variable influences of increasing dose and surface disorder (making the lattice more amorphous) and temperature (large vibrational amplitudes of the substrate ions reduce channel size), only the maximum penetration, R_{max}, that a perfectly channeled ion travels is a reproducible calculable number (Figure A-15). Thus, considering the ion beam to separate into independent random and channeled components, the resulting distribution profile of

-278-

Table A-3

CRITICAL ANGLES FOR CHANNELING NEAR
MAJOR CRYSTALLOGRAPHIC AXES OF SILICON
FOR SEVERAL ENERGIES
(Source: Ref. 27)

Ion	Energy (keV)	Channel Direction (degrees)		
		<110>	<111>	<100>
Boron	30	4.2	3.5	3.3
	50	3.7	3.2	2.9
Nitrogen	30	4.5	3.8	3.5
	50	4.0	3.4	3.0
Phosphorus	30	5.2	4.3	4.0
	50	4.5	3.8	3.5
Arsenic	30	5.9	5.0	4.5
	50	5.2	4.4	4.0
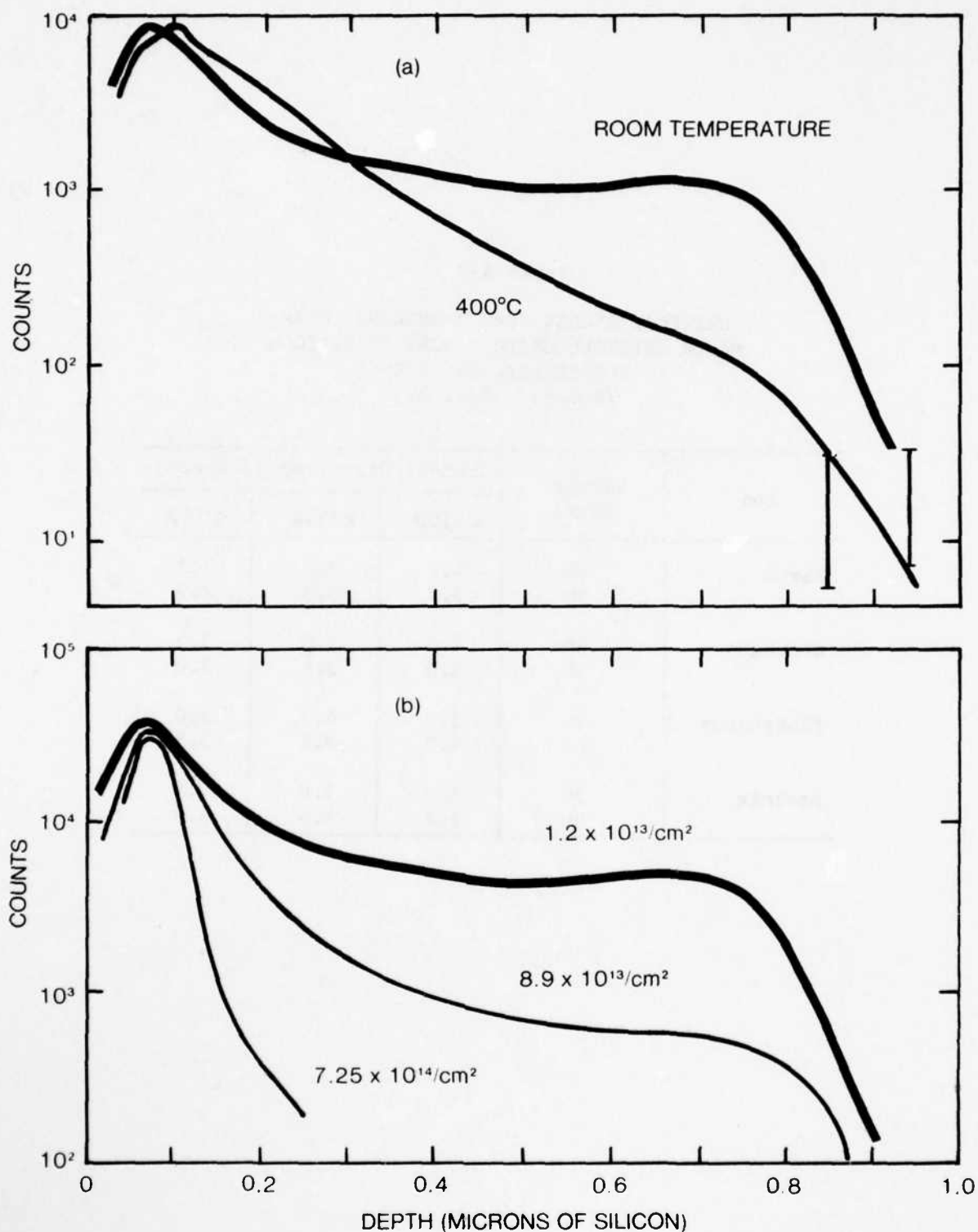
Figure A-15   Distribution Profiles of p+ Ions Implanted in Silicon
at 40 keV Along ⟨110⟩ Axis showing Variation with:
(a) Substrate Temperature and (b) Dose (Source: Ref. 34)

implanted ions is a superposition of statistics for each. This
results in a double peaked distribution, as shown in Figure A-16,
with a fraction, f_{random}, stopped near R_p and $(1 - f_{random})$ stop-
ping near R_{max}, with the area between peaks filled in by other
dechanneled ions (Refs. 24 and 36).

Perfectly channeled ion energy loss through nuclear processes
is negligible; therefore, energy loss may be described by

$$\frac{dE}{dx} \propto S_c(E) \qquad \text{(A-57)}$$

Using the Firsov formula

$$T = \frac{4.3 \times 10^{-8} (z_1 + z_2)^{5/2} \, v}{[1 + 3.1 \times 10^{-7} (z_1 + z_2)^{1/3} \, p]^5}$$

for energy T lost in each collision and substituting $d\Psi_c$ for p and
reduce atomic numbers Z_1' and Z_2', S_e can be estimated. However,
due to oscillations in S_e with Z_1 (Figure A-17), this method is
difficult. A more accurate technique utilizes measured S_e for the
desired ion target and orientation so that:

$$\frac{dE}{dx} = N S_e'(E) = K * E^{1/2}$$

$$\text{(A-58)}$$

and

$$R_{max} = \frac{2}{K*} (E_o)^{1/2}$$

$$\text{(A-59)}$$

where

$$K* = \frac{N S_e'(E_o*)}{(E_o*)^{1/2}} \qquad \text{(A-60)}$$

can be found from measurements performed at energy E_o^*. Thus the
maximum range of a channeled ion can be fond using

$$R_{max} = \frac{2 (E_o*)}{N S_e'(E_o*)} \cdot \left(\frac{E_o}{E_o*}\right)^{1/2} \qquad \text{(A-61)}$$

-281-
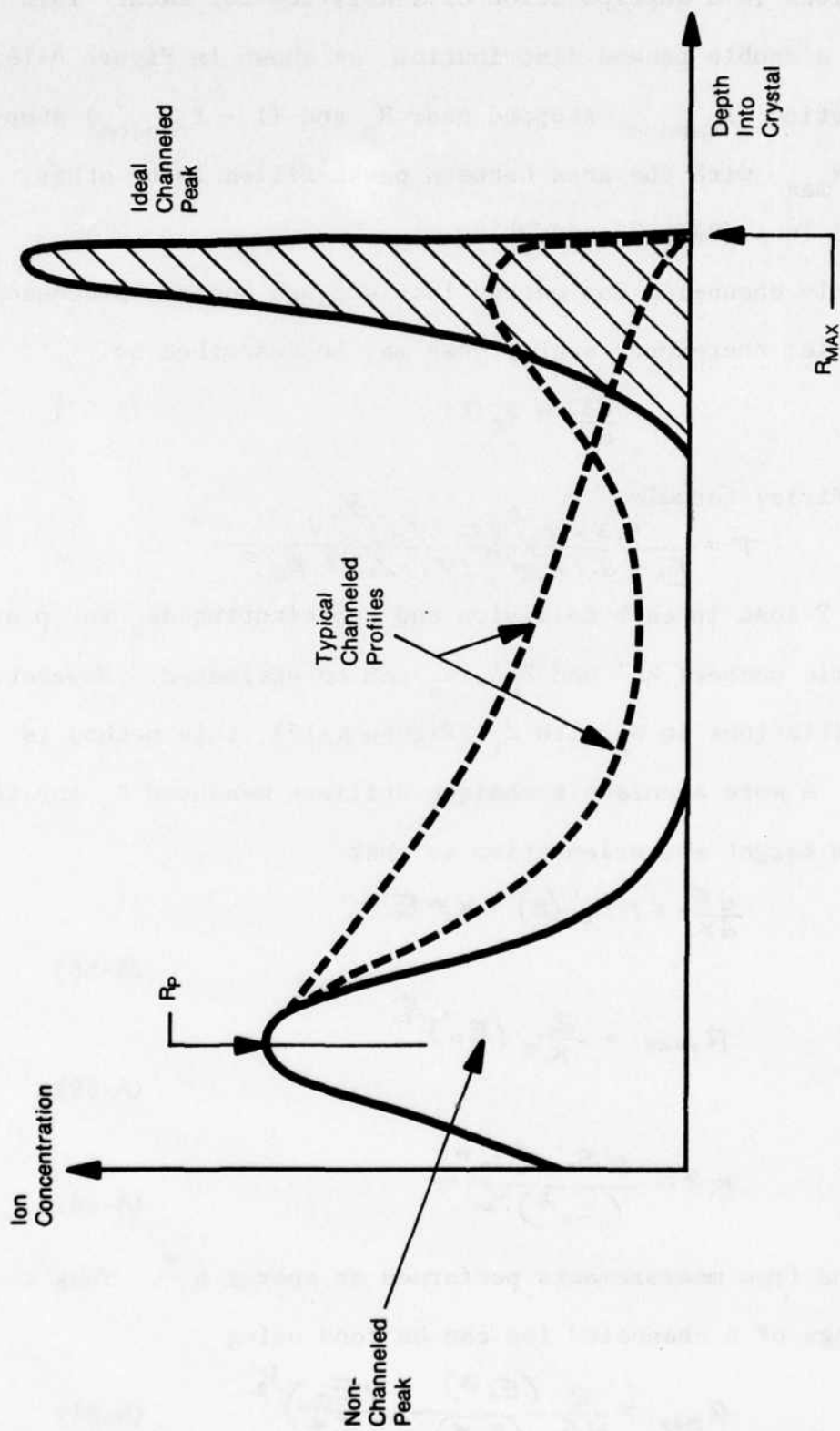
Figure A-16   Distribution of Implanted Ions in Single-Crystal with Ion Beam
Aligned with Major Crystallographic Axis (Source: Ref. 35)
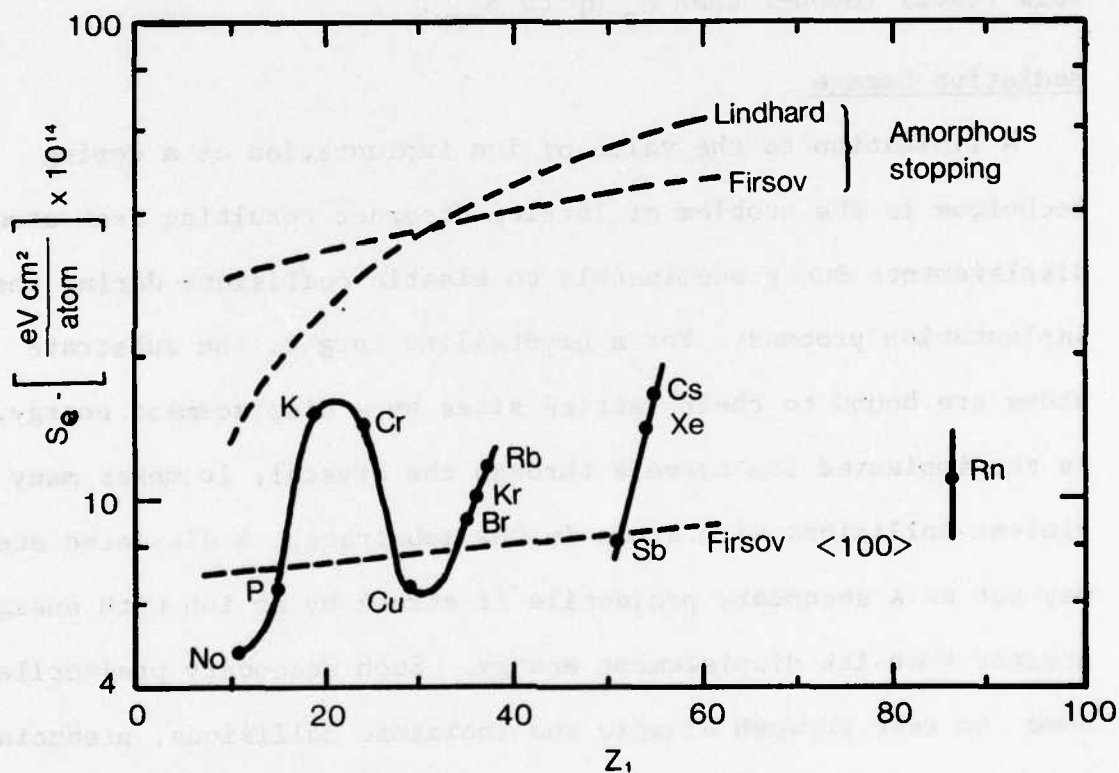
Figure A-17   Electronic Stopping Power as a Function of Atomic
               Number Showing Z_1 Oscillation Phenomena (Source:
               Ref. 37)

Figure A-18 gives R_{max} for various implantation conditions: however, the influence of crystallographic axis direction (varying channel size) is more graphically displayed in Figure A-19. Even when the target crystal is deliberately misaligned to reduce the amount of channeling, some channeling still may occur, causing the formation of tails in the range distribution as ions entering channels travel further than R_p up to R_{max}.

Radiation Damage

A limitation to the value of ion implantation as a doping technique is the problem of lattice disorder resulting from atomic displacements due predominately to elastic collisions during the implantation process. For a crystalline target, the substrate atoms are bound to their lattice sites by a displacement energy. As the implanted ion travels through the crystal, it makes many violent collisions with atoms in the substrate. A displaced atom may act as a secondary projectile if struck by an ion with energy greater than its displacement energy. Such secondary projectiles come to rest through elastic and inelastic collisions, producing another generation of projectiles if they are sufficiently energetic, and so on. Thus the damage production is a cascade process, with the incident ion the primary disorder causing projectile. The extent and character of the disorder zone or cluster are governed by the mass of implanted ion and its energy, the mass of the substrate atom, the ion fluence, and the substrate temperature.
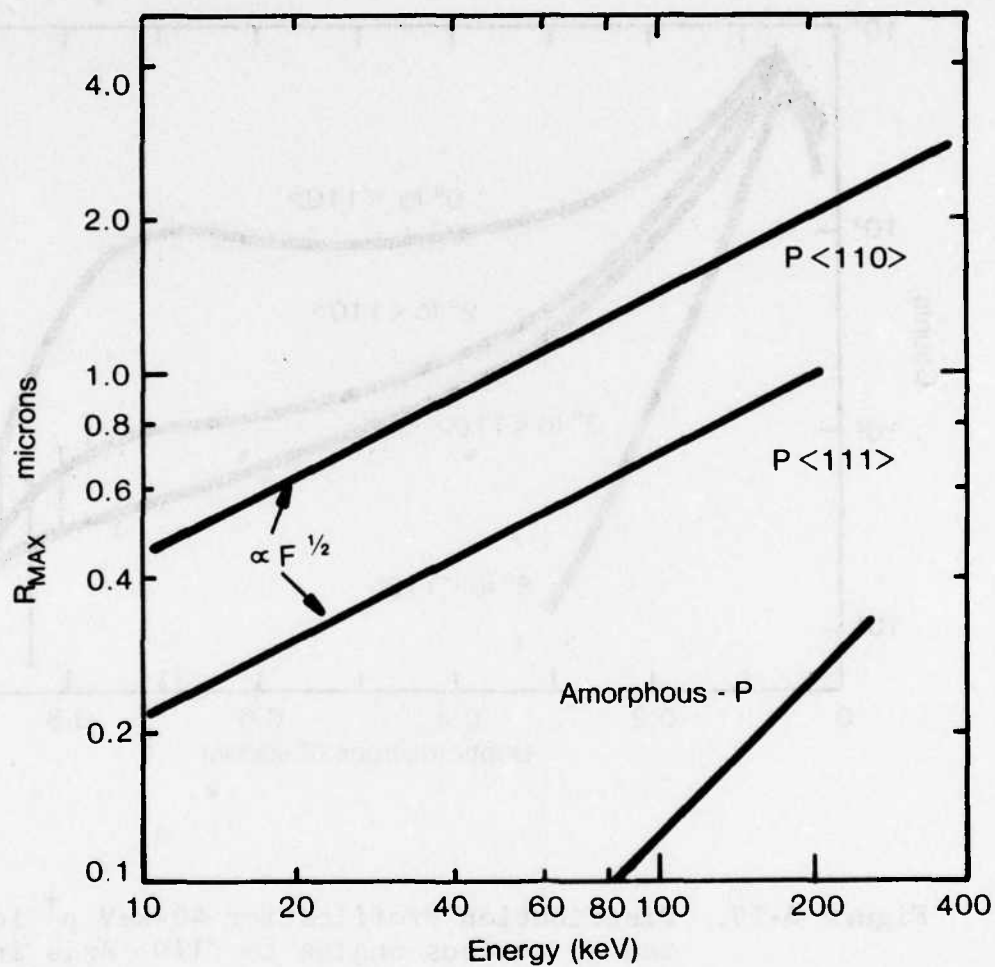
Figure A-18   Experimental Measurements of R_{max} for P Ions in
Silicon as a Function of Energy (After: Ref. 38)
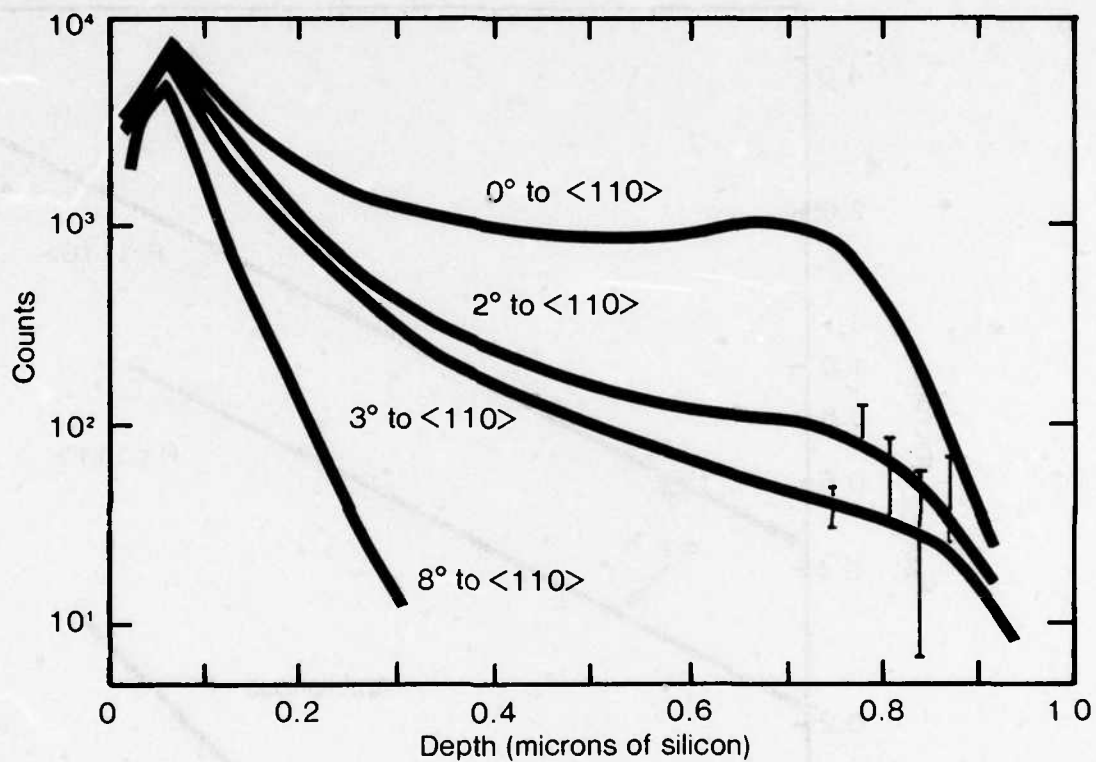
Figure A-19. Distribution Profiles for 40-keV p$^+$ ions implanted at various angles to <110> Axis in Silicon (Source: Ref. 34)

For relatively heavy ions such as phosphorus implanted in silicon, a large fraction of the energy goes into elastic collisions, resulting in more lattice damage. There is a greater tendency for the disorder to occur within a damage core, surrounded by point defects (Figure A-20). These point defects can diffuse away from the core. A considerable portion of the radiation damage stable at room temperature is believed to result not directly from the incident ion impinging, but instead from this migration of defects to nucleation centers.

Lighter ions such as boron lose a large part of their energy into inelastic, electronic processes. Most of the displaced atoms form isolated defects along the ion track (Figure A-21), rather than amorphous zones. Of course the substrate atomic mass is also an important parameter, determining the degree of elasticity in the collisions, depending on whether it / less or more than the incoming ion's mass.

As the fluence or dose of ions is increased, the number of damage zones increases linearly until they apparently begin to overlap, resulting in a continuous amorphous layer (Figure A-22). However, the substrate temperature has a marked effect on the amount of radiation damage produced during the implant process (Figure A-23). At low temperatures, the damage is frozen in as it occurs, and annealing of defects proceeds very slowly. With elevated temperatures, individual disordered zones can anneal, preventing the formation of disorder and resulting in less overall damage.
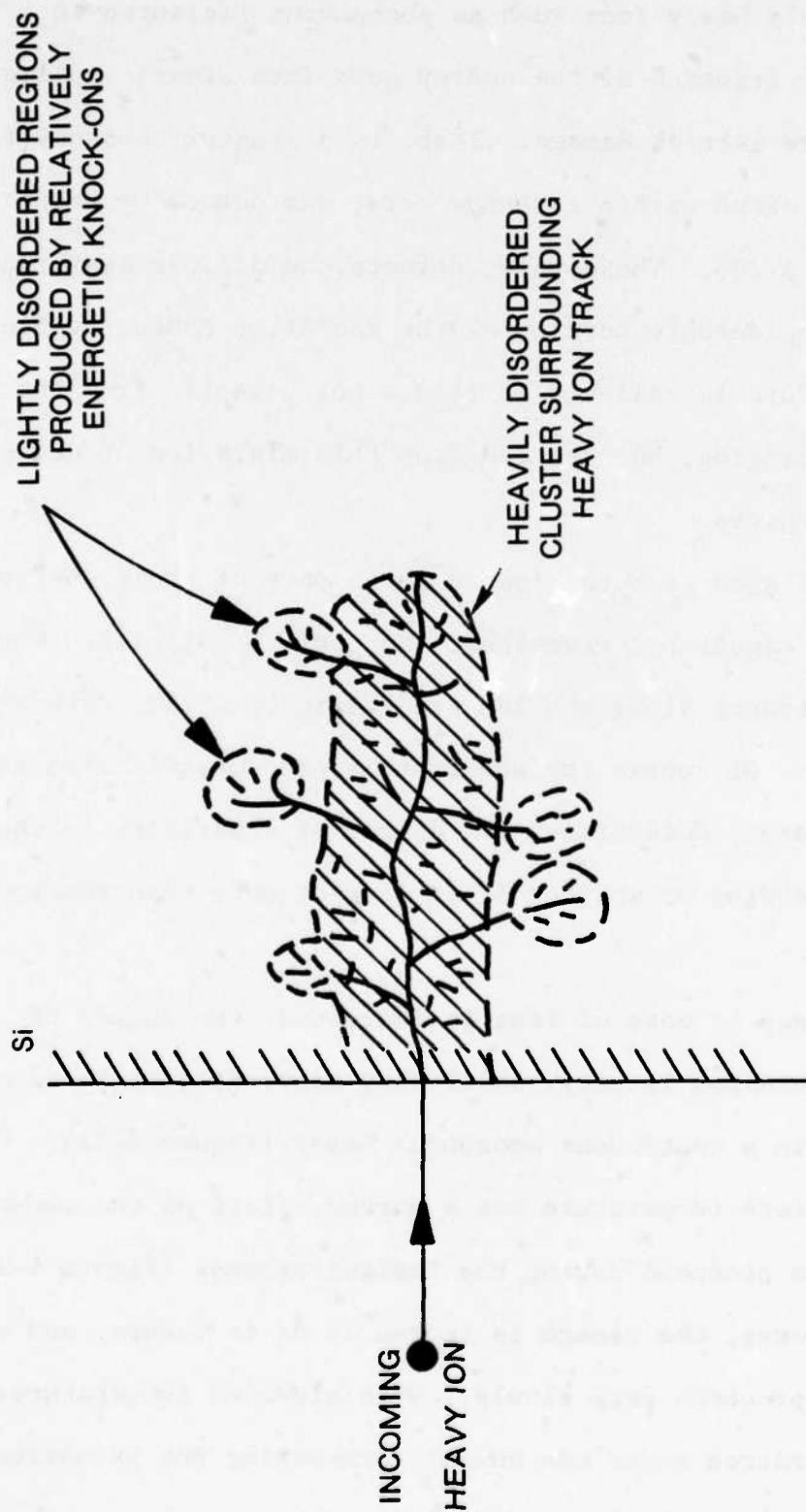
Figure A-20. Damage Cluster Formed by Heavy Ion Implantation
(Source: Ref. 39)
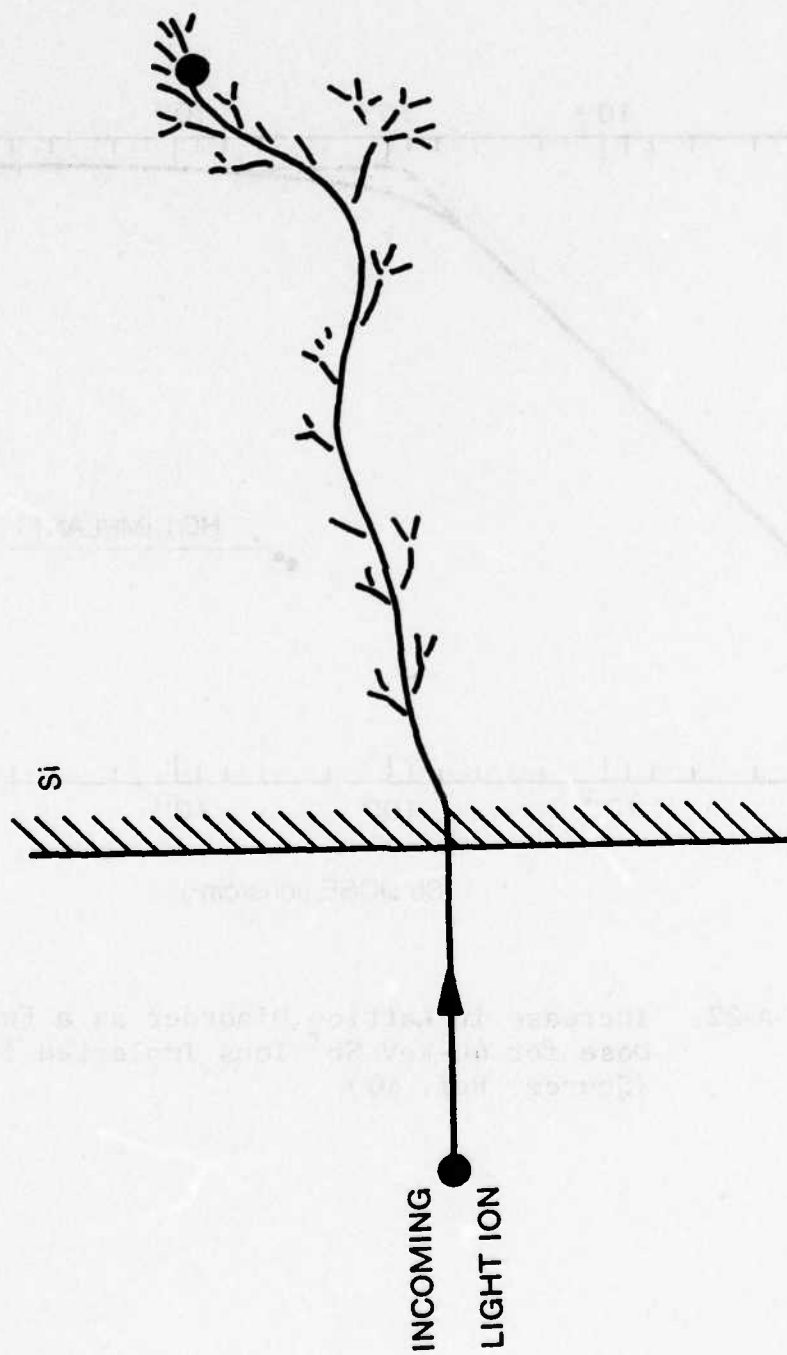
Figure A-21   Damage Track Produced by Light Ion Implantation
(Source: Ref. 39)
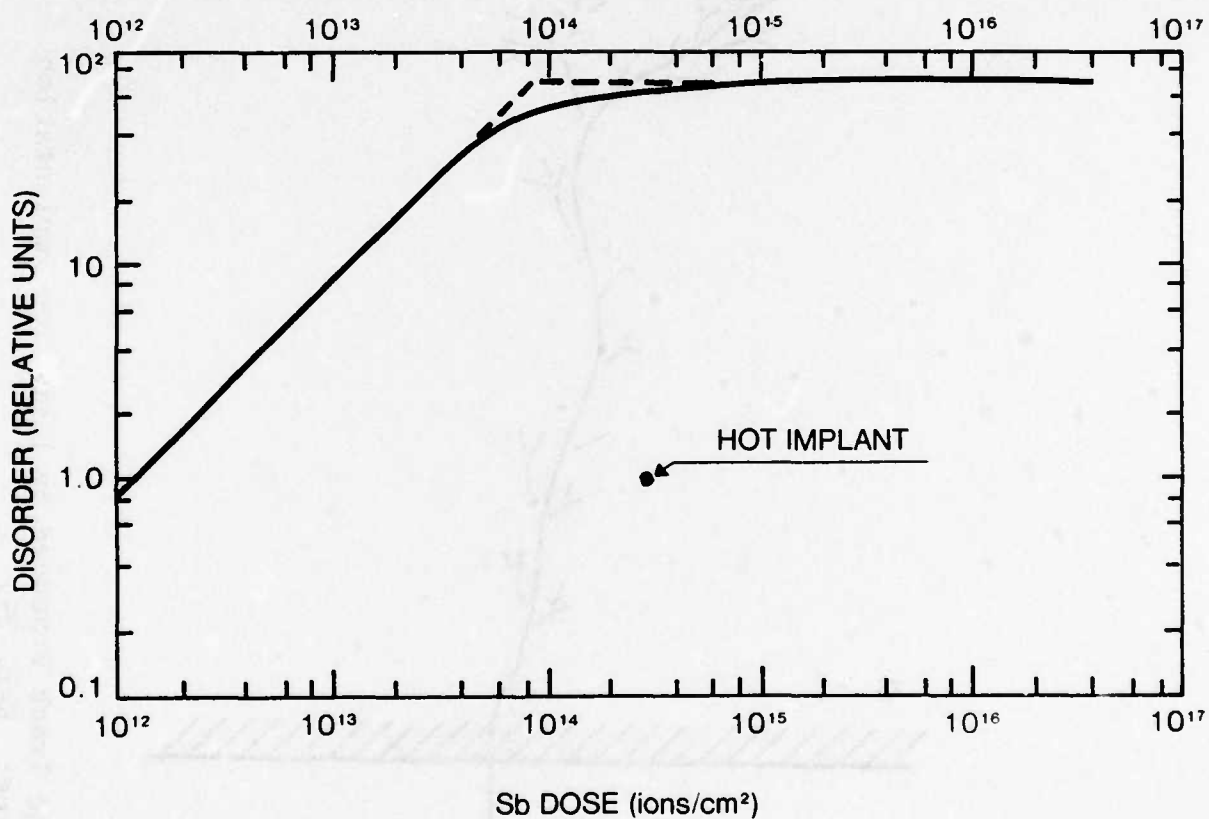
Figure A-22.   Increase in Lattice Disorder as a Function of
Dose for 40-keV Sb⁺ Ions Implanted in Silicon
(Source: Ref. 40)
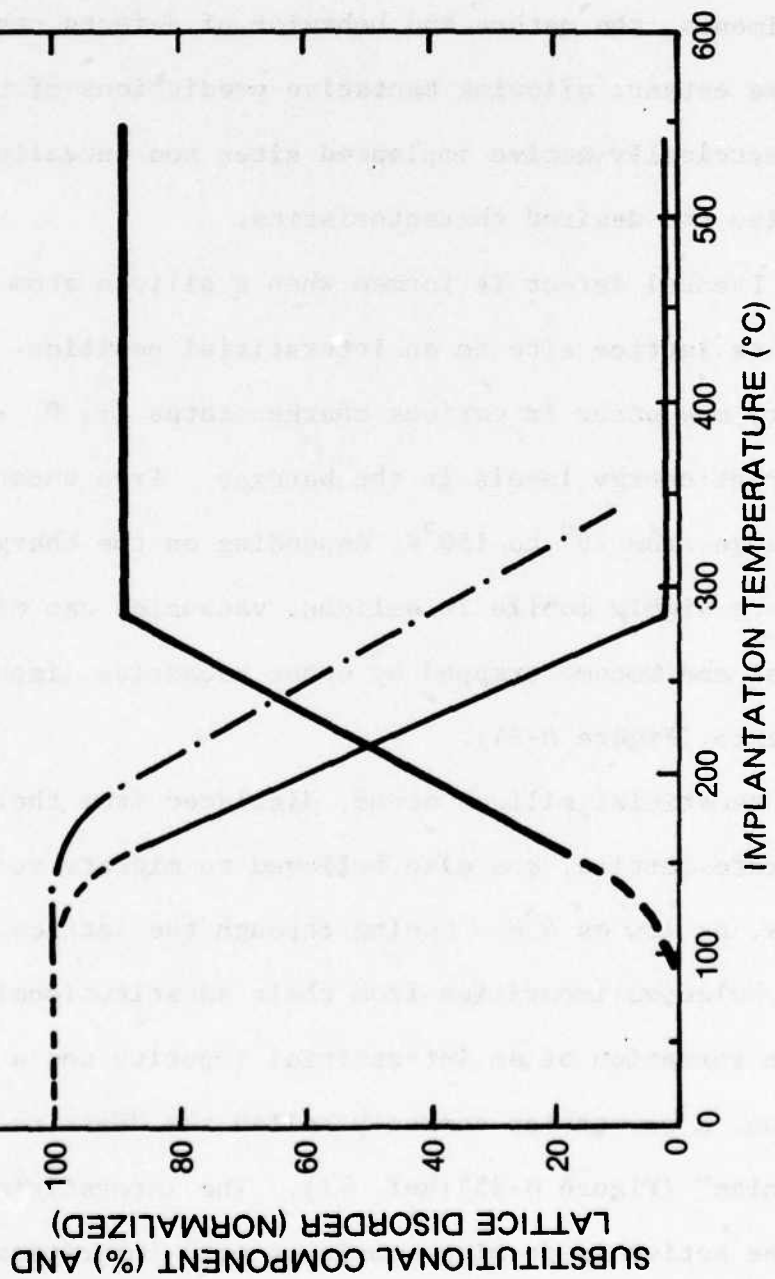
Figure A-23 Disorder as a Function of Implantation Temperature for 40-keV Sb⁺ in Silicon (Source: Ref. 41)

A variety of defects may be generated in the implantation process. These defects have been studied using tools such as EPR, IR absorption, luminescence, channeling and backscattering, transmission electron microscopy, and electrical measurements. Through such experiments, the nature and behavior of defects can be characterized to some extent, allowing tentative predictions of the percentage of electrically active implanted sites and annealing needed to maximize the desired characteristics.

A Frenkel defect is formed when a silicon atom is displaced from its lattice site to an interstitial position. The resulting vacancy may occur in various charge states (+, 0, -, and =) at different energy levels in the bandgap. Free vacancies anneal in the range from 70° to 150°K, depending on the charge state. Because they are highly mobile in silicon, vacancies can migrate through the crystal and become trapped by other vacancies, impurities, or defect complexes (Figure A-24).

Interstitial silicon atoms, displaced from their sites in the substrate lattice, are also believed to migrate at very low temperatures, as low as 4°K. Moving through the lattice, they may displace selected impurities from their substitutional sites, resulting in the formation of an interstitial impurity and a substitutional silicon, a conversion commonly called the "Watkins Replacement Mechanism" (Figure A-25) (Ref. 43). The interstitial silicon may also be active in forming complexes with impurities and other defects.
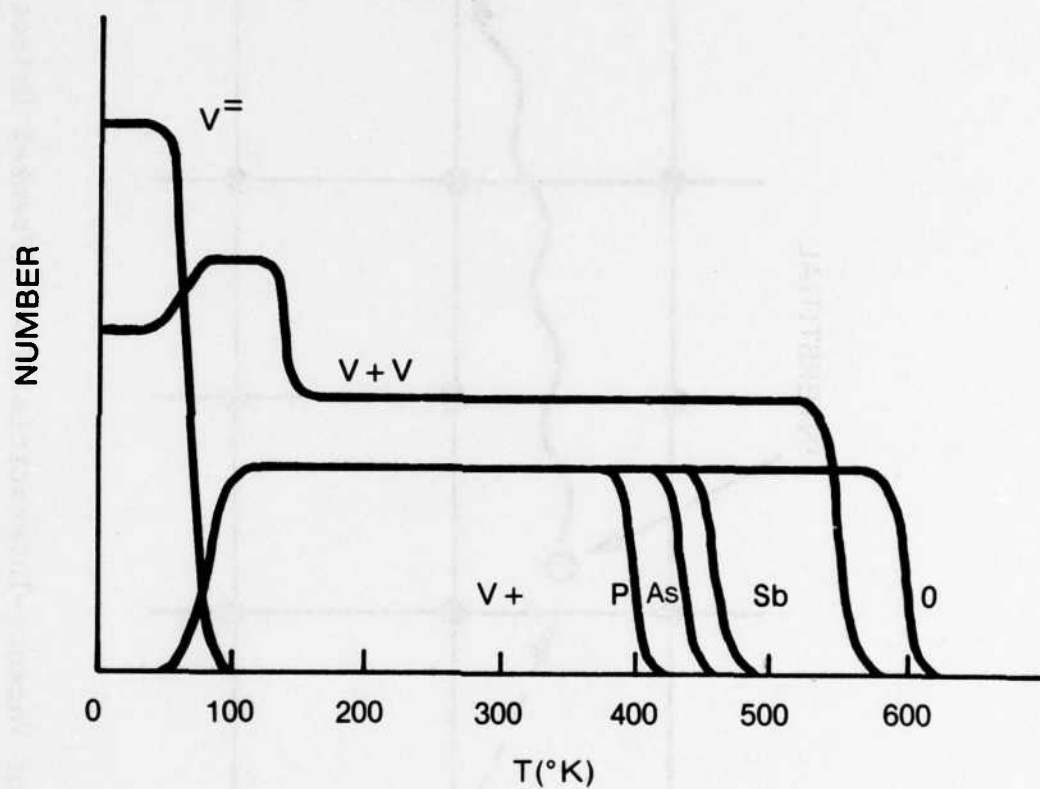
Figure A-24. Annealing Curves for Vacancy Complexes in
Radiation Damaged Silicon (Source: Ref. 42)
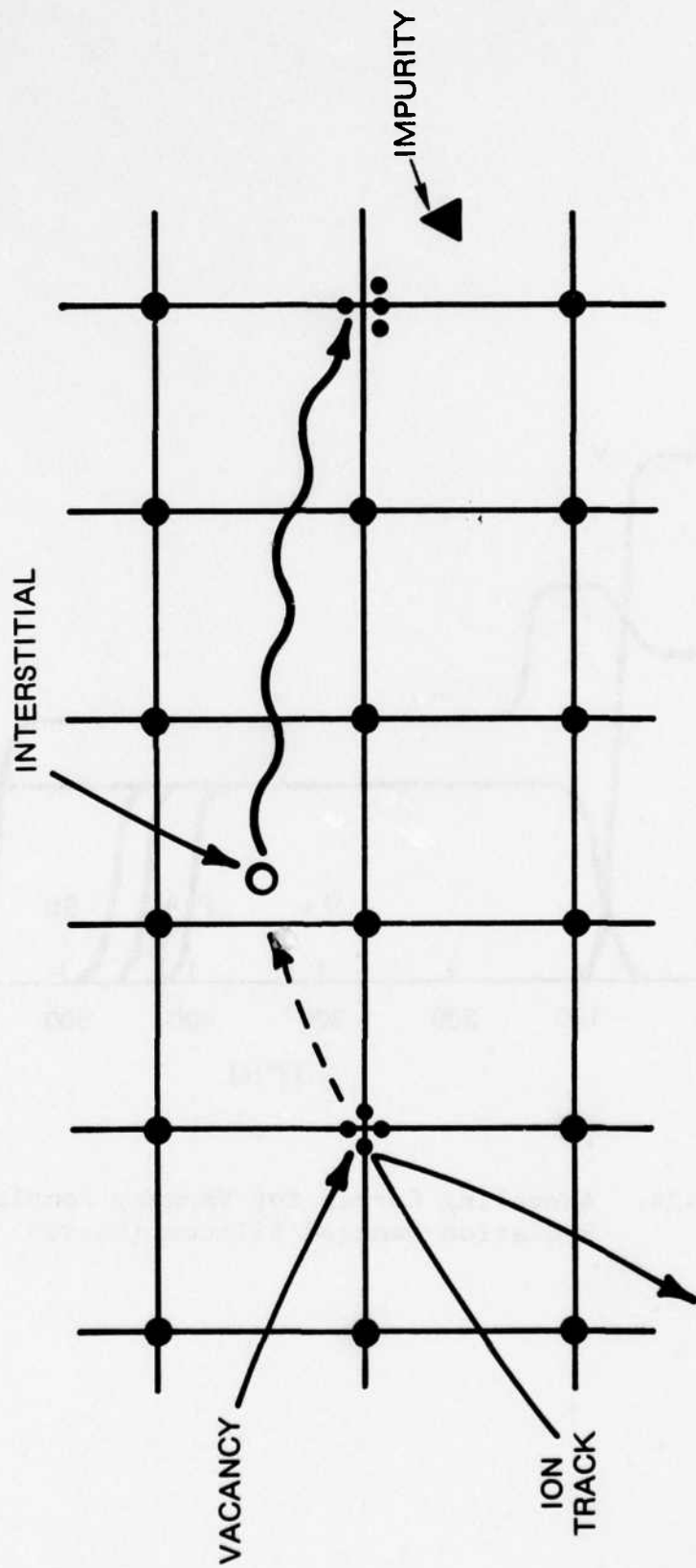
Figure A-25   Formation of Vacancy-Interstitial Pair (Frenkel Defect) and
Subsequent Watkins Replacement Mechanism.   (Source: Ref. 44)

-294-

The divacancy is particularly important in room temperature implanted silicon, because it is stable up to about 550°K. Divacancies may be formed directly when an energetic ion displaces adjoining silicon atoms or when vacancies of the same charge state combine in pairs. Like vacancies, divacancies appear in several charge states.

In addition, a number of more complicated defects are present in implanted material. Many of these defects have been studied through EPR and other measurements and identified as clustered defects and multiple vacancy complexes.

The number of point defects introduced by the implantation process can be estimated by modeling the situation after hard sphere collisions, providing that the incoming ion is not moving too fact, the limiting energy, E_A, for this assumption being

$$E_A = 2 \, E_R \, Z_1 Z_2 \left(Z_1^{2/3} + Z_2^{2/3}\right)^{1/2} \left(\frac{M_1 + M_2}{M_2}\right) \quad \text{(A-62)}$$

where $E_R = 13.6$ eV. This is the Coulomb interaction potential of two screened nuclei. If the incident ion has $E < E_A$. then an estimate for the number of substrate atoms displaced by primary recoils is given by

$$N_d = \frac{E}{2E_d} \quad \text{(A-63)}$$

where

E = Energy of primary recoil

-295-

E_d = Displacement energy of substrate atom (about 15 eV for silicon)

If $E > E_A$, not all of the nuclear interactions cause atomic displacements. For such an energy, E_B or greater

$$E_B = 4 \frac{M_1 M_2}{(M_1 + M_2)^2} \frac{E_A^2}{4 E_d} \tag{A-64}$$

where half of the nuclear collision energy goes into lattice vibrations instead of displacements, the number of displaced atoms is approximately

$$N_d = \frac{E}{4E_d} \tag{A-65}$$

In many situations the electronic stopping power dominates, $E > E_A$. Defining E_C as the energy for which the electronic energy loss is greater than the nuclear loss and E_o, the ion energy, is $\gg E_C$ and E_B, the total number of displaced atoms can be estimated by

$$N_t = \left\{ \frac{P(E_o - E_c) + b E_c}{E_d} \right\} \tag{A-66}$$

where $P \sim 10^{-3}$ and

$$b = 1/2 \quad E_B > E_C \tag{A-67}$$

$$b = 1/4 \quad E_B < E_C \qquad \text{(Ref. 45)} \tag{A-68}$$

and E_C is the energy for $S_n = S_e$.

Such calculations, for example, indicate that a heavy ion such as antimony will at 100 keV produce about 3000 displacements. A

much lighter boron ion of the same energy, which loses most of its energy to electronic scattering processes, produces only 700 displacements, most of which occur near the end of the ion track.

The distribution of defects penetrates, in general, slightly deeper than the actual implanted ion distribution (Figure A-26). Using an approximation to the Thomas-Fermi potential, numerical values for the spatial distribution of radiation damage can be calculated, giving results such as those of Figure A-27. These results exhibit the ratio between the projected range and depth of the damage and the straggling in these in relation to the ratio of the ion to the substrate mass. For relatively light ions, which can undergo wide angle scattering, the peaks for the range and defect distributions occur at nearly the same depth and the distribution shapes are similar, except the damage exhibits less straggling. If the ion is heavy and moving slowly, the ion's penetration depth can be half the disorder depth, since little wide angle scattering can occur and the range straggling is slight. As shown in Figure A-20, the damage for this case is spread along the extent of the ion path.

These defects in the crystalline structure can be healed through annealing for selected times and temperatures. Such annealing may also have the added benefit of increasing the number of electrically active implanted sites in the substrate. While some defects anneal at or near room temperature or below, in general the silicon lattice damaged by ion implantation starts to reorder above $200^{\circ}C$. If the

-297-
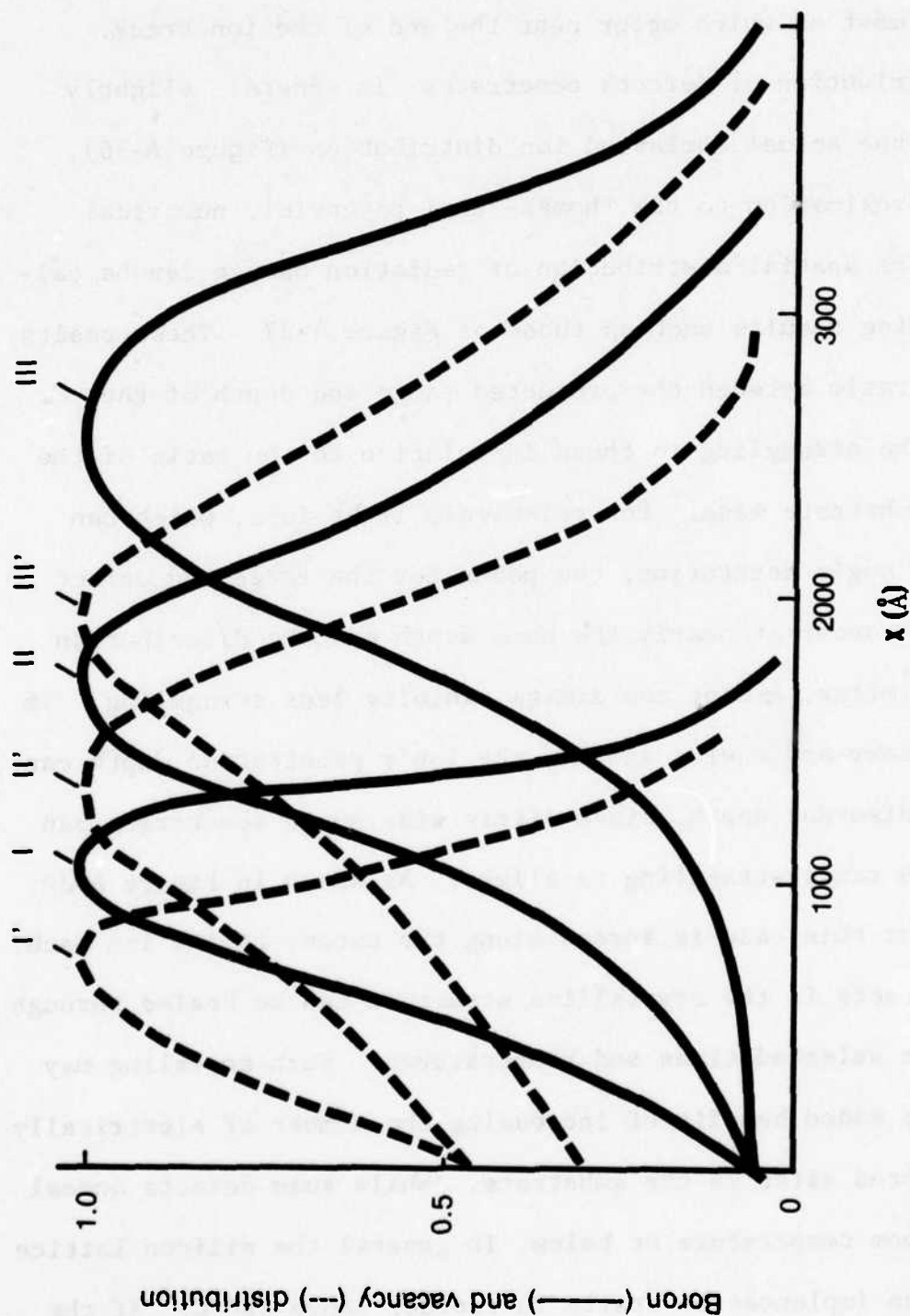
Figure A-26 Distribution of Implanted Boron Atoms (Solid Lines) and Vacancies (Dashed Lines) in Silicon for Ion Energies of 20 keV (I and I'), 40 keV (II and II'), and 60 keV (III and III') (Source: Ref. 46)
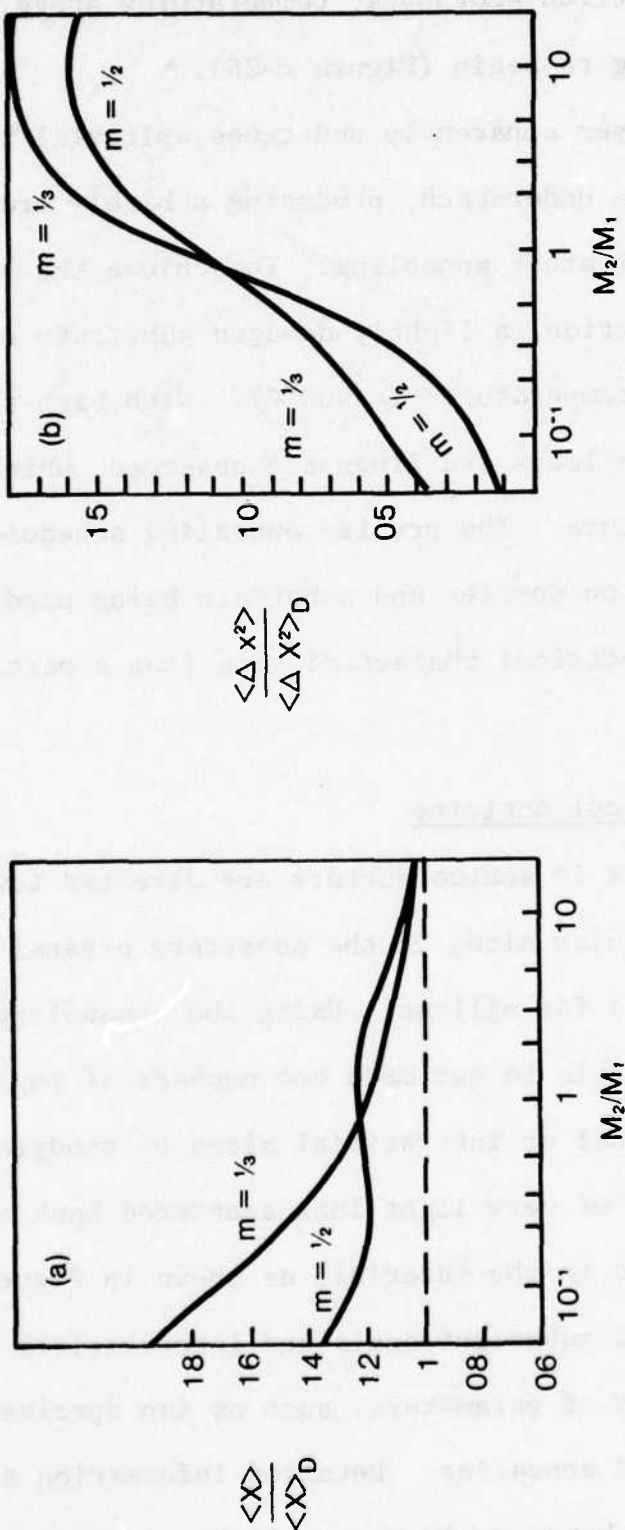
Figure A-27. Ratios of: (a) Projected Range to Damage Depth and (b) Range Straggling to Damage Straggling, as Functions of Substrate-to-Ion-Mass Ratio (Source: Ref. 47)

substrate has been driven amorphous, temperatures above 550°C are needed for reordering to begin (Figure A-28).

The amorphous layer apparently undergoes epitaxial regrowth on the silicon substrate underneath, producing a highly ordered electrically active layer after annealing. To achieve the same degree of crystalling perfection, a lightly damaged substrate would require considerably higher temperatures ($\sim 900^{o}$C). With high-temperature annealing dislocation loops and lines are observed, which increase in size with temperature. The precise annealing schedule followed is dependent on the ion species and substrate being used, in order to obtain maximum electrical characteristics from a particular implant.

Ion Sites and Electrical Activity

Most implantations in semiconductors are directed toward placing dopant ions at particular sites in the substrate crystal lattice, usually substitutional for silicon. Using the channeling phenomena as a tool, it is possible to estimate the numbers of implanted ions occupying substitutional or interstitial sites by studying the directional character of very light ions scattered back by heavier ions already implanted in the material, as shown in Figure A-29.

The proportions of substitutionals and interstitials are highly dependent on a variety of parameters, such as ion species, implant temperature, dose, and annealing. Detailed information allowing accurate estimations, however, is not available in many cases. Table
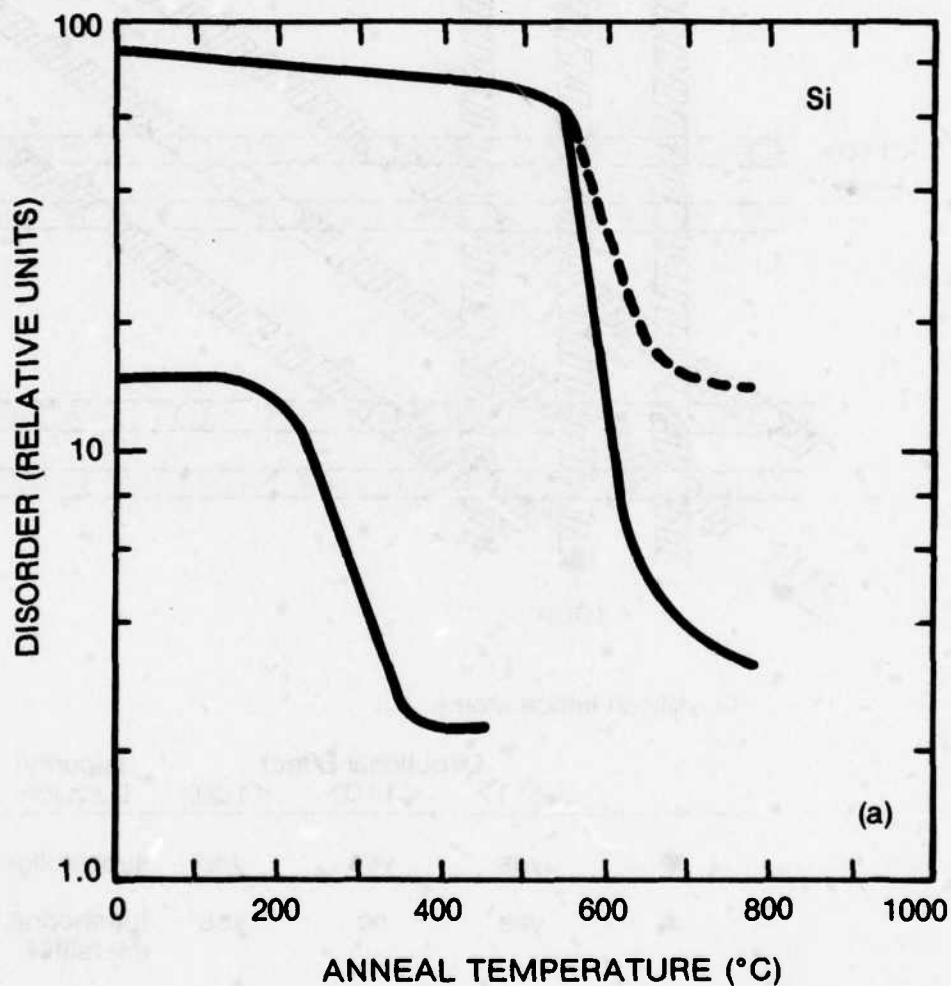
Figure A-28.   Lattice Disorder as a Function of Annealing Temperature for Doses in Silicon of o, 1.1 x 10^{13} Antimony Ions/cm^2; $\bigcirc$, 3 x 10^{15} Antimony Ions/cm^2; $\bigcirc$, 2.6 x 10^{15} Antimony Ions/cm^2;   4 x 10^{14} Ga Ions/cm^2; $\wedge$ 2.5 x 10^{15} As Ions/ cm^2 (Source: Ref. 48)
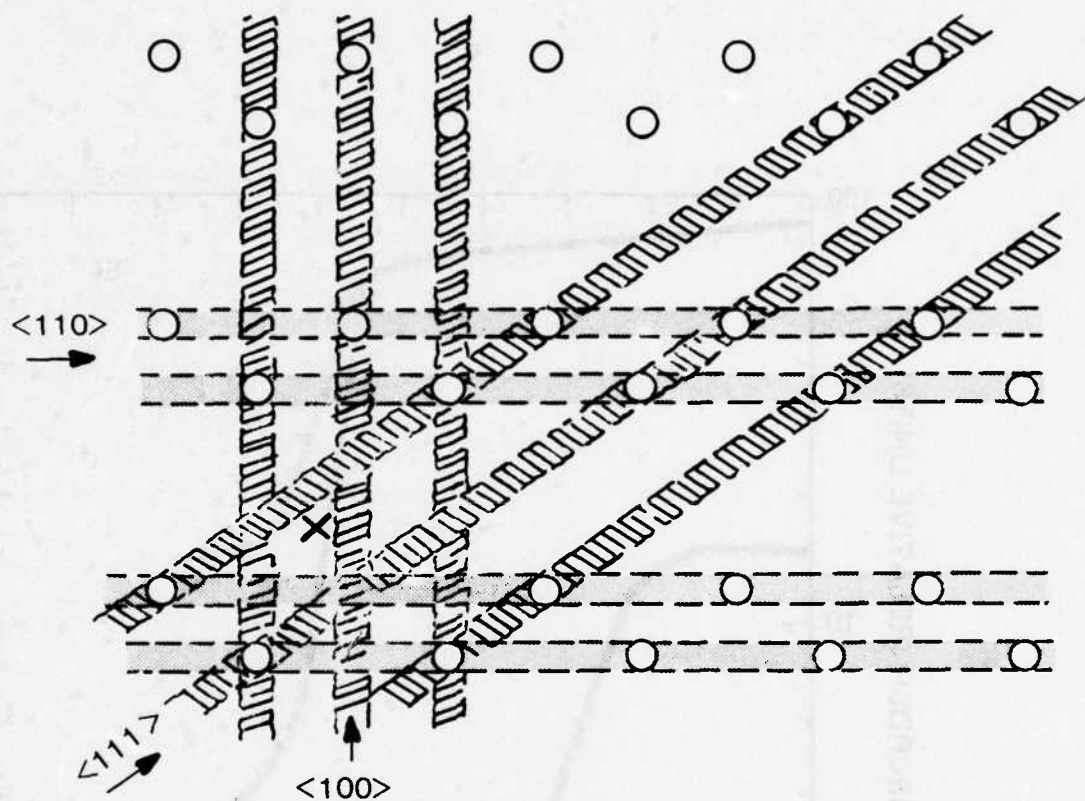
O - silicon lattice atoms

	Directional Effect			Impurity Location
	<111>	<110>	<100>	
●	yes	yes	yes	substitutional
▲	yes	no	yes	tetrahedral interstitial
X	no	no	no	off-lattice site

Figure A-29. Configuration Utilizing Channeling to Determine Impurity atom Locations (Source; Ref. 35)

A-4 indicates some results for hot implants in silicon.

Apparently some correlation exists between the number of sub-
stitutional sites and the chemical as well as electrical behavior
of the implanted ions, particularly if defect impurity interactions
are influential. The perfect substitutional species, in general,
could be expected to exhibit a radius near that of a substrate atom,
a slight variation in electronegativity from the host, and a valence
near that of the target atom. An ion that is stopped in the substrate
has to compete for lattice sites. If the energy needed to form an
interstitial impurity is greater than that needed for an inter-
stitial substrate atom, the ion can move onto an interstitial site.
Due to the lesser valence electron ionization of group III atoms,
silicon interstitials may compete for and win the available substit-
utional sites over some impurities. As the ionic radius increases,
this phenomenon is less marked. Because group V atoms need more
ionization than group IV substrate atoms, these impurities tend to
take up substitutional sites (Ref. 47). However, over a particular
temperature range, impurities may move on or off sites and then
sometimes return, depending on the particular species.

Using Hall effect measurements, a more exact determination of the
number of active ions in the implanted layer than estimations by
impurity locations can be made. The activity level depends not
only on the ion species and substrate temperature during implantat-
ion, but also on the anneal time, dose, and initial substrate resis-
tivity. As the dose is increased, higher annealing temperatures are

Table A-4

LATTICE LOCATIONS OF IONS IMPLANTED AT 350°C INTO SILICON
(I = Interstitial, S = Substitutional (Source: Ref. 49))

II B	III A	IV A	V A	VI A
	Boron	Carbon	Nitrogen	Oxygen
	$I(N) > S$			
	Aluminum	Silicon	Phosphorus	Sulfur
	$I > S$	—	$S > N$	
Zinc	Gallium	Germanium	Arsenic	Selenium
$I > S$	$I \approx S$	$S > N$	$S \gtrsim N$	$S > N$
Cadmium	Indium	Tin	Antimony	Tellurium
$I > S$	$I \approx S$	$S > N$	$S > N$	$S > N$
Mercury	Thallium	Lead	Bismuth	
$I > S$	$S > I$		$S(N) > N$	--

-304-

needed, in general, to achieve maximum activity, unless the substrate is driven amorphous. As the amorphous layer regrows through an epitaxial process, high electrical activity is possible as the damage anneals at lower temperatures. Increasing the implantation temperature often increases the temperature requirements for maximizing activity as well as reducing radiation damage.

Implanted layers usually show increased electrical activity for anneals above 300°C as the defects around the ion diffuse. However, annealing is not always necessary, because boron, for example, produces type conversion immediately after room temperature implantation. For most ion species, 900°C annealing maximizes the carrier density. As more implantation phenomena are studied, the mechanisms involved in determining the activity level of implanted ions will be better understood, and patterns in maximizing the number of carriers can be discerned.

Appendix B

ELECTRON PENETRATION INTO SOLIDS

(Summary of Experimental and Theoretical Understanding)

This appendix provides a brief overview of the present under-
standing of electron penetration into solids (and gases), with
emphasis on lateral scattering and energy deposition profiles at
beam energies less than 10 keV in low-z materials.

Historically, much of the early theoretical work in this area
was motivated by beta ray experiments, where the electron energies
are approximately 1 millen eV, and in more recent times by trans-
mission electron microscopy in the energy range of 30 to 100 keV.
Interest in energies below 10 keV was primarily motivated by a
desire to check certain aspects of the higher energy theories over
a wider energy range. More recently, interest in electron beam
lithography has generated renewed interest in this energy range.

Most experimental measurements have concentrated on secondary
emission, backscattering, and transmission through thin foils. Measure-
ments of lateral scattering are rare, because of their obvious diffic-
ulty.

When electrons penetrate a solid target, they can be scattered
either elastically or inelastically. Elastic collisions are primar-
ily due to the screened nuclear field and can result in large angle
(> 90 degrees) deflections, although most are smaller angle deflec-
tions. Inelastic collisions are primarily electron-electron events

that result in a substantial energy loss ($\sim$100 eV) but smaller
angular deflection, because of the small electron mass. Hence
the electron penetration process can be modeled as independent,
large angle, elastic scattering and zero angle inelastic scattering.

Inelastic collisions are generally treated in the continuous
energy loss approximation (Ref. 50). It was shown that the rate of
energy loss per unit of actual path length, s, is given by (Ref. 51):

$$-\frac{dE}{ds} = \frac{2\pi e^4 N_A \rho}{E}\left(\frac{Z}{A}\right) \ln\left(\frac{2E}{I}\right) \quad (B-1)$$

This formula is essentially exact for hydrogen, where the elec-
tron wave functions are known. For more complex atoms, it is only
a generalization. N_A is Avagadro's number, ρ is the mass density,
Z the atomic number, and A is the atomic weight. I is the mean
excitation energy (I $\sim$11.5 Z eV). The total path length, S,
traversed by an electron, slowing down from energy E_1 to E_2 is then
given by:

$$S = \int_{E_1}^{E_2}\left(\frac{dE}{ds}\right)^{-1}dE \quad (B-2)$$

A useful approximation to s is the Webster law (Ref. 52):

$$S = \frac{0.33 \times 10^{-5} A}{\rho Z}\left(E_1^{1.7} - E_2^{1.7}\right) \quad (B-3)$$

where ρ is given in g/cm^3, E in keV, and s in cm. Slight variations
on this relation are common to most theoretical treatments.

The elastic scattering is generally treated as Rutherford scattering from a screened Coulomb field. An example of such a calculation is due to Wentzel (Ref. 53); in which Cosslett and Thomas assumed an exponential screening field. They found the differential cross section/solid angle to be:

$$\frac{d\sigma}{d\Omega} = \frac{(Ze)^2}{4E_0}\left(\sin^2 \frac{1}{2}\Theta + \frac{1}{4}\Theta_0^2\right)^{-2}$$

(B-4)

where $\Theta_0 = 3.69 \times 10^{-2} Z^{1/3} E^{-1/2}$, with E in keV. For Z = 10, E = 10 keV and $\Theta_0 = 0.07$ radian.

Many theoretical models for electron penetration have been built on variations of these two equations. Among them are References 50, 52, and 55 through 69.

Most of these studies have attempted to describe x-ray production as a function of depth, secondary emission, and backscattered electrons. No attempt has been made to predict lateral scattering, although many models contain lateral scattering information. In these types of models, the electrons penetrate depth x_d into the material, losing energy according to the Bethe law and scattering according to a screened Coulomb cross section. At depth x_d, the scattering has essentially randomized the directions of the electrons. From this depth the electrons diffuse into a sphere, still losing energy according to the Bethe law. The treatment of the diffusion is, of course, difficult because the scattering events are not random in angle, so a Boltzmann equation is required. This

-309-

type of approach has been used by Bethe, Rose, and Smith (Ref. 60),
Brown and Ogilvie (Ref. 67), and Bennett and Roth (Ref. 68) to study
dE/dX, X-ray production, and secondary electron emission. In all
cases, only the variation with penetration depth was studied; how-
ever, the models contain lateral scattering information if it can
be solved. The division by Archard into penetration to diffusion
depth x_d and then radial diffusion from this point seems especially
promising, because then the Boltzmann equation has radial symmetry.

More sophisticated recent attempts to improve on this type of
approach are the plural scattering model of Greeneich and Van Duzer
(Ref. 70) and the multiple scattering model of Hawryluk et al. (Ref.
71). These models have been solved for lateral scattering information.
The work to date has been restricted to beam energies at or above
10 keV.

Monte Carlo calculations have also been applied with some success.
Among these are the calculations of Lifshin and Bolon (Ref. 72) of
Corporate Research and Development and Hawryluk et al. (Ref. 71).
Again the problem is that these calculations have not been applied
below 10 keV. Bolon feels that the Monte Carlo programs as
presently written may not be valid below 10 or 15 keV, because of
the simplified scattering laws used.

Experimental Knowledge: Energy Deposition Profiles and Electron Range

The dE/dx is defined as the energy deposited per unit of

penetration (x) into the material by a focused or defocused

electron beam incident on a flat, thick target. A typical plot

of dE/dx versus x is shown in Figure B-1. The linear portion of

the dE/dx curve is characteristic of electron penetration, and its

extrapolation defines the so called Grün range, $R_G(E)$. This is <u>not</u>

the definition of extrapolated range usually applied in electron

beam studies.

Typically measurements are made on thin foils, and the extra-

polated range is defined as the extrapolated thickness that reduces

the most probably transmitted electron energy to zero (Thomson-

Whiddington range R_{TW}), the mean energy to zero (R_m), or the extra-

polated beam energy, E_c, which reduces the number of transmitted

electrons to zero $R_X(E_0)$. Ranges based on energy, such as R_G, are

more relevant for devices that are sensitive to energy, but because

many published results are in terms of number ranges, they will also

need to be referred to.

In Figure B-2, ranges are shown as measured by several inves-

tigators using various methods. Because the definition of "range"

is not the same in all cases, exact numerical agreement is not to be

expected. However, all ranges scale approximately as $E^{1.75}$. This

is confirmation of the integral, S, of the Bethe energy loss relation,

because those electrons that penetrate farthest into the target suf-

fer few large angle scatterings, so $S \cong$ range. Note also that the

ranges are essentially independent of the atomic number, because the

Bethe energy loss mechanism depends primarily on the electron density
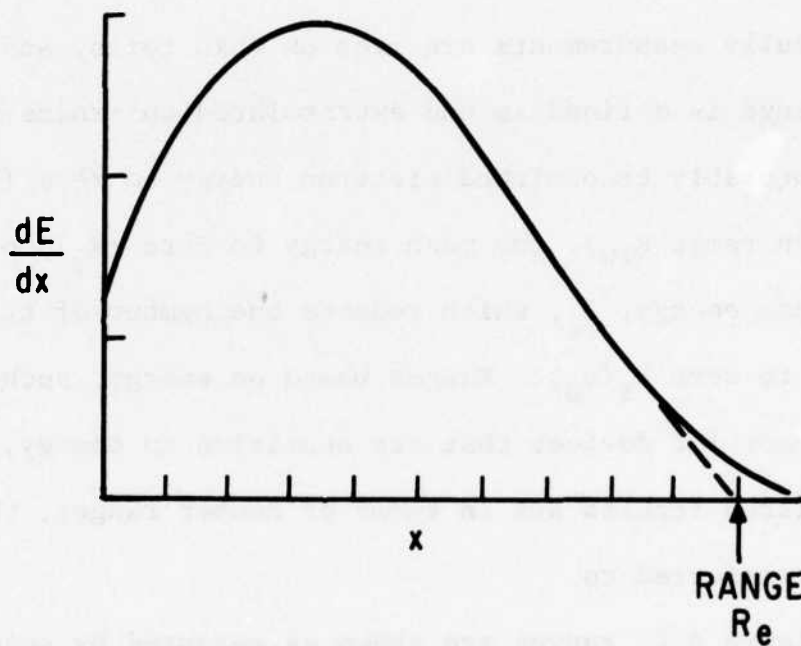
Figure B-1   General Shape of dE/dx Curves and Definition
of Grün Range

A) KANTER and STERNGLASS   NO. TRANSMISSION - R_x
B) COSSLETT and THOMAS

C) GRUN
D) EVERHART and HOFF   ENERGY ABSORPTION - R_e
E) COHN and CALDONIA

F) COLE   NO. TRANSMISSION - R_x

Na GAS (C) 5-50 kv

SiO$_2$ (D)

(F)

Au (B)

Al (A)

Au (A)

N$_2$ GAS (E)

COLLODIAN (F)

RANGE - $\left(\dfrac{mg}{cm^2}\right)$

E PRIMARY (kev)

Figure B-2   Electron Ranges in Solids and Gases

-313-

of the substance and is independent of Z (Z/A ~ 2). Feldman (Ref. 73) did find a strong variation in $_0R$ with Z, but his measurement technique was shown to be incorrect by Kanter and Sternglass (Ref. 74).

Measurements of dE/dx (x) are less common. The earliest are those of Grün Range (Ref. 75), who measured the fluorescent radiation from nitrogen gas at pressures of approximately 1/2 atm in the energy range of 5 to 50 keV. Cohn and Caledonia (Ref. 76) repeated these measurements between 2 and 5 keV, with $_0$ approximately 2 torr, and found very similar results, even though the dominant fluorescent energy mechanism is different at the reduced pressure. Everhart and Hoff (Ref. 77) measured dE/dx by an induced conductivity method in metal-SiO_2-Si capacitors between 5 and 25 keV. Possin and Norton (Ref. 78) measured dE/dx using enhanced etching in polym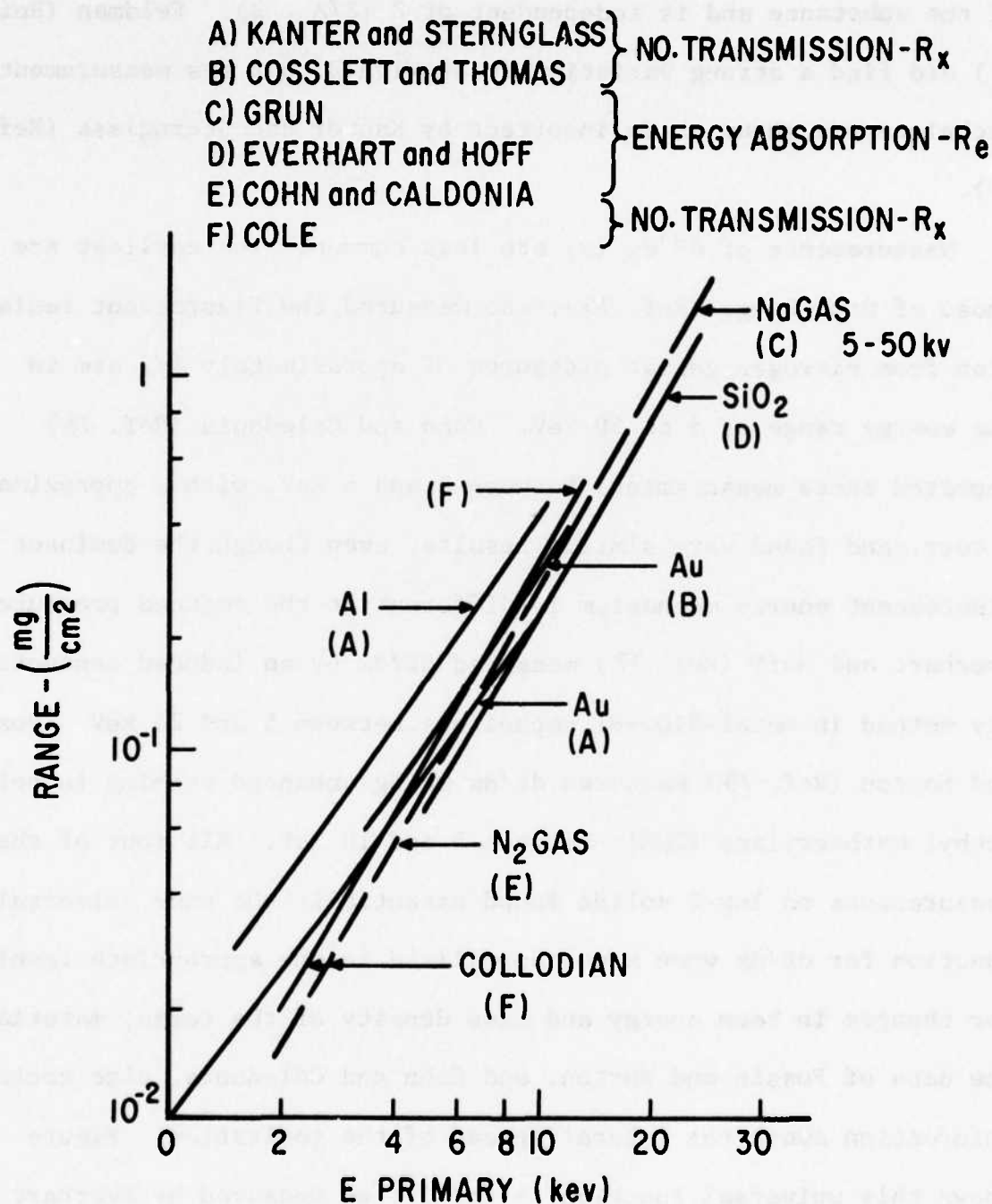ethyl methacrylate (PMM), between 5 and 10 keV. All four of these measurements on low-Z solids found essentially the same universal function for dE/dx when x was normalized in the appropriate fashion for changes in beam energy and mass density of the target material. The data of Possin and Norton, and Cohn and Caledonia, also contain information about the lateral spread of the ionization. Figure B-3 shows this universal function, λ (z/R_G), as measured by Everhart and Hoff and Grun.

Function dE/dx is given by:

$$-dE/dx = +(E_0/R_G)\,\lambda(x/R_0) \qquad (B-5)$$
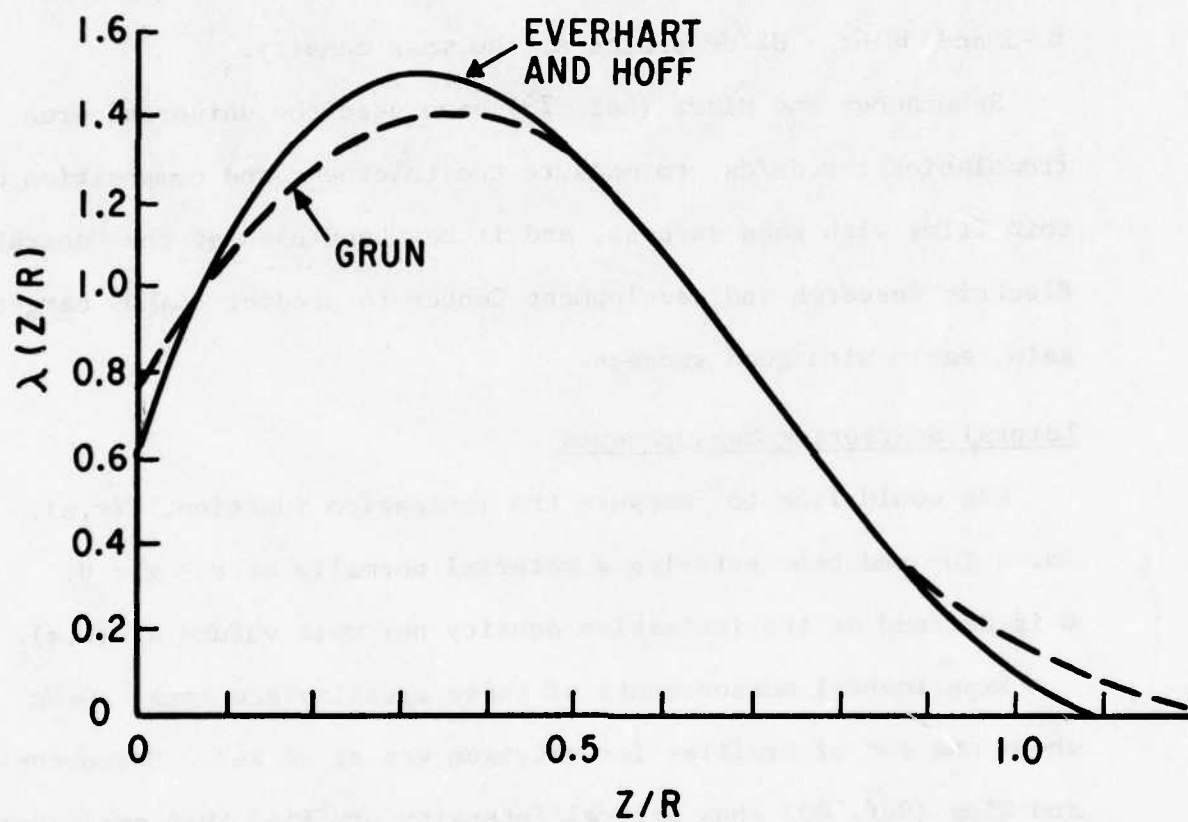
-314-

EVERHART AND HOFF

$\lambda(Z/R)$

GRUN

Z/R

Figure B-3   Empirical Universal Function $\lambda(Z/R)$

where Grün range $R_G = \beta E_0^{1.75}$ and E_0 = beam energy in keV. (B-6)
Constant β, as determined by the various investigators, varies bet-
ween 4.0 and 4.57 x 10^{-6} g/cm^2 as summarized in Table B-1. The
materials studied were N_2 gas, PMMM, and SiO_2. No dependence on
atomic number was found, as indicated by the form of Equations
B -5 and B -6; - dE/dx scales as the mass density.

Schumacher and Mitra (Ref. 79) have used the universal Grun
fromulation for dE/dx, to measure the thickness and composition of
thin films with good success, and it has been used at the General
Electric Research and Development Center to predict BEAMOS target
gain, again with good success.

Lateral Scattering Measurements

One would like to measure the ionization function, $G(r,z)$,
for a focused beam entering a material normally at $r = z = 0$.
G is defined as the ionization density per unit volume at (r,z).

Experimental measurements of these profiles are rare. Grün
shows one set of profiles for nitrogen gas at 32 keV. Ehrenberg
and King (Ref. 80) show several intensity profiles that are integrals
of G along the viewing direction. These profiles are, unfortunately,
only sketches.

Cohn and Caledonia measured G by electron beam induced fluor-
escence in nitrogen. This experiment is shown schematically in
Figure B -4.

A focused electron beam enters nitrogren gas at a low pressure,

Table B-1

GRÜN RANGE MEASUREMENTS

$(R_G = \beta E_B^{1.75}$ E_B = Beam Energy in keV)

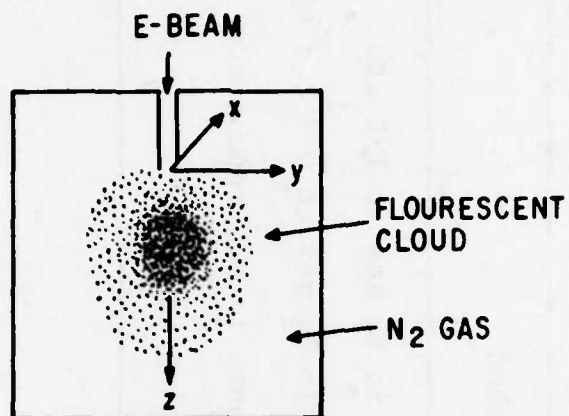| β ($\mu g/cm^2$)	Reference	Method
4.57	A. E. Grün, 1957	Luminescence in N_2 gas at 1/2 atm
4.27	Cohn and Caledonia, 1970	Luminescence in N_2 gas at 0.7-2.8 torr
4.0	Everhart and Hoff, 1971	Induced currents in MOS capacitors
4.1	Possin and Norton, 1975	Enhanced etching in PMM

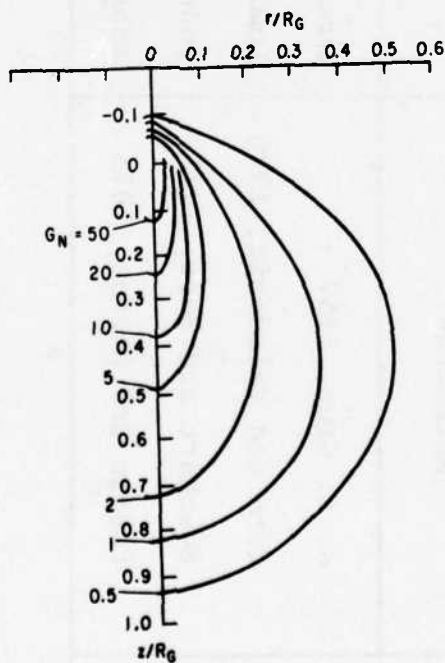Figure B-4   Arrangement for Gas Scattering Experiment

Figure B-5   Normalized Isointensity Plot of G_N (Ref. 55)

approximately 2 torr. The size of the luminescent cloud is approx-
imately 20 centimenters. Using a photomultiplier, Cohn and Caledonia
scanned the cloud in y and z, obtaining the sidewise intensity pro-
files, $I(y,z)$:

$$I(y,z) = \int_{-(L^2-y^2)^{\frac{1}{2}}}^{+(L^2-y^2)^{\frac{1}{2}}} G(r,z)\,dx \qquad (B-7)$$

By Abel inversion, I can be inverted to give $G(r,z)$:

$$G(r,z) = \pi^{-1} \int_{y}^{L(z)} \frac{dI(y,z)}{d(y^2)} \cdot \frac{d(y^2)}{(y^2-r^2)^{\frac{1}{2}}} \qquad (B-8)$$

The crosswise intensity profiles, $T(z)$:

$$T(z) = 2\pi \int_{0}^{L(z)} G(r,z)\,r\,dr = 2 \int_{0}^{L(z)} I(y,z)\,dy \qquad (B-9)$$

are proportional to the dE/dz depth profiles measured by Grün,
Everhard and Hoff, and Possin and Norton, and they agree well with
these other data.

The $G_N(r,z)$ profiles that they found are reproduced in Figure
B-5. They found that they obtained the same profiles (for electron
beam energies between 2 and 5 keV) if all distances were scaled to
the electron range, as defined by Grün. Unfortunately some prob-
lems exist in their analysis. The cutoff in their inversion inte-
grals, $L(z)$, was apparently determined from the scope traces where
the intensity, $I(y,z)$, fell to zero. However, an oscilloscope trace
only resolves zero to about 2 percent of the full scale, unless scale

-319-

changes were used. Cohn and Caledonia claim to have determined variations of G of at least x 200. Hence it would be necessary to measure changes in I(y,z) of at least x2000, because of the $2\pi r$ factor in the integrals.

To see this problem more clearly, consider calculating the Grün $T(z) \alpha \lambda(z/R)$ from their data. To do this graphically, one first plots $F = G_N(r/R,z)r/R$ and then integrates:

$$T(z) = \int_0^\infty F\left(\frac{r}{R}, z\right) d\left(\frac{r}{R}\right)$$

(B -10)

Plots of $G_N(r/R,z)r/R$ for several values of z are shown in Figure B -6. The curves are cut off at the last data point given by Cohn and Caledonia. Clearly, from Figure B-6, the data given in the paper do not extend to large enough values of r/L to perform the normalization integral or the inversion integral. However, some of the reduced data in the paper (particularly their Figures B -7 and 8) indicate that their data extend further than indicated by Figures B -5 and B -6, so their data may be more valid than indicated by this critique. We will return to this later.

Possin and Norton (Ref. 78) of General Electric Corporate Research and Development measured the lateral scattering of 5- and 10-keV electron beams by the enhanced etching method in PMM. This approach was originally proposed by Hatzakis; the method is described in Reference 78. The results are shown in Figures B-7 through B-9 for the line ionization distribution I(x,z) at 5 and 10 keV. Constant
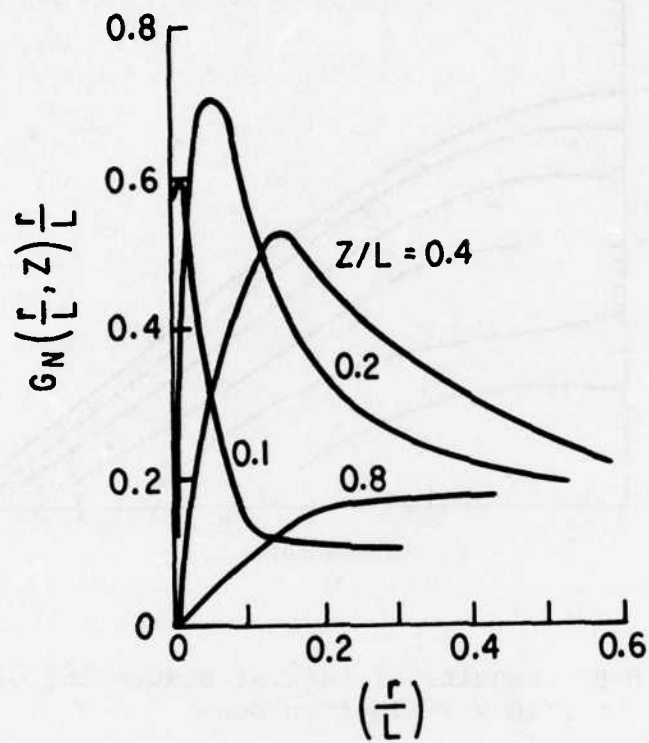
Figure B-6 $G_N(r,z)$ Profiles
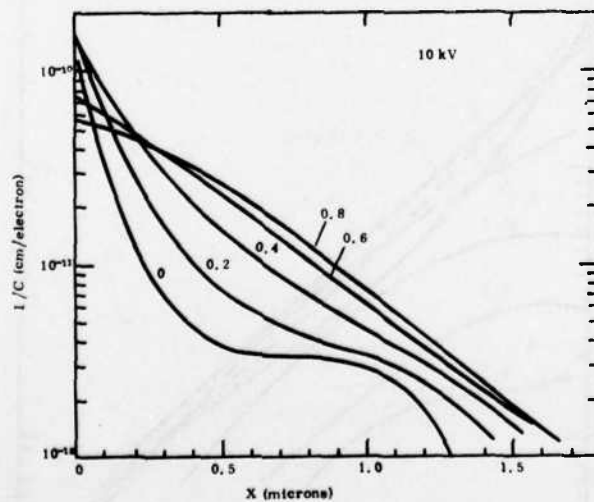

Figure B-7   Results of Lateral Scattering of 10-keV Electron Beam
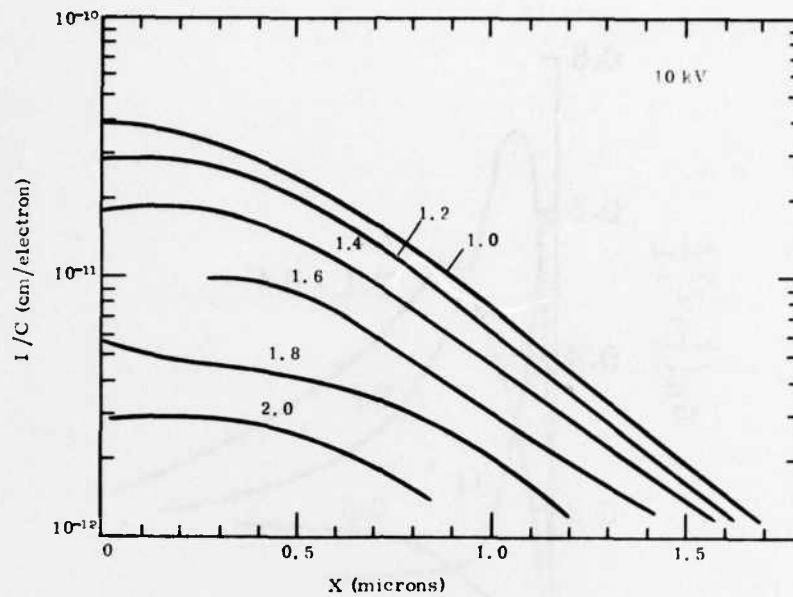
Figure B-8   Results of Lateral Scattering of
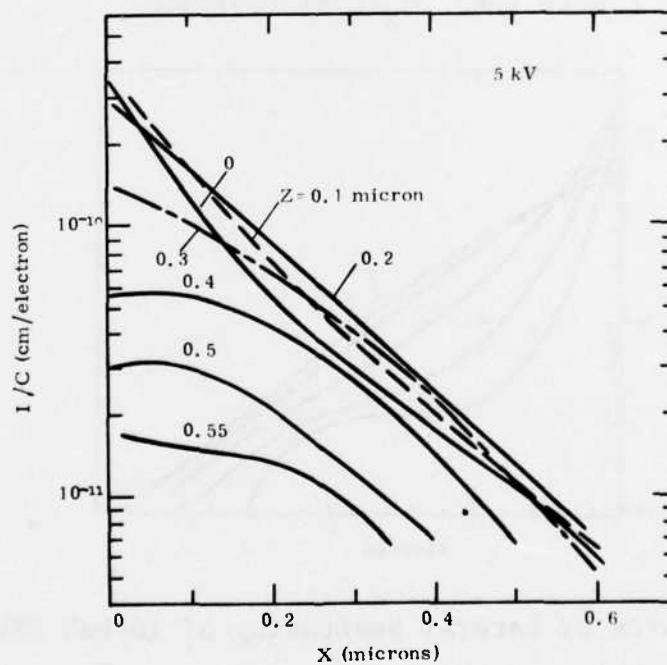   10-keV Electron Beam

Figure B-9   Results of Lateral Scattering of
               10-keV Electron Beam

Constant $C = 1.49 \times 10^{22}$ eV/cm^3. Selected results are compared to Cohn and Caledonia in Figures B-10 and B-11. These data are normalized as follows: all dimensions are normalized to Grün range $R_G = 4.1 \times E_0^{1.75} \times 10^{-6}$ g/cm^2 and $I_N(x/R_G, z/R_G) = E_0/R_G^2 I(x,z)$. This is analogous to the normalization of the Grün depth dose function, dE/dx. Note that the PMM data corroborates the Cohn and Caledonia data very well over the range given in their paper. The deviations for small x are probably due to a failure of the PMMM method. The deviations at large distances are probably due to the data range problem of Cohn and Caledonia. The poorer agreement at 5 keV is probably a partial failure of the PMM method, again because of the small distances involved.

In general it appears that the Cohn and Caledonia data fairly well describe the lateral scattering of bw (2 to 10 keV) electron beams in low Z solids. These data and the Possin and Norton data can be used to describe the generation of electron hole pairs in the archival target.

In many calculations it is important only that most of the ionization energy is contained within a hemisphere of depth 0.9 R_G and diameter 0.9 R_G. As in the section on resolution of the surface diode target, $I(x,z)$ or $G(r,z)$ can be integrated over an assumed electron beam spot profile to yield the ionization distribution in the target at various depths, Z.
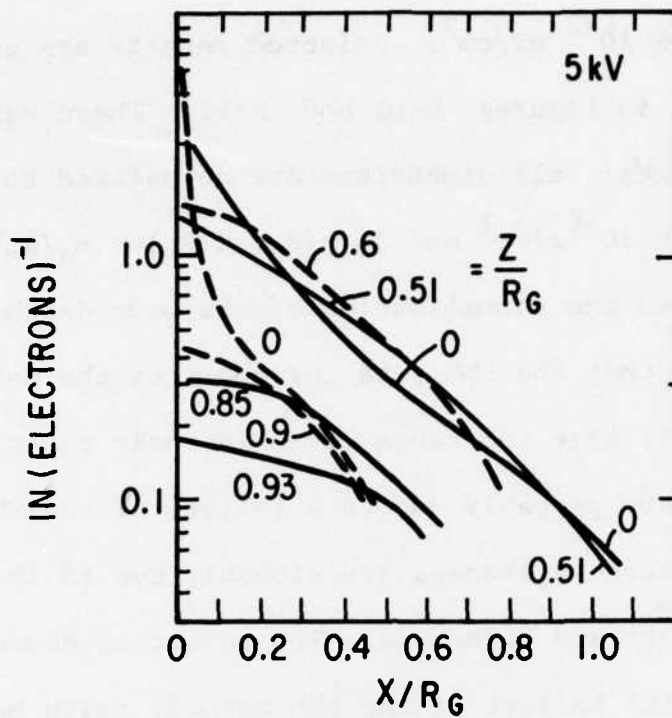
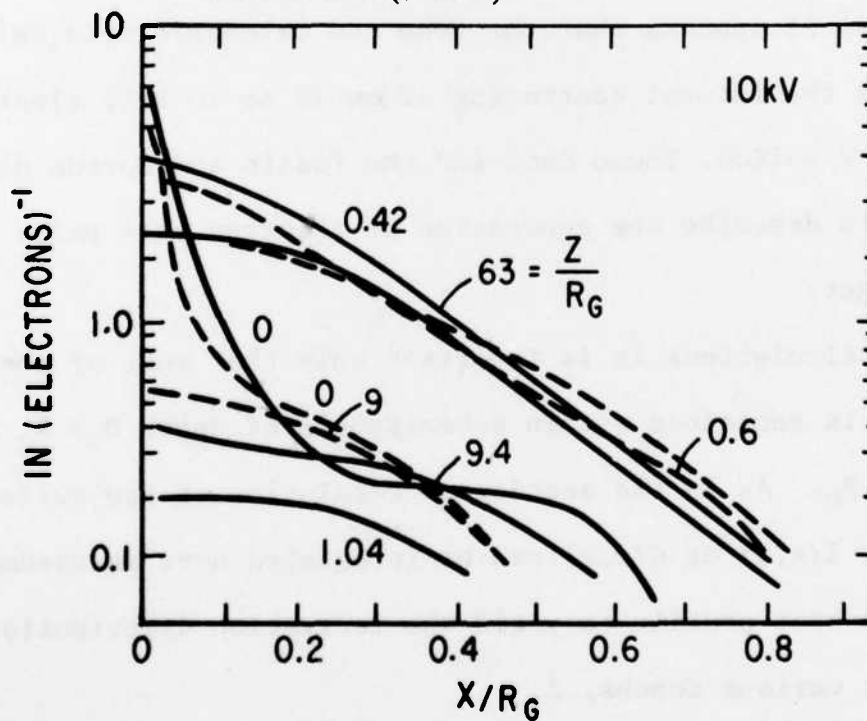**Figure B-10** Selected Results Compared to Cohn and
Caledonia (5 keV)

Figure B-11 Selected Results Compared to Cohn and
Caledonia (10 keV)

References

1. O. Meyer, Nucl. Instr. & Methods, $\underline{70}$, (1969) pp. 279-284.

2. J. Lindmayer and J. F. Allison, COMSTAT Tech. Rev., Vol. 3, No. 1, (1973) pp. 1-22.

3. J. Guildberg and D. Schroder, "Theoretical and Experimental Gain of Electron-Excited Silicon Targets," IEEE Transactions on Electron Devices, Vol. ED-18, November 1971, pp. 1029-1035.

4. H. Miller, W. K. Chu, J. W. Mayer, T. W. Sigmon, and T. R. Cass, Appl. Phys. Lett. $\underline{26}$, 292 (1975).

5. L. Csepregi, J. W. Mayer, T. W. Sigmon, Appl. Phys. Lett., $\underline{29}$, 92 (1976).

6. S. T. Pieraux, S. E. Westmoreland, J. W. Mayer, R. R. Hart and O. J. Marsh, Appl. Phys. Lett. $\underline{14}$, 7 (1969).

7. P. Glotin & J. Grappa, Int. Conf. on Application of Ion Beams to Semiconductor Tech., Grenoble, France, May 1967.

8. R. Bader & S. Kalbityer, Radiation Effects, $\underline{6}$, (1970) pp. 211-216.

9. See, e.g., W. R. Runyan, Semiconductor Measurements and Instrumentation (McGraw-Hill, New York, 1975) Chapter 3.

10. See, e.g., R. J. Archer and C. V. Shank, J. Opt. Soc., Am. 57, 191 (1967).

11. F. H. Hildebrand, Introduction to Numerical Analysis, McGraw-Hill Book Company (1956) p. 429.

12. William R. Smythe, Static and Dynamic Electricity, McGraw-Hill Book Company, 3rd Ed. 1968, pp. 189-190.

13. J. W. Mayer and O. J. Marsh, "Ion Implantation in Semiconductors", Applied Solid State Science, Vol. 1, (R. Wolfe, ed.), Academic Press, Inc., New York, N. Y., 1969, pp. 239-342.

14. J. F. Gibbons, "Ion Implantation in Semiconductors, Part II: Damage Production and Annealing," Proceedings of IEEE, Vol. 60, 1972, p. 1062.

References (continued)

15. Max Hansen, Constitution of Binary Alloys, McGraw-Hill Company, Inc., 1958.

16. Rodney P. Elliott, Constitution of Binary Alloys, First Supplement, McGraw-Hill Inc., 1965.

17. Francis A. Shunk, Constitution of Binary Alloys, Second Supplement, McGraw-Hill Book Company, Inc., 1969.

18. J. W. Mayer, J. M. Poate, K. Tu, "Thin Films and Solid Phase Reactions," Science, Vol. 190, pp. 228-234.

19. G. Ottaviani, V. Marrello, J. W. Mayer, M. S. Nicolet, J. M. Caywood, "Formation of Injecting and Blocking Contacts on High-Resistivity Germanium," Applied Physics Letters, Vol. 20, No. 8, April 15, 1972, pp. 323-325.

20. V. Marrello, T. A. McMath, J. W. Mayer, I. L. Fowler, "Nigh-Purity Germanium γ-Ray Spectrometers with Al Regrowth p^+ Contacts," Nuclear Instruments and Methods 108 (1973) pp. 93-97.

21. J. S. Best, J. O. McCaldin, "Interfacial Impurities and the Reaction Between Si and Evaporated Al," Journal of Applied Physics, Vol. 46, No. 9, September 1975, pp. 4071-4072.

22. K. Nakamura, M. A. Nicolet, J. W. Mayer, "Interaction of Al Layers with Polycrystalline Si," Journal of Applied Physics, Vol. 46, No. 11, November, 1975, pp. 4678-4684.

23. J. M. Caywood, A. M. Fern, J. O. McCaldin, G. Ottaviani, "Solid-Phase Growth of Ge from Evaporated Al Layer," Applied Physics Letters, Vol. 20, No. 8, April 15, 1972, pp. 326-327.

24. J. F. Gibbons, "Ion Implantation in Semiconductors--Part I: Range Distribution Theory and Experiments," Proceedings of the IEEE, Vol. 56 March 1968, pp. 295-319.

25. G. Dearnaley, J. H. Freeman, R. S. Nelson, and J. Stephen, Ion Implantation, American Elsevier, New York, N. Y., 1973.

26. H. Goldstein, Classical Mechanics, Addison Wesley Publishing Company, Reading, Massachusetts, 1950.

References (continued)

27. J. Lindhard, "Influence of Crystal Lattice on Motion of Energetic Charged Particles," _Matematisk-Fysiske Meddelelser_ (Denmark), Vol. 34, No. 14, 1965, 64 pp.

28. O. B. Firsov, "A Qualitative Interpretation of the Mean Electron Excitation Energy in Atomic Collisions," _Zhurnal Eksperimentnoi i Teoneticheskoi Fiziki_, Vol. 36, No. 5, 1959, pp. 1517-1523. English translation in Sovier Physics -- JETP, 36 (9), No. 5 pp. 1076-1080.

29. S. Furukawa and H. Matsumura, "Theoretical and Experimental Studies on Lateral Spread of Implanted Ions," _Third International Conference on Ion Implantation in Semiconductors and Other Materials_, Yorktown Heights, N. Y., 1972 (B. L. Crowder, ed.), Plenum Publishing Corporation, New York, N. Y., 1973, pp. 193-202.

30. J. Lindhard, M. Scharff, and H. E. Schott, "Range Concepts and Heavy Ion Ranges. II: Notes on Atomic Collisions," _Matematisk-Fysiskc Meddelelser_ (Denmark), Vol. 33, No. 14, 1963, 39 pp.

31. K. O. Nielsen, _Electromagnetically Enriched Isotopes and Mass Spectroscopy_, (M. L. Smith, ed.), Academic Press, Inc., New York, N. Y., 1956.

32. P. Jespersgard and J. A. Davies, "Ranges of Na, K, Kr, and Xe Ions in Amorphous Al2O3 in the Energy Region 40-1000 KEV," _Canadian Journal of Physics_, Vol. 45, No. 9, 1967, pp. 2983-2984.

33. Y. Akasaka, K. Horie, and S. Kawazu, "Lateral Spread of Boron Ion Implanted in Silicon," _Applied Physics Letters_, Vol. 21, No. 4, 1972, pp. 128-129.

34. G. Dearnaley, J. H. Freeman, G. A. Gard, and M. A. Wilkins, "Implantation Profiles of 32P Channeled into Silicon Crystals," _Canadian Journal of Physics_, Vol. 46, No. 6, 1968, pp. 587-596.

35. J. W. Mayer, L. Eriksson, and J. A. Davies, _Ion Implantation in Semiconductors_, Academic Press, Inc., New York, N. Y., 1970.

36. J. Lindhard, "Motion of Swift Charged Particles as Influenced by Strings of Atoms in Crystals," _Physics Letters_ (Netherlands), Vol. 12, No. 2, 1964, pp. 126-128.

References (continued)

37. L. Eriksson, J. A. Davies, and P. Jespersgard, "Range Measurements in Oriented Tungsten Single Crystals (0.1 - 1.0 MeV). I: Electronic and Nuclear Stopping Powers," _Physical Review_, Vol. 161, No. 2, 1967, pp. 219-342.

38. J. W. Mayer and O. J. Marsh, "Ion Implantation in Semiconductors," _Applied Solid State Science_, Vol. 1, (R. Wolfe, ed.), Academic Press, Inc., New York, N. Y., pp. 239-342.

39. J. F. Gibbons, "Ion Implantation in Semiconductors. Part II: Damage Production and Annealing," _Proceedings of IEEE_, Vol. 60, 1972, p. 1062.

40. J. A. Davies, J. Denhartog, L. Eriksson, and J. W. Mayer, "Ion Implantation of Silicon. I: Atom Location and Lattice Disorder by Means of 1.0 - MeV Helium Ion Scattering," _Canadian Journal of Physics_, Vol. 45, No. 2, 1967, pp. 4035-4072.

41. L. Eriksson, J. A. Davies, N. G. E. Johansson, and J. W. Mayer, "Implantation and Annealing Behavior of Group III and V Dopants in Silicon as Studied by the Channeling Technique," _Journal of Applied Physics_, Vol. 40, No. 2, 1969, pp. 842-854.

42. J. W. Corbett, "Radiation Damage in Silicon and Germanium," _Proceedings of the International Conference on Ion Implantation_, Thousand Oaks, California, November 1970.

43. G. D. Watkins, "A Review of EPR Studies in Irradiated Silicon," _Radiation Damage in Semiconductors_, (P. Baruch, ed.), Dunod, Paris, France, 1965, pp. 97-113.

44. G. D. Watkins, "EPR and Optical Absorption Studies in Irradiated Semiconductors," _Radiation Effects in Semiconductors; Proceedings_ (F. L. Vook, ed.), Plenum Publishing Corporation, New York, N. Y., 1968, 67-81.

45. G. H. Kinchin and R. S. Pease, "The Displacement of Atoms in Solids by Radiation," _Reports on Progress in Physics_, Vol. 18, No. 1, 1955.

References (continued)

46. P. V. Pavlov, D. I. Tetel'baum, E. I. Zorin, and V. I. Alekseev, "Distribution of Implanted Atoms and Radiation Defects in the Ion Bombardment of Silicon (Monte Carlo Calculation Method)," Soviet Physics - Solid State, Vol. 8, No. 9, 1967, pp. 2141-2146.

47. P. Sigmund and J. B. Sanders, Proceedings of the Internal Conference on Applications of Ion Beams to Semiconductor Technology, (P. Glotin, ed.), Editions Ophyrs, Grenoble, France, 1967.

48. J. W. Mayer, L. Eriksson, S. T. Picraux, and J. A. Davies, "Ion Implantation of Silicon and Germanium at Room Temperature; Analysis by Means of 1.0-MeV Helium Ion Scattering," Canadian Journal of Physics, Vol. 46, No. 6, 1968, pp. 663-674.

49. L. C. Kimerling and J. M. Poate, to be published.

50. H. A. Bethe, M. E. Rose, and L. P. Smith, "Multiple Scattering of Electrons," Proceedings of the American Philosophical Society, Vol. 78, No. 4, 1938, pp. 573-585.

51. N. E. Mott and H. S. W. Massey, The Theory of Atomic Collisions, Clarendon Press, Oxford, England, 1950.

52. D. B. Brown and R. E. Ogilvie, "An Evaluation of the Archard Electron Diffusion Model," Journal of Applied Physics, Vol. 35, 1964, pp. 2793-2795.

53. G. Wentzel, "Dispersion of Corpuscular Rays as Diffraction Appearances," Zeitschrift für Physik, Vol. 40, No. 8, 1926, pp. 590-593.

54. V. E. Cosslett and R. N. Thomas, "Multiple Scattering of 5-30 keV Electrons in Evaporated Metal Films. I: Total Transmission and Angular Distribution," British Journal of Applied Physics, Vol. 15, 1964, pp. 883-907.

55. W. Bothe, "Law of Probability in the Variations in a Dielectric and the Absorption of α-Rays," Zeitschrift für Physik, Vol. 5, No. 1, 1921, pp. 63-69.

56. W. Bothe, Handbuch der Physik, Vol. 22/21, Springer-Verlag, Berlin, Germany, 1933.

References (continued)

57. G. Wentzel, "Theory of Scattering of β-Rays," _Annalen der Physik_, Vol. 69, December 12, 1922, pp. 335-368.

58. G. Moliere, "Theory of Scattering of Fast Charged Particles. I: Single Scattering in a Screened Coulomb Field," _Zeitschift für Naturforschung_, Vol. 2a, March 1947, pp. 133-145.

59. F. Lenz, "On the Scattering of Electrons of Intermediate Energy Through the Smallest Angles," _Zeitschift für Naturforschung_, Vol. 9a, March 1954, pp. 185-204.

60. G. H. Smith and R. E. Burge, "A Theoretical Investigation of Plural and Multiple Scattering of Electrons by Amorphous Films, with Special Reference to Image Contrast in the Electron Microscope," _Proceedings of the Physical Society_ (GB), Vol. 81, Pt. 4, April 1963, pp. 612-632.

61. H. W. Lewis, "Multiple Scattering in an Infinite Medium," _Physical Review_, Vol. 78, June 1, 1950, pp. 526-529.

62. L. V. Spencer, "Theory of Electron Penetration," _Physical Review_, Vol. 98, June 15, 1955, pp. 1597-1615.

63. H. Meister, "On the Theory of the Absorption of Mono-energetic Electrons in Metal Foils," _Zeitschift für Naturforschung_, Vol. 13a, October 1958, pp. 809-820.

64. K. Kanaya and S. Okayama, "Penetration and Energy-Loss Theory of Electrons in Solid Targets," Journal of Physics D: Applied Physics, Vol. 5, January 1972, pp. 43-58.

65. R. Shimizu, T. Ikuta, and K. Murata, "The Monte Carlo Technique as Applied to the Fundamentals of EPMA and SEM," _Journal of Applied Physics_, Vol. 43, October 1972, pp. 4233-4249.

66. G. D. Archard, "Back Scattering of Electrons," _Journal of Applied Physics_, Vol. 32, August 1961, pp. 1505-1509.

67. D. B. Brown and R. E. Ogilvie, "An Electron Transport Model for the Prediction of X-Ray Production and Electron Back-scattering in Electron Microanalysis," _Journal of Applied Physics_, Vol. 37, November 1966, pp. 4429-4433.

68. A. J. Bennett and L. M. Roth, _The Effect of Primary Electron Diffusion on Secondary Electron Emission_, Report No. 71-C-318, General Electric Company, Schenectady, N.Y., November 1971.

References (continued)

69. E. Lifshin, _The Generation and Detection of X-Rays in the Electron Microprobe and Scanning Electron Microscope_, Report No. 72-CRD-163, General Electric Company, Schenectady, New York, May 1972.

70. J. S. Greeneich and T. VanDuzer, "An Exposure Model for Electron-Sensitive Resists," _IEEE Transactions on Electron Devices_, Vol. ED-21, May 1974, pp. 286-299.

71. R. J. Hawryluk, A. M. Hawryluk, and H. I. Smith, "Energy in a Thin Polymer Film by Electron Beam Scattering," _Journal of Applied Physics_, Vol. 45, June 1974, pp. 2551-2566.

72. R. Bolon and E. Lifshin, "The Use of Monte Carlo Techniques for X-Ray Analysis of Thin Films and Fine Structure in SEM," _Proceedings of the Sixth Annual Scanning Electron Microscope Symposium_, ITT Research Institute, Chicago, Illinois, April 1973, p. 285.

73. C. Feldman, "Range of 1-10 keV Electrons in Solids," _Physical Review_, Vol. 117, 1960, pp. 455-459.

74. H. Kanter and E. J. Sternglass, "Interpretation of Range Measurements for Kilovolt Electrons in Solids," _Physical Review_, Vol. 126, April 15, 1962, pp. 620-626.

75. A. E. Grün, "Luminescent-Photometric Measurements of the Absorption of Energy of Electron Sources. One Dimensional Case in Air," _Zeitschift für Naturforschung_, Vol. 12a, 1957, pp. 89-95.

76. A. Cohn and G. Caledonia, "Spatial Distribution of the Fluorescent Radiation Emission Caused by an Electron Beam," _Journal of Applied Physics_, Vol. 41, August 1970, pp. 3767-3775.

77. T. E. Everhart and P. H. Hoff, "Determination of Kilovolt Electron Energy Dissipation vs. Penetration Distance in Solid Materials," _Journal of Applied Physics_, Vol. 42, 1971 pp. 5837-5846.

References (continued)

78. G. E. Possin and J. F. Norton, "Spatial Distribution of 5 and 10 Kilovolt Electron Beam Ionization in Solids," Proceedings of the Eighth Annual Scanning Electron Microscope Symposium, Illinois Institute of Technology Research Institute, Chicago, Illinois, April 1975, pp. 457-464.

79. B. W. Schumacher and S. S. Mitra, "Measuring Thickness and Composition of Thin Surface Films by Means of an Electron Probe," Proceedings: 1962 Electronic Components Conference, Washington, D. C., May 1962, Institute of Electrical and Electronic Engineers, New York, New York, 1962.

80. W. Ehrenberg and D. E. N. King, "The Penetration of Electrons into Luminescent Materials, "Proceedings of the Physical Society (GB), Vol. 81, Pt. 4, April 1963, pp. 751-766.

-332-